ULTRA-WIDEBAND ANTENNA CHARACTERIZATION AND MEASUREMENTS

Stanislav Licul

Dissertation submitted to the Faculty of the
Virginia Polytechnic Institute & State University
in partial fulfillment of the requirement for the degree of

Doctor of Philosophy
in
Electrical Engineering

Committee Members:
William A. Davis, Chair
Warren L. Stutzman
Ioannis M. Besieris
Timothy Pratt
Werner E. Kohler

September 17, 2004
Blacksburg, Virginia

Keywords: Ultra-Wideband, Antenna, Pole/Residue Models

ULTRA-WIDEBAND ANTENNA CHARACTERIZATION AND MEASUREMENTS

Stanislav Licul

(ABSTRACT)

A new methodology is presented for characterizing an antenna system both in the time and frequency domain with one set of parameters using a singularity expansion method representation. A minimal set of parameter modeling antenna systems using the Matrix-Pencil method has been demonstrated. It has been shown that it is possible to obtain frequency-domain patterns from pole/residue models of antenna realized effective length. Thus, a pole/residue model of the antenna realized effective length presents a complete description in both the time and frequency domains. Once such a model is available, one can obtain the antenna pattern, directivity and gain in the frequency domain and the radiated transient waveform for an arbitrary excitation waveform and an arbitrary antenna orientation.

Acknowledgements

Prof. William A. Davis provided me with much needed advice and encouragement. Throughout the course of this research Prof. Davis generously provided his time to advise me and encourage discussion. I would like to thank Prof. Warren L. Stutzman for his support and encouragement throughout my time with the Antenna Group. Prof. Ioannis M. Besieris's support, throughout my education at Virginia Tech, is greatly appreciated. I would like to thank Dr. Argy Petros for his encouragement and support. I would like to thank Prof. T. Pratt and Prof. W. E. Kohler for serving as committee members.

Mr. Randall Nealy provided me with needed advice in the antenna measurements. I am very thankful for his advice and support in pursuing my research. I would to thank Ivan, Apostolos, Elisabeth, Nikola, and Davor for their encouragement during my studies.

I would like to thank all the members of Virginia Tech Antenna Group that I had the pleasure working with.

At the end, none of this would be possible without the support and love of my parents – Stanislav and Bruna Licul.

Table of Contents

List of Figures

List of Tables

Chapter 1

Introduction

"Ultra-wideband technology holds great promise for a vast array of new applications that have the potential to provide significant benefits for public safety, businesses and consumers in a variety of applications such as radar imaging of objects buried under the ground or behind walls and short-range, high-speed data transmission" [1.1].

This quote from the FCC press release on the authorization of ultra-wideband technology (UWB) clearly elevates the level of importance of the UWB technology. UWB applications are numerous. The FCC outlined imaging systems, ground penetrating radar systems, wall-imaging systems, through-wall imaging systems, medical systems, surveillance systems, vehicular radar systems, communications, and measurements systems as possible applications of UWB technology. The spectrum allocated for UWB is in the range from 1.99 GHz - 10.6 GHz, 3.1 GHz - 10.6 GHz, or below 960 MHz depending on the particular application [1.1].

The spectrum allocated certainly requires transmitters and receivers with wideband antennas. The type of modulation the UWB system is employing will determine the wideband antenna specifications. The most popular ones are pulse or impulse modulation approach (e.g. pulse position and amplitude modulation) and multi-carrier modulation approach (e.g. OFDM). Impulse modulation leads to interest in time-domain antenna characteristics (peak amplitude, pulse duration, pulse type) and multi-carrier modulation relates to frequency domain characteristics (gain, directivity, antenna pattern). Is it possible to obtain an antenna model that combines both time and frequency domain characteristics?

1.1 Ultra-wideband Technology

The major developments in UWB technology occurred when both Tektronix and Hewlett-Packard developed a sampling oscilloscope in the 1960s. The circuits used in these devices provided for sub-nanosecond baseband pulse generation. Robbins was the first to invent a sensitive baseband receiver in 1972. The first patented design of a UWB communication system was by Ross at the Sperry Rand Corporation [1.2]. Morey at the Geophysical Survey Systems Corporation commercialized the first ground penetrating radar based on UWB in 1974 [1.2].

A major breakthrough occurred in UWB communications when R. Scholtz at the University of Southern California presented a multiple access technique for UWB communications systems [1.2]. With that development, UWB was no longer limited to radar and point-to-point communication. It was possible also to implement wireless networks.

As mentioned earlier, two modulation schemes are used in implementation of UWB systems: impulse modulation and multi-carrier modulation. UWB system with impulse modulation transmits a stream of baseband pulses. The pulses are extremely short, in the range from nanosecond to subnanosecond duration. Two modulation schemes are pulse position modulation and amplitude modulation. Both of these modulation schemes are directly affected by antenna system. Both the transmit and the receive antenna will distort the pulse shape. In that sense, for optimal performance of impulse UWB system one needs to know what happens to the pulse while being transmitted and received. In the impulse modulation schemes, antenna effects play a significant role since each antenna system has it own unique transfer function.

One of the most popular multi-carrier modulation schemes is orthogonal frequency division multiplexing (OFDM), which uses densely spaced subcarriers and overlapping spectra to modulate information. OFDM transmits data by dividing a high rate data into several parallel bit streams. Each data stream is modulated on individual subcarriers. OFDM offers robustness against narrowband interference. The antenna effect in the multi-carrier systems is not very pronounced. Even dispersive antennas are easily handled by pilot carriers. In terms of multi-carrier modulation, primary concerns are antenna pattern and gain.

Channel characterization is performed with assumption about antenna effects. In UWB antenna characterization one should be able to exclude the antenna effects from the channel model since different systems would use different antenna types with their unique characteristics. Usually, UWB antennas are often modeled by a differentiation operation in some recent channel modeling techniques, but this is a wrong interpretation, as will be shown in Chapter 3 [1.3, 4].

The research presented in this work sheds new light on antenna design for UWB applications both in the time and frequency domain. Also, it provides a new methodology in measuring UWB antennas. The antenna models created can be used with either UWB modulation scheme because it provides a complete antenna description in both of the domains.

The research presented provides a unique representation of the antenna system. It provides a new methodology in measuring and modeling of antennas.

1.2 Dissertation Overview

Current frequency and time-domain models are limited to particular antenna geometry or domain. Thus, it is important to develop a methodology and a model that describes the antenna in both the time and frequency domain. The research presented in this work presents solutions to some of these problems by using the singularity expansion method representation and spectral estimation techniques.

A unified frequency and time-domain antenna representation via singularity expansion method is discussed in Chapter 2. By combining an effective length description with the singularity expansion method representation one can obtain a minimal unified (time and frequency domain) representation of the antenna system. The same set of parameters, s-plane singularities, can represent time and frequency antenna characteristics.

Measurement techniques using a vector network analyzer are discussed in Chapter 3. Also, a description is given of the properties of three classes of antennas. Resonant, traveling wave, and frequency independent antennas are investigated in terms of efficiency, peak power, pulse shape and duration, and their usefulness in terms of the UWB communications.

In Chapter 4, a discussion is given of the spectral estimation methods as a way to extract poles and residues from the measured transient waveform (e.g. antenna effective length). Prony's method and Matrix Pencil method are analyzed in depth and new modified techniques are presented.

Chapter 5 demonstrates a minimal model representation through antenna realized effective length and SEM representation of antenna system. After obtaining the antenna realized effective length, the Matrix Pencil method is applied in order to obtain poles and residues of a particular antenna system. This technique can be applied to any antenna structure providing both time and frequency characterization of the antenna.

Chapter 6 demonstrates, for the first time to our knowledge, the antenna pattern synthesis from the pole and residue model of the antenna realized effective length. The concept is demonstrated using Vivaldi antenna. Summary of all the results and proposal for future work is given in Chapter 7.

References

[1.1] New Public Safety Applications and Broadband Internet Access Among Uses envisioned by FCC Authorization of Ultra-Wideband Technology. Source: http://www.fcc.gov/Bereaus/Engineering_Technology/News_Releases/2002/nret0203.html

[1.2] J. H. Reed (editor), *Introduction to Ultra-Wideband Communications,* Prentice Hall, New York, 2004 (to be published).

[1.3] F. Ramirez-Mirales, "Signal Design for Ultra Wideband PPM Communications," *in Proceedings of MILCOM*, Vol. 2, pp. 1085-1088, Oct. 2002.

[1.4] B. Uguen, E. Plouhinec, Y. Lostanlen, and G. Chassay, " A Deterministic Ultra Wideband Channel Modeling," *IEEE Conference on Ultra Wideband Systems and Technologies*, pp. 1–5, May 2002.

Chapter 2

Unified Frequency and Time-Domain Antenna Representation via the Singularity Expansion Method

Antenna modeling for a dual frequency and time-domain representation is best performed using a fundamental quantity, the antenna effective length. Traditionally, antenna systems are modeled by the Friis transmission formula and impedance. However, antenna parameters, such as gain and aperture, are defined only in a narrowband sense (one frequency). Thus, the representation is not adequate for describing the antenna in the time domain. However, the antenna effective length describes the antenna system from a signal performance point of view rather than a power concept, allowing an ultra-wideband use [2.1].

The antenna effective length is in essence a transfer function between the input signal and the radiated field. By combining the effective length description with a singularity expansion method (SEM) representation, one can obtain a minimal unified (time and frequency domain) representation of the antenna system, to be described in the following chapters. Characterization of the antenna using the SEM point of view is discussed in this chapter. One has to note that SEM is not a numerical method or analytical formulation. In fact, SEM is a representation in terms of the s-plane singularities in whatever type of problem formulation is used and has a physical basis [2.2]. The same set of parameters, s-plane singularities (comprised of poles and residues), can represent both antenna time and frequency characteristics when one models the effective length of the antenna using the SEM representation.

Various approaches to obtaining the SEM representation of the antenna system are discussed in this chapter. We begin the chapter with a discussion of radiation and reception using the antenna effective length.

2.1 Modeling of Antenna Radiation and Reception via Antenna Effective Length

It is useful to define an antenna effective length $\vec{h}(\theta, \phi, \omega)$ in order to model the antenna radiation and reception in both the time and frequency domains. The antenna effective length is defined in the far field in terms of the current distribution[1] as [2.1]

$$\vec{h}(\theta,\phi,\omega) = -\frac{\hat{r}\times\hat{r}\times}{I_t}\int_V \vec{J}(\vec{r}^{\,'})e^{j\beta\hat{r}\cdot\vec{r}^{\,'}}\,dV^{'}, \tag{2.1}$$

---

[1] The effective length defined by W. L. Stutzman and G. A. Thiele is the complex conjugate, denoted h^*, since the effective length is associated with the transmitting case and the definition of the open-circuit voltage across the antenna terminals is a receiving relationship [2.3].

where I_t is an excitation current, $\vec{J}(\vec{r}\,')$ is antenna current density vector, $\beta = \omega/c$, and $\hat{r} = \vec{r}/|\vec{r}|$.

Three approaches are outlined in the following sections that model antenna reception and radiation characteristics using the antenna effective length. The first approach by D. L. Sengupta and C.-T. Tai is based on the frequency domain and obtains the effective lengths of both transmitting and receiving antennas [2.4]. The second approach by A. Shlivinski *et al.* uses time-domain techniques in order to obtain transmitting and receiving antenna effective lengths [2.5]. Both of these approaches are aimed mainly at describing the antenna transient characteristics.

The third approach, by W. A. Davis, is aimed at the development of a relationship between antenna gain and antenna aperture through a time-domain reciprocity theorem [2.1, 6]. This approach encompasses both the time and frequency domain. In a very elegant manner antenna characteristics (e.g., radiated field, directivity, gain, etc.) are described in both of the domains using the antenna effective length.

2.1.1 D. L. Sengupta and C.-T. Tai Approach

In the first approach, the far-field electric-field intensity produced by a transmitting antenna can be written in terms of the effective length in the following form [2.4]

$$\vec{E}(\vec{r},\omega) = -\frac{j\omega\mu}{4\pi r} I_t(\omega)\vec{h}(\omega)e^{-j\beta r} \tag{2.2}$$

The transmit antenna effective length is expressed in terms of the electric current as

$$\vec{h}(\omega) = -\frac{1}{I_t}\hat{r}\times\hat{r}\times \int\limits_{Antenna} \vec{J}(\vec{r}\,',\omega)e^{+j\beta\hat{r}\cdot\vec{r}\,'}dv' \tag{2.3}$$

In order to express the open-circuit voltage of the receiving antenna, Sengupta and Tai use the incident magnetic field, $\vec{H}^i(\omega)$, for a loop-type of problem as

$$V_{oc} = -j\omega\mu\vec{H}_i(\omega)\cdot\vec{S}(\omega) = \vec{E}^i(\omega)\cdot\vec{h}(\omega)\,, \tag{2.4}$$

where $\vec{S}(\omega)$ is vector effective area. The relationship between the vector effective area and the vector effective length is

$$\vec{S}(\omega) = \left(-\frac{j}{\beta}\right)\left(\hat{r}\times\vec{h}(\omega)\right). \tag{2.5}$$

The unit vector pointing opposite to the direction of incidence of the incoming wave is $\hat{r}$.

The expression for the load current for an incident field originating from a transmit antenna of vector effective length $\vec{h}_t(\omega)$ is

$$I_r(t) = \frac{-j\mu}{8\pi^2 r}\int_{-\infty}^{\infty} \omega I_t(\omega)\vec{h}_r(\omega)\cdot\vec{h}_t(\omega)(Z_r + Z_L)^{-1} e^{j\omega(t-\frac{r}{c})}\, d\omega\,, \tag{2.6}$$

where Z_r is the input impedance of the receiving antenna operating in the transmitting mode, Z_L is the load impedance, and $\vec{h}_r$ is the effective length of the receive antenna.

Sengupta and Tai applied the results to a linear traveling wave antenna and a short dipole antenna. This approach mainly focused on explaining the antenna transient characteristics. There were no attempts to relate classical frequency-domain antenna parameters to the transient domain.

2.1.2 A. Shlivinski *et al.* Approach through the Retarded Vector Potential

In the second approach, the electric field in the far zone of the transmitting antenna is defined as [2.5]

$$\vec{E}(\vec{r},t) = -\frac{\mu}{4\pi r} I^{+}(t) \otimes \vec{h}^{t}_{Shlivinski}(\theta,\phi,t-r/c)\,, \tag{2.7}$$

where $I^{+}(t)$ is the forward propagating current and does not include reflected components as in the total current I_t. The effective length can be put in the form

$$\vec{h}^{t}_{Shlivinski}(\theta,\phi,t) = -\hat{r}\times\left(\hat{r}\times\int_{Antenna}\frac{\partial}{\partial t}\frac{\vec{J}_a\left(\vec{r}\,',t+\hat{r}\cdot\vec{r}\,'/c\right)}{I^{+}}dv'\right), \tag{2.8}$$

for an impulse input current $I^{+}(t) = \delta(t)$. In this effective length formulation, the time derivative is included in the definition of the antenna effective length, which is not the case with the expressions (2.1) and (2.7). Through the reciprocity theorem the following relationship between the transmitting and receiving antenna effective lengths is obtained:

$$\frac{1}{2}\vec{h}^{t}_{Shlivinski}(\hat{r},t) = \frac{\partial}{\partial t}\vec{h}^{r}_{Shlivinski}(\hat{r},t) \tag{2.9}$$

Finally, Shlivinski *et al.* give the antenna load current as

$$I_L(t) = \frac{\mu}{16\pi r}\frac{1}{Z_{0t}Z_{0r}}\left[\left(\vec{h}^{t}_{T}(\hat{r}_{TR},\cdot)\overset{\bullet}{\otimes}\vec{h}^{t}_{R}(\hat{r}_{RT},\cdot)\right)\otimes\partial_t^{-1}V_g(\cdot)\right](\tau), \tag{2.10}$$

where ∂_t^{-1} is an integration operation, τ is the delay time over the propagation path. In their formulation, Shlivinski *et al.* have incorrectly represented the antenna match at the transmit and receive antennas with the simplified assumption of a Z_0 antenna impedance. This assumption is valid only for a limited set of antennas. Shlivinski *et al.* do discuss the match issue further, but add a confusing set of notations to account for the process.

The results obtained in this time-domain antenna characterization were applied to a short dipole system. This approach also considers the relationships to antenna gain and the Friis transmission formula. The results are of analytical nature and are based on the slant stack transform (SST) of the time-domain current distribution.

2.1.3 W. A. Davis Approach Through Reciprocity Theorem

In order to investigate the receive and transmit antenna relationships, one has to start with the reciprocity theorem as outlined in [2.1, 6]

$$\int_V \bar{J}_1 \cdot \bar{E}_2 dV = \int_V \bar{J}_2 \cdot \bar{E}_1 dV \, . \tag{2.11}$$

It is possible to obtain an expression of the open-circuit voltage in the far-field as

$$V_{oc} = -\frac{1}{I_t} \int_{Antenna} \bar{J}_a(\bar{r}') \cdot \bar{E}_{inc}(r')\, dv' \, , \tag{2.12}$$

where the open-circuit voltage is defined as

$$V_{oc} = \vec{h} \cdot \vec{E}_{inc}^{(0)} \, , \tag{2.13}$$

$\vec{E}_{inc}^{(0)}$ is the incident field at the antenna reference point, I_t is the excitation current, and $\vec{h}$ is antenna effective length. The antenna effective length can be expressed in terms of radiated field ($\vec{E}_{rad}$) as

$$\vec{h} = \frac{\vec{E}_{rad}(\theta,\phi)}{j\omega\mu\Psi(r)I_t}, \Psi(r) = \frac{e^{-j\beta r}}{4\pi r} \tag{2.14}$$

The time-domain expression for the effective length with an input current of $I_t\delta(t)$ is

$$\vec{h}(\theta,\phi,t) = -\hat{r} \times \left(\hat{r} \times \int_{Antenna} \frac{\vec{J}_a(\vec{r}', t + \hat{r}\cdot\vec{r}'/c)}{I_t} dv' \right) \tag{2.15}$$

The corresponding open-circuit voltage is

$$v_{oc}(t) = \vec{h}(\theta,\phi,t) \overset{\bullet}{\otimes} \vec{E}_{inc}(\theta,\phi,t)\,, \tag{2.16}$$

where $\overset{\bullet}{\otimes}$ represents the dual convolution and dot product operation. In the next section it will be shown how this representation is applied to obtain the antenna directivity and gain in terms of the antenna effective length.

2.1.4 Antenna Directivity

It is important to define the antenna in terms that are useful for specific communication applications. If time-domain modulation is used, an obvious choice will be to characterize the antenna in the terms of the radiated pulse width/type and peak amplitude (e.g. pulse position modulation - PPM). If frequency modulation schemes are used, then it is more useful to define the antenna in terms of classical frequency domain concepts as directivity and gain (e.g. OFDM/CDMA modulation schemes)

One definition of the directivity in the time domain is proposed in the first approach by D. L. Sengupta and C.-T. Tai. It could be useful to define a directivity of the antenna radiating a transient signal in terms of the energy content of the signal. The directivity in terms of the vector effective length is classically defined as

$$D(\theta,\phi,\omega) = \left|\vec{h}(\theta,\phi,\omega)\right|^2 \left(\frac{1}{4\pi} \int_0^{4\pi} \left|\vec{h}(\theta,\phi,\omega)\right|^2 d\Omega \right)^{-1}. \tag{2.17}$$

In the time domain, such a definition does not have direct meaning. Two options are available. First, the $\left|\vec{h}(\theta,\phi,t)\right|$ might be replaced in time by the maximum in time of $\left|\vec{h}(\theta,\phi,t)\right|$. However, this replacement does not conserve power as formed in the frequency-domain form. An alternate form that is consistent with a correlation receiver is given in terms of the signal energy as

$$D(\theta,\phi) = \frac{\left(\int_{-\infty}^{\infty} \left|\vec{h}(\theta,\phi,t)\right|^2 dt \right)}{\frac{1}{4\pi} \int_0^{4\pi} \int_{-\infty}^{\infty} \left|\vec{h}(\theta,\phi,t)\right|^2 dt d\Omega}. \tag{2.18}$$

Using Parseval's theorem, Eq. (2.18) can be written in the frequency domain as an alternate definition. The gain of the antenna, which is related to the antenna efficiency, was not attempted by D. L. Sengupta and C.-T. Tai.

2.1.5 Antenna Efficiency, Gain, and Polarization

The definitions of gain, polarization, and efficiency of the antenna in the frequency domain are not applicable to the time-domain antenna description. The frequency domain interpretation of the realized gain is [2.7][2]

$$G_R = e\,qD\,, \tag{2.19}$$

where e is the radiation efficiency due to radiation resistance, q is the radiation efficiency due to impedance mismatch.

The IEEE definition of the antenna efficiency is [2.7][2]

$$e = \frac{P_{rad}}{P_{accepted}}\,, \tag{2.20}$$

where P_{rad} is total power radiated and $P_{accepted}$ is the net power accepted by the antenna at its terminals during the radiation process. This definition is restricted to narrowband concepts. H. S. Schantz proposes a wideband definition of the antenna efficiency in the following way [2.8]

$$e_{Schantz} = \frac{P_{rad}}{P_{applied}}\,. \tag{2.21}$$

Here $P_{applied}$ is the net power applied at the antenna terminals. In an UWB sense, or short pulse radiating antenna, efficiency is a function of frequency.

In the third approach by W. A. Davis, the antenna realized gain is obtained through definitions of the effective aperture. The realized effective area in terms of the antenna effective length could be defined as [2.1,6]

$$A_R = e\,q\frac{120\pi}{4R_{rad}}\left|\vec{h}(\theta,\phi,\omega)\right|^2 \tag{2.22}$$

Now, one can define the classical frequency-domain antenna gain in terms of the effective length as [2.1,6]

$$G_R(\theta,\phi) = \frac{120\pi^2}{\lambda^2 R_{rad}}\left|\vec{h}(\theta,\phi,\omega)\right|^2 \tag{2.23}$$

---

[2] The definition of the realized gain is put in the notation used by W. L. Stutzman and G. A. Thiele [2.20]. The IEEE standard uses η to denote the antenna efficiency and M to denote the radiation efficiency due to impedance mismatch.

The antenna polarization depends on the polarization of the incoming wave, thus the polarization mismatch is not included in the definition of the realized gain. Circular polarization in the time domain is not a very meaningful concept. Measurements of the polarization in the time domain mostly relate to the orientation of the radiated pulse.

As is shown, it is possible to express all classical antenna radiation parameters in terms of the antenna effective length. However, in order to transform between the time and frequency domain representations, one needs to perform a Fourier transformation. By using the singularity expansion method, one is able to use a single set of parameters to represent the antenna in both domains and simplify the representation. In the following section we will discuss the properties of the singularity expansion method (SEM) and ways of obtaining the antenna representation.

2.2 Singularity Expansion Method (SEM)

The singularity expansion method (SEM) is used to characterize the electromagnetic response of structures (e.g. aircraft, antennas) in both the time and complex frequency domains. SEM was first introduced by C. E. Baum and was inspired by typical transient responses of various complicated scatterers [2.2, 9]. The measured transient responses were usually a few-cycles of damped sinusoids. The two-sided Laplace transform of a damped sinusoid is one real pole or a pair of conjugate poles in the complex frequency plane. Thus, the resonant frequencies of the specific object are expected to correspond to frequencies near these poles.

The Laplace transform[3] of $f(t)$ is usually an analytical function $F(s)$. “A function $F(s)$ is said to be analytical at a point $s = s_0$ if it is defined and has a derivative at every point in some neighborhood of s_0” [2.10]. However, for some values of *s* the Laplace transform will not be an analytical function of *s*. Thus, it is important to characterize the properties of these singularities in order to define $F(s)$ everywhere in the *s*-plane. The various methods of integration in order to avoid singularities, either poles, branch point, and branch cut, are described in [2.11, 12, 13]. The usual procedure is to use contour integration.

Once the singularity is defined and analytically treated, it is added as a contribution to the rest of the analytical function. The singularity contributions are utilized in characterization of the transient response of an object. Moreover, single singularities (first-order poles) are used in the SEM representation of an antenna. For passive systems (e.g., antennas), the first-order poles are located on the left-hand *s*-plane.

To develop general SEM equations one needs to start with the integral equation in terms of the current density source. This requires a dyadic operator. The formulation of SEM presented below follows the development of C. E. Baum [2.2,9]. The following expression is a convenient starting point [2.2]

---

[3] The two-sided Laplace transform of an arbitrary function $f(t)$ is defined as $F(s) = \int_{-\infty}^{\infty} f(t)e^{-st}dt$, where $s = \sigma + j\omega$ is a complex variable.

$$\int_V \overline{\overline{\Gamma}}(\vec{r},\vec{r}',s)\cdot J(\vec{r},s)dv' = I'(\vec{r},s) \tag{2.24}$$

In this relationship, $\overline{\overline{\Gamma}}(\vec{r},\vec{r}',s)$ is dyadic Green's function (C. E. Baum calls this the dyadic kernel of the integral equation) and $I'(\vec{r},s)$ is a forcing function (e.g. the electric field). Singular forms of the spatial integral may be required for proper definition in the region of the spatial singularity. The current source $J(\vec{r},s)$ could be volume current density, surface current density, or line current.

To obtain the most convenient expression for the development of the general SEM equations, the forcing function $\vec{I}(\vec{r},s)$ needs to be replaced with an appropriately normalized temporal delta function or frequency equivalent. With this new formulation Eq. (2.25) can be written as

$$\int_V \overline{\overline{\Gamma}}(\vec{r},\vec{r}',s)\cdot U(\vec{r},s)dv' = \vec{I}(\vec{r},s). \tag{2.25}$$

The quantity $\vec{U}(\vec{r},s)$ are surface currents induced by delta function excitation on finite-size perfectly conducting objects in free space. The equation above can be solved numerically using the method of moments (MOM) by converting it into a matrix equation

$$\left[\overline{\overline{\Gamma}}_{n,m}(s)\right]\cdot\left[U_n(s)\right] = \left[I_n(s)\right] \qquad n,m = 1,2,3,......,N \tag{2.26}$$

One has to note that $\left[\overline{\overline{\Gamma}}_{n,m}(s)\right]$ are analytic functions of s and related to the dyadic Green's function. Baum expanded the currents induced on finite-size perfectly conducting objects in free space in a pole series as

$$\vec{U}(\vec{r},s) = \sum_{\alpha}\frac{\eta_\alpha(1_0,s)\vec{v}_\alpha(\vec{r})}{(s-s_\alpha)^{m_\alpha}} + W(1_0,s) \tag{2.27}$$

In this expression η_α is a coupling coefficient, v_α is natural mode, s_α is a natural frequency (pole), 1_0 is unity dyadic, m_α is a positive integer (often unity), and W is an entire function. The coupling coefficients are dependent on the antenna orientation while the poles are independent of antenna orientation.

In SEM computations the incident waveform is usually known. Thus, SEM is used to represent an antenna response in terms of the natural frequencies s_α, coupling coefficients η_α, and natural modes v_α. The natural modes and natural frequencies can be calculated from

$$\int_V \overline{\overline{\Gamma}}(\vec{r},\vec{r}',s_\alpha)\cdot\vec{v}_\alpha(\vec{r}') = 0, \tag{2.28}$$

where s_α define the null space of the operator. The MOM formulation of this equation is

$$\left\lfloor \overline{\overline{\Gamma}}_{n,m}(s_\alpha) \right\rfloor \cdot [v_n]_\alpha = [0_n]. \tag{2.29}$$

The natural frequencies are found through

$$\det\left\lfloor \overline{\overline{\Gamma}}_{n,m}(s_\alpha) \right\rfloor = 0. \tag{2.30}$$

To find the coupling coefficients, it is first useful to find the coupling vectors from

$$\int_V \mu_\alpha(\vec{r}) \cdot \overline{\overline{\Gamma}}(\vec{r}, \vec{r}\,', s_\alpha) dv' = 0 \tag{2.31}$$

or

$$[\mu_n]_\alpha \cdot \left\lfloor \overline{\overline{\Gamma}}_{m,n}(s_\alpha) \right\rfloor = [0_n]. \tag{2.32}$$

From these coupling vectors, Baum shows that the coupling coefficients are given by

$$\eta_\alpha(s_\alpha) = \frac{\int_V \mu_\alpha(\vec{r}) I(\vec{r}, s) dv}{\int_V \mu_\alpha(\vec{r}) \int_{V'} \frac{\partial}{\partial s} \overline{\overline{\Gamma}}(\vec{r}, \vec{r}\,', s) \nu_\alpha(\vec{r}\,') dv' dv} \tag{2.33}$$

Once the poles, coupling coefficients, and natural modes are obtained, one is able to describe the antenna response. The next section discusses the application of the SEM representation of a thin-wire scatterer. The results use Pocklington's equation for a numerical solution.

2.2.1 SEM Representation of the Thin-Wire Scatterer

The monopole/dipole configurations of a thin wire scatterer were analyzed in the early 1970s primarily to investigate the effects of the electro-magnetic pulse (EMP) on electronic systems [2.14, 15, 16]. F. M. Tesche used the SEM representation to obtain the poles and residues of a thin wire scatterer [2.16]. The following development by F. M. Tesche uses the Pocklington type integro-differential equation in terms of complex frequency $s = j\omega + \sigma$. The equation is written in the following form:

$$-s\varepsilon_0 E^{inc}(z, s) = \int_0^L I(z', s)\left(\frac{\partial^2}{\partial z^2} - \frac{s^2}{c^2}\right) K(z, z', s) dz'. \tag{2.34}$$

Here, the kernel K is given by

$$K(z,z',s) = \frac{1}{2\pi a}\int_0^{2\pi} \frac{e^{(-sR/c)}}{4\pi R} a\, d\phi \tag{2.35}$$

with

$$R = \left[(z-z')^2 + d^2 \sin^2\left(\frac{\phi}{2}\right)\right]^{1/2}. \tag{2.36}$$

Eq. (2.34) is put into matrix form using the method of moments formulation, originally developed by Harrington [2.32],

$$[Z(s)]\,[I(s)] = [V(s)]. \tag{2.37}$$

The poles of a current function $I(z,s)$ in the complex plane are equivalent to finding the frequencies at which there exists a nontrivial solution of (2.34) with $E^{inc} = 0$ [2.16]. In essence the poles of the thin wire, s_α, are such that

$$[Z(s_\alpha)]\,[I(s_\alpha)] = 0, \tag{2.38}$$

where $I(s_\alpha)$ represents the ν_α of the SEM formulation. The equation for obtaining the poles of a thin wire could be cast in the following form

$$\det[Z(s_\alpha)] = 0 \tag{2.39}$$

The coupling vector $[C_\alpha]$ is determined from

$$[Z(s_\alpha)]^T\ [C_\alpha] = 0 \tag{2.40}$$

The coupling vector $[C_\alpha]$ represents $[\mu_n]_\alpha$ of the SEM formulation. The resultant time-domain SEM representation of the current given by Tesche on the thin wire becomes

$$[i(t)] = \sum_\alpha [C_\alpha][C_\alpha]^T [U(t)][V(s)]e^{s_\alpha t}, \tag{2.41}$$

where $[U(t)]$ is a diagonal matrix of unit Heaviside functions, which serves to enforce the requirements of causality. One has to note that the denominator of Eq. (2.33) was set to unity in order to obtain the representation in Eq. (2.41). The frequency domain solution could be obtained easily with only 10 inversions of the integral equation. This reduces the computation time compared to the classical Fourier transform method. Even a more computationally efficient method is the time-domain SEM proposed by W. A. Davis and

J. T. Cordaro [2.19]. Fig. 2.1 shows a typical pole plot for a dipole antenna structure [2.15].

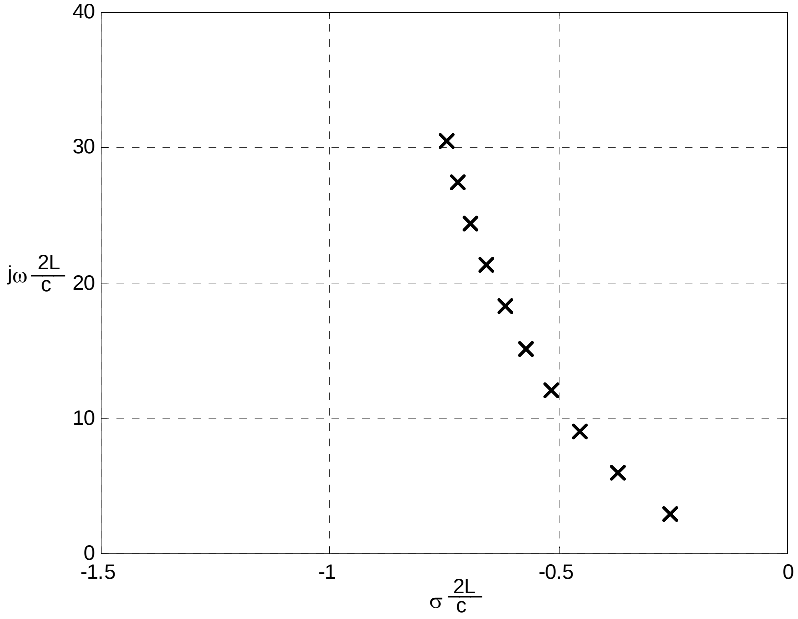

Figure 2.1. Typical pole plot of a dipole antenna [2.15]

The SEM representation modeling of the current in terms of poles and residues, of a current on a thin wire provides some interesting observations. First, for the late time response ($ct/L > 3$) only 3 to 4 poles may be required for an accurate description. The complete time response can be accurately described with ten poles for practical systems. The advantage of fewer poles is that only a few parameters are needed to represent the antenna current. Second, it is important to notice that any pole contributing to radiation must not lie on the $j\omega$ axis. The reason for such a condition is that the radiation process requires the current on the wire to eventually reach a zero value as power is radiated. Next, by increasing the diameter of a wire the poles move further away from the $j\omega$ axis. This indicates that broadband antenna structures would have poles located further from the $j\omega$ axis than narrow band antenna structures. Finally, it is stated by F. M. Tesche and L. Marin, that the response function for bodies of finite extent has only poles and no brunch cuts [2.16,17,18].

2.2.2 SEM Representation via other Computational Techniques

The antenna current, radiated field, link response of two antennas, and the antenna effective length can be obtained using various numerical methods. Once a numerical solution is obtained one can apply spectral estimation techniques to obtain the SEM representation.

The method of moments, MOM, is the integral-equation method mainly used for analyzing wire antennas [2.3,20]. The MOM was used by Tesche to obtain the SEM representation of the current on a thin wire scaterrer as in the last section. The method provides accurate results if used properly. The MOM method has been used to model surfaces, dielectrics, and to obtain the antenna response in the time domain.

The finite-difference time-domain, FDTD, method is a differential equation based method [2.21]. The basic principle of FDTD is in applying second-order central difference approximations to the space and time derivatives of the electric and magnetic fields for the corresponding differential operators of Maxwell's equations [2.21]. The FDTD method is used in analyzing both time and frequency-domain radiation characteristics of an antenna that forms a boundary of the solution region. The frequency-domain response is obtained by using a Fourier transformation. FDTD is typically found to provide excellent results for finite-size dielectrics. Using FDTD one can obtain the antenna effective length by modeling the whole link or by obtaining the radiated field at specific points in space. However, in FDTD one needs to model antennas and the space in between to obtain a solution for a two-antenna link. In that sense, if one puts the antennas at a far-field distance, the problem space becomes extremely large. A computationally efficient solution is provided by J. M. Johnson and Y. Rahmat-Samii [2.22].

The finite element method, FEM, is a differential equation, frequency-domain based method where the electric field is approximated on a set of finite elements or cells [2.23,24,25]. The FEM requires introduction of a radiation boundary condition for open-region antenna problems. The boundary conditions simplify the problem and reduce simulation time. To obtain a time-domain solution one needs to solve the problem for a set of frequencies and perform a Fourier inversion. Thus, the problem becomes computationally very large.

The transmission-line modeling method, TLM, became feasible when G. Kron developed an equivalent transmission-line circuit to model free space [2.26]. The technique allows solution of Maxwell's equations in a circuit simulator. Further advances have been achieved with the theory of pulse propagation on transmission lines and development of a numerical technique compatible with computational techniques for the solution of two-dimensional electromagnetic problems [2.27]. The TLM method is a powerful time-domain method for numerous applications (e.g., antenna, waveguide, diffusion, acoustics).

The geometrical theory of diffraction, GTD, is an analytic field-based method, and it is used for scattering and antenna analysis [2.3, 28, 29]. It is a very good tool for large objects. The GTD method has been improved through the years. The physical theory of diffraction, PTD, is a related analytic method mostly used in scattering problems. Both PTD and GTD are mostly used in scattering, reflection, and diffraction problems at high frequencies. Since SEM represents global features of an object, the SEM representation is not adequate to represent some diffraction contributions to the problem solution. A hybrid method has been devised by E. Heyman and L. B. Felsen that combines both SEM and GTD/PTD methodology [2.30].

In essence, one is able to obtain the antenna effective length from the MOM, FDTD, FEM, or TLM methods. One could simulate a total link and obtain the received current (through specified load) and the open circuit voltage, or obtain antenna-radiated field. For frequency-domain techniques one would need to solve a problem for a large number of frequencies, which makes a problem computationally intensive.

2.3 Conclusions

By using the antenna effective length, one can model antennas in both the time and frequency domains through a common set of parameters using the SEM representation. Since antennas are finite size objects, the SEM representation would only have singularities (poles/residues) in the left hand complex plane (passive systems).

Numerical methods are very computationally intensive and antenna type selective. Thus, it becomes a question of convergence and accuracy of numerical results for a broad range of frequencies or corresponding time. Both numerical and measurement approaches provide advantages and disadvantages [2.31]. We will take a measurement approach in obtaining the antenna effective length.

The next chapter discusses the time and frequency-domain response properties of three different classes of antennas: resonant, traveling-wave, and frequency-independent antennas.

References

[2.1] W. A. Davis and S. Licul, “Ultra-Wideband Antennas,” in *Introduction to Ultra-Wideband Communications*, edited by J. H. Reed, Prentice Hall, New York, 2004 (to be published).

[2.2] C. E. Baum, “The Singularity Expansion Method,” in *Transient Electromagnetic Fields*, pp. 129-179.

[2.3] W. L. Stutzman and G.A. Thiele, *Antenna Theory and Design 2nd edition*, John Wiley & Sons, New York, 1998.

[2.4] D. L. Sengupta and C.-T. Tai, ”Radiation and Reception of Transients by Linear Antennas,” in *Transient Electromagnetic Fields*, pp. 181-235

[2.5] A. Shlivinski, E. Heyman, and R. Kastner, “Antenna Characterization in the Time Domain,” *IEEE Trans. Antennas Propagat.*, Vol. 45, No. 7, July 1997.

[2.6] W. A. Davis, ”A Reciprocity Development of the Relationship between Antenna Gain and Antenna Aperture,” *Personal Notes*, 2002.

[2.7] IEEE Standard Definitions of Terms for Antennas, IEEE Std 145-1993 (Revision of IEEE Std 145-1983).

[2.8] H. G. Schantz, “Radiation Efficiency of UWB Antennas,” *IEEE Conference on Ultra Wideband Systems and Technologies*, May 2002.

[2.9] C. E. Baum, “On the Singularity Expansion Method for the Solution of Electromagnetic Interaction Problems,” *Interaction Notes 88*, Dec. 1971.

[2.10] R. E. Ziemer, W. H. Tranter, and D. R. Fannin, *Signals and Systems: Continuous and Discrete 3rd edition*, Macmillan, New York, 1993.

[2.11] B. Van Der Pol and H. Bremmer, *Operational Calculus Based on the Two-Sided Laplace Integral*, Cambridge University Press, London, 1959.

[2.12] R. V. Churchill, *Operational Mathematics 3rd edition*, McGraw-Hill Book Company, New York, 1972.

[2.13] R. V. Churchill, *Modern Operational Mathematics in Engineering*, McGraw-Hill Book Company, New York, 1944.

[2.14] F. M. Tesche, “On the singularity expansion method as applied to electromagnetic scattering from thin-wires,” *AFWL Interaction Note 102*, April 1972.

[2.15] P. R. Barnes, "On the singularity expansion method as applied to the EMP Analysis and Simulation of the Cylindrical Dipole Antenna," *AFWL Interaction Note 102*, April 1972.

[2.16] F. M. Tesche, "On the Analysis of Scattering and Antenna Problems Using the Singularity Expansion Technique," *IEEE Trans. Antennas Propagat.* , vol. AP-21, No. 1, pp. 53-62, Jan. 1973.

[2.17] L. Marin, "Application of the Singularity Expansion Method to Scattering from Imperfectly Conducting Bodies and Perfectly Conducting Bodies within a Parallel Plate Region", *Interaction Note 116*, June 1972.

[2.18] L. Marin, "Transient Electromagnetic Properties of Two Parallel Wires," *Sensor and Simulation Note 173*, March 1973.

[2.19] J. T. Cordaro, W. A. Davis, "Time-Domain Techniques in the Singularity Expansion Method," *IEEE Trans. Antennas Propagat.* , vol. AP-29, No. 3, pp. 534-538, May 1981.

[2.20] C. A. Klein and R. Mittra, "The effect of different testing functions in the moment method solution of thin wire antenna problems," *IEEE Trans. Antennas Propagat.* , Vol. 23, No. 9, pp. 258-261, March 1975.

[2.21] C. G. Buxton, "Design of a broadband array using the foursquare radiating element," *Ph. D. Dissertation,* Virginia Polytechnic Institute and State University, USA, 2001.

[2.22] J. M. Johnson and Y. Rahmat-Samii, "MR/FDTD: A Multiple-Region Finite-Diffrence Time-Domain Method," *Microwave and Optical Technology Letters*, Vol. 14, No. 2, February 5, 1997.

[2.23] W. A. Davis, Class Notes ECE6124, Advanced Numerical Electromagnetics, 2001.

[2.24] J. Jin, *The Finite Element Method in Electromagnetics 2nd edition*, John Wiley & Sons, New York, 2002.

[2.25] Agilent HFSS 5.5 User's Manual, Agilent Technologies, December 1999.

[2.26] G. Kron, "Equivalent circuit of the field equations of Maxwell – I," *Proc. IRE*, vol. 32, pp. 289-299, 1944.

[2.27] Rao, S. M., *Time Domain Electromagnetics,* Academic Press, San Diego, 1999.

[2.28] F. A. Molinet, "Geometrical Theory of Diffraction (GTD) – Part I: Foundation of the Theory," *IEEE Antennas Propagat. Society Newsletter*, August 1987.

[2.29] F. A. Molinet, “Geometrical Theory of Diffraction (GTD) – Part II: Extensions and Future Trends of the Theory,” *IEEE Antennas Propagat. Society Newsletter*, October 1987.

[2.30] E. Heyman and L. B. Felsen, “A wavefront interpretation of the singularity expansion method,” *IEEE Trans. Antennas Propagat.* , vol. AP-33, No. 7, pp. 706-718, July 1985.

[2.31] R. Mittra, “Integral Equation Methods for Transient Scattering,” in *Transient Electromagnetic Fields*, pp. 73-128.

[2.32] R. F. Harrington, *Field Computation by Moment Methods*, Macmillan, New York, 1968.

Chapter 3

The Properties of Antennas Excited by a Gaussian Pulse

The properties of a 5.0 GHz resonant monopole, a TEM horn, a ridged TEM horn, a log-periodic toothed trapezoid antenna (LPTA), an Archimedean spiral, a Vivaldi antenna, and a bi-conical antenna were investigated. The impulse and frequency responses were compared and the usefulness in UWB technology evaluated based on duration, type, and amplitude of the radiated transient waveform.

Two identical antennas were measured using a HP8510. The antennas were separated by 1.20 meters and oriented in a co-polarized position. The HP8510 measurement ports were calibrated at the antenna connectors inside an anechoic chamber. In our experiment we obtained a 50% pulse width of 50 ps corresponding to a 20 GHz frequency spectrum from an inverse fast-Fourier transform (IFFT). The impulse response, s_{21} transmission coefficient, and s_{11} reflection coefficient were measured. The measurement setup is illustrated in Fig. 3.1.

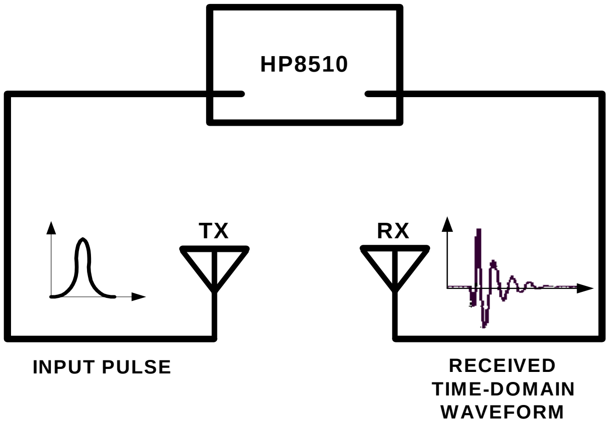

Figure 3.1. Measurement Setup

3.1 HP8510 Time-Domain Data Processing

The HP8510 measures both amplitude and phase of the DUT/AUT in the frequency domain. To obtain the time-domain response, one needs to perform a discrete Fourier transform (DFT). The DFT can be performed using readily available FFT algorithms or a chirp-z algorithm. In this section we explain time-domain processing by the HP8510 and present an alternative method of obtaining the time-domain response using MATLAB®.

The HP8510 collects the data in the frequency domain and internally uses a chirp-z transform to convert the frequency-domain data to the time domain. The data in this dissertation was typically processed separately and did not use the internal transform feature. The antennas were measured inside the anechoic chamber with HP8510. The calibration was done at the antenna ports over a frequency range of 50.0 MHz to 20.05 GHz.

The calibration is essential to good data collection and precautions were made to ensure good dynamic range and valid calibration up to 20 GHz. Fig 3.2 shows the total cable loss and the noise level present in the anechoic chamber measurements. The cable loss at 20.0 GHz is around 40.0 dB. The noise level stays constant in the range from 50 MHz - 11.0 GHz at a relative level of –110 dB. The noise increased in the range of 11 - 20 GHz due to a signal generator problem to around –90 dB. The signal generator level was 20 dB lower than expected. This problem was fixed for some later measurements for a noise level around –110 dB level.

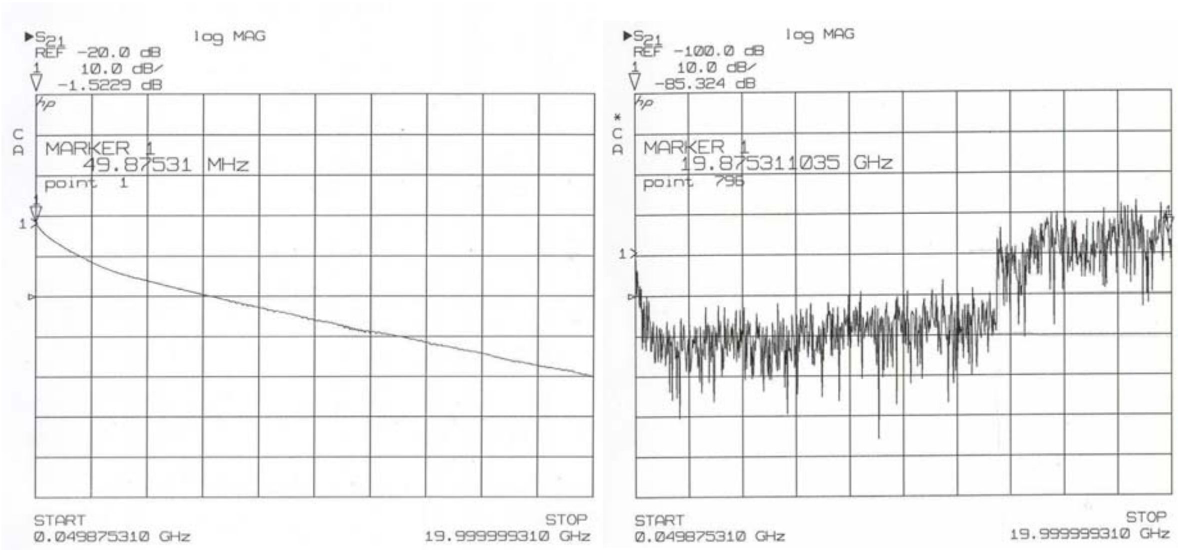

Figure 3.2. Measured cable loss and the noise level in the anechoic chamber measurements

There are several parameters that need to be set to take the measurements: start and stop frequency, number of data points, step/ramp mode, and time delay due to long cables. The start and stop frequencies and number of points (np) determine the time range of measurement with the following relationship

$$Range = \frac{(np-1)}{\Delta f}. \tag{3.1}$$

In our case $np = 801$, $\Delta f = (20.05 - 0.050)\,GHz$, and the calculated Range is $40\,ns$. Thus, the time-domain data is displayed at Δt samples

$$\Delta t = \frac{40\,ns}{801} = 50\,ps.$$

However, in the time-domain the data is actually sampled every 25 ps due to the inclusion of the negative frequencies. When the range on the HP8510 is reduced, the data is interpolated by a built in HP8510 interpolation routine.

The HP8510 can operate either in a ramp-sweep mode or a step-sweep mode. In the ramp-sweep mode, the network analyzer directs the source to sweep in a linear ramp over the selected frequency range. The synthesized sweepers use the “Lock-and-Roll” tuning technique. With this technique, the first frequency of the sweep is set with synthesizer accuracy and a linear analog sweep increases to the stop frequency. In the step-sweep mode, synthesizer-class frequency accuracy and repeatability is obtained by phase locking the source at each frequency step over the selected frequency range. This mode provides the highest accuracy, although at a reduced measurement speed [3.1].

The HP8510 measurements were compensated for the cable length. The total cable length in the anechoic chamber was 15.2 m. Thus, the signal coming from the AUT might not be at the same frequency as the network analyzer frequency. This can lead to ambiguous measurement results. If the AUT is connected to a long cable with time delay T and the network analyzer sweep rate is df/dt, the signal frequency at the end of the cable (input to the network analyzer receiver) will lag behind the network analyzer source frequency by the amount $f = T \cdot df/dt$. If this frequency shift is appreciable compared to the network analyzer IF detection bandwidth (typically in few kHz), then the measured result will be in error by the roll off of the IF filter [3.2]. The 16.24 m cable (including the line-of-sight path) will cause a delay of 90 ns. The receiver DWELL TIME parameter was set to 1 ms. This gives ample of time for the receiver to lock at the specific frequency and measure the response at the identical frequency that the receiver is locked on.

The conversion of data from the frequency domain to the time domain is done in the HP8510 using a chirp-z transform and windowing the frequency-domain data by a Kaiser window with an α=6 parameter. The Kaiser or Kaiser-Bessel window is defined by the relationship [3.3]

$$w(n) = \frac{I_0\left[\pi\alpha\sqrt{1.0 - \left(\frac{n}{N/2}\right)^2}\right]}{I_0\left[\pi\alpha\right]}, 0 \le |n| \le \frac{N}{2}, \tag{3.2}$$

where the zero-order modified Bessel function, $I_0(x)$, is defined by

$$I_0(x) = \sum_{k=0}^{\infty}\left[\frac{(x/2)^k}{k!}\right]^2. \tag{3.3}$$

The measured s_{21} frequency domain response was converted to a time-domain impulse response using the following expression:

$$s_{21}^{i}(t) = sf \cdot CZT\left[s_{21}(j\omega) \cdot w(n|\alpha = 6)\right], \tag{3.4}$$

where CZT is a chirp-z transform and ***sf*** is an appropriate scale factor. The scale factor is used to normalize the input pulse to amplitude of 1.0 Units. The scale factors (***sf***) used in the transformations are shown in Table 3.1. The measured s_{21} frequency domain response may be converted to the time-domain step response using the following expression:

$$s_{21}^{s}(t) = sf \cdot CZT\left[\frac{1}{j\omega} \cdot s_{21}(j\omega) \cdot w(n|\alpha = 6)\right] . \tag{3.5}$$

The $1/j\omega$ term is present because the step response transform pair is defined as

$$u(t) \Leftrightarrow \frac{1}{2\pi f} + \frac{1}{2}\delta(f) . \tag{3.6}$$

The equivalent procedure using an inverse fast-Fourier transform (IFFT) was used in order to obtain impulse and step responses using the frequency-domain data measured by HP8510 for external processing. A measured TEM horn/1.0 GHz monopole link response was used to compare the results from HP8510 time-domain processing and IFFT computations using MATLAB®.

Table 3.1. Different scaling factors (***sf***) used in transformation

Transform	*Response*	*sf*[4]
IFFT	Impulse	2
IFFT	Step	N/(2π)
Chirp-z	Impulse	2/N
Chirp-z	Step	1/(2π)

The amplitude s_{21} frequency response of the TEM Horn/1.0 GHz monopole link and Kaiser window are shown in Fig. 3.3. In order to use FFT, the low frequency points 0 MHz and 25 MHz were interpolated. For simplicity, the values were set to zero since interpolation provides identical results. The total number of points N is 1606 after adding in the negative frequency data. The point 804 was set to 0 to avoid Nyquist sampling ambiguity. The frequency is related to the sample number by the following expressions:

$$\begin{aligned} f_k &= k \cdot 25MHz, 0 \le k \le \frac{N}{2} - 1 \\ f_{-k} &= -k \cdot 25MHz, \frac{N}{2} + 1 \le k \le N \end{aligned} \tag{3.7}$$

The units of the s_{21} frequency response are dimensionless since s-parameters are ratios of power waves. The units for the s_{21} frequency response are unity giving the time-

---

[4] ***sf***(scale factor)*TF (amplitude after the transform) = amplitude of the received time-domain waveform
N = number of points used in transform

domain units as $[s^{-1}]$. The reasons for this notation comes from a Fourier transform defined by

$$\begin{gathered} s_{21}(t) = \frac{1}{2\pi}\int s_{21}(\omega)e^{j\omega t}d\omega \\ [s^{-1}] = [1/rad][unity][rad/s] \end{gathered} \tag{3.8}$$

The units are represented by a $[*]$ notation.

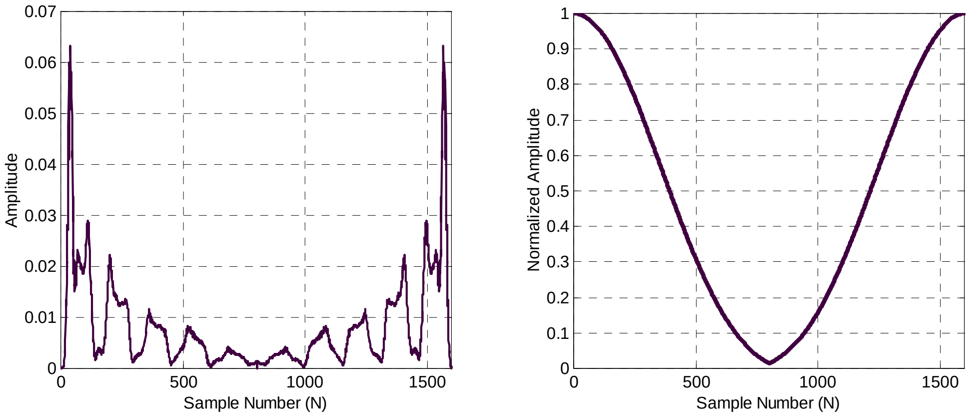

Figure 3.3. Measured s_{21} frequency response and Kaiser window

After applying the Kaiser window the lower frequencies in the spectrum are enhanced while the higher frequencies are attenuated. The resulting spectrum and the equivalent time-domain response are shown in Fig. 3.4.

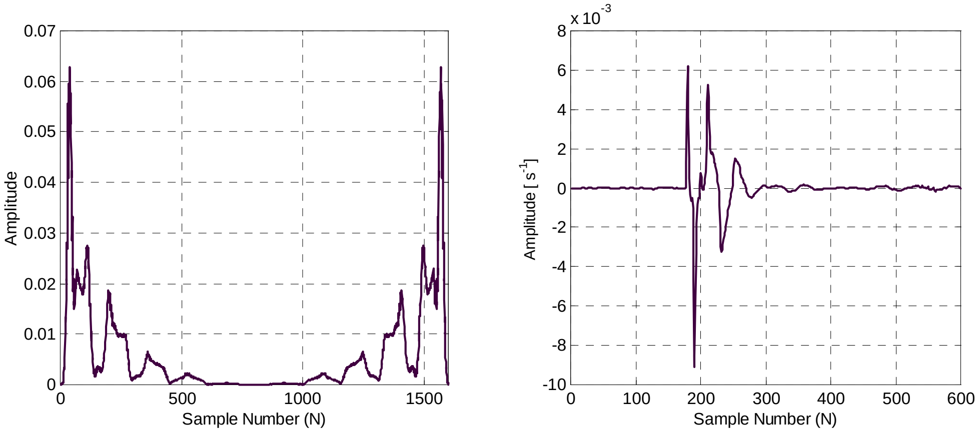

Figure 3.4. Measured s_{21} frequency response after applying Kaiser window and equivalent time-domain response

By comparing the time-domain responses, shown in Fig. 3.5, one can conclude that the processing is equivalent. The IFFT processing was done with MATLAB®.

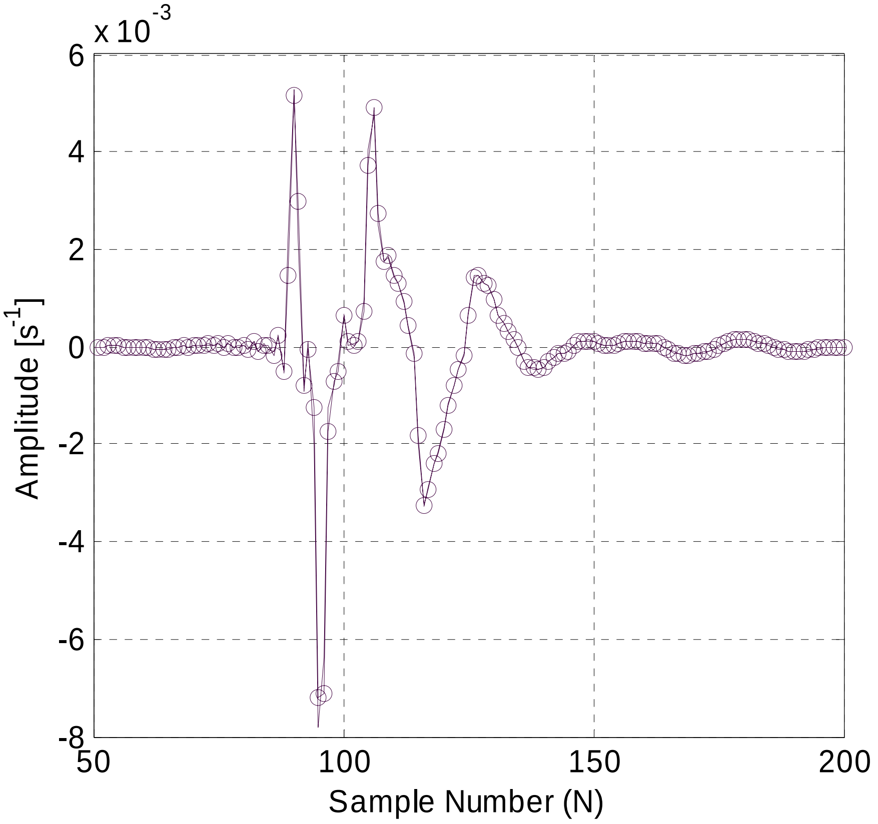

Figure 3.5. Comparison between the HP8510 (-) and MATLAB® processing (o)

The step response is obtained by using Eq. (3.5). The factor $1/j\omega$ acts as a low-pass filter that significantly attenuates the high frequency components. It is evident from Fig. 3.6 that the time-domain waveform does not reflect high frequency contributions. The equivalent step time-domain response is shown in Fig. 3.7. The waveform is much smoother than the impulse response and of little use in obtaining system poles.

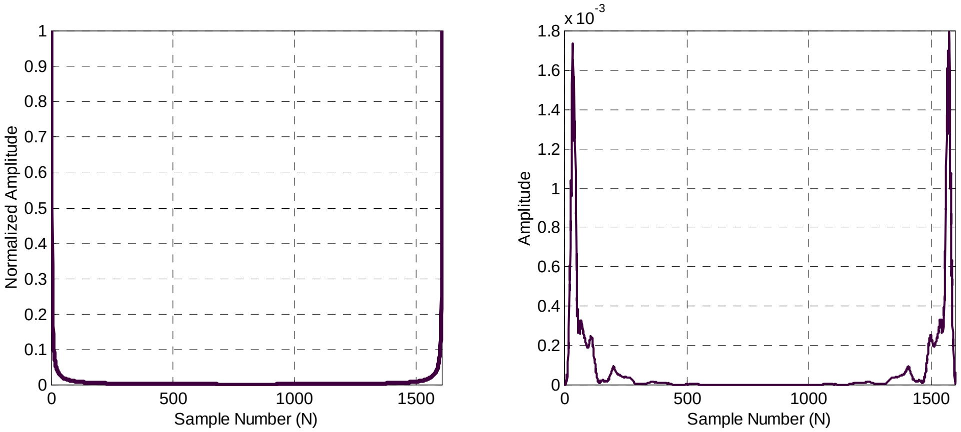

Figure 3.6. Low-pass filter and resulting s_{21} frequency response

In this section we investigated the processing of frequency-domain data using measured results in order to obtain the time-domain equivalent waveform. It was shown that the chirp-z and IFFT give the same results.

The Kaiser window and the step response both lower the sensitivity to the high frequency response and impair accuracy of high-frequency pole computation.

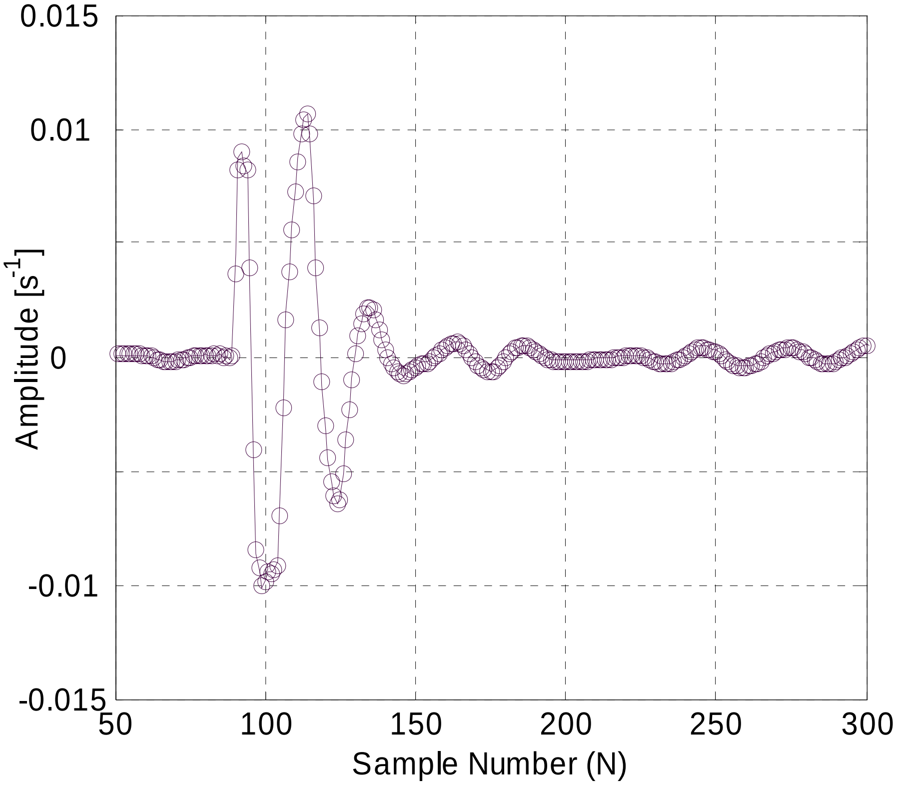

Figure 3.7. Comparison between the HP8510 (-) and MATLAB® processing (o)

3.2 TEM Horn and Ridged TEM Horn Antenna

To illustrate this processing we initially consider the TEM Horn. The TEM horn is a traveling wave antenna. TEM horns have been traditionally used for low-dispersion launching and receiving of ultra-wideband pulses. Research was conducted since the late 1970’s to further reduce dispersion caused by the TEM horn abrupt edges. In order to suppress the reflection from the TEM horn edges, the antenna is commonly loaded with chip resistors. Experiments were also conducted with tapered resistive coatings. The TEM horn may be used as a source for radiation through a tapered aperture. A tapered aperture reduces reflections of the aperture edges, enabling the incident wave to have a smooth transition. This configuration achieves lower side lobe levels [3.4,5,6].

One of the limitations the TEM horn antenna exhibits in terms of the bandwidth is the feeding structure. The antenna bandwidth is limited by a balun (feed) bandwidth. In order to use the TEM horn without balun, a ground plane is used with one of the TEM horn flanges placed above the finite size ground plane, as shown in Fig. 3.8.

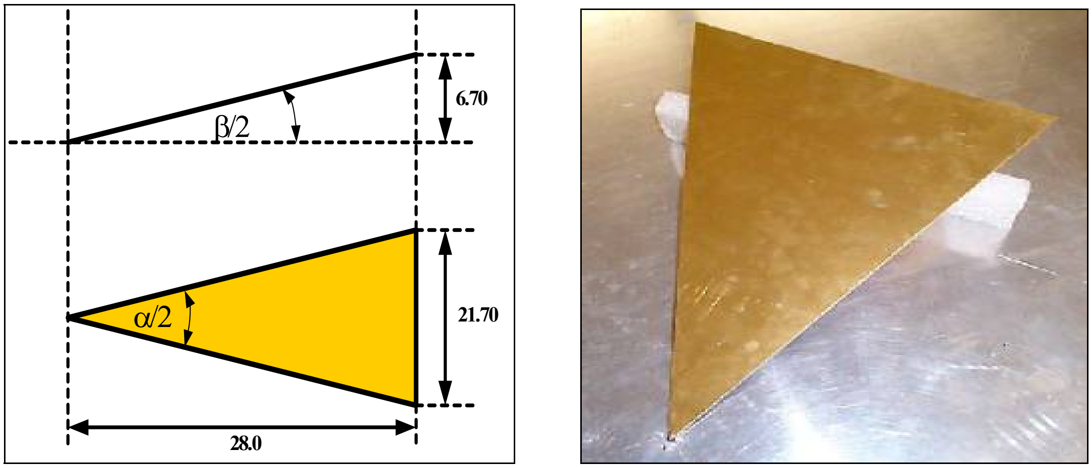

Figure 3.8. Geometry of the TEM horn antenna placed above the ground plane (all units in cm)

The usual procedure in designing the TEM Horn antenna is to determine the desired characteristic impedance. The solution presented by Yang and Lee is implicit [3.7]. The characteristic impedance is defined by

$$Z_c = \frac{\eta_0}{2}\frac{K(m_1)}{K(m)}\,. \tag{3.9}$$

By setting the characteristic impedance to a certain value one can solve for m where

$$K(m) = \int_0^{\pi/2} \frac{d\theta}{\sqrt{1 - m\sin^2\theta}}\,. \tag{3.10}$$

This is the complete elliptic integral of the first kind. In the integral, m is a parameter that can be set and $m_1 = 1 - m$. Next, one can find a parameter n by choosing a particular angle β using the following expression:

$$n = (m)\sin^2\left[K(m)\left(1 - \frac{\beta}{\pi}\right)\middle| m\right]. \tag{3.11}$$

Once n is determined the following set of equations is used to determine the parameters A, B, G, and R:

$$A = \frac{K(m)}{\Pi(n;\tfrac{\pi}{2}|m)} \tag{3.12}$$

$$B = \frac{1 - A}{\sqrt{n}} \tag{3.13}$$

$$G = \frac{1}{2}\ln\left[\frac{\sqrt{(1-n)(1-mB^2)} - \sqrt{(m-n)(1-B^2)}}{\sqrt{(1-n)(1-mB^2)} + \sqrt{(m-n)(1-B^2)}}\right] \tag{3.14}$$

$$R = \exp\left\{\frac{\sqrt{(1-n)(m-n)}}{A\sqrt{n}}\left[F(\arcsin B|m) - A\Pi(n;\arcsin B|m)\right] - G\right\}. \tag{3.15}$$

At the end, the angle α can be determined using the following expression:

$$\alpha = 2\arcsin\left(\frac{R^2 - 1}{R^2 + 1}\right). \tag{3.16}$$

The function Π is an elliptic integral of the third kind and is defined as

$$\Pi(n;\varphi|m) = \int_0^{\varphi} \frac{d\theta}{(1 - n\sin^2\theta)\sqrt{1 - m\sin^2\theta}}. \tag{3.17}$$

Recently, R. T. Lee and G. S. Smith presented results on TEM Horn antenna design [3.8]. The design curves were presented with on-axis gain related to physical parameters of the TEM Horn antenna.

The TEM Horn antenna design presented in Fig. 3.8 was optimized for maximum s_{21} impulse response amplitude. The TEM Horn antennas were separated 130.2 cm (distance to the antenna feed points) and placed on the 122x122 cm ground plane. The frequency and impulse response of the TEM Horn antenna link is shown in Fig. 3.9. The frequency response shows a broad peak centered around 4.0 GHz. The frequency response is less than 10 dB down from the peak in the range from 400 MHz to 14.0 GHz. Below 400 MHz, the frequency response exhibits sharp drop, characteristic for low frequency antenna response. A gradual drop in the frequency response is observed above 14 GHz. The peak value of the impulse response is $63 \cdot 10^{-3}\ s^{-1}$ and the impulse response duration is 0.4 ns. The impulse response shows some multi-path contributions in the range 5.5 to 7.0 ns, thought not significant.

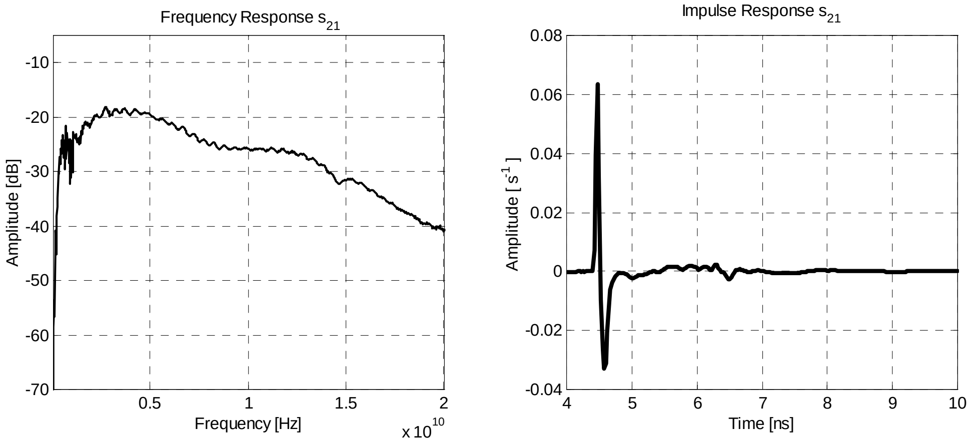

Figure 3.9. Measured frequency response and received time-domain waveform of the 2 TEM horn antenna link

The TEM Horn return loss and phase response of the link are shown in Fig. 3.10. The TEM Horn shows acceptable performance based on the return loss up to 15 GHz. The return loss is on average 10 dB down in the frequency range 1.0 to 15.0 GHz. The 2 TEM Horn link phase response is linear, as expected.

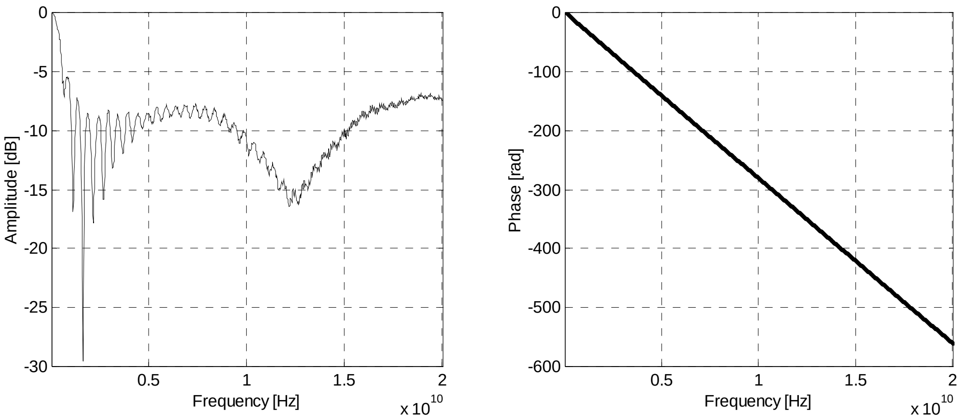

Figure 3.10. TEM horn return loss and phase of 2 TEM Horn antenna link

A commercial product, a variation of the TEM horn, is shown in Fig. 3.11. The manufacturer rated frequency-operating range of the double ridge TEM horn is 1.0 to 18 GHz. The antenna has an integrated balun.

Figure 3.11. Ridged TEM horn antenna[5]

The ridged TEM Horn s_{21} frequency and impulse response is shown in Fig. 3.12. The frequency response has a peak value slightly below 2 GHz. The frequency response drops sharply below 1.0 GHz. The impulse response is a damped sinusoid in the duration of 2.75 ns. The peak amplitude of the radiated waveform is $24 \cdot 10^{-3}\ s^{-1}$.

---

[5] Ridged TEM – Manufacturer: Antenna Research Associates (ARA); Model: DRG –118/A; Freq: 1.0-18.0 GHZ

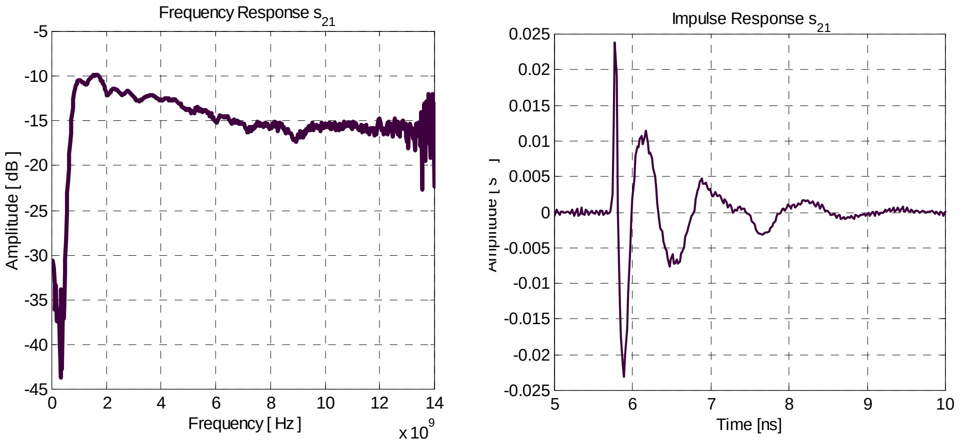

Figure 3.12. Measured frequency and time-domain response of 2-ridged TEM horn antenna link

The ridged TEM Horn return loss and the link phase response are shown in Fig. 3.13. The return loss is below 10 dB for most of the antenna operating frequency range. The return loss is few dB higher in the range 1.5 GHz to 3.5 GHz. The phase response of 2-ridged TEM Horn link is linear.

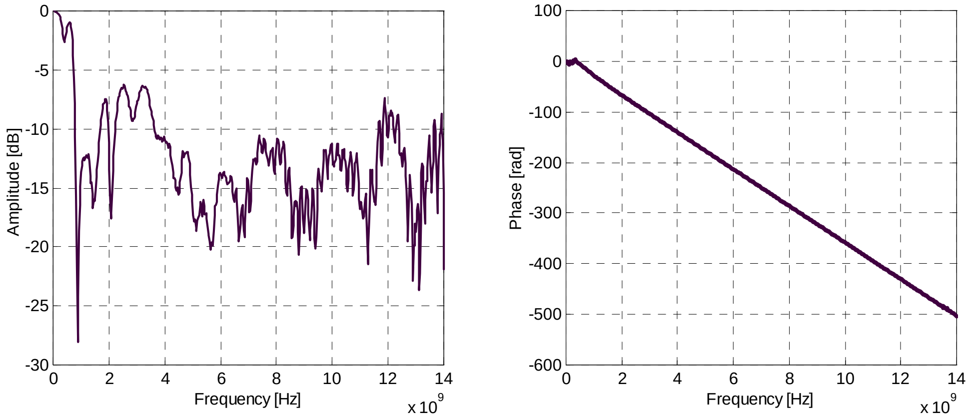

Figure 3.13. Ridged TEM horn return loss and phase of 2 TEM Horn antenna link

The designed TEM Horn antenna shows a less dispersive impulse response than ridged TEM Horn antenna with a slight nonlinear phase performance at low frequencies. The time domain amplitude of TEM Horn antenna is 2.6 higher compared to ridged TEM Horn antenna.

3.3 Resonant Monopole

Dipole radiation, excited by a short pulse, has been investigated and some of the results have been reported in [3.10-14]. Bantin [3.10] suggests the radiation occurs only at the dipole feed point and the dipole edges. Smith [3.12] suggests that the whole length of the dipole contributes to the antenna radiation. However, only one paper discusses the possibility of using a pair of 2-meter dipoles as a link for ultra-wideband communications [3.11]. A 5.0 GHz monopole on a 6λ circular ground plane is shown in Fig. 3.14.

Figure 3.14. 5.0 GHz monopole antenna on a 6λ circular ground plane

The frequency response shown in Fig. 3.15 addresses the issues of the efficiency of this transmission, compared to the TEM Horn. The frequency response shows the most efficient transmission at the resonant frequency around 5.0 GHz. The frequency response shows that the signal amplitude decays with a slope of 1 dB/GHz as the frequency increases from 4 GHz to 13 GHz. This type of response suggests that the monopole acts as a constant gain antenna. However, the response reflects the monopole impedance mismatch, which is very high in broad sense (e.g. 0-20 GHz), compared to the TEM Horn, with compensation of a higher boresight gain.

The impulse response is shown in Fig. 3.15. The measured waveform is a damped sinusoid. The damped ringing is in the duration of 1.00 ns, with a peak amplitude of the damped at about $1.5 \cdot 10^{-3}$ s^{-1}. The reflection of the ground plane edges is seen from 5.5 to 6.2 ns.

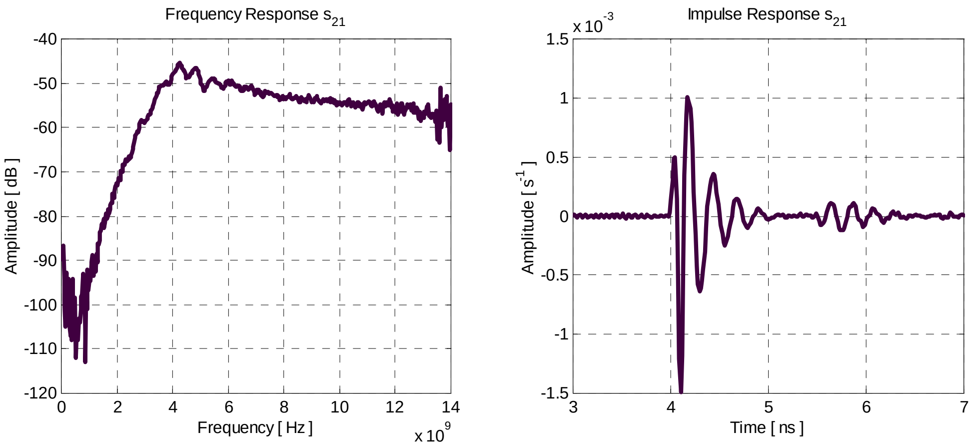

Figure 3.15. Measured frequency and time-domain response of the monopole link

We could argue the presence of the three loss mechanisms in this link: pattern mechanism, Friss transmission formula mechanism, and reflection coefficient mechanism. All these three mechanisms contribute to the overall efficiency of the system.

First, the monopole pattern changes while making the transition from the first to second resonant frequency. So, the co-polarized position of the monopoles at the first resonant frequency is no guarantee for the co-polarization at other frequencies. Second, the antenna path loss increases with frequency due to the Friss transmission formula. Finally, the reflection coefficient shown in Fig. 3.16 shows significant amount of energy is not propagated as the frequency increases before the second resonance at 15 GHz, though not as low a radiation as might be expected.

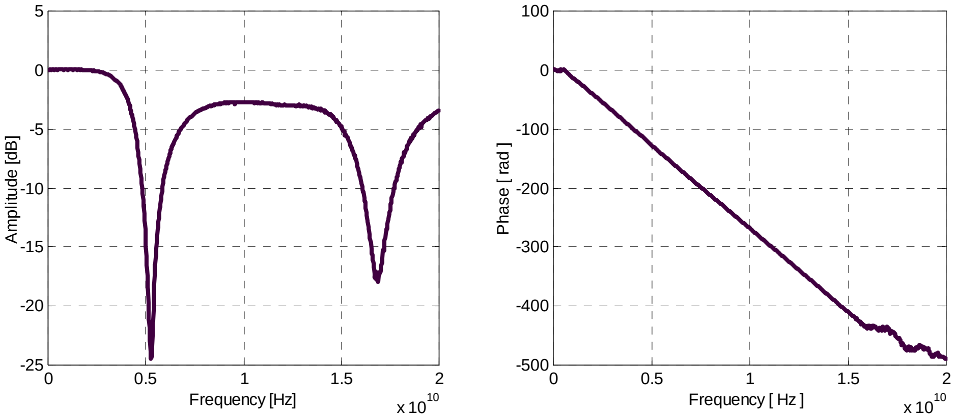

Figure 3.16. Return loss and phase response of the 5.0 GHz monopole link

The results indicate that two resonant monopoles could be used in an ultra-wideband communication link. The 5.0 GHz monopole link has time-domain response duration of 1.0 ns. The frequency response resembles a constant gain antenna response but the behavior is attributed to the very high monopole impedance mismatch, with a corresponding increase in the directional gain.

3.4 Log-Periodic Toothed Trapezoid Antenna (LPTA)

The log-periodic toothed trapezoid antenna (LPTA) belongs to a family of log-periodic antennas. The log-periodic antennas have a structural geometry such that their impedance and radiation characteristics repeat periodically as the logarithm of frequency [2.3]. Log-periodic antennas belong to the class of frequency-independent antennas. A commercial product LPTA is shown in Fig. 3.17. The LPTA is fed at the apex.

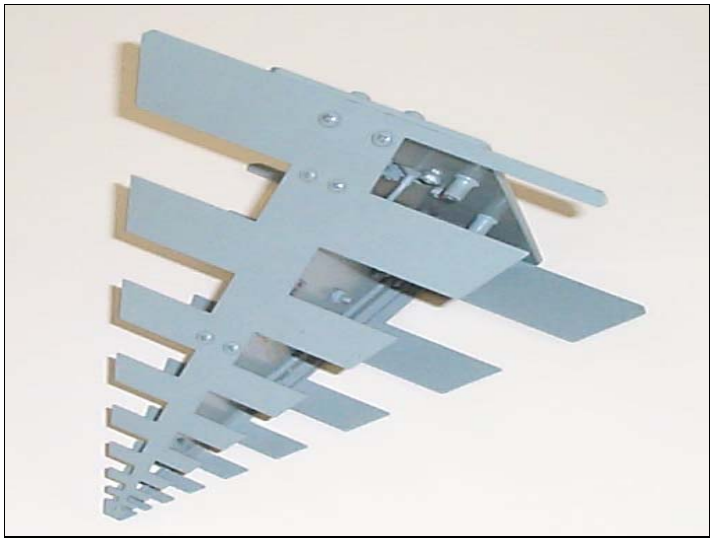

Figure 3.17. Log-periodic toothed trapezoid antenna

The frequency and time-domain behavior of a two LPTA link is shown in Fig. 3.18. The smallest antenna element radiates the highest frequency component while the largest antenna element radiates the lowest frequency component at a later time after the pulse has had time to propagate to the low-frequency end. As the pulse travels along the antenna surface, radiation occurs toward the feed end, causing the frequency dispersion. Thus the pulse (chirp) duration is prolonged compared to the TEM horn and the resonant monopole. The chirp duration is around 11 ns and the peak amplitude is $5 \cdot 10^{-3}\ s^{-1}$.

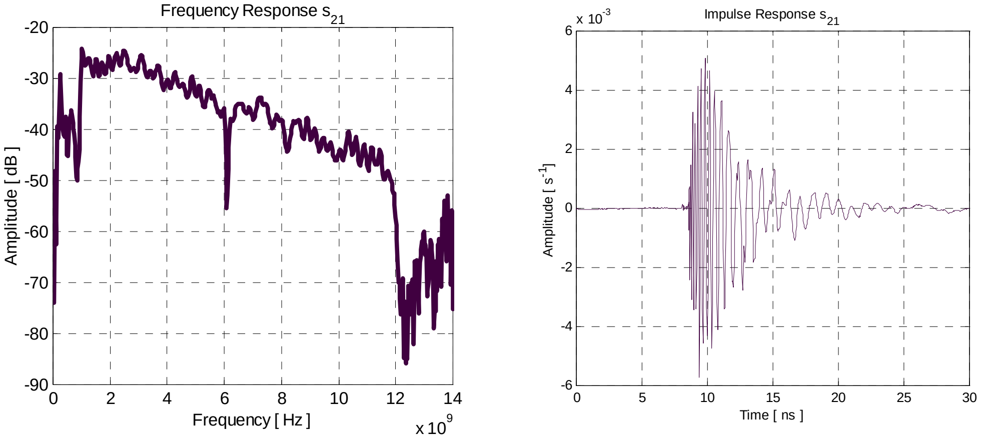

Figure 3.18. Frequency and time-domain response of 2 LPTA link

The pyramidal log periodic frequency response shows $1/\omega^2$ decrease in power (ratio between output and input power) above the fundamental resonant frequency at 1.0 GHz. Below the fundamental resonance the LPTA shows one more resonant frequency at around 400 MHz at relative amplitude of –30 dB. The amplitude decay is very sharp below 1.0 GHz and 400 MHz resonant frequencies. The 400 MHz resonant frequency is associated with a radiation of the whole structure in a dipole mode type of radiation. The fundamental radiation at 1.0 GHz is the beginning of the frequency range where the LPTA acts in a frequency-independent mode. One can notice that the LPTA upper frequency operation is 12.0 GHz.

The return loss of the LPTA, shown in Fig. 3.19, exhibits many resonant frequencies very closely spaced. The return loss is on average –8 dB in the frequency range 1.0-4.0 GHz, –15 dB in the range 4.0-10.0 GHz, and -10 dB in the range 10.0-12.0 GHz. The 2 LPTA link shows a nonlinear phase response as shown in Fig. 3.11. The nonlinear effect is not very pronounced as will be shown later with the Archimedean spiral antenna.

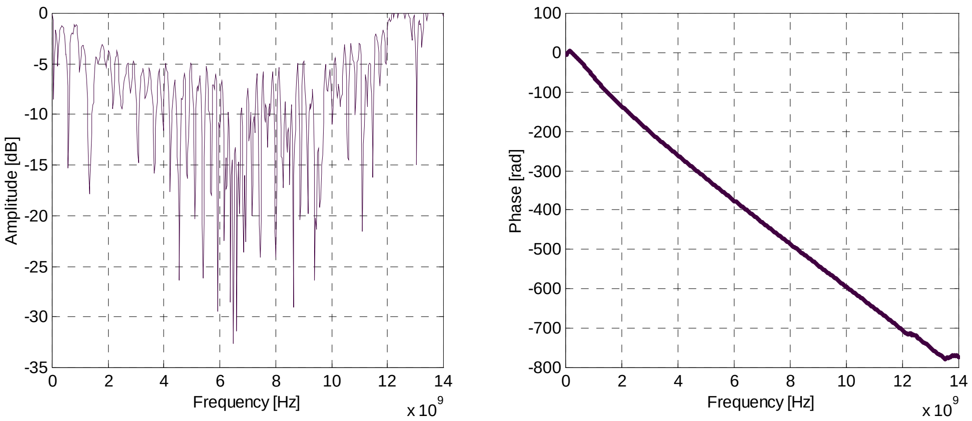

Figure 3.19. LPTA return loss and phase response of 2 LPTA antenna link

The LPTA link exhibits a chirp response in a time domain and frequency-domain response shows approximately $1/\omega^2$ decrease in power above the fundamental resonant frequency of 1.0 GHz.

3.5 Archimedean Spiral Antenna

The Archimedean spiral antenna is another type of frequency independent antenna. Fig. 3.20 shows a typical commercial spiral antenna. The Archimedean spiral antenna is backed by a cavity in order to achieve a unidirectional beam. The cavity is also loaded with an absorbing material since the cavity is introducing a resonant behavior altering the frequency independent nature of the spiral antenna [2.3]. The design parameters such as cavity depth, spiral diameter, spiral rate of growth, conductor width and spacing, and antenna feed have been studied in order to aid a designer in acheiveing certain radiation characteristics [3.15]. An important part of any spiral design is a wideband balun.

Figure 3.20. Cavity backed Archimedean spiral antenna

The dispersive nature of the time-domain response, shown in Fig. 3.21, may be explained by physically tracing the path of a transmited pulse along the spiral. As the pulse travels from the center of the spiral towards the edge, radiation occures. The higher frequency components are radiated first, followed by lower frequency componets causing the frequency dispersion. One can notice that antenna is basically ringing within an envelope. The ringing is due to a phase delay between the different frequency components of the radiated field. The chirp duration is 13.5 ns and the peak amplitude is$1.1\cdot 10^{-3}\ s^{-1}$. Fig. 3.21 also shows the frequency response of Archimedean spiral. This type of structure exhibits significantly different frequency magnitude behavior, since it keeps the amplitude in the frequency range 2.0-11.0 GHz at an average level of –45 dB. All other structures investigated show approximately $1/\omega^2$ decrease in power above the fundamental resonant frequency. Below the fundamental resonance the waveform is changing like other structures investigated so far.

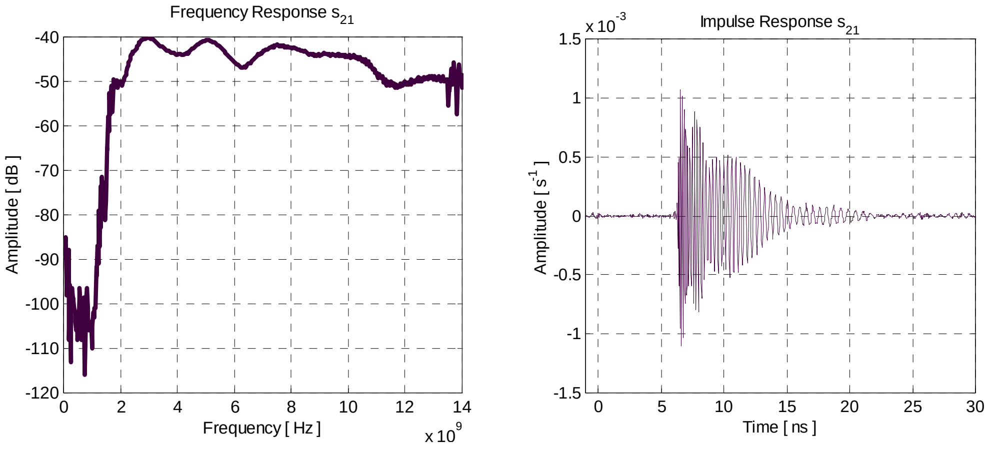

Figure 3.21. Measured frequency and time-domain response of the Archimedean spiral antenna link

The Archimedean spiral shows on average a better than 10 dB return loss in the range 2.5-14 GHz. The phase response of two-spiral antenna link shows a non-linear nature. The nonlinear phase effect is characteristic for dispersive antennas as is shown with the LPTA antenna system. The return loss and phase of the spiral link is shown in Fig. 3.22.

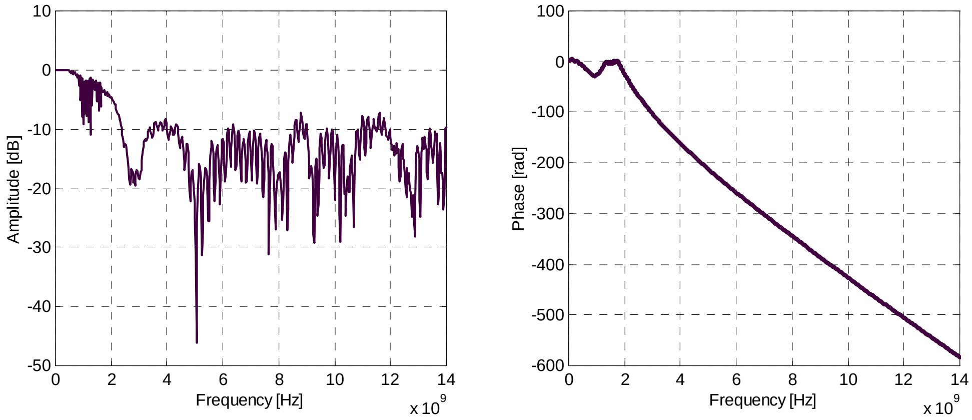

Figure 3.22. Archimedean spiral return loss and phase response of 2 Archimedean spiral antenna link

The Archimedean spiral shows interesting behavior in both the time and frequency domains. In the time domian, the spiral antenna exibits a dispersive nature – a chirp. In the frequency domain, it is not exibiting $1/\omega^2$ behavior and has a nonlinear phase. The LPTA and Archimedean spiral both show a dispersive time-domain response. This is an indication that frequency independent antennas, in general, would have a chirp type of time-domain response. However, in the frequency domain, a spiral antenna exhibits a constant frequency response over a range of frequencies while the LPTA exhibits $1/\omega^2$ behavior.

3.6 Vivaldi Antenna

The Vivaldi antenna is a slow-wave, leaky, end-fire, traveling-wave antenna. Theoretically, the Vivaldi antenna has an unlimited operating frequency range, with constant beamwidth over the entire bandwidth [3.16]. The Vivaldi antenna was first introduced by P. J. Gibson [3.17]. Gibson constructed the Vivaldi antenna by using the following function

$$y = \pm 0.125 \cdot e^{0.052x} . \tag{3.18}$$

The units used are millimeters. Since the antenna dimensions have to be finite, the maximum negative *x* dimension controls the highest frequency of operation and the lowest frequency is controlled with the maximum positive *x* dimension [3.17].

The antenna bandwidth is limited in practice by the feeding arrangement. The transmission line has to be matched to the slot line of the antenna. The second limiting factor in a practical Vivaldi antenna design is the antenna shape and dimensions. The antenna shape and the dimensions determine the beamwidth, side lobes, and back lobe radiation.

The Vivaldi antenna was designed by J. N. A. Noronha, T. M. Bielawa, and C. R. Anderson using an integrated balun [3.18]. The geometry of the designed antenna is shown in Fig. 3.23. The antenna was etched on a RO4003C PCB substrate with $\varepsilon_r = 3.38$. The antenna consists of three parts: a microstrip feed, a paired-strip middle section, and the radiating section. The microstrip feed section was matched to 50 Ω by using standard formulas. The paired-strip middle section served as a transition region. It was empirically discovered that the transition region should be three to five wavelengths long to prevent a sharp discontinuity between the feed and the radiating region. The equation used to calculate the impedance of the paired strip as a function of width, dielectric constant, and thickness of the substrate is the following [3.19]:

$$Z_0 = \frac{\eta_0}{\sqrt{\varepsilon_r}}\left\{\frac{a}{b} + \frac{1}{\pi}\ln 4 + \frac{\varepsilon_r + 1}{2\pi\varepsilon_r}\ln\left[\frac{\pi\left(a/b + 0.94\right)}{2}\right] + \frac{\varepsilon_r - 1}{2\pi\varepsilon_r^2}\ln\frac{e\pi^2}{16}\right\}^{-1} \Omega\left(a/b > 1\right) \qquad (3.19)$$

Although, Gibson used an exponential taper for the radiation section of Vivaldi, the antenna was designed using spline function. The spline function was created using the AutoCAD® SPLINE function with start point at the end of the paired-strip and an endpoint at the end of the antenna.

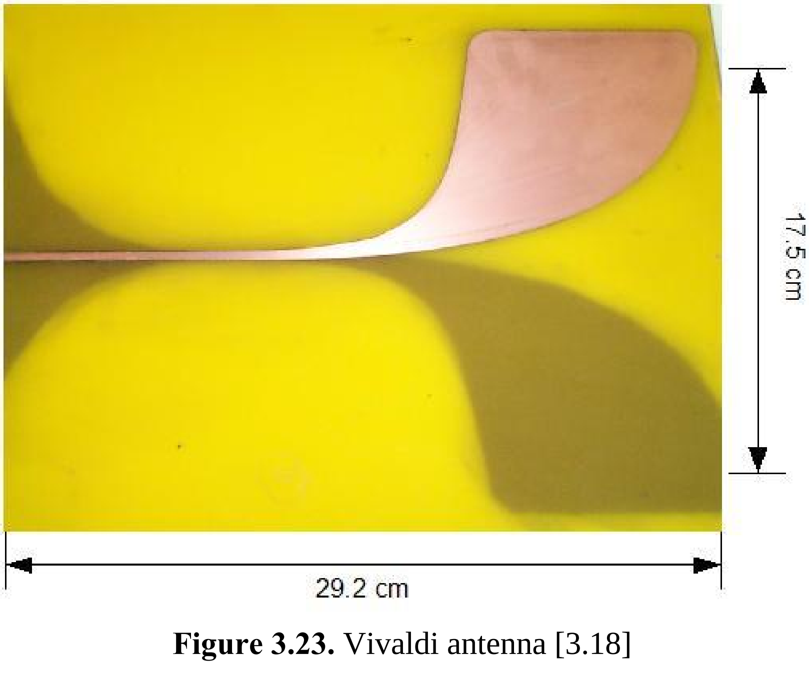

Figure 3.23. Vivaldi antenna [3.18]

One can relate the Vivaldi antenna physical dimensions to antenna resonances. The Vivaldi antenna aperture opening is 17.5 cm. The aperture opening corresponds to guided wavelength of $\lambda_g = 9.5$ cm. The lowest measured operating frequency of the designed Vivaldi antenna is 1.6 GHz and the corresponding half wavelength is 9.4 cm.

Thus, as mentioned by Gibson, regardless of the radiation section taper function, the lowest operating frequency of the antenna is determined by the taper opening length and corresponds to half wavelength.

Fig. 3.24 shows the Vivaldi antenna frequency and impulse response. The frequency response exhibits three significant peaks (resonances). The peaks are located at 400 MHz, 1.6 GHz, and 6.0 GHz. In general, the frequency response exhibits $1/\omega^2$ behavior. The Vivaldi antenna shows a hybrid type of operation between the TEM horn and the monopole antenna. The response shows multiple peaks, monopole type of response, but broad in nature as the TEM horn response. The 400 MHz resonant frequency is associated with a radiation of the whole structure in a dipole mode type of radiation. The same effect is observed with LPTA antenna.

The time-domain response shown in Fig. 3.24 resembles a "doublet" type of waveform. The doublet is associated with a first derivative of a Gaussian pulse. The "doublet" duration is 0.5 ns and the peak amplitude is $19 \cdot 10^{-3}\ s^{-1}$.

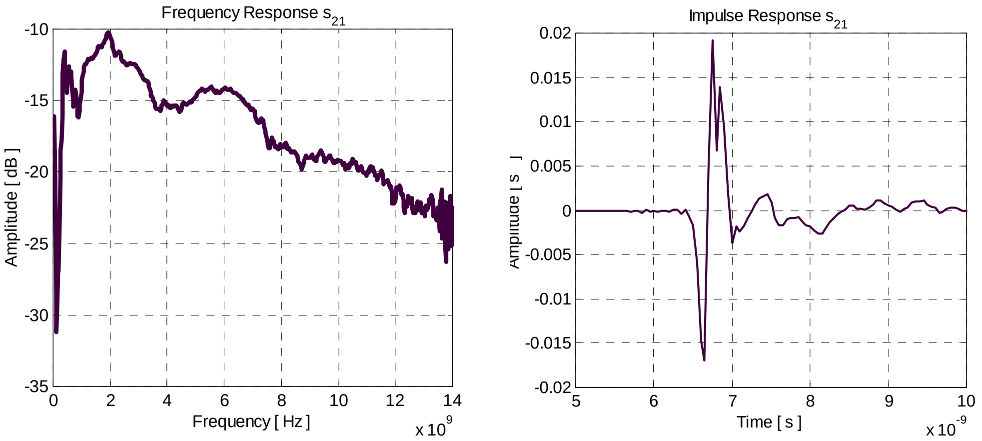

Figure 3.24. Measured frequency and time-domain response of the 2 Vivaldi antenna link

The Vivaldi return loss and phase response of 2 Vivaldi antenna link is shown in Fig. 3.25. The return loss is less than –10 dB for frequency range 1.6-14 GHz. This shows the Vivaldi antenna is a very efficient radiator. The 2 Vivaldi antenna link phase response is linear and is shown in Fig. 3.25.

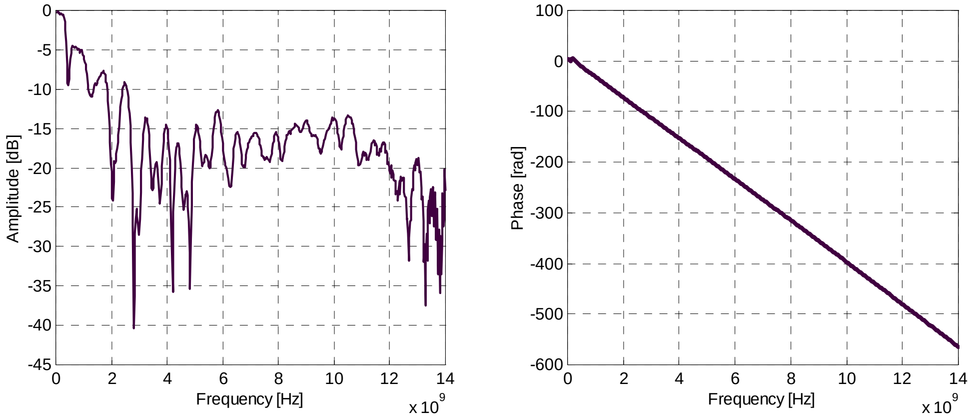

Figure 3.25. Vivaldi antenna return loss and phase response of 2 Vivaldi antenna link

The 2 Vivaldi antenna link shows a “doublet” type of response in the time-domain. The frequency domain exhibits in general $1/\omega^2$ behavior, with an overall performance desired in a UWB antenna.

3.7 Bi-conical Antenna

The bi-conical antenna is a variation of a dipole antenna. In order to increase the antenna bandwidth the conductors are flared to form a bi-conical structure [2.3]. The bi-conical antenna is analyzed as an infinite bi-conical antenna in order to have analytical solutions for radiated fields and antenna input impedance. The finite bi-conical antenna, as shown in Fig. 3.26, has been investigated in terms of the antenna height and flare angle [3.20]. The bi-conical antenna exhibits a behavior where the reactive part of the antenna impedance can be held to a minimum over a progressively wider bandwidth by increasing the flare angle.

Much of the work on the bi-conical antenna structure in the time-domain has been presented by C. W. Harris and C. S. Williams [3.21]. The authors show the time-domain bi-conical antenna response due to a pulse for several values of flare angles and antenna heights. They investigate the transmission of two bi-conical antennas under matched source and matched load conditions for transmission and reception, respectively. The expression for a wide-angle conical antenna effective length is

$$\beta h(f) = \frac{E^{rad}(f)}{(j\eta/2\pi)(e^{-j\beta r}/r)I_0(f)}, \tag{3.20}$$

where $I_0(f)$ is antenna current, $E^{rad}(f)$ is radiated field, and η is characteristic free space radiation of $120\pi\ \Omega$. The effective length is a transfer function that relates antenna open-circuit voltage to the incident field. The authors also define the reception transfer function as

$$S(f) = \frac{-h(f)Z_L(f)}{Z_0(f)+Z_L(f)}, \tag{3.21}$$

where $Z_L(f)$ is load impedance and $Z_0(f)$ is antenna impedance.

The investigated bi-conical antennas had a flare angle of 49.6 degrees and a height of 14.4 cm. The s_{21} frequency and time-domain response of two bi-conical antennas is shown in Fig. 3.27. The frequency domain response shows the presence of the multi-path since the bi-conical antennas were not measured inside the anechoic chamber. The frequency response shows a distinct peak (resonance) around 400 MHZ. The frequency response after the first resonant frequency, on average, shows a linear decay.

Figure 3.26. Bi-conical antenna

The frequencies below the first resonant frequency are significantly attenuated. Actually, the bi-conical antenna broadband properties are attributed to many resonant frequencies combined together as indicated by the return loss of the antenna. The peak time-domain amplitude is $9.0 \cdot 10^{-3}\ s^{-1}$. One might conclude that a bi-conical antenna has no effect (either on receive or transmit side) on the pulse that was used to excite the antenna, however the pulse nature results from multi-mode cancellations.

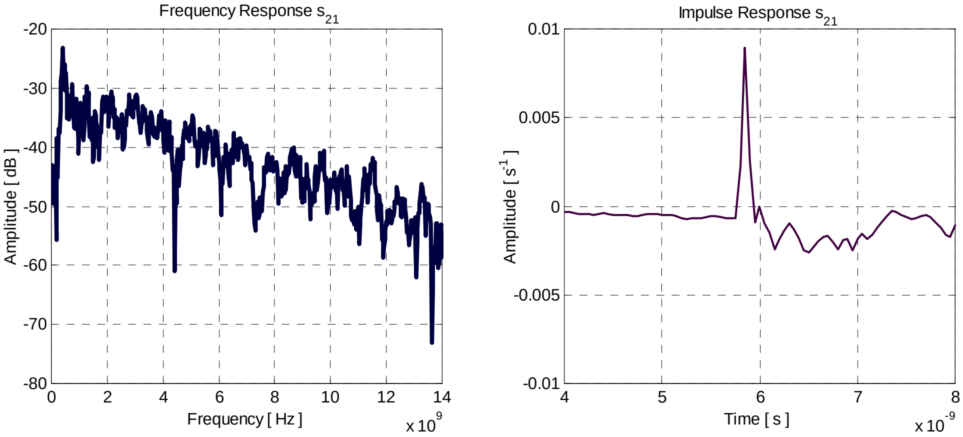

Figure 3.27. Measured frequency and time-domain response of 2 bi-conical antenna link

The return loss of the antenna is shown in Fig. 3.28. The return loss of the bi-conical antenna is -15 dB for the frequency range of 2.0 to 14 GHz. The antenna return loss is below -10 dB for the range of 1.0 to 20 GHz. The return loss shows many resonant frequencies spaced closely together. The phase response of the 2 bi-conical antenna link is linear.

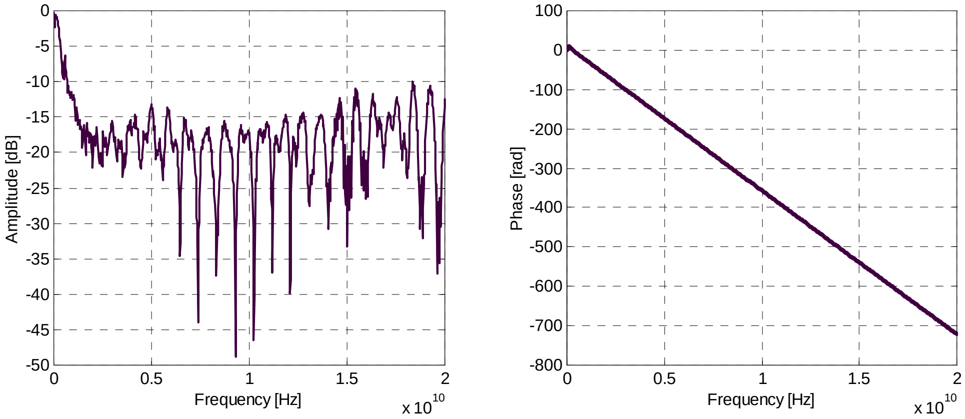

Figure 3.28. Bi-conical antenna return loss and phase response of 2 bi-conical antenna link

The bi-conical antenna was measured for different angles in the antenna E-plane. Fig. 3.29 shows the antenna transient response for different antenna orientations. One can notice the transient response amplitude is decreasing and the pulse width is slightly increasing as the antenna is rotated away from the bore-sight direction.

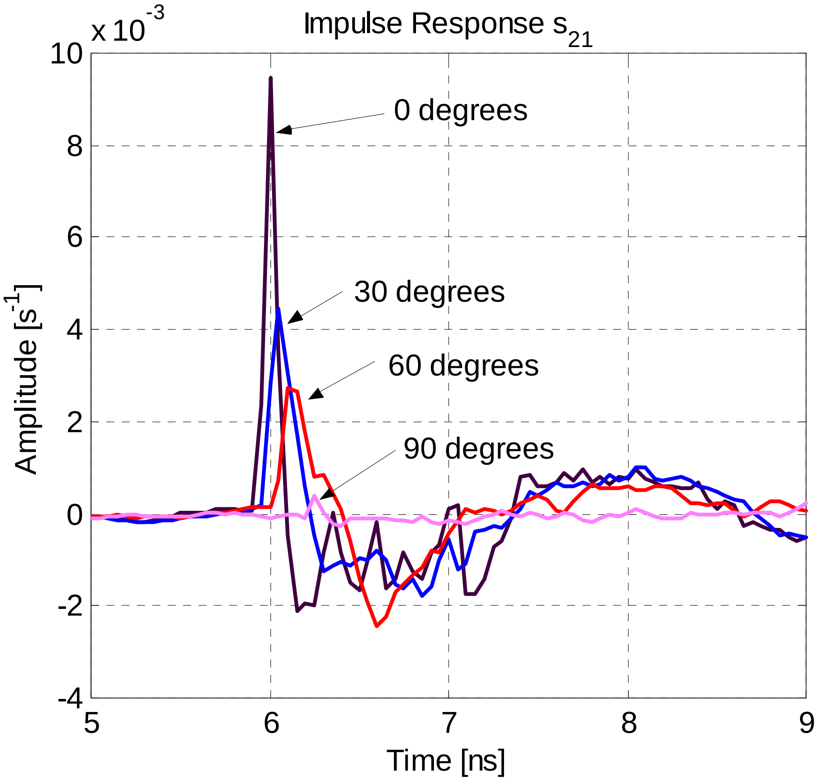

Figure 3.29. Measured bi-conical antenna transient waveforms for different antenna orientations

The bi-conical antenna represents a very good UWB omni-directional radiator. The antenna efficiency is excellent resulting in the higher amplitude of the transient waveform compared to a resonant monopole antenna. The time-domain response is a "doublet" type with a prolonged negative tail part. The frequency response shows $1/\omega^2$ behavior.

3.8 Some Observations on Canonical Antenna Structures

The parametric study of different classical broadband structures with regard to their possible use in UWB communications has revealed some interesting observations tabulated in Tables 3.2, 3.3, and 3.4.

Table 3.2 compares three different and distinct types of antenna structures. The monopole antenna time-domain response is a damped sinusoid as expected for a highly resonant antenna. The TEM Horn also exhibits a damped sinusoid, but with significantly reduced ringing and a significantly higher peak amplitude. The spiral antenna, representing the family of frequency-independent antennas, exhibits a chirp response and an interesting frequency domain behavior. The relative amplitude stays relatively constant for wide range of frequencies while other antennas exhibit approximately $1/\omega^2$ behavior in the frequency domain.

For directional applications, the TEM Horn offers a good option with a short time-domain response at the output. For omni-directional antennas, the monopole performs fairly well with reduced amplitude on the boresight, due to both the impedance mismatch and reduced gain, with the bi-conical structure extending the usefulness of the dipole type antenna.

Table 3.2. Principal Structures - Link Response

Antenna	Geometry	$s_{21}(t)$	$\lvert s_{21}(j\omega)\rvert$
Monopole (5 GHz)		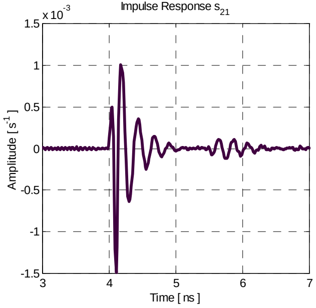	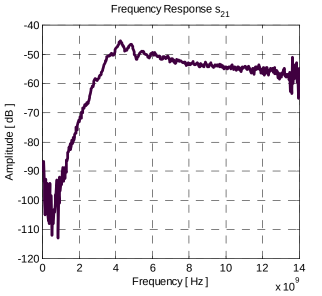
TEM Horn		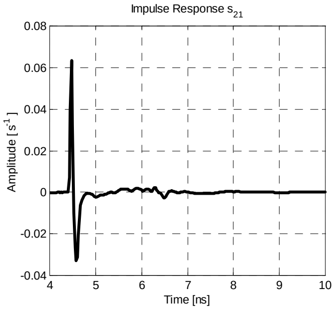	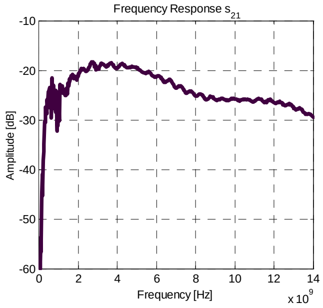

Spiral[6]		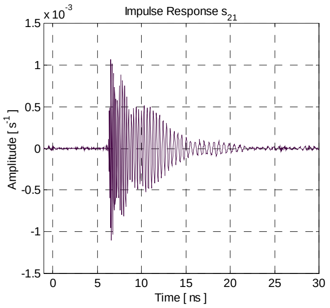	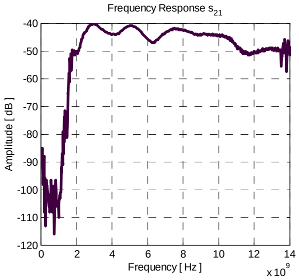

Table 3.3 summarizes additional types of antenna systems. It is interesting to note, in the class of the traveling wave antennas, that Vivaldi antenna exhibits a large early negative peak followed by a large positive peak. This is not the case with bi-conical and TEM Horn antenna. The reason for such a behavior is the Vivaldi antenna integrated balun, which contributes in the radiation process causing the early negative peak.

The performance of frequency independent antennas, LPTA and Archimedean spiral, in terms of time-domain communication systems is not acceptable due to significant dispersion. In the time-domain, the LPTA exhibits a chirp type of response, similar to Archimedean spiral antenna, but in the frequency domain it follows a $1/\omega^2$ behavior, which is not the case with the Archimedean spiral antenna

Table 3.3. Additional Structures - Link Responses

Antenna	Geometry	$s_{21}(t)$	$\lvert s_{21}(j\omega)\rvert$
Ridged TEM	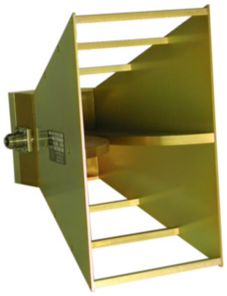	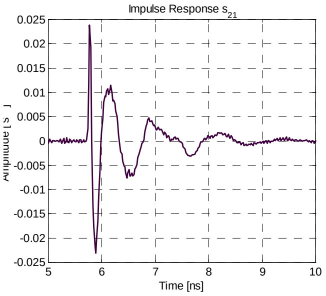	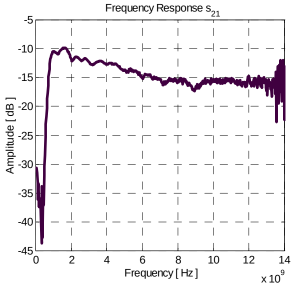
Bi-conical Antenna[7]		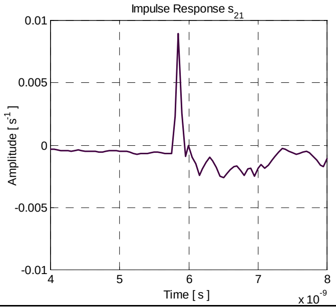	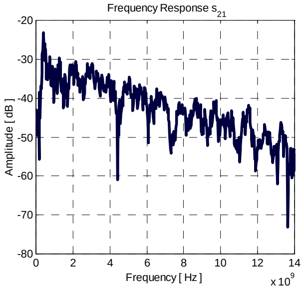

---

[6] Spiral – Manufacturer: American Electronic Laboratories (AEL); Model: AST-1492AA; Freq: 2.0-18.0 GHZ

[7] Bi-conical Antenna –Manufacturer: Kin Tronic Laboratories; Model: S/N 000; Freq: 0.8 – 20.0 GHz. Dimensions: Height (14.4 cm), Diameter of the top and bottom plate (31.2 cm), Angle approx. 49.6 degrees

Vivaldi Antenna		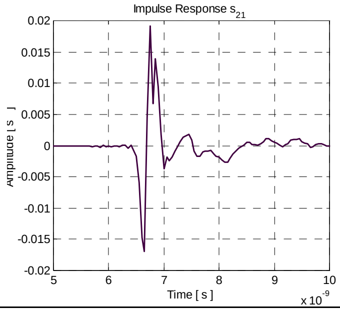	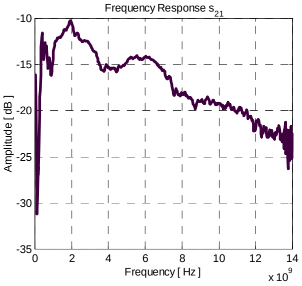
LPTA[8]		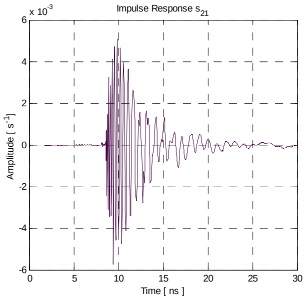	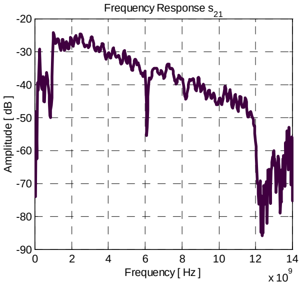
Monopole[9] (1 GHz vs. 1.1 GHz)		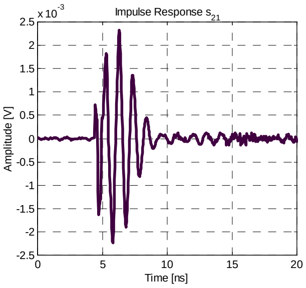	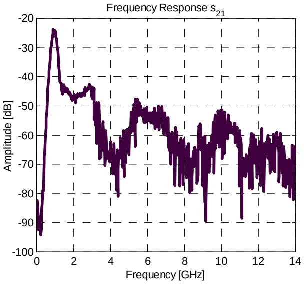

In general one might expect a chirp response in the time-domain from frequency-independent antennas. However the frequency-domain response will differ depending on the structure of the antenna.

Resonant antennas provide a good alternative, based on pulse shape and duration, but suffer low efficiency and gain. The 5.0 GHz link exhibits a $1/\omega^2$ behavior in the frequency domain, which is characteristic of constant gain antennas. As explained earlier this loss is due to impedance mismatch and corresponding gain increase, which is evident from the 5.0 GHz monopole return loss. The 1.0/1.1 GHz monopole link shows distinct peaks in the frequency domain, which correspond to monopole resonant frequencies. In the time-domain 1.0/1.1 GHz link shows more pronounced ringing. The duration of 5.0 GHz monopole link ringing in the time-domain is 1.0 ns in duration, while 1.0/1.1 GHz link is 5.0 ns. The 1.0/1.1 GHz link is also more efficient.

All the results on the pulse type, pulse duration, and relative amplitude are summarized in Table 3.4 for different antenna structures. The shortest pulse is obtained by bi-conical antenna structure. The most efficient transmission and overall best performance is by TEM Horn antenna.

---

[8] LPTA - Manufacturer: American Electronic Laboratories (AEL); Model: APN –101B; Freq: 1.0-12.4 GHZ

[9] 1.0 GHz monopole was measured at the same distance as TEM Horns on the 4x4 ft ground plane. The distance between reference planes was 130.2 cm. Rests of the measurements were performed at 120.0 cm distance

Table 3.4. Properties of different UWB radiators in terms of the pulse duration, pulse type, and peak amplitude

Antenna	*Pulse Duration [ns]*	*Pulse Type*	*Peak Received Amplitude* $[m\,s^{-1}]$	*Peak Received Amplitude*[10]
Vivaldi	0.5	Damped Sinusoid	19	0.80
Ridged TEM Horn	2.74	Damped Sinusoid	24	1.00
TEM Horn	0.4	Damped Sinusoid	63	2.6
Bi-conical Antenna	0.2	Damped Sinusoid[11]	9.5	0.40
LPTTA	11	Chirp	5	0.21
CBAS	13.5	Chirp	1.1	0.05
Monopole (5GHz)	1.0	Damped Sinusoid	1.5	0.06
Monopole (1.0/1.1 GHz)	5.0	Damped Sinusoid	2.4	0.1

Based on the observations one may be able to create a simple model for the Vivaldi, TEM Horn, bi-conical antenna, and ridged TEM Horn excited by a broadband pulse. The "doublet" produced by these antenna structures may not be assigned to inherent differentiation in the time-domain but to the band-limited nature of the antenna. This and some other conclusions, including a simple transmission model, are presented in the following section.

3.9 Band-Limited Antennas and the Relationship to Differentiation in UWB

From the measured results the time-domain impulse response of UWB antennas generally has a doublet type of form. This "doublet" form is true for the Vivaldi, TEM horn, and Bi-conical antennas. Such a response suggests that the antenna is a constant aperture antenna with the following behavior:

$$\frac{P_o}{P_i} = \frac{A_t A_r}{4\pi R^2}\frac{4\pi}{\lambda^2} \propto \omega^2 \qquad (3.22)$$

---

[10] Relative to ridged TEM Horn

[11] Damped sinusoid with cancellation effects (5.9 ns to 7.3 ns)

However, the frequency response suggests a different interpretation. The antennas appear to act as constant gain antennas. In fact, the Vivaldi and TEM horn antenna pattern measurements confirm that the antenna acts as a constant gain antenna. A constant gain antenna response

$$\frac{P_o}{P_i} = \frac{G_t G_r}{4\pi R^2}\frac{\lambda^2}{4\pi} \propto \frac{1}{\omega^2} \tag{3.23}$$

is found for the response of the antenna above the fundamental resonance.

What seems to be the difference in the interpretations? If we expand the observation frequencies below the fundamental resonance the antenna, we indeed find that the antennas often act approximately like constant aperture antennas. The response of these antennas can be explained by the band-limited nature of the antennas.

The "doublet" type radiation that is produced by the Vivaldi and other UWB antennas is represented by a differentiation that is expected in the radiation in the time-domain transmission. This differentiation is inherent to any antenna radiation mechanism. However, it is typically a result of the lower band response of the antenna where the constant aperture nature dominates.

In observing the waveform, it is found that the duration of the "doublet" corresponds to the fundamental resonant frequency of the antenna. From previous measurements, the TEM Horn "doublet" duration is around 250 ps, which corresponds to a fundamental resonance of 4 GHz. If an antenna system is band limited by filters in the system, a similar result occurs due to the band-limited nature.

From the measured result observations one can introduce a simple model that represents an antenna system. The antenna system can be modeled as a constant aperture antenna below the fundamental resonance and as a constant gain antenna above the fundamental resonance. Fig. 3.30 shows the simple model representation.

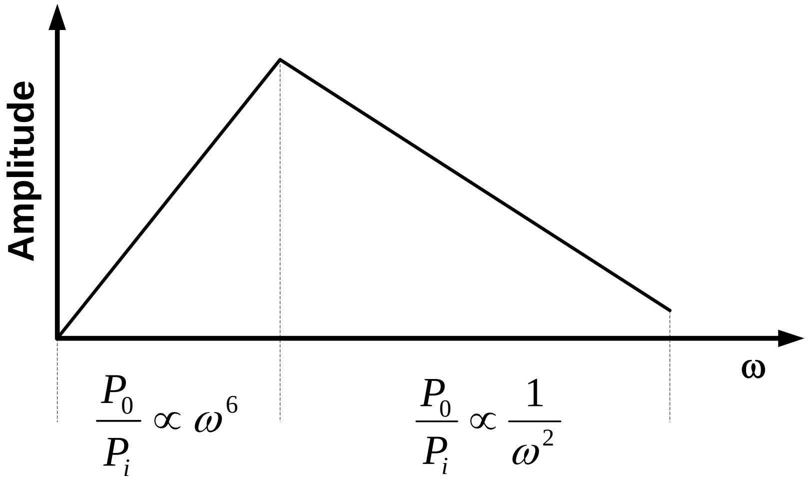

Figure 3.30. Simple antenna system link model [3.22]

Using a simple function to represent a frequency domain spectrum, as shown in Fig. 3.31, one can obtain the time-domain response of the antenna using the inverse

Fourier transform. The Q-factor defines the sharpness of the peak. The more resonant structures have a sharp peak. Fig. 3.31 shows a Hi-Q antenna example with a distinct peak, which results in a damped sinusoid time-domain waveform. The ringing is similar to the ridged TEM Horn antenna structure.

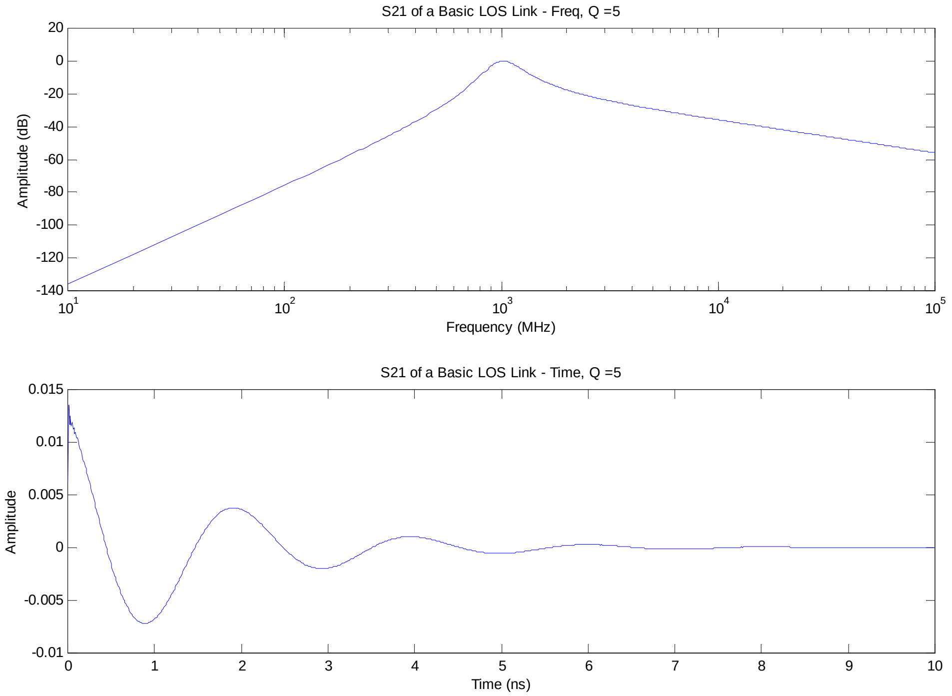

Figure 3.31. Hi-Q link example [3.22]

If a simple function used to represent a frequency domain spectrum represents a Low-Q antenna, the time-domain waveform is damped more rapidly. This represents a TEM, bi-conical, or Vivaldi type of structure. The time and frequency-domain responses are shown in Fig. 3.32.

The model is reasonable for traveling wave ultra-wideband antennas with low mismatch loss. It predicts the pulse length of the antenna in the time-domain. Also, this model is useful for extrapolating the antenna response below the fundamental resonance to 0 Hz in order to obtain time-domain equivalent response using IFFT transform from the frequency domain measurements.

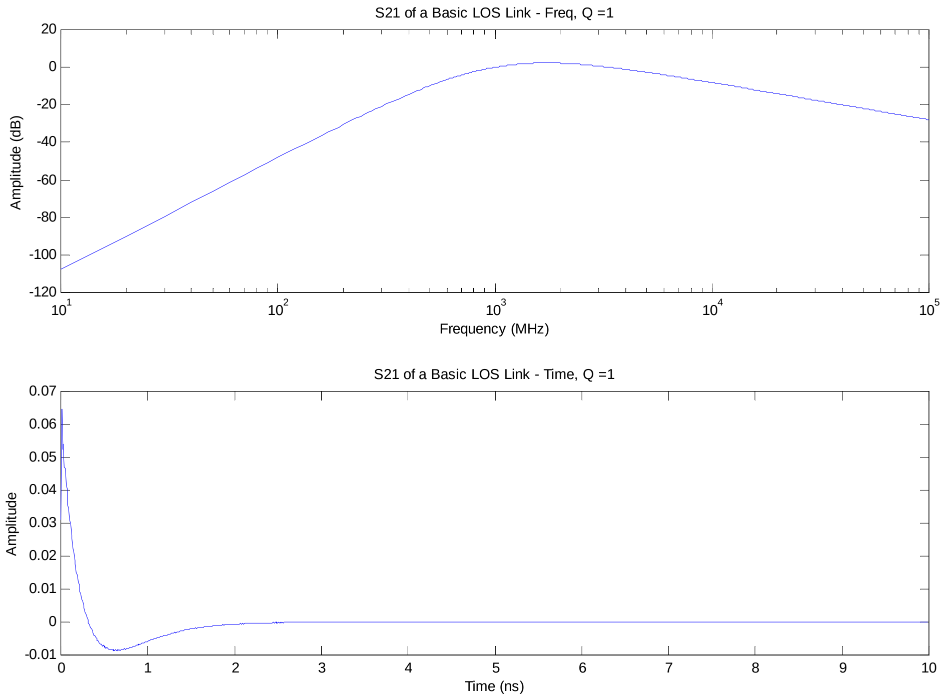

Figure 3.32. Low-Q link example [3.22]

3.10 Conclusions

The processing in the time-domain by the HP8510 was investigated. It was found that the impulse response is obtained by using a chirp-z transform and a Kaiser-Bessel window with $\alpha=6$ parameter. The step response is obtained by using effectively a low pass filter. A MATLAB® program was written that obtains the same results as the HP8510 time-domain processing using FFT transforms. For improved response prediction, an external IFFT was used to avoid the low-pass problem.

All the antennas investigated exhibit a damped sinusoidal behavior due to the finite sizes. A simple model is presented showing that in the time domain the fundamental resonant frequency has the most pronounced effect on the antenna pulse width and the basic pulse shape. The simple model approximates well the behavior of the class of traveling wave antennas: TEM Horn, Vivaldi antenna, bi-conical antenna, and ridged TEM Horn antenna.

The class of frequency independent antennas exhibits a chirp type of response in the time-domain. In the frequency domain, the response differs depending on the geometry of the frequency independent antenna.

The class of the resonant antennas suffers from very low efficiency. The pulse width is in duration of $5 \cdot 1/f_r$, where f_r is the fundamental resonance of the monopole antenna. The time-domain response is a damped sinusoid. The frequency response for 5.0 GHz monopole link exhibits a $1/\omega^2$ behavior in the frequency domain. The 1.0/1.1 GHz link shows distinct peaks in the frequency domain, which corresponds to resonant frequencies of the monopole antenna.

Due to a damped sinusoidal behavior of antennas it is possible to apply a damped sinusoidal model to approximate the measured results. In the next chapter, we will discuss the methods to approximate the measured results in terms of poles and residues (rational function). The methods typically used to develop the model for a damped exponential model are Prony’s method and the Matrix-Pencil method.

References

[3.1] 8510C Network Analyzer: System Operating and Programming Manual Edition 2, Agilent Technologies, January 31, 1994.

[3.2] HINT 2: Compensate for time-delay for better cable measurements. AGILENT Manual AN1291-10.

[3.3] F. J. Harris, "On the Use of Windows for Harmonic Analysis with the Discrete Fourier Transform," Proceedings of the IEEE, Vol. 66, No. 1, January 1978.

[3.4] Bertoni, H. L., Carin, L., Felsen L. B. (editors), *Ultra-wideband, Short-Pulse Electromagnetics*, Plenum Press, New York, 1993.

[3.5] Carin, L., Felsen L. B. (editors), *Ultra-wideband, Short-Pulse Electromagnetics 2,* Plenum Press, New York, 1995.

[3.6] Baum, C. E., Carin, L., Stone A. P. (editors), *Ultra-wideband, Short-Pulse Electromagnetics 3,* Plenum Press, New York, 1997.

[3.7] F. C. Yang and K. S. H. Lee, "Impedance of a Two-Conical-Plate Transmission Line," Sensor and simulation notes, no. 221, U.S. Air Force Research Lab, Kirkland AFB, NM, 1976.

[3.8] R. T. Lee and G. S. Smith, "A Design Study for the Basic TEM Horn Antenna," IEEE Antennas and Propagation Magazine, Vol. 46, No. 1, Feb. 2004.

[3.9] S. N. Samaddar and E. L. Mokole, "Some Basic Properties of Antennas Associated With Ultrawideband Radiation", in Ultra-Wideband, Short-Pulse Electromagnetics 3, edited by Baum *et al.*, Plenum Press, New York, 1997. (pp. 147-164)

[3.10] Bantin, C. C., "Radiation from a Pulse-Excited Thin Wire Monpole," IEEE Antennas and Propagation Magazine, Vol. 43, No. 3, June 2001.

[3.11] Bantin, C. C., "Pulsed Communication Link Between Two Dipoles," IEEE Antennas and Propagation Magazine, Vol. 44, No. 5, October 2002.

[3.12] Smith, G. S, "On the Interpretation for Radiation from Simple Current Distributions," IEEE Antennas and Propagation Magazine, Vol. 40, No. 4, August 1998.

[3.13] I. M. Besieris, "Far-Zone Radiation of Pulsed Thin-Wire Antennas," Personal Notes

[3.14] Felsen, L. B. (editor), *Transient Electromagnetic Fields,* Springer-Verlag, Berlin, 1976.

[3.15] R. Bawer and J. J. Wolfe, “The spiral antenna,” IRE International Convention Record, Vol. 8, pp. 84-95, Mar 1960.

[3.16] E. Gazit, “Improved Design of the Vivaldi Antenna,” *IEE Proceedings*, Vol. 135, No. 2, April 1988.

[3.17] P. J. Gibson, “The Vivaldi Aerial,” 9th European Microwave Conference, 1979 (Philips Research Laboratories, Redhill, Surrey, England)

[3.18] J. N. A. Noronha, T. M. Bielawa, C. R. Anderson, D. G. Sweeney, S. Licul, W. A. Davis, “Designing Antennas for UWB Systems,” *Microwaves & RF*, June 2003.

[3.19] B. C. Wadell, *Transmission Line Design Handbook*, Artech House, Norwood, MA, 1991

[3.20] H. Jasik, Ed., *Antenna Engineering Handbook*, McGraw-Hill, New York, 1961, Chap. 6.

[3.21] C. W. Harrison and C. S. Williams, ”Transients in Wide-Angle Conical Antennas,” IEEE Transactions on Antennas and Propagation, March, 1964.

[3.22] W. A. Davis and S. Licul, “Band-limited Antennas and the Relationship to Differentiation in UWB,” International Union of Radio Science, (Boulder, Colorado), Jan. 2004 – presentation slides.

Chapter 4

Methods for Approximating a Function by a Sum of Complex Exponentials/Damped Sinusoids

In this chapter, we present spectral estimation methods. The model used in our calculations is a damped sine or a sum of complex exponential functions. The methods that handle this type of model are Prony's method, the Matrix-Pencil method, E. C. Levy's complex-curve fitting frequency-domain technique, and Prony's equivalent frequency-domain technique. These types of methods handle deterministic signals. In electromagnetic transmission/receiving antenna problems and certain scattering problems signals can be represented by damped sinusoids. As we have seen in Chapter 3, the measured waveforms appear as a few-cycle damped sinusoids. Thus, a damped sinusoid model is appropriate for modeling antenna systems.

There also exist autoregressive, moving average, and autoregressive-moving average models. Some of the methods that handle these types of models are: Yule-Walker (YW), Burg, Modified Covr., Adaptive LMS, Adaptive RLS, High-Order AR, and Modified YW [4.1]. In each, an appropriate parametric time-series model is selected to represent the measured data. Then, an estimate of the parameters of the model is made. In the third step, the estimated parameters are inserted into the theoretical power spectral density expression appropriate for that model [4.1]. The model parameter estimates (e.g. the autocorrelation function) are obtained using the methods listed above. Once the autocorrelation function is obtained, one can obtain poles and residues of the system. However, these poles and residues are called equivalent minimal phase system poles and residues, which represent the system in a probabilistic way [4.2]. The extracted poles and residues could be true parameters of the system but not necessarily. Autoregressive methods use second order statistics. By using higher order statistics one could obtain better estimates of the poles and residues of the system.

Chapter 4 addresses the issues with the use of Prony's and Matrix-Pencil methods. A modified Prony's method formulation is proposed for handling complex conjugate double poles and variable sampling. Variable sampling provides a fixed time-domain window preserving spectral composition of the waveform of interest. The Matrix-Pencil method is described as a more efficient numerical way of computing the poles and residues of the system. Finally, available frequency-domain methods for pole/residue extraction are discussed.

4.1 Prony's Method

In 1795 Baron de Prony introduced a technique for modeling sampled data as a linear combination of damped exponentials [4.3]. Prony's method was used in the description of laws governing the expansion of various gases. This method has been applied to various areas, notably electromagnetic scattering and antenna problems. Prony's method has been modified to handle a purely sinusoidal model with no damped components [4.4] as well as more noise-prone data [4.5].

We start with a basic derivation of Prony's method. For particular applications, it is desired to determine an approximation of the form

$$v(t) = \sum_{n=1}^{N} R_n e^{s_n t},\ t > 0. \tag{4.1}$$

In practice we usually deal with discrete and sampled data, so it is useful to express the equation above as [2.31]

$$v(t_k) = \sum_{n=1}^{N} R_n e^{s_n k \Delta t} = \sum_{n=1}^{N} R_n z_n^k,\ k \in (0, K), \tag{4.2}$$

where $z_n = e^{s_n \Delta t}$. The size of the sampling interval is defined as Δt.

Prony's method is separated into two problems. The first problem consists of determining the poles (s_n), and the second one determines the corresponding residues (R_n). Prony has shown that there exists a vector $\{\alpha\}$ with elements $\alpha_1, \alpha_2, \ldots\ldots, \alpha_N$ such that [2.31]

$$\sum_{n=0}^{N} \alpha_n v_{n+m} = 0, m \in (0,\ M-1). \tag{4.3}$$

If we set the leading coefficient $\alpha_N = 1$ without the loss of generality we obtain the following expression [2.31]:

$$\sum_{n=0}^{N-1} \alpha_n v_{n+m} = -v_{N+m}. \tag{4.4}$$

In this expression α_n are our unknown coefficients and v_{n+m} are the sampled transient data values. If $K = 2N$ in this matrix system, then the solution is just the inverse of a real symmetric matrix. If $K > 2N$ then the solution is obtained through a least-squares problem. Substituting Eq. (4.2) into Eq. (4.3) we obtain a polynomial

$$\sum_{n=0}^{N} \alpha_n z^n = 0,\quad \{z : z_1, \ldots, z_N\}. \tag{4.5}$$

The roots of this polynomial are obtained by a root finding routine. From the roots we obtain the poles

$$s_n = \frac{\ln z_n}{\Delta t}. \tag{4.6}$$

The corresponding residues are obtained from Eq. (4.1).

In building the Prony's method algorithm for accurate pole extraction, it is necessary to investigate the effects of the major parameters in the algorithm (see Fig. 4.1): the size of the sampling interval (Δt), the window shift (Δp), the number of assumed poles (N), the number of samples in a window (M), and the total number of the samples (K) are the parameters in the Prony's method that have a major effects on the successful pole extraction. Fig. 4.1 illustrates the parameters in the Prony's method algorithm.

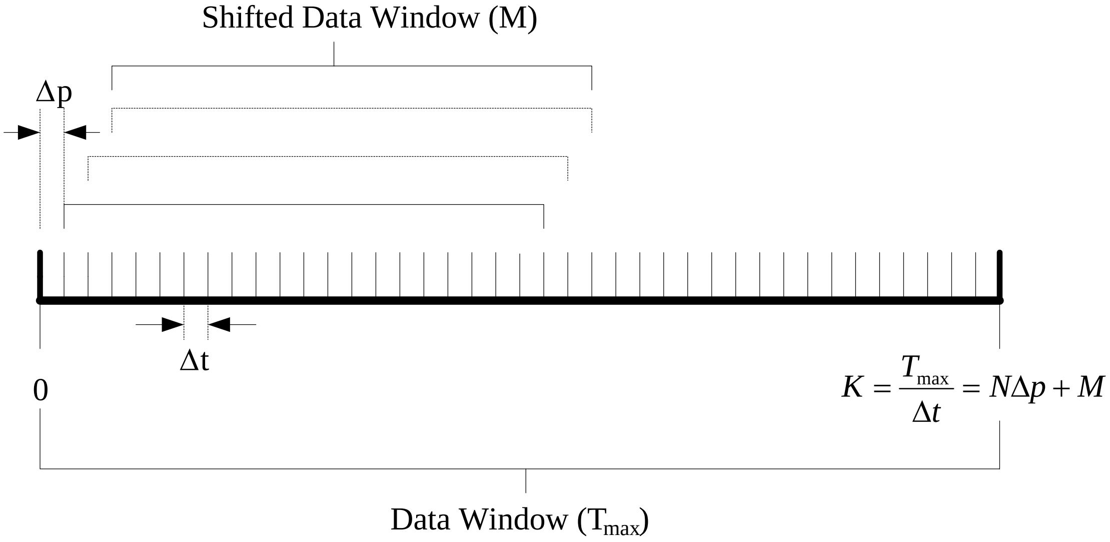

Figure 4.1. Parameters in the Prony's method algorithm implementation

We will investigate the effects of N, K, and Δt on the pole/residue extraction in systems with multiple single poles, multiple pair of complex conjugate poles, and multiple pair of complex conjugate double poles. Modest numerical results are presented in a context of sampling requirements and number of poles in the system.

4.1.1 Prony's Method Parameter Study – Multiple Single Poles

Let us consider a system with a single pole. The system (function) can represent a transfer function (effective length) of the antenna. The function is shown in the Laplace domain and an equivalent time domain as follows:

$$F(s) = \frac{1}{s+1} \Leftrightarrow f(t) = e^{-t} . \tag{4.7}$$

The function $F(s)$ has one pole located at *–1* on the real axis in the left hand complex plane. If the system is passive all the poles will be located on the left hand side of the complex plane. The function $F(s)$ is shown in Fig. 4.2. In order to isolate the effect of one parameter all other parameters in the algorithm must be constant. For all the computations we will keep $2N = K$. First, the value of the sampling interval is changed while all other parameters are kept constant. The results are summarized in Table 4.1.

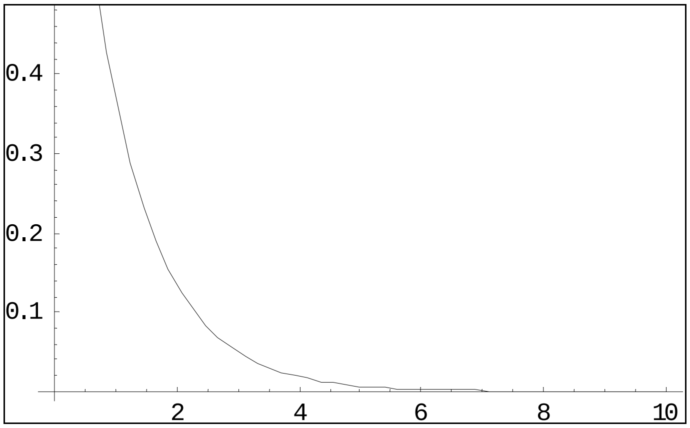

Figure 4.2. Function with a single pole

One should notice that in almost all cases the correct pole is extracted. By increasing the sampling rate, the accuracy of the residues is reduced. The effect is noticeable on the 7th decimal place not shown in Table 4.1. However, the accuracy of the pole is constant as long as the Nyquist sampling criterion holds. The second pole that appears has no effect on the waveform since the residue value is zero. As the sampling interval increases, the value of the second pole also acquires some finite value. The error is primarily due to rounding error.

Table 4.1. Variable Δt ($K = 4$, $N = 2$, and $\Delta p = 1$)

Δt	Poles	*Residues*
1	-1.0000 3.2633 + 3.1416i	1.0000 + 0.0000i 0.0000 - 0.0000i
2	-1.0000 -1.0000 + 1.5708i	1.0000 - 0.0000i -0.0000 - 0.0000i
4	-1.0000 -1.2205 + 0.7854i	0.9999 - 0.0000i 0.0000 + 0.0000i
10	-1.0000 -1.1362 + 0.3142i	1.0000 + 0.0000i -0.0000 + 0.0000i

Table 4.2 summarizes the pole/residue extraction by varying the values of N. The parameter K represents the total number of points used in the pole/residue extraction. By increasing the value of N, the value of the pole stays constant. However the value of the residue loses its accuracy. One can notice that the residues of the artificially created poles are zero. However, for $K = 36$ case, the residues of the artificially created poles have some finite value. By increasing value of N, the size of the matrix increases. Thus, the rounding error also increases.

Table 4.2. Variable K and N ($\Delta t = 1$ and $\Delta p = 1$)

K	*N*	*Poles*	*Residues*
6	3	-1.0000	1.0000 - 0.0000i
		-2.6027 + 3.1416i	0.0000 + 0.0000i
		-4.0239	-0.0000 - 0.0000i
10	5	-1.0000	1.0000 - 0.0000i
		-1.1903 + 3.1416i	-0.0000 - 0.0000i
		-1.4086 + 1.4558i	-0.0000 + 0.0000i
		-1.4086 - 1.4558i	-0.0000 - 0.0000i
		-3.0037	0.0000 + 0.0000i
30	15	-0.8141 + 0.8262i	0.0000 + 0.0000i
		-0.8141 - 0.8262i	-0.0000 - 0.0000i
		-1.0000	1.0000 - 0.0000i
		-0.9544 + 0.5512i	0.0000 - 0.0000i
		-0.9544 - 0.5512i	0.0000 - 0.0000i
		-0.6780 + 1.9531i	-0.0000 + 0.0000i
		-0.6780 - 1.9531i	0.0000 + 0.0000i
		-0.9564 + 1.4425i	0.0000 - 0.0000i
		-0.9564 - 1.4425i	0.0000 - 0.0000i
		-0.8969 + 2.0745i	0.0000 - 0.0000i
		-0.8969 - 2.0745i	0.0000 - 0.0000i
		-0.9922 + 2.5227i	0.0000 - 0.0000i
		-0.9922 - 2.5227i	0.0000 - 0.0000i
		-1.0412 + 3.1416i	0.0000 - 0.0000i
		-5.5710	-0.0000 + 0.0000i
36	18	-0.3836	0.0000 - 0.0000i
		-0.7156 + 3.1416i	-0.0000 - 0.0000i
		-0.7790 + 1.9767i	-0.0000 - 0.0000i
		-0.7790 - 1.9767i	-0.0000 + 0.0000i
		-0.9762 + 3.1416i	0.0001 + 0.0000i
		-1.0401 + 2.6612i	0.0001 - 0.0000i
		-1.0401 - 2.6612i	0.0001 + 0.0001i
		-1.0212 + 2.1172i	0.0001 - 0.0001i
		-1.0212 - 2.1172i	0.0001 + 0.0001i
		-1.0219 + 1.5536i	0.0001 - 0.0001i
		-1.0219 - 1.5536i	0.0001 + 0.0001i
		-1.0000	0.9998 + 0.0000i
		-1.0270 + 0.4572i	-0.0002 - 0.0001i
		-1.0270 - 0.4572i	-0.0002 + 0.0001i
		-0.9480 + 0.8625i	-0.0002 - 0.0000i
		-0.9480 - 0.8625i	-0.0002 + 0.0001i
		-1.0508 + 1.0379i	0.0001 - 0.0004i
		-1.0508 – 1.0379i	0.0002 + 0.0003i

When extracting a single pole, it is necessary to satisfy the Nyquist sampling rate. The latter is defined as

$$f_s \geq 2 f_h . \tag{4.8}$$

The Nyquist time-domain requirement is

$$\Delta t = t_s \leq \frac{1}{2 f_h}. \tag{4.9}$$

In the measurements, where the highest frequency is 20 GHz, the required sampling step is $t_s \leq 25$ ps.

By increasing the number of poles, extraneous poles are created which are characterized by zero residue values. However, as the number of poles increases, the extraneous poles start to have a finite residue value introducing more error to the pole/residue calculations. The error is introduced due to increased matrix size creating higher rounding errors.

Let us now assume a new function with multiple poles as follows:

$$F(s) = \frac{1}{(s+1)} \frac{1}{(s+2)} \frac{1}{(s+3)} \frac{1}{(s+20)} \Leftrightarrow f(t) = -\frac{e^{-20t}}{5814} + \frac{e^{-3t}}{34} - \frac{e^{-2t}}{18} + \frac{e^{-t}}{38} \tag{4.10}$$

The poles are –1, -2, -3, -20 and the residues are $1/38$ (0.0263158), $1/18$ (0.0555556), $1/34$ (0.0294118), $1/5814$ (0.000171999). The function is shown in Fig. 4.3.

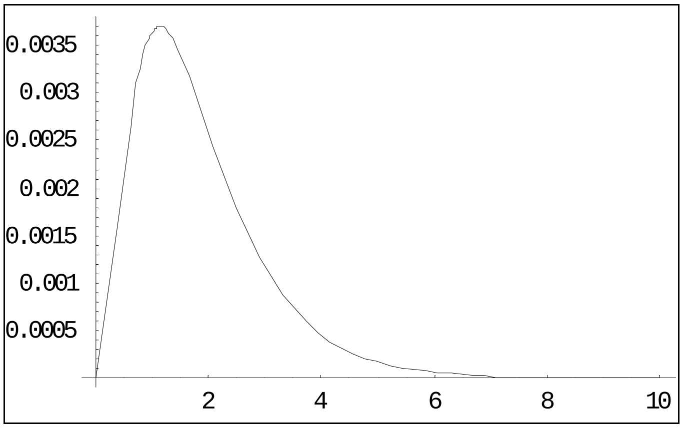

Figure 4.3. Function with multiple single poles

If we increase the sampling rate (Δt) of the waveform as shown in Table 4.3 the values of the poles and residues degrade. One can notice that the pole located far on the omega axis is not extracted. However, if we sample more finely (Δt < 1) we get significant improvement in the results. As we can see from the results for Δt = 1, the pole at –20 is not extracted; the extracted value is completely wrong. The waveform was not sampled finely enough to extract the pole at –20 and requires Δt of 0.157 in order to capture that particular pole.

In conclusion, to achieve a maximum accuracy, it is important to predict how many poles are present in the system. By choosing more poles than the system has, the accuracy of the residues of the true poles is reduced. Also, the waveform has to be properly sampled in order to obtain correct pole/residue values; the sampling rate has to meet the Nyquist criteria. If the function is undersampled, the Prony's method will not be able to extract that particular pole/residue value.

Next, Prony's method will be used in the extraction of multiple pairs of complex conjugate poles. Since the pole/residue representation describes a system in both the time and frequency domain, poles of the system appear in complex conjugate pairs in order to represent a real function.

Table 4.3. Variable Δt ($K = 8$, $N = 4$, and $\Delta p = 1$)

Δt	*Poles*	*Residues*
1	-1.0000	0.0263 + 0.0000i
	-2.0000	-0.0556 - 0.0000i
	-2.9998	0.0294 + 0.0000i
	-7.8204 + 3.1416i	-0.0002 - 0.0000i
2	-1.0000	0.0263 + 0.0000i
	-1.1360 + 1.5708i	-0.0000 - 0.0000i
	-2.0000	-0.0556 - 0.0000i
	-2.9960	0.0293 + 0.0000i
4	-0.9899 + 0.7854i	0.0000 + 0.0000i
	-1.0000	0.0263 + 0.0000i
	-2.0100	-0.0598 - 0.0000i
	-2.6053	0.0334 + 0.0000i

4.1.2 Prony's Method – Multiple Pairs of Complex Conjugate Poles

The measured waveform is a real function, which is the case with all measurements. In order to have a real function in the frequency domain one needs to have a pair of complex conjugate poles. For a numerical investigation using the Prony's method, a simple function with a pair of complex conjugate poles can be represented as follows:

$$F(s) = \frac{1}{(s+1-2i)} + \frac{1}{(s+1+2i)} \Leftrightarrow f(t) = e^{(-1+2i)t} + e^{(-1-2i)t}. \qquad (4.11)$$

The function is basically a damped sinusoid and is shown in Fig. 4.6. The conjugate pole set $s_n = -1 \pm 2i$ has residue value of one. The more general expression of the pole is $s_n = \sigma_n + j\omega_n$, where σ_n is a damping coefficient and ω_n is the resonant frequency of the pole. The value of the damping coefficient determines how fast the waveform is decaying. The value of the resonant frequency determines the frequency of the oscillation of the waveform.

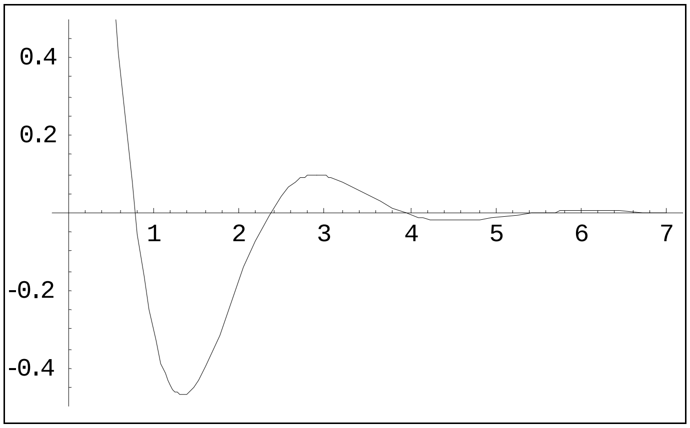

Figure 4.4. Function with a pair of complex conjugate poles

The numerical results on pole/residue extraction by varying different algorithm parameters are identical to those obtained using single pole and multiple pole functions. One can also consider a function with multiple pairs of complex conjugate poles. One example of a function with two complex conjugate poles is as follows:

$$\begin{aligned} F(s) &= \frac{1}{(s+1-2i)} + \frac{1}{(s+1+2i)} + \frac{1}{(s+2+4i)} + \frac{1}{(s+2-4i)} \\ &\Updownarrow \\ f(t) &= e^{(-1+2i)t} + e^{(-1-2i)t} + e^{(-2+4i)t} + e^{(-2-4i)t} \end{aligned} \qquad (4.12)$$

The function is shown in Fig. 4.5.

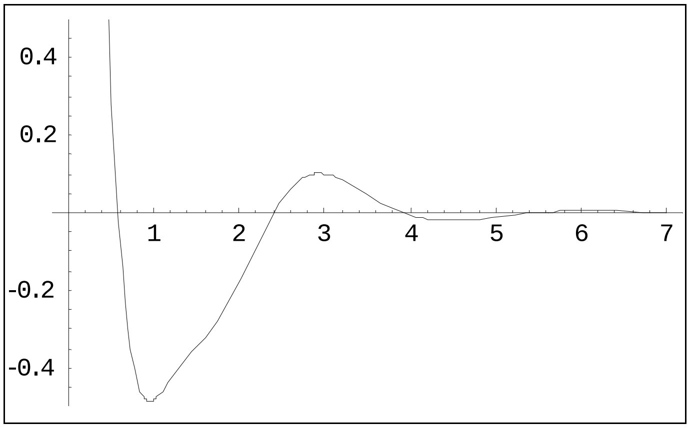

Figure 4.5. Function with 2 pairs of complex conjugate poles

As in the case with poles on the real sigma axis, the complex conjugate poles have similar behavior in terms of setting the correct parameters in the Prony's algorithm. One needs, again, to satisfy the Nyquist criteria and as accurately as possible predict the number of the poles in the system.

The work in [4.5] shows that it is possible to proceed with the Prony's method of finding multiple poles without knowing if the poles exist. However, the pole extraction was successful but the residues values were not correct. The presence of more poles than the system has causes the residues of the true poles to be inaccurate. This was also observed in our modest numerical results. To find the number of poles in the system, it is useful to perform singular value decomposition (SVD). The number of poles in the system prediction will be addressed in later sections.

4.1.3 Prony's Method – Multiple Pairs of Complex Conjugate Double Poles

Another function that can be encountered in communication systems is a function with complex conjugate double poles. This type of waveform can be encountered when measuring two identical antennas. A simple complex conjugate double pole function is given by

$$\begin{aligned} &F(s)=\frac{1}{(s+1-2i)^2}+\frac{1}{(s+1+2i)^2} \\ &\Updownarrow \\ &f(t)=te^{-1+2i}+te^{-1-2i}. \end{aligned} \tag{4.13}$$

The function $F(s)$ is shown in Fig. 4.6.

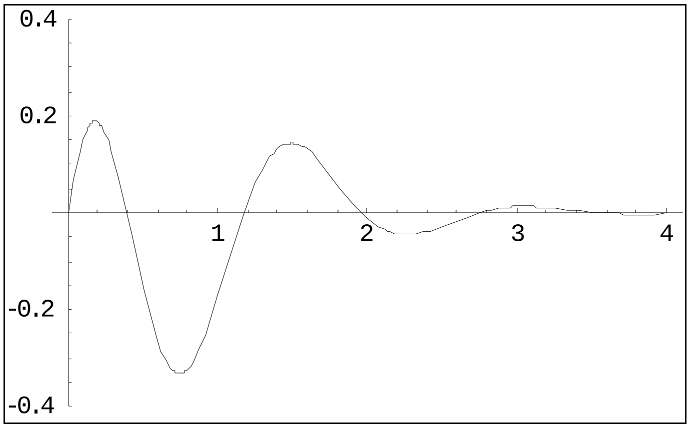

Figure 4.6. Function with a pair of complex conjugate double pole

This function has two double poles at –1-2i and –1+2i. Using Prony's method, one obtains results as shown in Table 4.4.

Table 4.4. Prony's method results ($\Delta t = 0.2$, $\Delta p = 1$, $K = 8$, $N = 4$)

Poles	***Residues*** $\cdot 10^4$
-1.0000 + 2.0000i	5.4958 + 8.9060i
-1.0000 - 2.0000i	5.4960 - 8.9065i
-1.0000 + 2.0000i	-5.4958 - 8.9060i
-1.0000 - 2.0000i	-5.4960 + 8.9065i

If one picks the correct parameters, the poles are correct. However, the residue values are completely wrong as a result of the double pole form. A more complicated function can be represented as follows:

$$
\begin{aligned}
&F(s) = \frac{1}{(s+1-2i)^2} + \frac{1}{(s+1+2i)^2} + \frac{1}{(s+2+4i)^2} + \frac{1}{(s+2-4i)^2} \\
&\Updownarrow \\
&f(t) = te^{-1+2i} + te^{-1-2i} + te^{-2+4i} + te^{-2-4i}.
\end{aligned}
\tag{4.14}
$$

The function $F(s)$ is shown in Fig. 4.7.

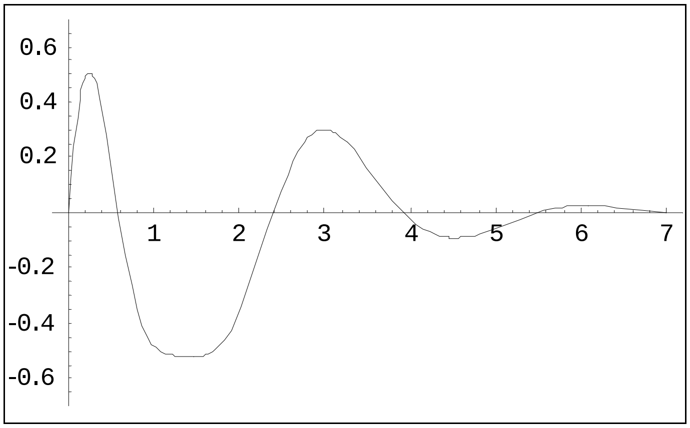

Figure 4.7. Function with 2 pairs of complex conjugate double poles

The pole/residue extraction using Prony's method on a more complicated function shows the same problems. While the poles are correct, the residue values are completely wrong. Table 4.5 shows the results using Prony's method.

Table 4.5. Prony's method results (K = 16, N = 8, Δt = 0.5)

Poles	*Residues* $\cdot 10^5$
-0.9999 + 2.0000i	2.1553 - 0.7245i
-0.9999 - 2.0000i	2.1599 + 0.7246i
-1.0000 + 1.9999i	-2.1553 + 0.7245i
-1.0000 - 1.9999i	-2.1599 - 0.7246i
-1.9999 + 3.9999i	0.3733 + 0.0597i
-1.9999 - 3.9999i	0.3682 - 0.05604i
-2.0000 + 4.0000i	-0.3733 - 0.0597i
-2.0000 - 4.0000i	-0.3682 + 0.0560i

In order to obtain the correct results for the residues of the double poles one needs to modify Prony's method. A more general expression must be assumed. In the next section, we will discuss a modified Prony's method that will be able to calculate correct residues for double pole systems. Also, we will address the advantages of variable sampling (changing Δp parameter). The new variable sampling Prony's method formulation will show significant advantages in extracting the correct poles/residues of the system.

4.1.4 Modified Prony's Method - Variable Sampling and Double Pole Systems

Two new formulations of Prony's method are presented. As shown in the previous section, Prony's method cannot obtain correct residues if the waveform contains complex conjugate double poles. A new formulation is presented in this section that is suitable for extraction of correct residues in systems where double poles are present.

The second formulation allows for variable sampling by arbitrarily varying the Δp parameter. The new formulation allows keeping the time-domain window of interest constant while changing the number of poles (N) present in the system. Van Blaricum and Mittra have addressed similar issues. However, in their work they resampled the whole waveform [2.31]. In essence, they kept Δp constant and increased Δt by factor of 2. Our way is more optimal because it keeps the original measured sampling rate.

4.1.4.1 Double Pole Systems

There is a need to modify Prony’s method in order to accommodate cases where we need to extract correct residue values from waveforms with complex conjugate double poles. An attempt to modify Prony’s method to accommodate for a double pole is presented in [4.5]. However, the algorithm can handle double single poles but it is not suitable for calculation of residues when double conjugate poles are present. The simple solution is presented where Prony’s difference equation order needs to be increased in order to accommodate double poles [4.5]. This is only sufficient for calculating the correct poles but the corresponding residues are incorrect.

In order to accommodate Prony’s method for calculation of double poles and residues, we start with the more general expression

$$v(t) = \sum_{n=1}^{N} \left(A_n + B_n t\right) e^{s_n t} \; . \tag{4.15}$$

This expression is a true representation of a function with double conjugate poles that we encountered in the previous sections. Since the measured data is sampled, it is convenient to put the expression in the following form:

$$v(t_k) = \sum_{n=1}^{N} (A_n + k\Delta t B_n) e^{s_n k\Delta t}, k \in (0, K) \, . \tag{4.16}$$

In order to have the correct residues, we need to accommodate the residue matrix in a different way as follows:

$$A = \begin{bmatrix} e^{s_1 0\Delta t} & 0 & e^{s_2 0\Delta t} & 0 & e^{s_3 0\Delta t} & 0 & e^{s_4 0\Delta t} & ..... & ..... & 0 \\ e^{s_1 1\Delta t} & 1e^{s_1 1\Delta t} & e^{s_2 1\Delta t} & 1e^{s_2 1\Delta t} & e^{s_3 1\Delta t} & 1e^{s_3 1\Delta t} & e^{s_4 1\Delta t} & . & . & . \\ e^{s_1 2\Delta t} & 2e^{s_1 2\Delta t} & e^{s_2 2\Delta t} & 2e^{s_2 2\Delta t} & e^{s_3 2\Delta t} & 2e^{s_3 2\Delta t} & e^{s_4 2\Delta t} & . & . & . \\ e^{s_1 3\Delta t} & 3e^{s_1 3\Delta t} & e^{s_2 3\Delta t} & 3e^{s_2 3\Delta t} & e^{s_3 3\Delta t} & 3e^{s_3 3\Delta t} & e^{s_4 3\Delta t} & . & . & . \; .. \\ . & . & . & . & . & . & . & . & . & . \\ . & . & . & . & . & . & . & . & . & . \\ . & . & . & . & . & . & . & . & . & . \\ e^{s_1 h\Delta t} & pe^{s_1 h\Delta t} & e^{s_2 h\Delta t} & pe^{s_2 h\Delta t} & e^{s_3 h\Delta t} & pe^{s_3 h\Delta t} & e^{s_4 h\Delta t} & ..... & ..... & . \end{bmatrix}, h = K.$$

The x matrix is

$$x = \left[A_1 \;\; \Delta t B_1 \;\; A_2 \;\; \Delta t B_2 \; \ldots \; \Delta t B_{(K)} \right]^T .$$

Finally, the *B* matrix consists of the known sample voltage values in the $A\,x = B$ system. Now, we are ready to deal with the residues of the double poles. If we calculate the values of the residues for the complex multiple conjugate function from the previous section, we get the results shown in Table 4.6.

Table 4.6. Modified Prony's method approximation of complex multiple conjugate double poles function in Eq. (4.12)

Poles	$A \cdot 10^{-5}$	*B*
-1.0000 + 2.0000i	0.0261 - 0.0087i	0.5000 - 0.0000i
-1.0000 - 2.0000i	0.0261 + 0.0087i	0.5000 + 0.0000i
-1.0000 + 2.0000i	-0.0261 + 0.0087i	0.5000 + 0.0000i
-1.0000 - 2.0000i	-0.0261 - 0.0087i	0.5000 - 0.0000i
-2.0000 + 4.0000i	0.1628 + 0.0239i	0.5000 + 0.0000i
-2.0000 - 4.0000i	0.1628 - 0.0239i	0.5000 - 0.0000i
-2.0000 + 4.0000i	-0.1627 - 0.0238i	0.5000 - 0.0000i
-2.0000 - 4.0000i	-0.1627 + 0.0238i	0.5000 + 0.0000i

Fig. 4.8 shows the plot of the results from the modified Prony's method and a function shown in Fig. 4.7. The functions are almost identical. The modified Prony's method introduces small error since *A* should be zero as shown in Eq. (4.12).

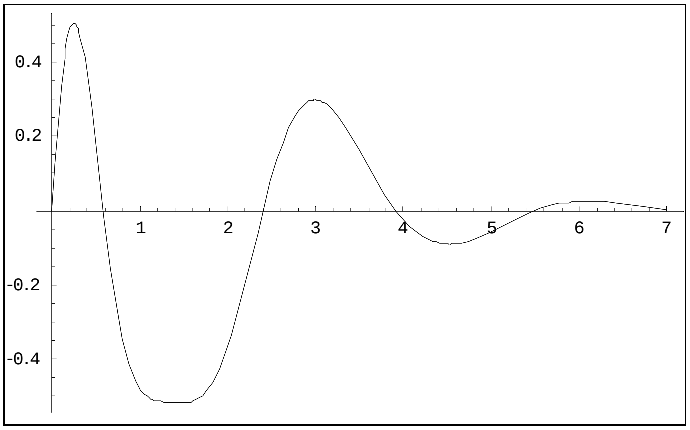

Figure 4.8. Comparison between the function shown in fig. 4.7 (-) and the results obtained with modified Prony's method (--)

4.1.4.2 Variable Sampling

Without variable sampling, one is windowing the data by including more poles in the computation and changing the spectral composition of the waveform of interest. We will show that with variable sampling it is possible to obtain more optimal solutions and gain more insight into the behavior of a particular system due to a fixed time-domain window of interest.

First, we need to re-examine Eq. (4.4), which is repeated here for convenience

$$\sum_{n=0}^{N-1} \alpha_n v_{n+m} = -v_{N+m},$$

note that $m \in (0, M-1)$. In this formulation, the maximum window is defined by $N+M$. The maximum window defines the time window on which the processing is going to be performed. It is necessary to have a correct window in order to quantify the system correctly. If the time window is too short one might miss some essential system characteristics. If the time window is too long one might include multi-path, which does not characterize the system by itself.

In this formulation, in order to control the window one needs to decrease or increase the number of poles for an optimum time window. Another way is to increase the parameter M while keeping the number of poles N constant. However, this increases the size of a matrix and the matrix is not symmetric. This method of adjusting the time window proved to be very inaccurate.

In order to satisfy two criteria: (1) keeping the symmetric matrix $2N = K$ or use a least-squares pseudo-inverse to obtain a square formulation and (2) keeping the number of poles fixed while adjusting for an optimum window a new formulation is required. We introduce a new parameter, called the window shift (Δp). Eq. (4.4), then, can be rewritten in the following way:

$$\sum_{n=0}^{N-1} \alpha_n v_{n\cdot\Delta p+m} = -v_{N\cdot\Delta p+m}. \tag{4.17}$$

Now, one is able to satisfy conditions (1) and (2) while adjusting for an optimal window. In essence, by introducing the window shift (Δp) one is able to sample at least a full cycle at the lowest frequency of interest. This formulation gives more insight into the pole/residue composition of the system since one is able to keep the time widow constant. By changing the time window, the system’s frequency spectrum is changing. Thus, the pole and residue composition changes. We present some of the results using Prony’s method on an arbitrary time-domain waveform.

The waveform used in the study is shown in Fig. 4.9 in the time and frequency domains. The duration of the time-domain waveform is 2.5 ns.

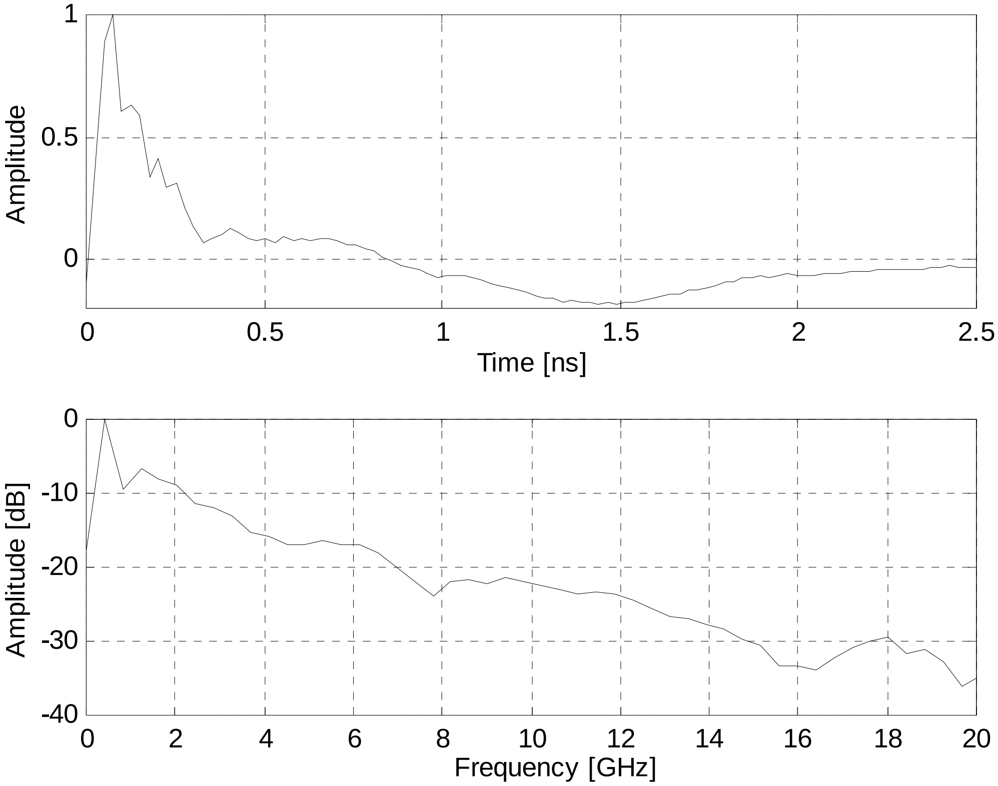

Figure 4.9. Time and frequency-domain representation of a waveform

If one uses Eq. (4.4) the window is defined by $M+N$. The parameters used in Prony's method implementation are shown in Fig. 4.1. Thus, if one would like to investigate the pole structure with reduced number of poles while keeping conditions (1) and (2), one is not able to keep the time window shown in Fig. 4.9. By just reducing the number poles one is not able to capture all the features of the antenna response. The effect is illustrated in Figs. 4.10 and 4.11. By changing the window, one changes the spectrum composition of the waveform, thus not representing the real antenna system. Prony's method provides a fit to the response in both the time and frequency domain. However, the pole structure is not a true representation of the system.

If one tries to implement a variable sampling method using the expression in Eq. (4.15), the time-domain window in Fig. 4.9 is preserved. Prony's method is extracting the poles from a window that represents all the waveform essential features. The results are shown in Figs. 4.12 and 4.13. One can notice that Prony's method achieves a very good match up to 4.0 GHz in both amplitude and phase in the frequency domain. The results show that the poles match low frequency contributions of the antenna. This is more apparent in Fig. 4.13 looking at the time-domain response of the antenna. The low frequency contributions are characterized by smooth transitions while the high frequency components have very abrupt transitions. We see that the poles model smooth transitions or low frequency components. This indicates that more poles are needed to model the waveform. However, the results show this pole set captures all the essential features of the antenna at the lower frequencies.

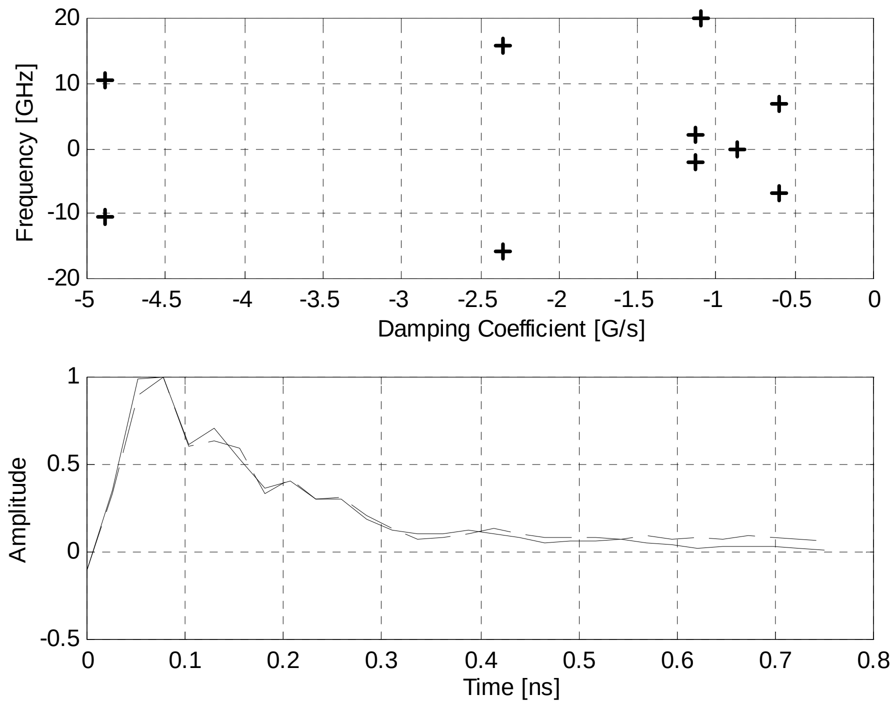

Figure 4.10. Prony's method approximation (-) using Eq. (4.4) without variable sampling – pole structure and time-domain waveform (--)

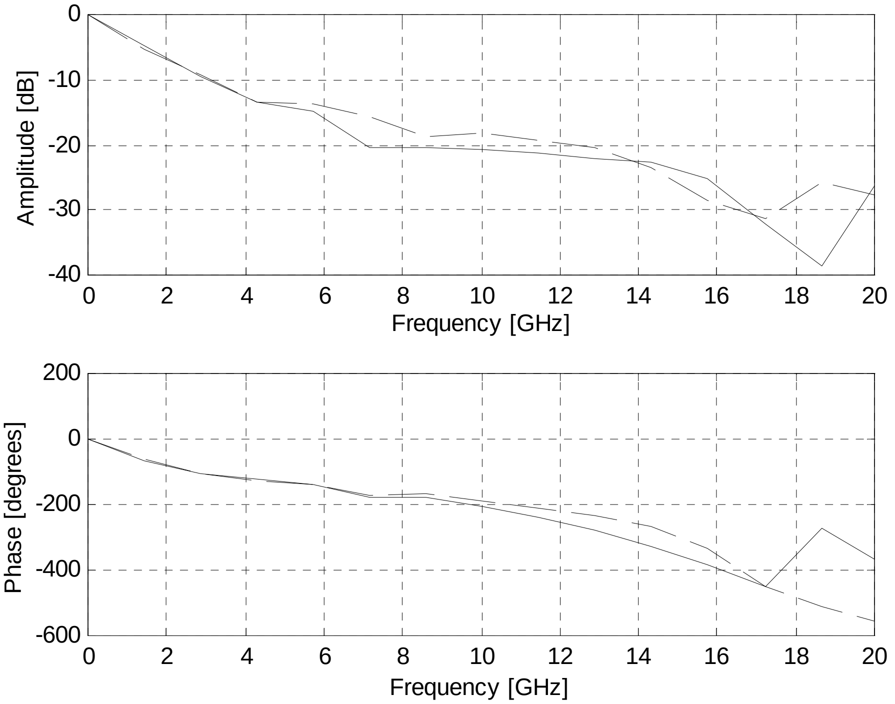

Figure 4.11. Prony's method approximation (-) using Eq. (4.4) without variable sampling – frequency domain response amplitude and phase (--)

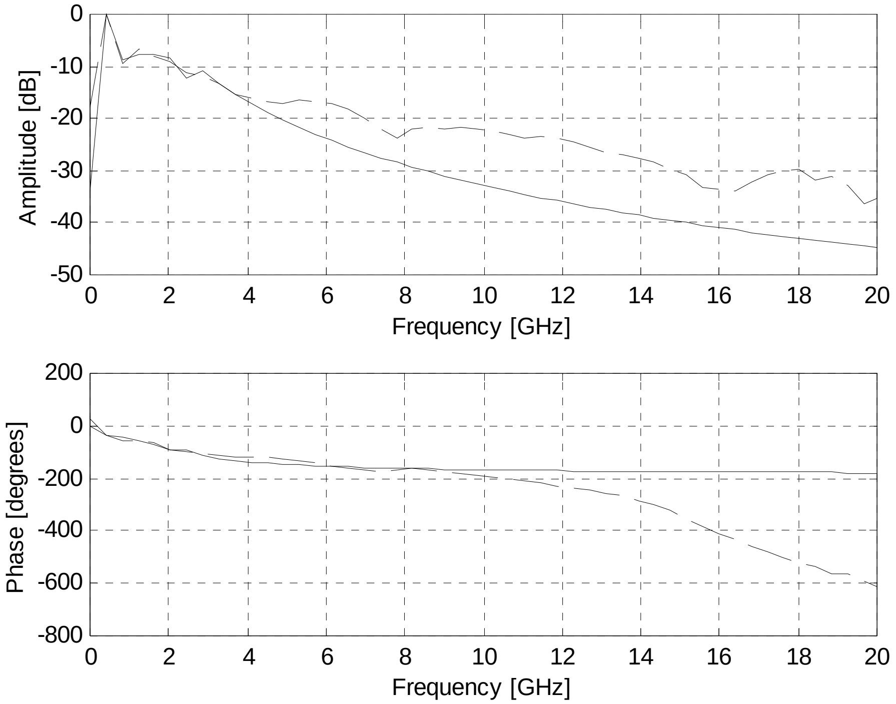

Figure 4.12. Prony’s method approximation (-) using Eq. (4.15) with variable sampling ($\Delta p = 8$) – frequency domain response amplitude and phase (--)

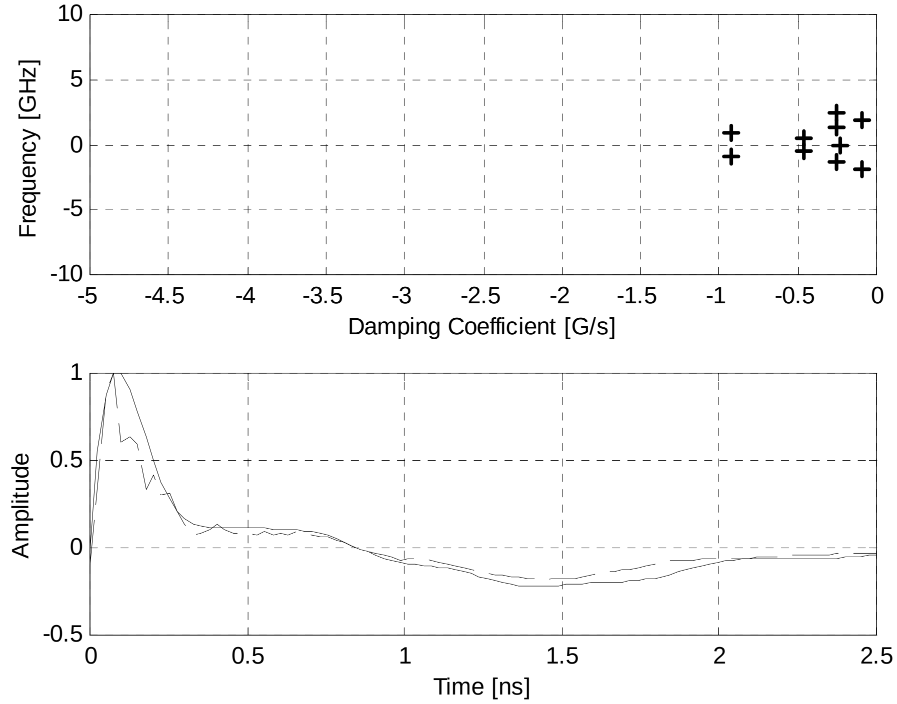

Figure 4.13. Prony’s method approximation (-) using Eq. (4.15) with variable sampling ($\Delta p = 8$) – pole structure and time-domain waveform (--)

In conclusion, is this an optimal way to sample a waveform? No. The best possible sampling would be a nonlinear sampling. The nonlinear sampling would sample finely where a waveform has lot of details (high frequency contributions) and course where the waveform exhibits just a basic sinusoidal behavior (low frequency contributions). However, linear sampling is inherent in the Prony's method. Next, we will investigate the Matrix-Pencil method, which provides some advantages over Prony's method.

4.2 Matrix-Pencil Method

The Matrix-Pencil method is a more elegant way of obtaining the poles and residues of the system. This method is a one-step process compared to Prony's method where the poles are obtained through finding roots of a characteristic polynomial. In this section we present derivations of Matrix-Pencil method.

4.2.1 Matrix Pencil Method in the Noiseless Environment

The Matrix-Pencil method originated from a definition of a matrix pencil. If two functions are combined on a common interval with a scalar parameter λ in the manner

$$f(t,\lambda) = g(t) + \lambda h(t)\,, \tag{4.18}$$

then $f(t,\lambda)$ is called the pencil of the functions $g(t)$ and $h(t)$. The pencil-of-function contains very important features in extracting information about the poles present in the particular function [4.6,7,8]. The derivation below follows the Y. Hua and T. K. Sarkar development of the Matrix-Pencil method formulation. Using the idea of the pencil-of-function method, one can model a transient signal as

$$y(t_k) = \sum_{n=1}^{N} R_n e^{s_n k\Delta t}\,, \tag{4.19}$$

where $k \in (0,K)$ (K is number of sampled data), R_n are complex residues, s_n are the complex poles, and Δt is sampling interval. It is important to notice that $z_n = e^{s_n \Delta t}$ are the poles on the *z*-plane.

We start with the Matrix-Pencil method development for a noiseless case. One needs to consider the following set of vectors $v_{0,} v_1, ..., v_L$ where

$$v_i = [y_i, y_{i+1}, ..., y_{i+M-1}]^T \tag{4.20}$$

The superscript **T** denotes the transpose of a matrix. Now, it is possible to define matrices Y_1 and Y_2 as follows:

$$Y_1 = [\ v_0, v_1, ..., v_{N-1}\ ] \tag{4.21}$$

$$Y_2 = [\ v_0, v_1, ..., v_N\ ] \tag{4.22}$$

The matrices above can be decomposed in the following manner:

$$[Y_2] = [Z_1][R][Z_0][Z_2] \tag{4.23}$$

$$[Y_1] = [Z_1][R][Z_2] \tag{4.24}$$

In this formulation matrix $[Z_0]$ is a diagonal matrix with a desired pole values. The details of the definitions of matrices Z and R can be found in [4.6]. Now, it is possible to consider the matrix pencil

$$[Y_2] - \lambda[Y_1] = [Z_1]\ [R]\ [Z_0] - \lambda[\mathbf{I}][Z_2], \tag{4.25}$$

where $[\mathbf{I}]$ is $N \times N$ identity matrix. On can show that the parameters z_i (poles) can be found as the generalized eigenvalues of the matrix pair $\{[Y_2];[Y_1]\}$ [4.9]. Thus, the problem for solving for z_i (poles) is put in the following ordinary eigenvalue problem:

$$\{[Y_1]^+ [Y_2] - \lambda[\mathbf{I}]\} \tag{4.26}$$

where $[Y_1]^+$ is the Moore-Penrose pseudoinverse of $[Y_1]$.

4.2.2 Matrix Pencil Method in the Presence of the Noise

If the noise-affected data is $y(t)$, then it is possible to create a data matrix $[Y]$ as a combination of the matrix pair $\{[Y_2];[Y_1]\}$ in the following manner:

$$[Y] = \begin{bmatrix} y(0) & y(1) & \cdots & y(L) \\ y(1) & y(2) & \cdots & y(L+1) \\ \vdots & \vdots & & \vdots \\ y(N-L-1) & y(N-L) & \cdots & y(N-1) \end{bmatrix}_{(K-L)\times(L+1)}$$

The singular value decomposition (SVD) of the matrix $[Y]$ is carried out. The SVD of $[Y]$ can be written as

$$[Y] = [U][\Sigma][V]^H \tag{4.27}$$

The parameter M is chosen in such a way that the singular values beyond M are set to zero. A good way to pick M is through looking at the ratio between the maximum singular value and all other singular values in the matrix. Formally, this can be written as

$$\frac{\sigma_c}{\sigma_{\max}} \approx 10^{-p}, \tag{4.28}$$

where p is the number of significant decimal digits in the data. One should note that if the ratio in Eq. (4.27) is not decreasing, then the sum of damped complex exponentials model is not a correct way to model the data [4.6].

Next, the "filtered" matrix $[V']$ is constructed so that it contains only M dominant right-singular vectors of $[V]$:

$$[V'] = [v_1, v_2, \ldots, v_N]. \tag{4.29}$$

The singular vectors that correspond to small singular values are discarded. These vectors go from $N+1$ to L. Now, one can form the matrix pair $\{[Y_2];[Y_1]\}$ as

$$[Y_1] = [U][\Sigma'][V_1']^H \tag{4.30}$$

$$[Y_2] = [U][\Sigma'][V_2']^H \tag{4.31}$$

The matrix $[V_1']$ is obtained from $[V']$ by deleting the last row of $[V']$. In a similar manner, $[V_2']$ is obtained by removing the first row of $[V']$ and $[\Sigma']$ corresponds to N columns of $[\Sigma]$ which correspond to N dominant singular values. The problem is now reduced to solving an eigenvalue problem. The poles are eigenvalues of the following matrix system:

$$[V_2'] = \lambda [V_1']^H \Rightarrow [V_2']^H [V_1'] = \lambda [\mathbf{I}][V_1']^H [V_1']. \tag{4.32}$$

Now, it is possible to obtain the z_i (poles) of the system. Once poles and M are known, the residues R_i are found from the following least squares problem:

$$\begin{bmatrix} y(0) \\ y(1) \\ \vdots \\ y(N-1) \end{bmatrix} = \begin{bmatrix} 1 & 1 & \cdots & 1 \\ z_1 & z_2 & \cdots & z_M \\ \vdots & \vdots & & \vdots \\ z_1^{N-1} & z_2^{N-1} & \cdots & z_M^{N-1} \end{bmatrix} \begin{bmatrix} R_1 \\ R_2 \\ \vdots \\ R_M \end{bmatrix}. \tag{4.33}$$

By obtaining both the poles and residues of the system, one can approximate a system with a reduced set of parameters. Next, we will consider a Matrix-Pencil method where the size of the matrix will be actually reduced through singular value decomposition, which is not evident from the above presentation.

4.2.3 Matrix-Pencil Method - Reduced Size Matrix Formulation

If one considers the singular value decomposition in Eq. (4.26), it is evident that some of the values due to low singular values could be ignored in the computation. Some of the lower singular values could be noise contribution. However, by setting non-significant singular values to zero, the size of the matrix is not reduced. The size of the problem, number of poles, stays the same. Thus, it is important to investigate the properties of the singular value decomposition in order to obtain a reduced set.

The singular value decomposition is defined as

$$[Y] = [U][\Sigma][V]^H , \tag{4.34}$$

where U is a $M \times L$ matrix, Σ is a $L \times L$ matrix, and V is an $L \times L$ unitary matrix. The matrix Σ has singular values on its diagonal and 0's elsewhere. One has to notice that the singular values are nonnegative square roots of the eigenvalues of $Y^* \cdot Y$.

By observing the matrix composition of the collected data one can reduce the size of the matrix by reconstructing the $[Y]$ matrix as

$$[Y] = [U]_{M \times L}[\Sigma]_{L \times L} \tag{4.35}$$

The values of L are determined in the similar fashion as defined by Eq. (4.27). However, the criterion was used differently in the composition of $[Y]$ matrix. Now, one can form a new matrix pair $\{[Y_2];[Y_1]\}$ as

$$[Y_1] = [U][\Sigma_1] \tag{4.36}$$

$$[Y_2] = [U][\Sigma_2]. \tag{4.37}$$

The matrices $[V_1^{'}]$ and $[V_2^{'}]$ are obtained as indicated before. Thus, one can pose the same eigenvalue problem as shown in Eq. (4.31). The residues could be calculated using Eq. (4.32). With reduced form, one can reduce the rank of the $[Y]$ matrix, reduce number of poles present in the system, and obtain more accurate results.

The reduced size matrix formulation was not evident from the presentation by T. K. Sarkar and O. Pereira [4.6]. However, the Matrix-Pencil subroutine at the end of the paper reveals this formulation. In fact, the matrix $[Y]$ can be reconstructed by just using either the $[U]$ or $[V]$ matrix.

4.2.4 Matrix-Pencil Method in the Presence of Noise

In order to verify the Matrix-Pencil method, a known set of poles was used to create the time-domain waveform. The time-domain waveform was processed, and the Matrix-Pencil method was used to extract the poles and the residues. The additive white Gaussian noise, AWGN, was introduced to the time-domain waveform in order to estimate the performance of the method in the presence of the noise. ADWG was defined by

$$N(t) = \frac{1}{\sqrt{2\pi\sigma^2}} e^{\frac{-(t-m)^2}{2\sigma}} , \tag{4.38}$$

where σ is a variance and *m* is the mean. For the noise study, the mean was set to zero. Now one is able to calculate the signal-to-noise ratio as

$$\frac{E_b}{N_0} = \frac{\int_0^{t_1} (s(t))^2 dt}{\sigma^2} , \tag{4.39}$$

where $s(t)$ is the desired signal. Tables 4.7 and 4.8 show the results of the noise study.

Table 4.7. The Matrix-Pencil Method in the Presence of Noise – Poles

Original Poles $\cdot 10^{10}$	Extracted $\sigma^2 = 0$	% Error Real/Imag	Extracted $\sigma^2 = 7 \cdot 10^7$	% Error Real/Imag	Extracted $\sigma^2 = 2 \cdot 10^8$	% Error Real/Imag
-0.1257 - 1.6965i	-0.1257 - 1.6965i	0.0/0.0	-0.1239 - 1.7043i	6.1/0.1	-0.0915 - 1.6277i	37.3/4.2
-0.0628 - 0.6283i	-0.0628 - 0.6283i	0.0/0.0	-0.0631 - 0.6309i	1.8/0.04	-0.0616 - 0.6300i	2.0/0.3
-0.0628 - 0.4398i	-0.0628 - 0.4398i	0.0/0.0	-0.0641 - 0.4443i	2.4/0.3	-0.0630 - 0.4357i	0.2/0.9

The study shows that the higher frequency poles are more prone to the noise and require higher SNR values. The σ^2 value of $7 \cdot 10^7$ corresponds to SNR value of 46 dB and the σ^2 value of $2 \cdot 10^8$ corresponds to SNR value of 35 dB for a signal described by poles and residues used in this study. Even though the SNR is signal specific, the calculations show that the Matrix-Pencil method requires around 30 dB of SNR for accurate pole/residue extraction.

Table 4.8. The Matrix-Pencil Method in the Presence of Noise – Residues

Original Residues $\cdot 10^9$	Extracted $\sigma^2 = 0$	% Error Abs	Extracted $\sigma^2 = 7 \cdot 10^7$	% Error Abs	Extracted $\sigma^2 = 2 \cdot 10^8$	% Error Abs
0.5000 - 0.0200i	0.5000 - 0.0200i	0.0	0.4930 - 0.0143i	2.3	0.3142 - 0.1722i	39.7
-1.0000 - 1.3000i	-1.0000 - 1.3000i	0.0	-0.9526 - 1.3140i	2.3	-0.9665 - 1.3429i	0.9
-0.0600 - 1.0000i	-0.0600 - 1.0000i	0.0	-0.1145 - 1.0645i	0.9	-0.0305 - 0.9892i	1.2

4.3 Data Estimation Using Frequency Domain Techniques

The poles and residues of a system can be directly obtained from the frequency domain data set. This is an alternative approach to time-domain spectral estimators as Prony's method and the Matrix-Pencil method. However, if the frequency domain data contains multi-path components, it is extremely difficult to eliminate the multi-path directly from the frequency domain. So, in general, one needs to eliminate the multi-path by obtaining the time-domain equivalent through an IFFT transform. Also, it is a much easier task to eliminate the path loss and obtain the minimal phase of the system in the time domain.

Two frequency-domain methods are presented in this section. The first one is based on the work by E. C. Levy [4.9]. The second method was introduced by R. Kumersan and is a frequency-domain equivalent of Prony's method in the time-domain [4.10]. The frequency-domain pole and residue extraction is also discussed in [4.11-14].

4.3.1 Levy's Frequency Domain Technique

This method is restricted to systems which have no poles on the imaginary axis; i.e., to systems having a finite, steady-state (zero frequency) magnitude. The derivations follow Levy's work [4.9]. The complex frequency response of the system can be described by the following expression:

$$G(j\omega) = \frac{A_0 + A_1(j\omega) + A_2(j\omega)^2 + A_3(j\omega)^3 + ...}{B_0 + B_1(j\omega) + B_2(j\omega)^2 + B_3(j\omega)^3 + ...} \tag{4.40}$$

One can define $F(j\omega)$, which represents the measured data exactly. The function $F(j\omega)$ has real and imaginary parts and it is defined as:

$$F(j\omega) = R(\omega) + jI(\omega) \tag{4.41}$$

The error between the measured data and the complex frequency approximation is the following:

$$\begin{aligned} \varepsilon(\omega) &= F(j\omega) - G(j\omega) \\ G(j\omega) &= \frac{N(\omega)}{D(\omega)} \end{aligned} \tag{4.42}$$

This can be rewritten in the following manner:

$$D(\omega)\varepsilon(\omega) = a(\omega) + jb(\omega) \tag{4.43}$$

The functions $a(\omega)$ and $b(\omega)$ depend on frequency and the unknown coefficients A_i and B_i. For a specific frequency,

$$\left|D(\omega_k)\varepsilon(\omega_k)\right|^2 = a^2(\omega_k) + b^2(\omega_k) \tag{4.44}$$

By summing over the sampling frequencies ω_k, one defines a function E as

$$E = \sum_{k=0}^{m}\left[a^2(\omega_k) + b^2(\omega_k)\right] \tag{4.45}$$

The unknown coefficients A_i and B_i are found by minimizing the function E. By differentiating with the respect to the each of the unknown coefficient and by setting the results equal to zero one obtains the following expression (for coefficient A_0):

$$\frac{\partial E}{\partial A_0} = \sum_{k=0}^{m} -2(\sigma_k R_k - \omega_k \tau_k I_k - \alpha_k) = 0 \tag{4.46}$$

Using linear transformations and defining certain relationships one can obtain the following equation (details can be found in [4.9]):

$$A_0\lambda_0 - A_2\lambda_2 + A_4\lambda_4 - A_6\lambda_6 + ... + B_1T_1 + B_2S_2 - B_3T_3 - B_4S_4 + B_5T_5 + ... = S_0 \tag{4.47}$$

This equation can be put in the matrix form

$$(M)\cdot(N) = (C) \tag{4.48}$$

By solving for (N), one can obtain the unknown coefficients and estimate the frequency-domain data set.

4.3.2 Prony's Frequency Domain Equivalent Method

A method of obtaining the transfer function from the frequency-domain response values has its roots in the 19th century work of Cauchy and Jacobi. A modern revision is presented by Kumaresan [4.10]. Even though the problem is nonlinear in nature, the method involves solving a set of simultaneous linear equations. Thus, this method is similar to Prony's method used in parameter extraction in time-domain based systems. The development of the frequency domain Prony's method follows the work by Kumaresan.

The pole/residue system can be described by the following transfer function

$$H(z) = \frac{A(z)}{B(z)} = \frac{\sum_{k=0}^{q} a_k z^k}{1 + \sum_{k=1}^{p} b_k z^k}. \tag{4.49}$$

The problem is posed in the following way: if we are given the frequency response values of the system $H(u_0),\ H(u_1),...,\ H(u_n)$ at the frequencies $u_0,\ u_1,\ ...,\ u_n$, how do we determine the coefficients of the polynomials $A(z)$ and $B(z)$ [4.10]? The unknown variables *p, q* (degree of the polynomial) and coefficients a_k and b_k.

If we consider an arbitrary set of complex values $H(u_i),\ i = 0,1,2,\ ...,\ n\ \left(n > (p+q)\right)$ at $u_i,\ i = 0,1,2,...,n$ it is required to interpolate these points by a ratio of polynomials $A(z)/B(z)$. Then, one can use a relational interpolation originated by Cauchy in 1821. Basically, Cauchy made the problem linear in the following way. Since,

$$H(u_i) = \frac{A(u_i)}{B(u_i)},\ i = 0,1,2\ldots n \tag{4.50}$$

it follows that

$$H(u_i)B(u_i) - A(u_i) = 0,\ i = 0,1,2\ldots n \tag{4.51}$$

Eq. (4.43) can be put in the matrix –vector form

$$\lfloor \Lambda_H U_{p+1}, -U_{q+1} \rfloor x = 0 \tag{4.52}$$

, where $x = \left(1, b_1, b_2, ..., b_p, a_0, a_1, ..., a_q\right)^T$ and Λ_H is an $(n+1 \times n+1)$ diagonal matrix with entries $H(u_i)$, $i = 0,1,2,...,n$ along the diagonal in order. U_{p+1} and U_{q+1} are $(n+1 \times p+1)$ and $(n+1 \times q+1)$ matrices whose $(i,j)th$ elements are defined as follows:

$$\begin{aligned} U_{p+1}(i,j) &= u_i^j, \quad i = 0,1,2,...,n \quad \textit{and} \quad j = 0,1,2,...,p \\ U_{q+1}(i,j) &= u_i^j, \quad i = 0,1,2,...,n \quad \textit{and} \quad j = 0,1,2,...,q \end{aligned} \tag{4.53}$$

In a case where $n = p + q$, the formulation in Eq. (4.44) is an undetermined system and will always have a nontrivial solution. However, Jacobi addressed a problem of 'unattainable points' with this approach. Thus, *H(z)* may not interpolate all the given points. But if the data originates from a pole/residue system there exists a valid solution to Eq. (4.44).

The other problem arises from not knowing the exact values of *p* and *q*. So, one has to try various values in order to obtain a solution. The author proposes two approaches to this problem. In first approach is to assume some *p'* and *q'* values that are higher than the true *p* and *q* values. Then one constructs the matrix on the left of Eq. (4.44) with the size of $(n+1) \times (p'+q'+2)$, where *n* is sufficiently large and the rank of the matrix is determined. The rank of the matrix will be $p + q$ if $p + q \leq n$. This process requires a lot of time. The second approach is decoupling the degrees and coefficients of $A(z)$ and $B(z)$, which was originally proposed by Jacobi.

4.4 Conclusions

It is shown, through modest numerical results that Prony's method works well if Nyquist criteria are satisfied and the number of poles in the system are known. It is of the most importance to relate a physical interpretation of the waveform to Prony's method. Prony's method will always yield inaccurate poles and residues if used blindly. The new Prony's method formulations are introduced to handle double poles and variable sampling.

The presence of double poles (e.g. antennas in the link are identical) can be handled by using a modified Prony's method that accommodates the extraction of double poles. In Chapter 5, we will demonstrate a technique where a single antenna response is obtained and double poles are no longer present in the waveform.

Variable sampling, using a modified Prony's method formulation, gives better insight in the pole/residue extraction of antenna systems and keeps the time-domain window of interest constant. By keeping the time-domain window of interest constant, one can capture all the significant features of the particular response.

The Matrix-Pencil method is a more elegant way of obtaining the poles/residues of a system. This method gives more accurate results since it is a one step procedure that reduces round-off error problems.

The frequency-domain methods are advantageous if the measurements are performed in the frequency domain. Thus, one does not need to perform IFFT to obtain time-domain equivalent and introduce more errors due to Fourier transforms. The other problems are associated with eliminating the multi-path contributions and obtaining the minimal phase distance. In addition, the frequency-domain approach generally favors a curve fit across all frequencies, rather than be dominated by the low-frequency terms that dominate the time-domain waveform.

In the next chapters we will use the Matrix-Pencil method in order to obtain poles/residues of different classes of antenna systems. We will investigate traveling wave antennas, resonant antennas, and frequency-independent antennas. Later, in Chapter 6, the Matrix-Pencil method will be used to extract the antenna pattern from the realized effective length of the Vivaldi antenna.

References

[4.1] S. L. Marple Jr., Digital Spectral Analysis with Applications. Englewood Cliffs: Prentice-Hall, 1987, pp. 303-350.

[4.2] K. Dietze – Personal Communication

[4.3] R. Prony, “Essai experimental et analytique ...,” *Paris J. l’Ecole Poltechnique*, 1, cahier 2, 24-76, (1795).

[4.4] G. K. Smyth, “Employing Symmetry Constraints for Improved Frequency Estimation by Eigenanalysis Methods,” Dept. of Math., University of Queensland, Australia.

[4.5] M. L. Van Blaricum, R. Mittra, “Problems and Solutions Associated with Prony’s Method for Processing Transient Data,” *IEEE Trans. Antennas Propagat.* , vol. 26, No. 1, pp. 174-182, Jan. 1978.

[4.6] T. K. Sarkar, O. Pereira, “Using the Matrix Pencil Method to Estimate the Parameters of a Sum of Complex Exponentials,” *IEEE Antennas and Propagaion Magazine*, vol. 37, No. 1, pp. 48-55, Feb. 1995.

[4.7] Y. Hua, T. K. Sarkar, ”Matrix Pencil Method for Estimating Parameters of Exponentially Damped/Undamped Sinusoids in Noise,” *IEEE Trans. on Acoustics, Speech, and Signal Processing*, vol. 38, No. 5, pp. 814-824, May 1990.

[4.8] Y. Hua, T. K. Sarkar, ”Generalized Pencil-of-Function Method for Extracting Poles of an EM System from Its Transient Response,” *IEEE Trans. Antennas Propagat.* ,vol. 37, No. 2, pp. 229-234, Feb. 1989.

[4.9] E. C. Levy, “Complex Curve Fitting, ” IRE Transactions on Automatic Control, vol. AC-4, pp. 37-44, May 1959.

[4.10] R. Kumaresan, “ Identification of Rational Transfer Function from Frequency Response Samples,” IEEE Transactions on Aerospace and Electronic Systems, Vol. 26, No. 6, pp. 925-934, November 1990.

[4.11] J. M. Pond, T. B. A. Senior, ”Determination of SEM Poles from Frequency Responses,” *Interaction Notes (IN 408)* , Jul. 1981.

[4.12] T. B. A. Senior, J. M. Pond, ”Pole Extraction in the Frequency Domain,” *Interaction Notes (IN 411)*, Dec. 1981.

[4.13] C. B. Sharpe, C. J. Roussi, ”Equivalent Circuit Representation of Radiation Systems,” *Interaction Notes (IN 361)*, April 1979.

[4.14] J. N. Brittingham, E. K. Miller, J. L. Willows, “Pole Extraction from Real-Frequency Information,” *Proceedings of the IEEE*, vol. 68, No. 2, pp. 263-273, 1980.

Chapter 5

Pole and Residue Modeling of Antenna Systems – Minimal Representation

The method for numerically extracting the poles and residues from a transient waveform has been addressed by Van Blaricum and Tesche [5.1,2,2.14]. Prony's method was used to extract poles and residues from a transient response obtained using numerical methods [5.1]. The numerical results were followed by an experiment [5.1]. A Gaussian pulsed plane wave was used to excite a 1.0-meter resonant monopole and the current was measured through a 50 Ω load. There were no attempts to model some other antenna structures or other frequency ranges. The model represents a monopole/TEM Horn link response.

In this chapter, a minimal type of model representation study for antenna systems using the Matrix-Pencil method (MP) is presented. The pole/residue characterization provides the following advantages:

-Complete frequency and time-domain characterization (once the pole and residues of an antenna system are obtained, it is easy to compute the time-domain waveforms or frequency-domain response). Later in Chapter 6, a frequency-domain pattern synthesis from pole/residue model will be demonstrated.

-Minimal type of representation model (minimal data set to represent an antenna system)

-The antenna model can be used with channel models in order to predict the received time-domain/frequency waveform (the effects of different antennas on received waveforms can be easily obtained).

Pole/residue models for a TEM horn, bi-conical antenna, 1.0 GHz resonant monopole, and Archimedean spiral are presented.

5.1 Measurement Modeling using SEM

The measurement setup described in Chapter 3 consists of two identical antennas. The derivations below assume no radial dependence ($\vec{a}_r$) because the far-field conditions are applied. The equation representation is in the Laplace domain for simpler formulation. The antenna effective length in terms of poles and residues can be represented by the following expression:

$$\vec{h}(s,\theta,\phi) = \sum_n \frac{\vec{R}_n(\theta,\phi)}{s - s_n} \tag{5.1}$$

The effective length in the frequency domain for a given polarization can be described as

$$h(j\omega,\theta,\phi)=\sum_{n=1}^{N}\frac{R_n}{-\sigma_n+j(\omega-\omega_n)}+C\,. \tag{5.2}$$

The poles are $s_n=\sigma_n+j\omega_n$ and R_n are the residues. The constant C gives rise to a delta function at $t=0$ and may be represented by a more complete analytical function to represent the turn-on transient.

The antenna open-circuit voltage is a combination of the effective lengths of both antennas. Thus, the expression for the open-circuit voltage is [2.1]

$$V_{oc}(s)=s\frac{\mu}{Z_0}\left(\sum_m\frac{\vec{R}_{1m}(\theta,\phi)}{s-s_m}\right)\cdot\left(\sum_n\frac{\vec{R}_{2n}(\theta,\phi)}{s-s_n}\right)\frac{e^{-s\frac{r}{c}}}{4\pi r}I(s) \tag{5.3}$$

or

$$V_{oc}(s)=s\frac{\mu}{Z_0}\left(\sum_m\sum_n\frac{\vec{R}_{1m}(\theta,\phi)\cdot\vec{R}_{2n}(\theta,\phi)}{(s-s_m)(s-s_n)}\right)\frac{e^{-s\frac{r}{c}}}{4\pi r}I(s)\,. \tag{5.4}$$

The representation in Eq. (5.4) indicates the presence of multiple, complex conjugate, and double poles if the antennas are identical ($m=n$). The term $e^{-s\frac{r}{c}}\Big/4\pi r$ represents the phase delay and the classical amplitude decay. The function $I(s)$ is the excitation function, in our case the antenna excitation current. In both of the expressions r is the distance between the two antennas.

The time-domain representation of the open-circuit voltage is the following [2.1]:

$$v_{oc}(t)=\frac{1}{4\pi r}\frac{\mu}{Z_0}\frac{\partial}{\partial t}\left(\vec{h}_r(t,\theta,\phi)\overset{\bullet}{\otimes}\vec{h}_t(t-\frac{r}{c},\theta,\phi)\right)\otimes i(t) \tag{5.5}$$

In order to include the impedance in the antenna representation, let's consider the receiving and transmitting antenna circuit description shown in Fig. 5.1. It is possible to define relationships between the antenna impedance and measured output voltage. We first start with the excitation current on the transmitting antenna that is defined as

$$I=\frac{2V_S}{Z_0+Z_A} \tag{5.6}$$

The antenna impedance in terms of the reflection coefficient is:

$$Z_A=Z_0\frac{1+\Gamma_t}{1-\Gamma_t}\,. \tag{5.7}$$

The antenna excitation current in terms of the reflection coefficient is

$$I = \frac{V_S(1-\Gamma_t)}{Z_0} \Leftrightarrow i(t) = \frac{1}{Z_0}(\delta(t)-\Gamma_t(t)) \otimes v_S(t)\,, \tag{5.8}$$

where V_S is the excitation voltage. The voltage across the load at the receiving end is defined as

$$V = \frac{(1-\Gamma_r)}{2}V_{oc} \Leftrightarrow v(t) = \frac{1}{2}(\delta(t)-\Gamma_r(t)) \otimes v_{oc}(t)\,. \tag{5.9}$$

Now, it is possible to express the measured voltage including the antenna impedance as

$$V(s) = s(1-\Gamma_r(s))\left(\sum_m \frac{\vec{R}_{1m}(\theta,\phi)}{s-s_m}\right)\cdot\left(\sum_n \frac{\vec{R}_{2n}(\theta,\phi)}{s-s_n}\right)\frac{e^{-s\frac{r}{c}}}{4\pi r}\,\frac{\mu}{Z_0}\left[\frac{V_S(s)}{2}\right](1-\Gamma_t(s))\,. \tag{5.10}$$

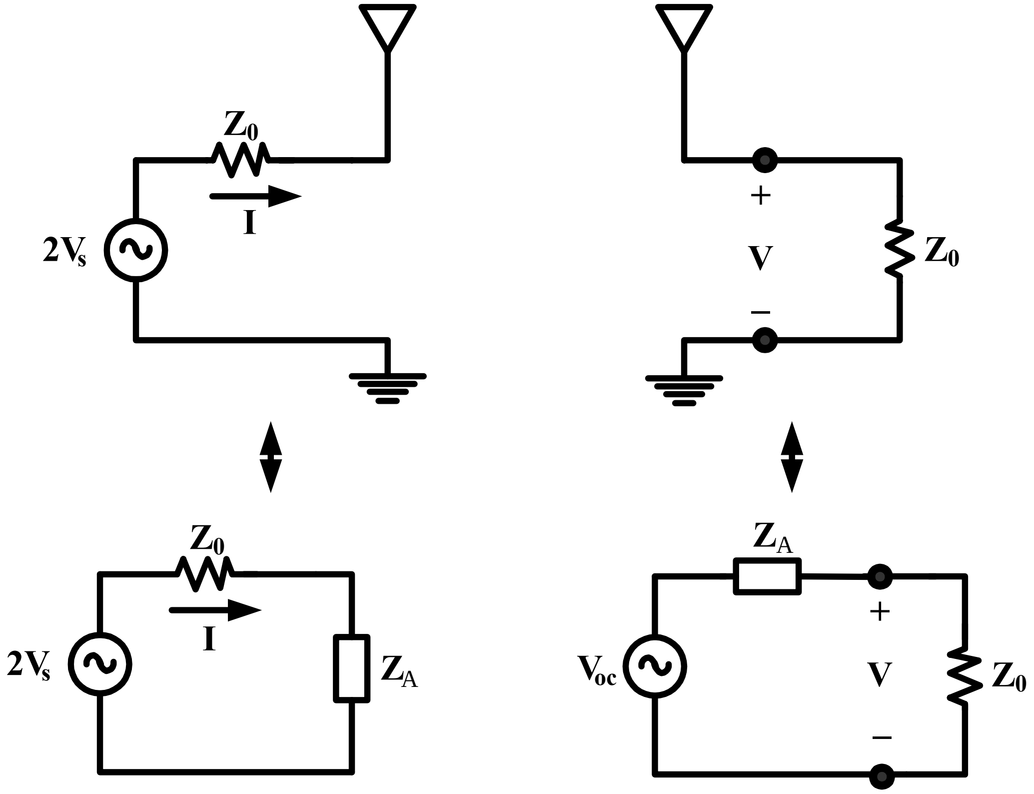

Figure 5.1. The circuit description of the receiving and transmitting antenna

The time-domain equivalent representation is as follows:

$$v(t) = (\delta(t) - \Gamma_r(t)) \otimes \frac{\partial}{\partial t}\left(\vec{h}_r(t,\theta,\phi) \overset{\bullet}{\otimes} \vec{h}_t(t - \frac{r}{c}, \theta, \phi) \right) \frac{1}{4\pi r} \otimes \frac{\mu}{Z_0} (\delta(t) - \Gamma_t(t)) \otimes \left[\frac{v_S(t)}{2} \right]. \tag{5.11}$$

Eq. (5.12) could be expressed in terms of $s_{21}(t)$ as

$$v(t) = s_{21}(t) \otimes \frac{v_s(t)}{2} \tag{5.12}$$

In order to model the antenna system, one needs to obtain the realized effective length of the antenna and extract poles/residues using an appropriate modeling method. First, we will present a way of obtaining the realized effective length from HP8510 measurements. After obtaining the realized effective length, MP will be applied in order to obtain poles and residues of the particular antenna system. Emphasis will be on limitations of the minimal models and their physical interpretations.

5.2 Realized Effective Length from Vector Network Analyzer (VNA) Measurements

The measured link, s_{21}, of a two-antenna system contains the response of both antennas and the channel between the antennas. The corresponding time-domain waveform reflects the contributions of both the transmit and receive antenna in the link as well as the channel in a convolution form. This section demonstrates how to obtain the response of a single antenna (realized effective length - $\vec{h}_R(j\omega,\theta,\phi)$) in both the time and frequency domains from the frequency-domain s_{21} measurements using a vector network analyzer.

Recently, a new need arose to measure an antenna time-domain response using a vector network analyzer. The usual procedure is to measure the received waveform of two identical antennas, reflecting the contributions of both transmit and receive antennas, and performing an inverse transform to obtain the time-domain equivalent waveform. The measured received waveform can be represented in the following form for a line-of-sight link [2.1]:

$$s_{21}(j\omega,\theta,\phi) = \frac{j\omega\mu}{Z_o} \vec{h}_{Rr}(j\omega,-\theta,-\phi) \cdot \vec{h}_{Rt}(j\omega,\theta,\phi) \frac{e^{-j\beta r}}{4\pi r}. \tag{5.13}$$

In Eq. (5.13), $\vec{h}_{Rr}$ and $\vec{h}_{Rt}$ represent realized effective lengths of the receive and transmit antennas, respectively. The realized effective length includes the impedance mismatch not normally included in the effective length. If we ignore the angular dependence of Eq. (5.13), we obtain the simplified representation

$$s_{21}(j\omega) = \frac{j\omega\mu}{Z_0} h_{Rt}(j\omega) h_{Rr}(j\omega) \frac{e^{-j\beta r}}{4\pi r}. \tag{5.14}$$

The realized effective length product is then given by

$$h_{Rt}(j\omega) h_{Rr}(j\omega) = \frac{Z_0}{j\omega\mu} 4\pi r e^{j\beta r} s_{21}(j\omega). \tag{5.15}$$

If the antennas are identical the realized effective length is

$$h_R(j\omega) = \sqrt{\frac{Z_0}{j\omega\mu} 4\pi r e^{j\beta r} s_{21}(j\omega)}. \tag{5.16}$$

The realized effective length of the antenna can also be obtained by using a known realized effective length of a reference antenna ($h_{ref}(j\omega)$)

$$h_R(j\omega) = \frac{s_{21}(j\omega) \cdot Z_0 \cdot 4\pi r e^{j\beta r}}{\mu \cdot h_{ref}(j\omega)}. \tag{5.17}$$

Once the realized effective length is obtained in the frequency domain one can perform an inverse transform (IFFT) to obtain the time-domain realized effective length of the single antenna.

The realized effective length includes the effects of the antenna impedance. In order to obtain the effective length one needs to use the following expression:

$$h(j\omega) = \frac{1}{(1 - s_{11}(j\omega))} \cdot h_R(j\omega). \tag{5.18}$$

For wideband antennas, the realized effective length is almost identical to the antenna effective length due to a very good impedance match across a wide range of frequencies (above the antenna fundamental resonance). For resonant structures, the realized effective length is an approximation of the antenna effective length since the impedance match is poor for some frequencies of interest.

The measurement of a monopole-TEM horn link and a Vivaldi antenna link was performed and the realized effective length was obtained for a 1.0 GHz resonant monopole and Vivaldi antennas. The realized effective length of a monopole was obtained using the TEM Horn antenna as a reference. The measurements were done using a 4.0 x 4.0 ft ground plane in order to eliminate a wideband balun. The distance between the reference planes of the monopole and the TEM Horn antenna was 1.3500 meters. The s_{21} measurement of the TEM Horn/monopole link and monopole realized effective length is shown in Figs. 5.2 and 5.3 in both time and frequency domains.

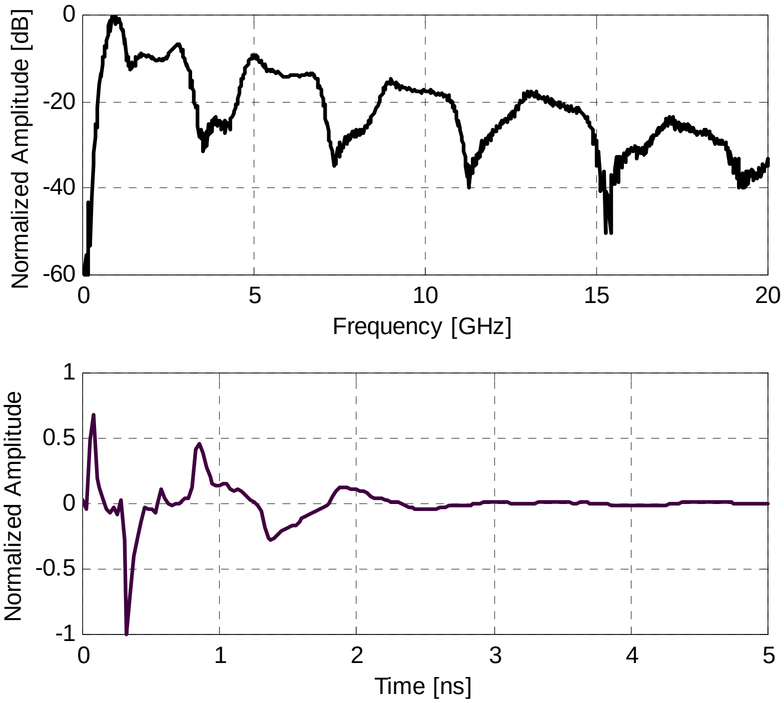

Figure 5.2. Measured s_{21} response of the TEM horn and monopole link (frequency/time)

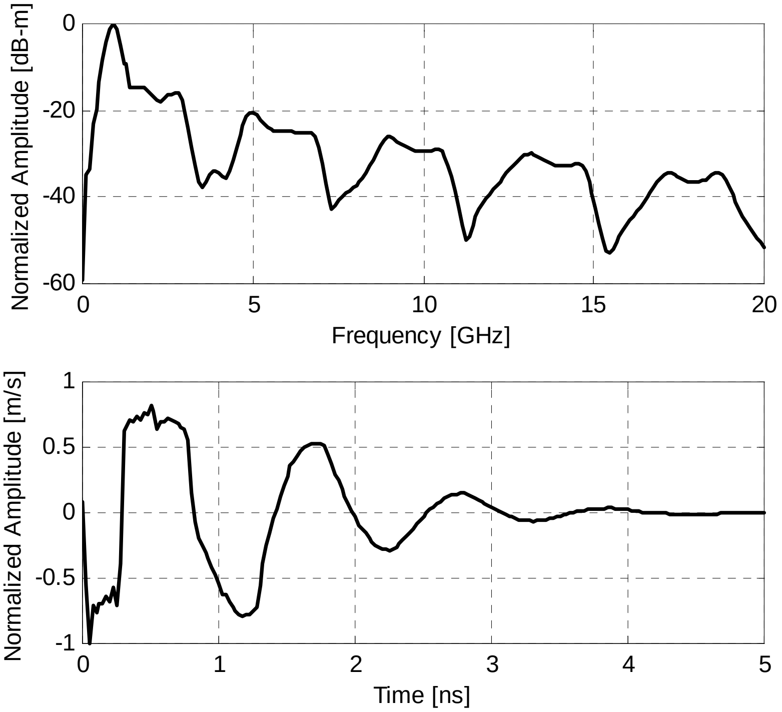

Figure 5.3. Realized effective length of a monopole in frequency and time

The s_{21} measurement shows all odd monopole resonant frequencies, with the fundamental monopole resonance at 1.0 GHz clearly visible. The peak time-domain amplitude of the link response is located at 0.35 ns. The peak time-domain amplitude of the realized effective length is at 0.3 ns. The time-domain link and realized effective length waveforms are different in shape, but have the peak amplitude at the same time location. Also the frequency response of the link is very similar to the frequency-domain realized effective length. However, one can notice that the realized effective length decays more rapidly than the response of the link.

The distance between the reference planes of the measured Vivaldi antennas was 2.0625 meters. The s_{21} response of the Vivaldi antenna link is shown in Fig. 5.4 with a fundamental resonance at 1.9 GHz. The amplitude decay is approximately 2.3 dB/GHz and the peak amplitude is located at 0.35 ns. The amplitude decay of the Vivaldi antenna realized effective length, shown in Fig. 5.5, is approximately 1.9 dB/GHz and the peak amplitude is located at 0.35 ns.

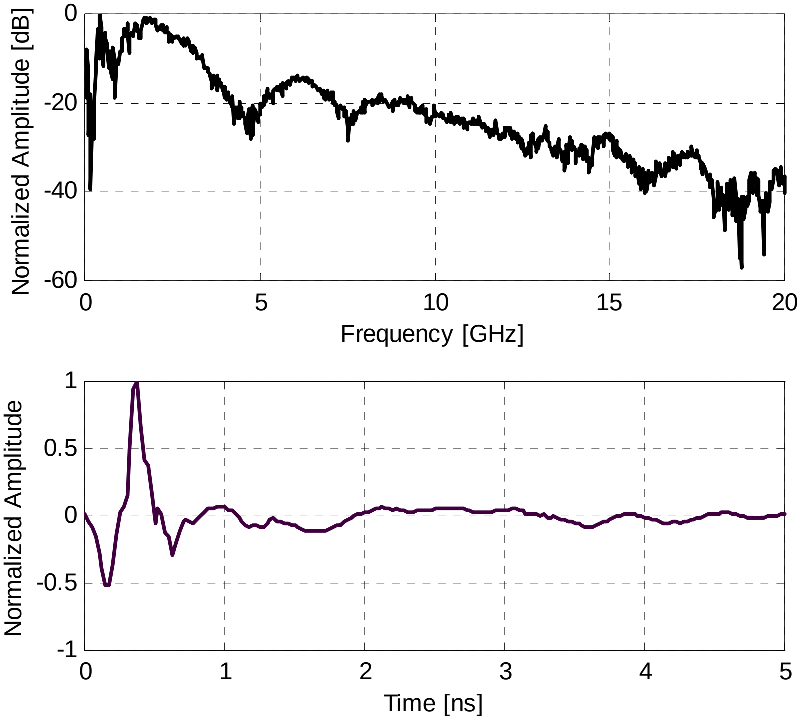

Figure 5.4. Measured s_{21} response of the two Vivaldi antenna link in frequency and time

The procedure developed was used to obtain the realized effective length of an antenna. The results show that a resonant antenna (the monopole) shows significant ringing in the response as might be expected for a highly resonant structure. However, the Vivaldi antenna provides a simple impulse response as is desired for antennas for UWB applications. It is important to note that by measuring the antennas using a vector network analyzer (VNA) one effectively measures the antenna response across a 50 Ω load and not an open circuit voltage response.

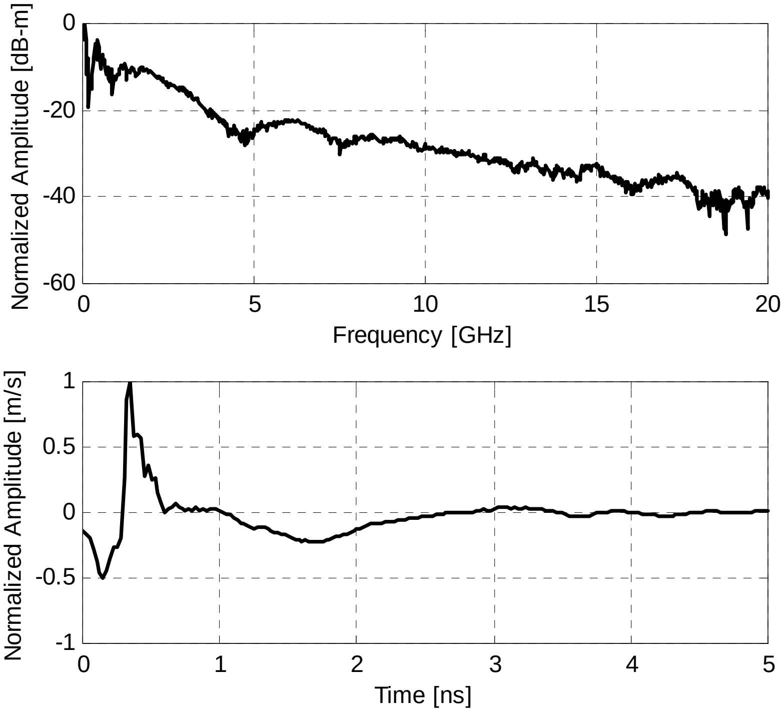

Figure 5.5. Realized effective length of a Vivaldi antenna in frequency and time

5.3 Data Processing/Windowing and Matrix Pencil Method

The antenna pole/residue models in the next sections are obtained using a processing scheme as shown in Fig. 5.6. The measured frequency-domain data was not time windowed since the multi-path component on the bore-sight measurements is not significant. This reduces the number of transforms that are needed to pre-condition the data.

The realized effective length in the frequency domain was obtained using Eq. (5.16). The VNA measured data is in the range from 50 MHz to 20.05 GHz and for proper inverse Fourier transform (IFFT) 0 and 25 MHz frequency points need to be interpolated. The 0 and 25 MHz points were set to zero and a rectangular window was used in the transform. This gives good results and it is almost identical to the transform performed by the HP8510 time-domain routine.

Once the time-domain equivalent of the realized effective length is obtained, one can use a pole/residue extraction technique to obtain poles and residues of the antenna system. In this case, the Matrix-Pencil method (MP) was used (see Chapter 4 for an outline). The MP sets the time-domain window used in the comparison between the frequency domain model and frequency domain measured data.

Next, we will investigate the properties of a TEM Horn, bi-conical antenna, 1.0 GHz resonant monopole, and Archimedean spiral antenna. The emphasis will be placed on a reduced model size.

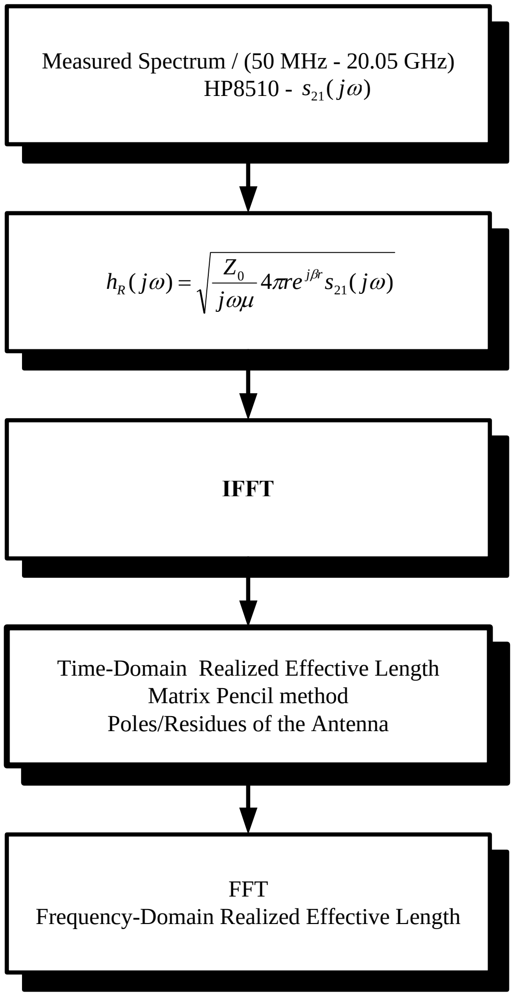

Figure 5.6. Obtaining the pole/residue model of an antenna for the bore-sight direction

5.4 TEM Horn Minimal Model – Directional/Broadband Antenna

The TEM Horn is a classical antenna used in broadband applications due to its broadband characteristics as the measurements show in Chapter 3. The TEM Horn was measured on a 122 x 122 cm ground plane and the distance between the reference planes was 1.3275 m.

The s_{21} frequency response and the equivalent time-domain response of a two TEM Horn link is shown in Fig. 5.7. The noise level is also shown in order to estimate the signal to noise ratio (SNR) present in the measurements. The SNR ratio is greater then 40 dB. As the frequency increases, the noise level increases due to loss in cables. The s_{21} response is almost flat for 2-6 GHz frequency range and after 6 GHz decreases to –40 dB at 20 GHz. The s_{21} impulse response shows a very sharp decaying sinusoid and the response is not a doublet as suggested on many occasions. The response reflects the band-limited nature of the antenna as discussed in Chapter 3. The units of the time-domain response are *Units/s* since s_{21} is a voltage ratio, where $Units = 1$. The peak has a very high value but it is very short in duration.

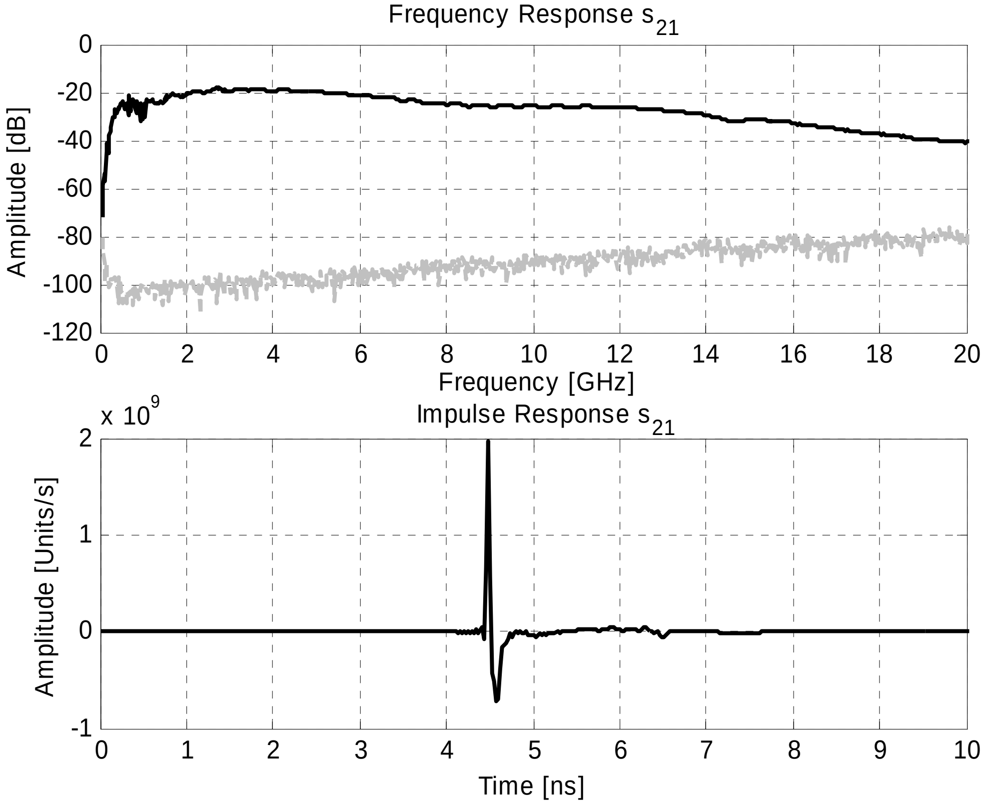

Figure 5.7. Measured s_{21} frequency response (black) vs. noise (grey) and corresponding s_{21} impulse response for 2 TEM Horn antenna link

Beside the noise criteria, the measured data was investigated based on the singular value decomposition (SVD). The SVD shows the relationship and relative strength between different components within a data set. Fig. 5.8 shows the SVD of the measured realized effective length of the TEM horn antenna. One can notice that the 5th component is almost 10 times smaller than the 1st one. The singular values reflect the energy content of the pole/residue pair. The SVD decomposition indicates that only five or fewer poles could describe the time-domain realized effective length of the TEM horn.

The MP was used to investigate the minimum number of parameters required to model the TEM Horn antenna. Table 5.1 shows the model order and associated parameters used in the MP method.

Table 5.1. MP method parameters used in modeling of the TEM Horn antenna

Model	**Time Window[12] [ns]**	**Singular Value Amplitude**
4	2.5 -> K=100	0.2
6	2.5 -> K=100	0.1
35	2.5 -> K=100	0.008

The model number corresponds to the number of poles/residues used to model the waveform. The time-window of 2.5 ns eliminates the multi-path in the frequency and time domain. The singular value amplitude is a criterion that determines how many singular values will be used in the modeling process. The number of singular values corresponds to the number of poles/residues. From Fig. 5.8, one can notice that if the amplitude criterion is 0.2, four singular values will be used in the MP method modeling.

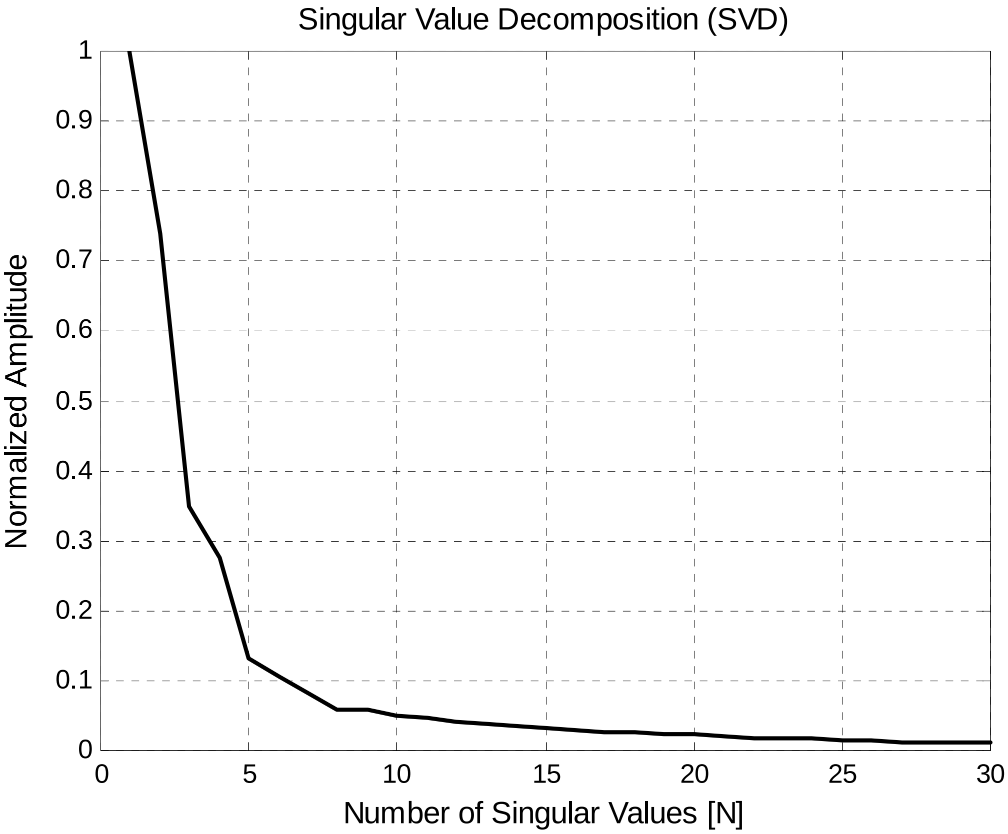

Figure 5.8. Singular value decomposition of the TEM Horn antenna time-domain realized effective length

Three pole/residue models are investigated: 4-, 6-, and 35-pole models. The models are compared to the measured frequency/time-domain realized effective length. The frequency-domain response is compared both in terms of the amplitude and phase.

---

[12] r= 1.3275 m distance between the antennas/200.25 MHz resolution in the frequency domain

The pole structure is also shown in order to illustrate the pole locations and the corresponding residue amplitudes. Lastly, the 35-pole model is reduced by eliminating poles with low residue amplitudes and then the residues recomputed.

The first pole model presented is a 4-pole/residue model. The frequency-domain and phase response is shown in Fig. 5.9. The frequency amplitude response shows a good match up to 10.0 GHz with only four poles. The frequency amplitude, of the realized effective length, indicates the TEM Horn antenna is dominated by two frequencies: 370 MHz and 4.0 GHz. The phase response is also relatively accurate up to 10.0 GHz. The phase shows a linear decay from 0 to 120 degrees up to 10 GHz. This decay (time delay) is associated with the required time for the pulse to travel from the reference plane through the antenna connector to the antenna structure.

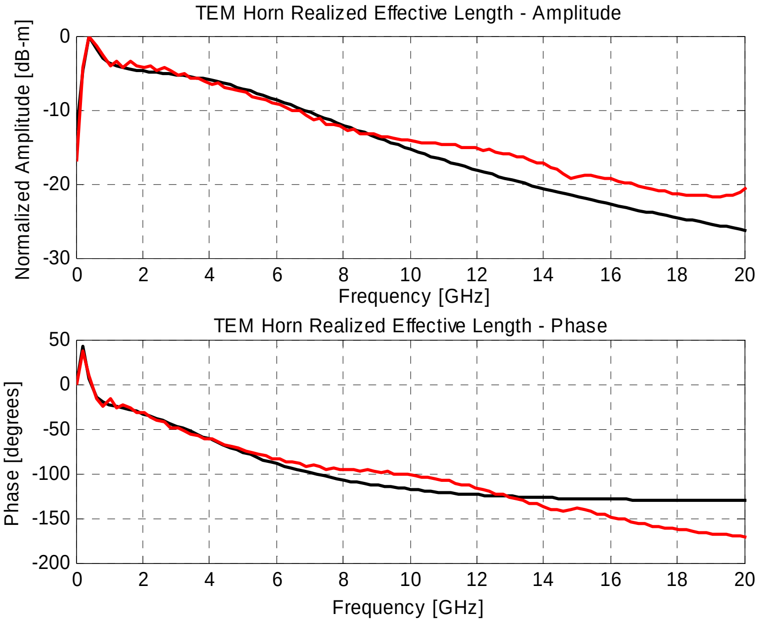

Figure 5.9. Comparison between 4-pole model approximation (red) and frequency-domain realized effective length (black)

The frequency domain amplitude response can be also shown on a linear scale. The linear plot response shows a better match than illustrated by the dB plot since the amplitude past 10 GHz is 15 dB down from the peak value. One can notice that there are some minor variations in the range from 1.0 to 3.0 GHz.

The time-domain response is almost completely characterized by a 4-pole model. The time-domain shows a sharp peak and low frequency contribution from 0.25 to 2.5 ns in duration. The time-domain response is shown in Fig. 5.10.

The pole structure is shown in Fig. 5.11. The pole structure shows two poles with relative low residue value and two poles with high residue value. The first pole set is very low in frequency (around 370 MHz) and corresponds to the first peak in the frequency amplitude plot. The second set of poles is higher in frequency and corresponds to a gradual decay of the peak centered at 4.0 GHz. At this point one can postulate poles with high damping coefficients show a gradual variation about the frequency peak, while poles with low damping coefficients show sharp peaks.

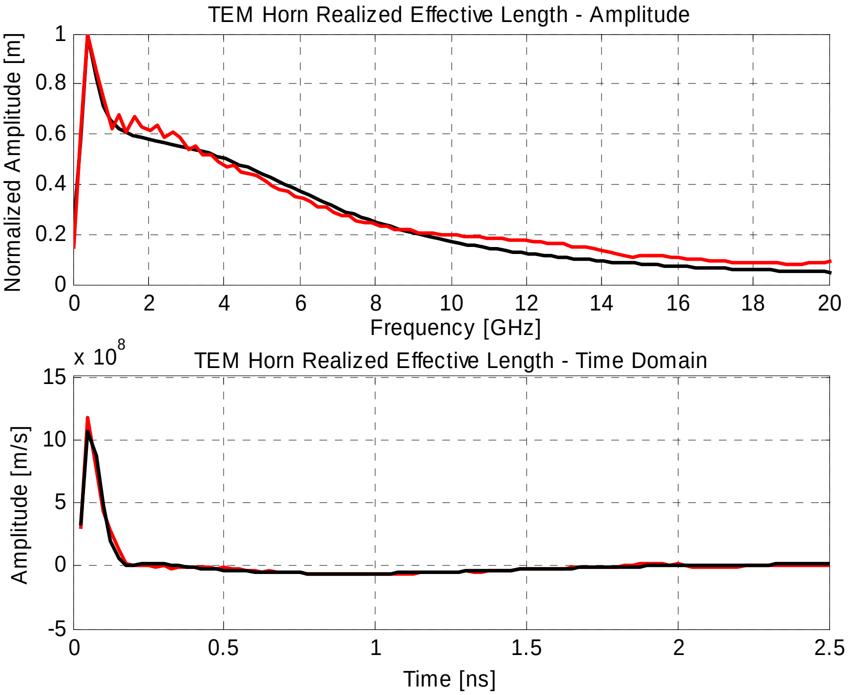

Figure 5.10. Frequency and time-domain realized effective length (black) vs. 4-pole model approximation (red)

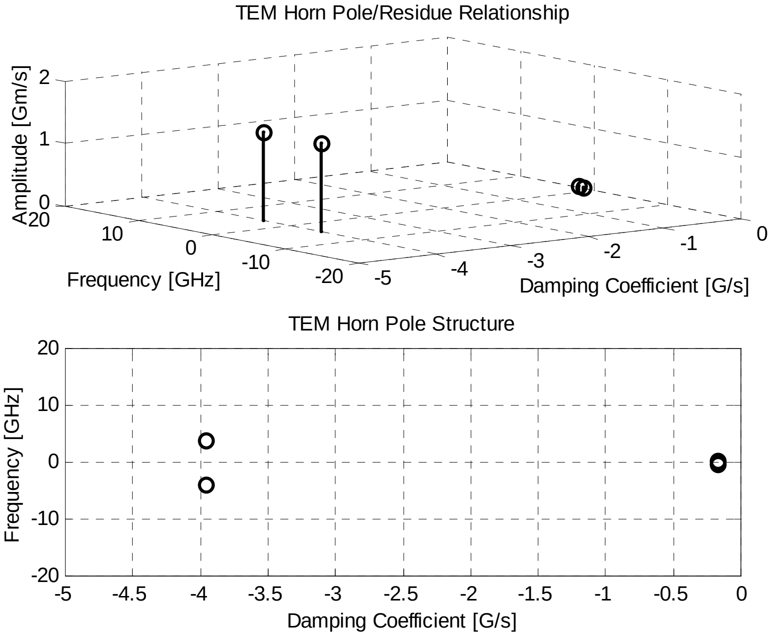

Figure 5.11. Pole/Residue relationship and pole structure for a 4-pole model

The 6-pole model is presented next. The 6-pole model shows some improvement in the frequency-domain match. The time-domain realized effective length was adequately represented with a four-pole model. The measured frequency and time-domain realized effective length compared to pole/residue model are shown in Figs. 5.12 and 5.13, respectively.

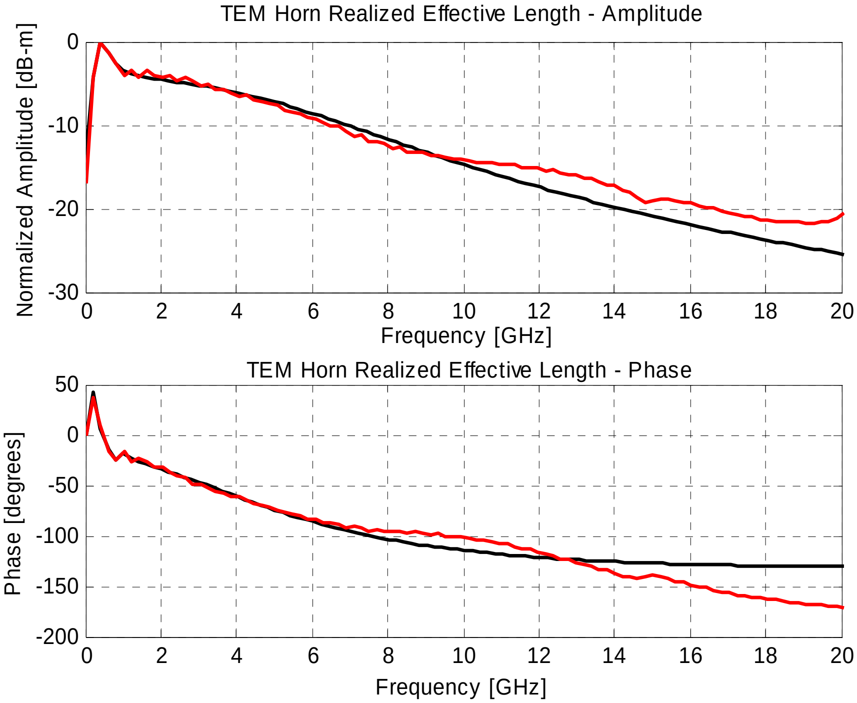

Figure 5.12. Comparison between 6-pole model approximation (red) and frequency-domain realized effective length (black)

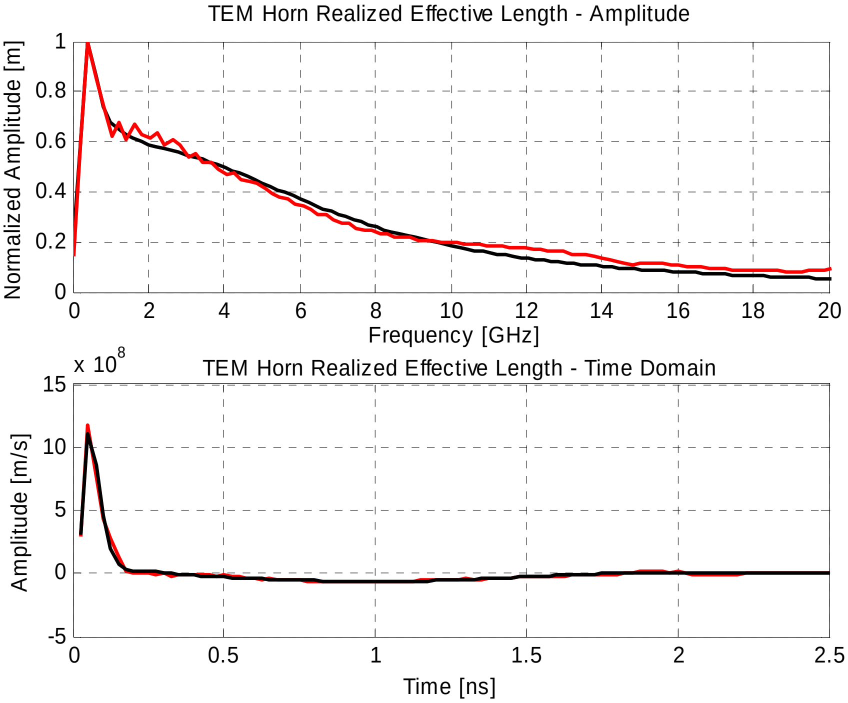

Figure 5.13. Frequency and time-domain realized effective length (black) vs. 6-pole model approximation (red)

The two additional poles created by a 6-pole model are located near $j\omega$ axis but with small residues. The added pole set is around 900 MHz in frequency. By increasing the number of singular values the algorithm is trying to match poles with higher amplitude residues even they reflect only local effects. This pole set is trying to match small variations in the region from 500 MHz to 3.0 GHz. The relative residue amplitude, value of the damping coefficient, and frequency of the 4-pole set were not significantly changed.

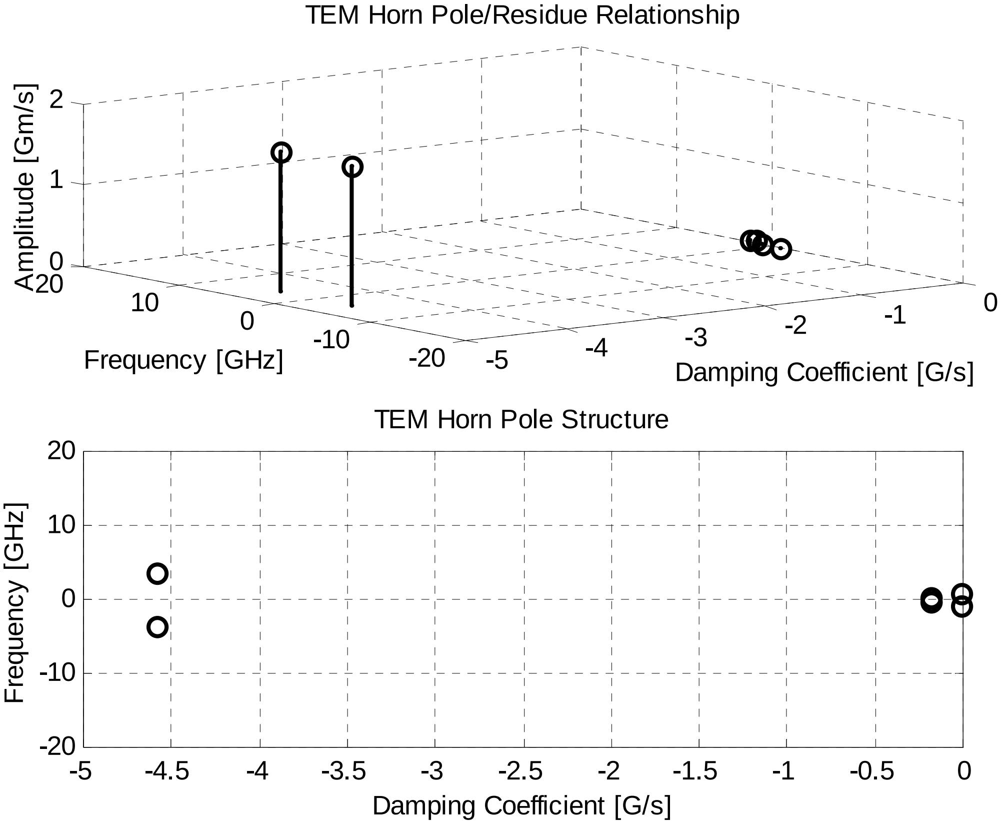

Figure 5.14. Pole/Residue relationship and pole structure for a 6-pole model

The 35-pole model shows a very detailed match up to 17 GHz. The frequency domain amplitude response in Fig. 5.15 shows that the model matches all small variations of the frequency response very well. In order to achieve a very good global match, the algorithm first forces the match with higher singular values occurring lower in frequency and it requires more poles to achieve a better global match.

The pole structure shown in Fig. 5.17 indicates that most of the new poles are very low in residue and have low damping coefficient indicating they model only small variations of the realized effective length waveform.

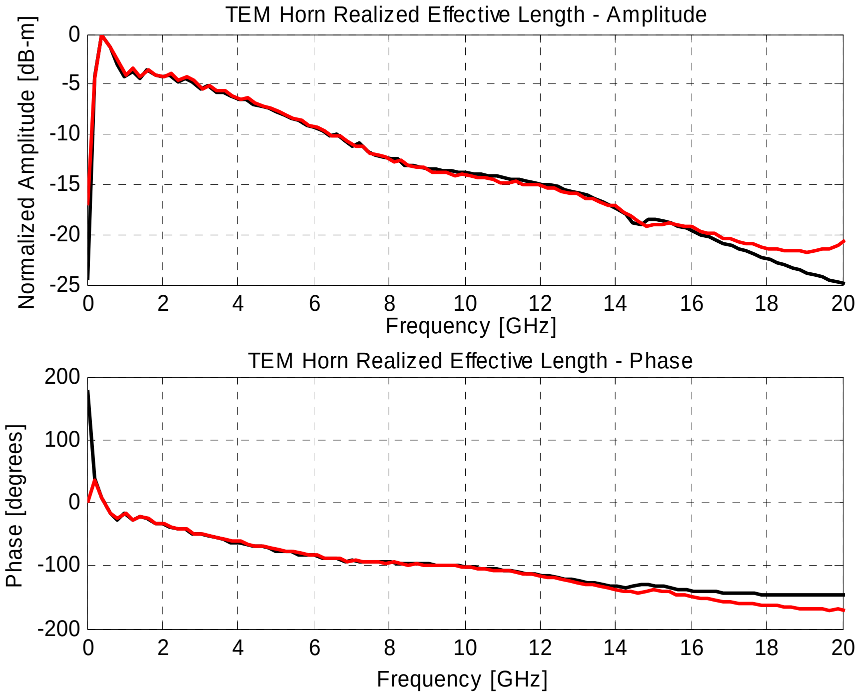
TEM Horn Realized Effective Length - Amplitude

TEM Horn Realized Effective Length - Phase

Figure 5.15. Comparison between 35-pole model approximation (red) and frequency-domain realized effective length (black)

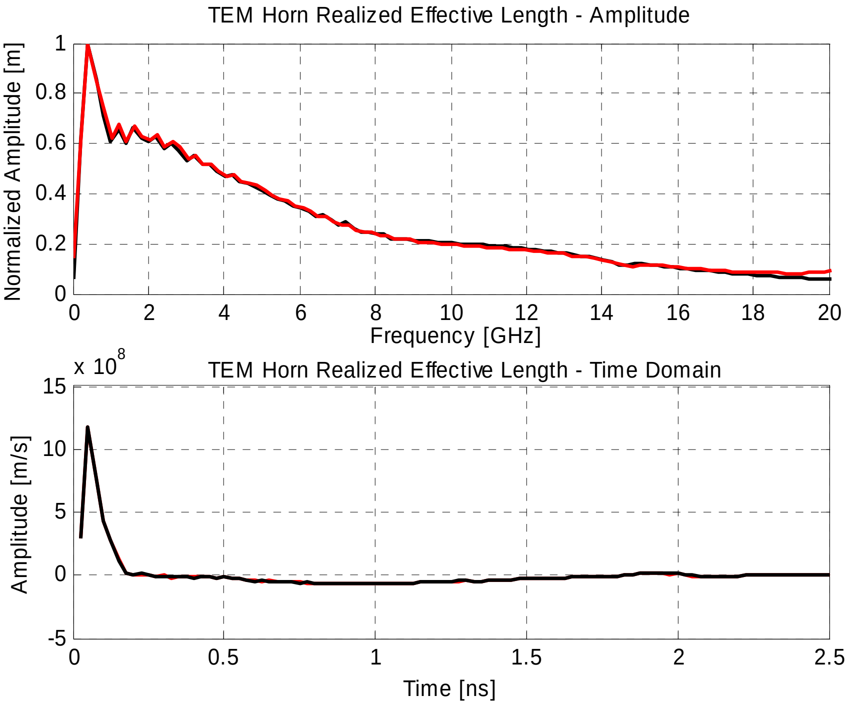
TEM Horn Realized Effective Length - Amplitude

TEM Horn Realized Effective Length - Time Domain

Figure 5.16. Frequency and time-domain realized effective length (black) vs. 35-pole model approximation (red)

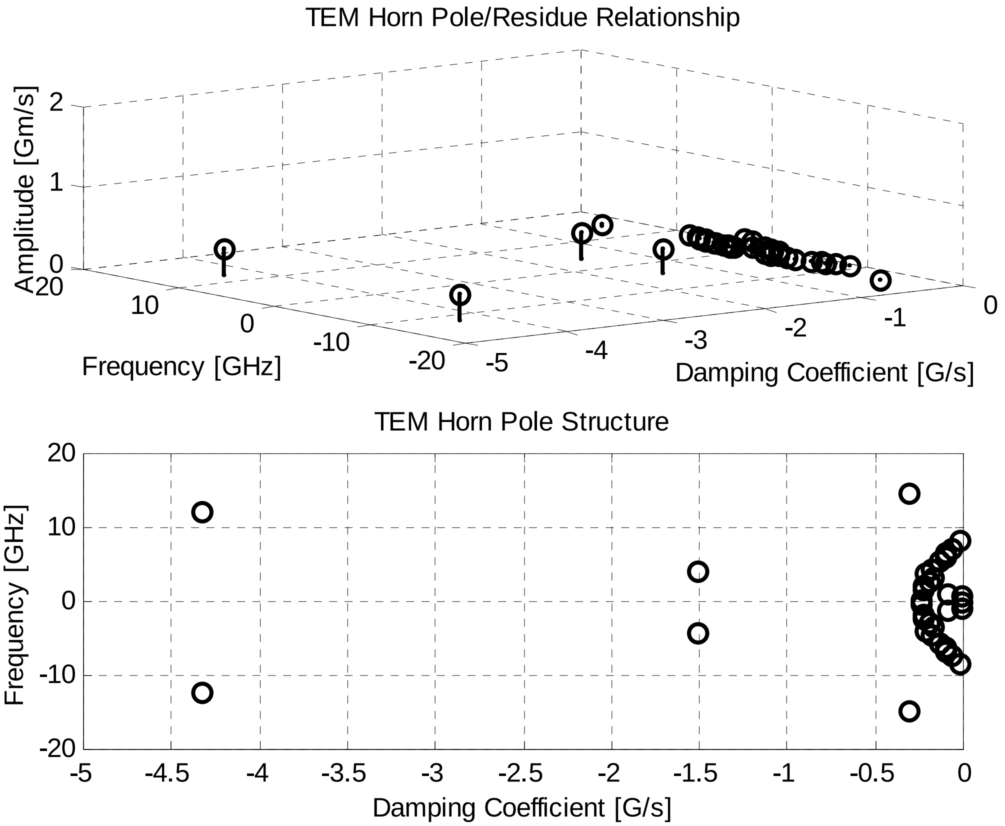

Figure 5.17. Pole/Residue relationship and pole structure for a 35-pole model

By examining all three-pole models, one can notice that the major composition of TEM Horn antenna consists of four poles. One pole is a low frequency pole around 400 MHz and the second one is at around 3.8 GHz. The first pole has a small damping coefficient, reflecting a sharp peak, and the second pole has fast damping coefficient reflecting broad peak.

By adding additional poles to the approximation of the antenna realized effective length one can notice that the added poles are very close to $j\omega$ axis and have very low residue/damping coefficient contributing to small variations to the realized effective length waveform. This is illustrated in Fig. 5.18.

One can notice the variations in the 3.8 GHz pole/residue. As the number of poles increases the 3.8 GHz shifts in frequency slightly and reduces the value of the residue amplitude and damping coefficient value. Essentially, the MP models first the poles that according to the SVD have more significance. The overall match is more important, but higher frequency poles are low in the SVD amplitudes and do not occur unless the number of poles is increased. This gives a locally good match but suffers on the global level. Thus, by using a large number of poles and then removing low amplitude residues and associated poles one can reduce the size of a pole set. A simple study indicated that actually the residue amplitude corresponds closely to the energy of a residue/pole pair.

By using the criteria to remove all residues and associated poles with the amplitude less than $0.01 \cdot 10^9$ one can obtain a very accurate 16-pole model as shown in

Figs. 5.19-5.21. Thus, one can conclude that low residues are not significant in antenna modeling.

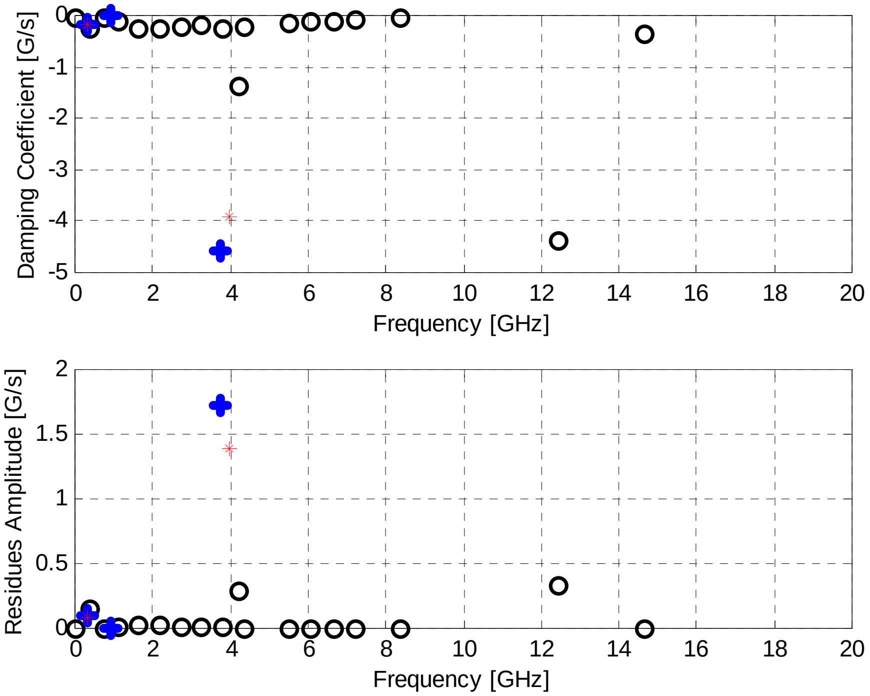

Figure 5.18. Pole/residue comparison for different models: 4-pole model (*), 6-pole model (+), and 35-pole model (o)

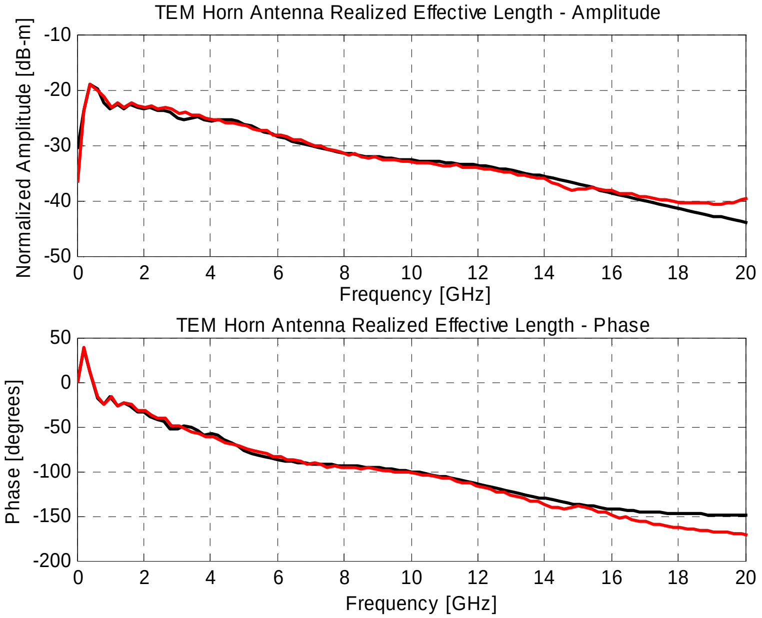

Figure 5.19. Comparison between 16-pole model approximation (red) and frequency-domain realized effective length (black)

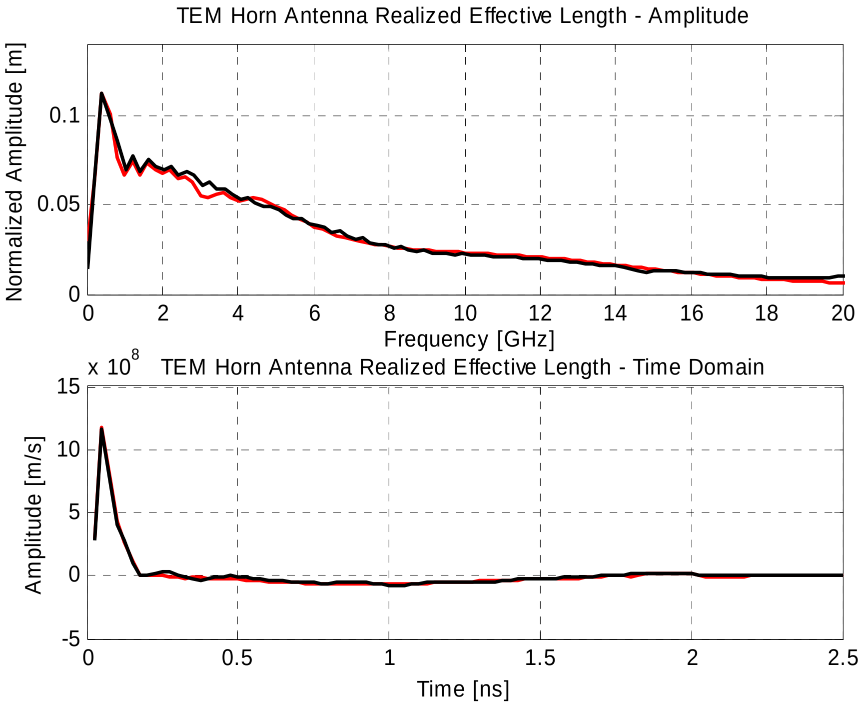

Figure 5.20. Frequency and time-domain realized effective length (black) vs. 16-pole model approximation (red)

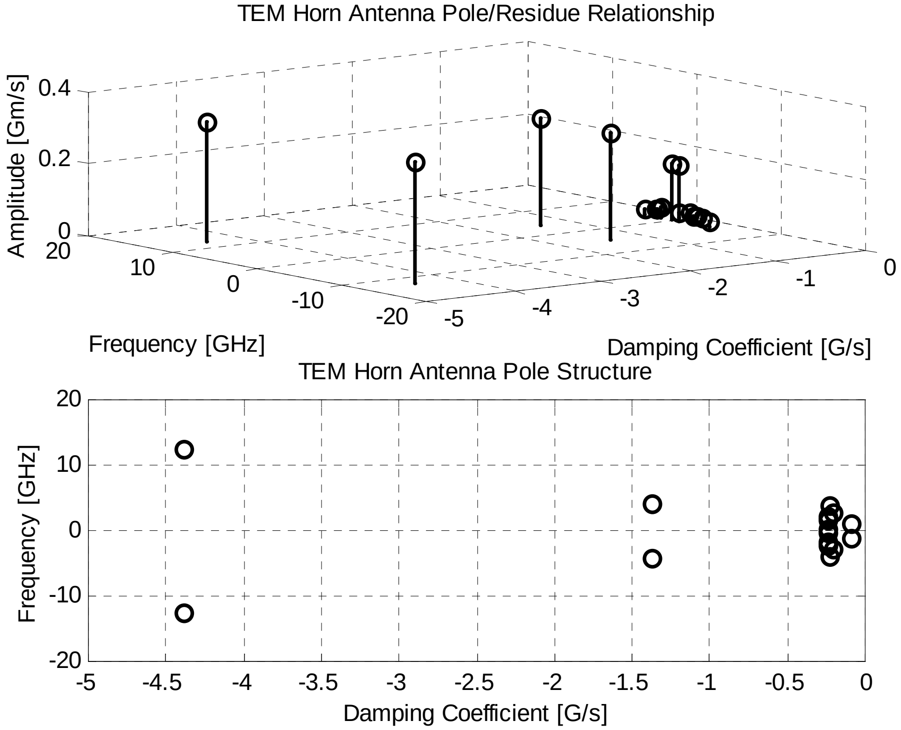

Figure 5.21. Pole/Residue relationship and pole structure for a 16-pole model

In conclusion, the sharp peaks are characterized by low damping coefficient values while the broad peaks are characterized by high damping coefficients. The residue amplitude reflects how significant the corresponding pole set is.

In summary, the complex poles and corresponding residues for 4-pole model are:

$$s=1\cdot 10^{9}\begin{bmatrix} -3.9567-3.9481i \\ -3.9567+3.9481i \\ -0.1686-0.3122i \\ -0.1686+0.3122i \end{bmatrix},\ \vec{R}\left(0,\frac{\pi}{2}\right)=1\cdot 10^{9}\begin{bmatrix} 0.1099+1.3993i \\ 0.1099-1.3993i \\ 0.0529-0.0717i \\ 0.0529+0.0717i \end{bmatrix}.$$

The poles and corresponding residues at the boresight direction for a 6-pole model are:

$$s=1\cdot 10^{9}\begin{bmatrix} -4.5901-3.7063i \\ -4.5901+3.7063i \\ -0.0121-0.8986i \\ -0.0121+0.8986i \\ -0.1895-0.3045i \\ -0.1895+0.3045i \end{bmatrix},\ \vec{R}\left(0,\frac{\pi}{2}\right)=1\cdot 10^{9}\begin{bmatrix} 0.1031+1.7274i \\ 0.1031-1.7274i \\ -0.0043-0.0014i \\ -0.0043+0.0014i \\ 0.0570-0.0848i \\ 0.0570+0.0848i \end{bmatrix}.$$

5.5 Bi-Conical Antenna Minimal Model – Omni-Directional/Broadband Antenna

The bi-conical antenna is an interesting structure, since it is variation of a simple dipole/monopole configuration in order to improve the impedance bandwidth. The bi-conical antenna shows a response similar to the TEM Horn but with more local variations in the spectrum. This is illustrated in Fig. 5.22, which shows the s_{21} frequency response and equivalent time-domain response of a two bi-conical antenna link. The SNR is better than 20 dB up to 14 GHz. The amplitude of the frequency domain waveform appears noisy since the antennas were measured in an open room with multiple scatterers present. The main reflection is from the room floor. However, most of the multi-path could be eliminated by applying a 2.5 ns time-domain window while pre-conditioning the data.

The time-domain response shows a sharp peak with some minor variations in the range from 6 to 8 ns. The peak is around $2.3\cdot 10^{8}$ Units/s, which is about the same as the monopole structure of $2.5\cdot 10^{8}$ Units/s. The TEM Horn has a significantly larger peak of $2.0\cdot 10^{9}$ Units/s. However, the monopole was measured in a link with the TEM Horn.

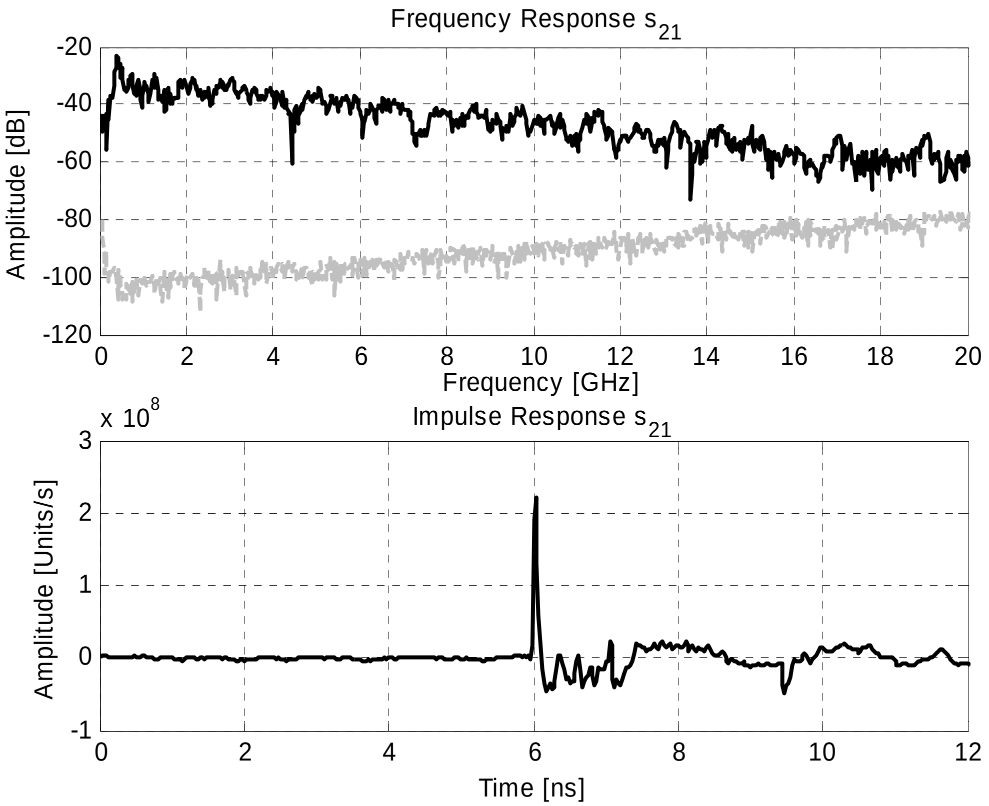

Figure 5.22. s_{21} frequency response (black) vs. noise (grey) and corresponding s_{21} impulse response for 2 bi-conical antenna link

In essence the bi-conical structure has a better efficiency than a monopole antenna. It is an expected conclusion since the return loss of the bi-conical antenna is considerably better than that of a monopole antenna, which exhibits 20% bandwidth or less at the resonant frequencies.

After the realized effective length was extracted, as outlined in section 5.2, poles and residues were obtained using MP. The parameters used in the MP method are shown in Table 5.2. The time domain window used in extracting poles and residues of the bi-conical antenna was 2.5 ns in duration.

Table 5.2. MP method parameters used in the bi-conical antenna modeling

Model	**Time Window[13] [ns]**	**Singular Value Amplitude**
6	2.5 -> K=100	0.1
12	2.5 -> K=100	0.07
52	2.5 -> K=100	0.007

The SVD of the bi-conical antenna measured data is shown in Fig. 5.23. The 10th singular value is 10 times smaller than the first singular value. This indicates that one

---

[13] r= 1.7700 m distance between the antennas/ 200.25 MHz resolution in the frequency domain

would need ten or fewer poles to adequately model the antenna time-domain realized effective length.

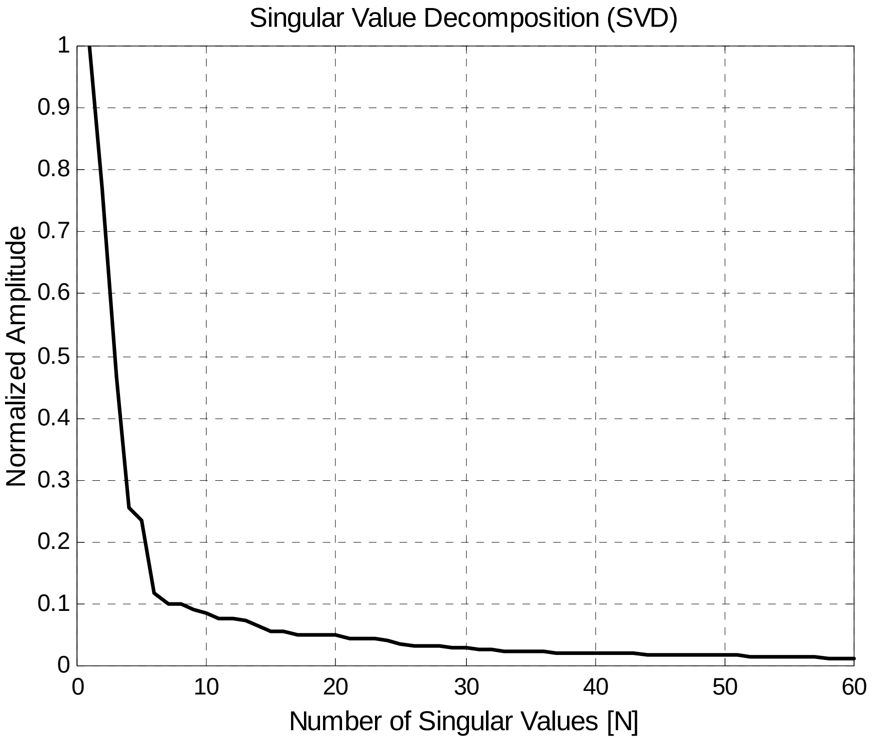

Figure 5.23. Singular value decomposition of bi-conical antenna time-domain realized effective length

The 6-pole model is investigated first. The 6-pole model approximates the realized effective length with high degree of accuracy up to 4.0 GHz. The frequency response is shown in Fig. 5.24. The phase decreases from 0 to around 520 degrees at 20 GHz. The phase (time delay) is associated with a pulse travel from the connector to the antenna structure. The linear plot shown in Fig. 5.25 shows a very good match since Fig. 5.24 indicates that the data is already 20 dB down at 6.0 GHz from the peak value.

The model shows a very good approximation of the time-domain realized effective length as indicated before based on the singular value decomposition of the measured data. The pulse consists of a sharp peak in duration of 0.25 ns and a low frequency component in the interval 0.25 ns - 2.5 ns.

The pole residue relationship is shown in Fig. 5.26. Similar to the TEM Horn 4-pole model a bi-conical antenna has two poles with high damping coefficients relative to other poles and 4 additional poles situated close to $j\omega$ axis. The frequencies dominating the time-domain realized effective length are 60 MHz, 366 MHz, and 3.1 GHz. The 60 MHz pole models the low frequency contributions mainly below the fundamental resonance. The fundamental resonance of the antenna (corresponds to the sharp peak) is modeled with 366 MHz frequency poles with a low value of a damping coefficient. The 3.1 GHz frequency pole models a broad peak centered at that particular frequency with a high value of a damping coefficient.

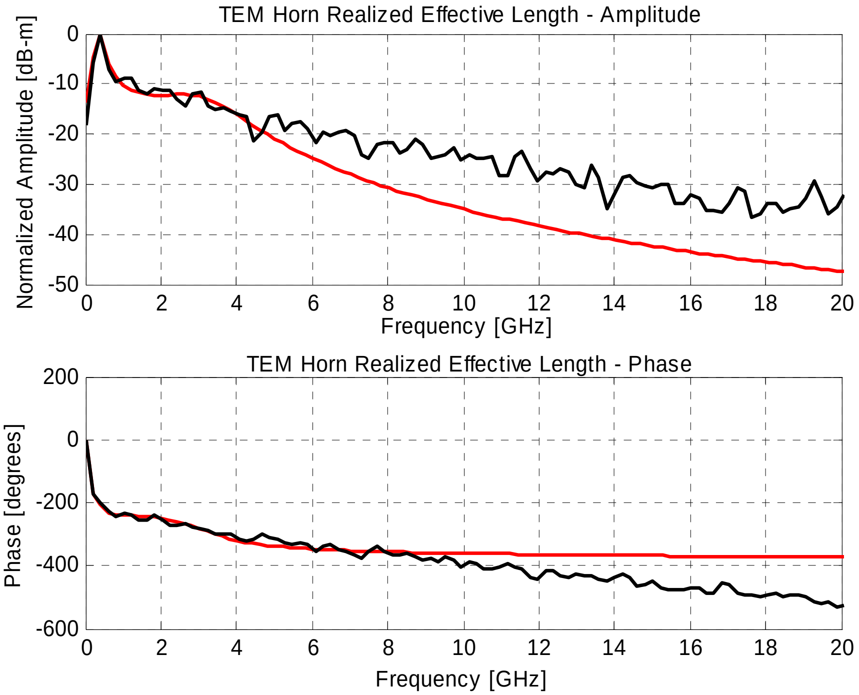

Figure 5.24. Comparison between 6-pole model approximation (red) and frequency-domain realized effective length (black)

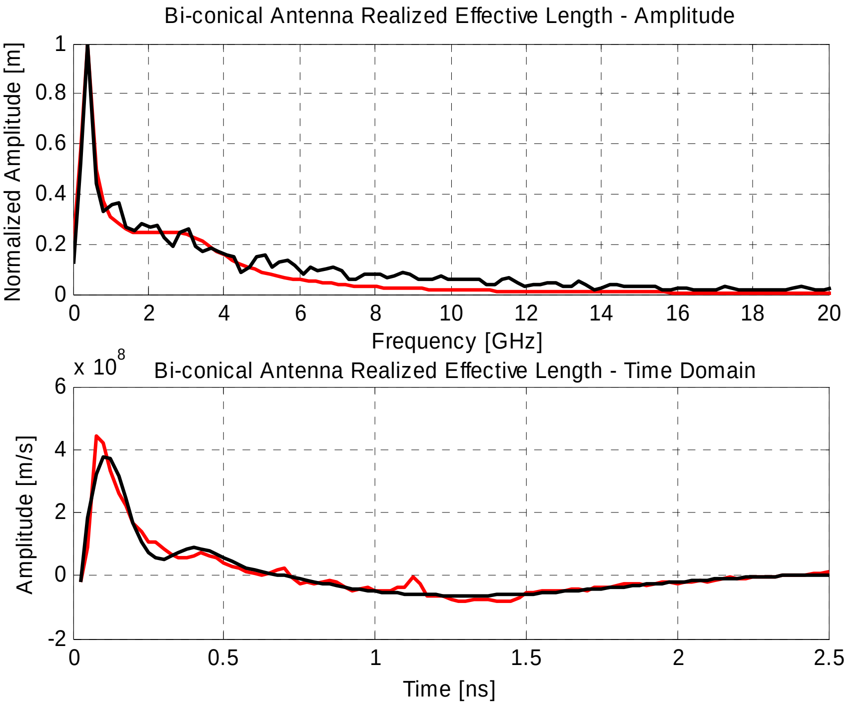

Figure 5.25. Frequency and time-domain realized effective length (red) vs. 6-pole model approximation (black)

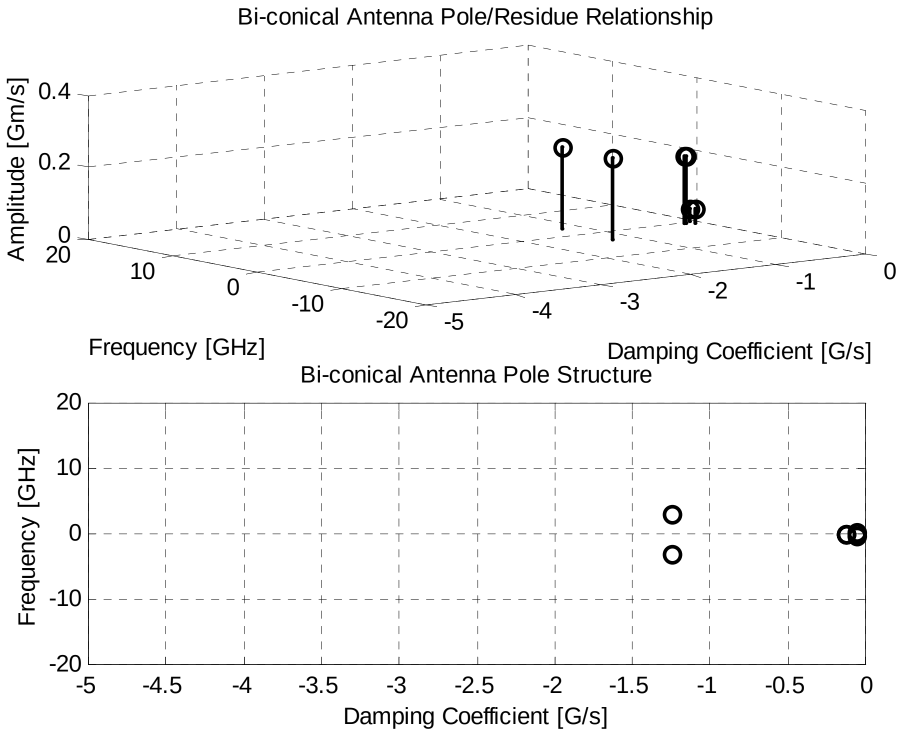

Figure 5.26. Pole/Residue relationship and pole structure for a 6-pole model

Next, we will investigate 12-pole model. The 12-pole model approximates the measured results to a fair degree of accuracy up to 8.0 GHz. Thus, by increasing the model size by two, the frequency domain realized effective length approximation is improved by a factor of two, from 4 to 8 GHz. The 12-pole model approximation compared to frequency-domain realized effective length is shown in Fig. 5.27. The phase is also approximated fairly well up to 8.0 GHz.

The linear amplitude frequency plot shown in Fig. 5.28 indicates that MP is matching finer details of the frequency-domain realized effective length on a local level as noticed before with TEM Horn antenna models. The small variations with higher energy content are matched first obtaining a better match locally but not giving a significant improvement on a global level.

The time-domain response shown in Fig. 5.28 shows an improved match compared to a 6-pole model. The peak in duration of 0.25 ns is very well matched and the low frequency component in the interval 0.25 ns up to 2.5 ns shows also improvement compared to 6-pole model. However, the 12-pole model introduces slight variations in the interval 0.25 ns to 0.5 ns by overestimating the measured results.

The pole residue relationship plot is shown in Fig. 5.29. Again, one could notice similarities with a TEM Horn model, where few poles with higher damping coefficients and slightly higher residues are combined with low residue poles close to jω axis. The frequencies of high residue/damping coefficient poles are 3.2 and 6.8 GHz. Next; the 52-pole model will be presented.

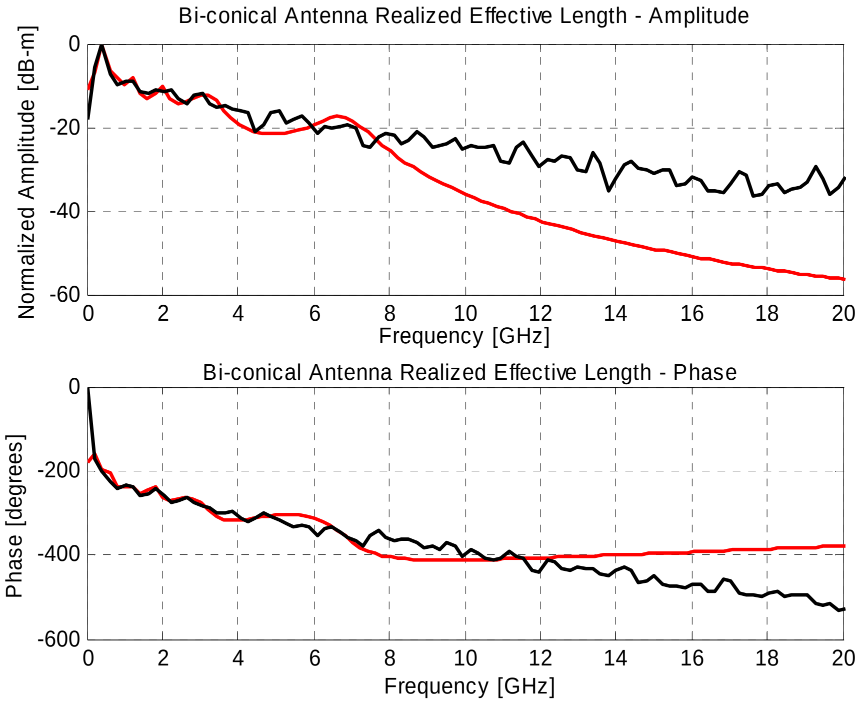

Figure 5.27. Comparison between 12-pole model approximation (red) and frequency-domain realized effective length (black)

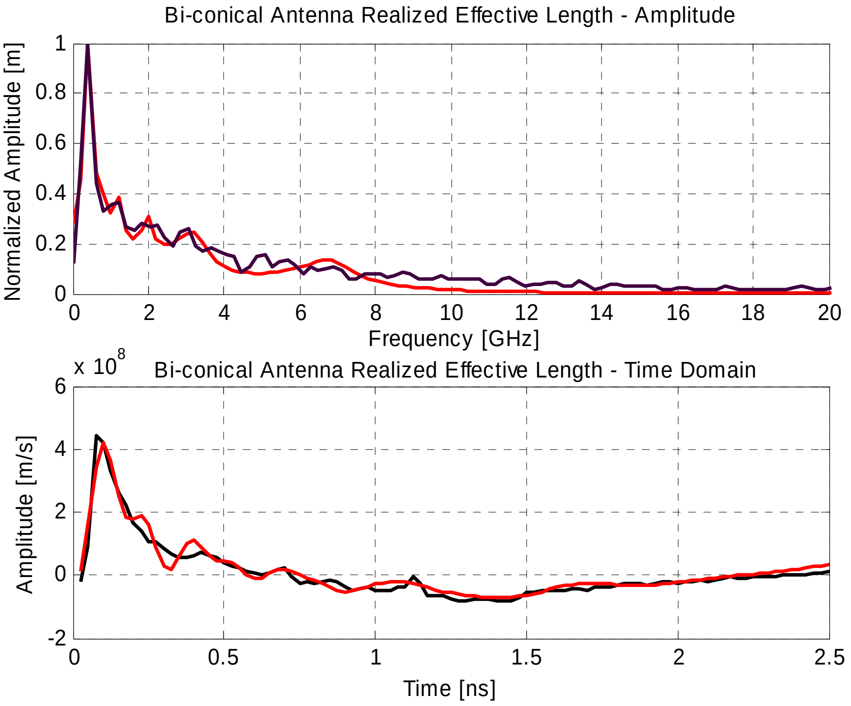

Figure 5.28. Frequency and time-domain realized effective length (black) vs. 12-pole model approximation (red)

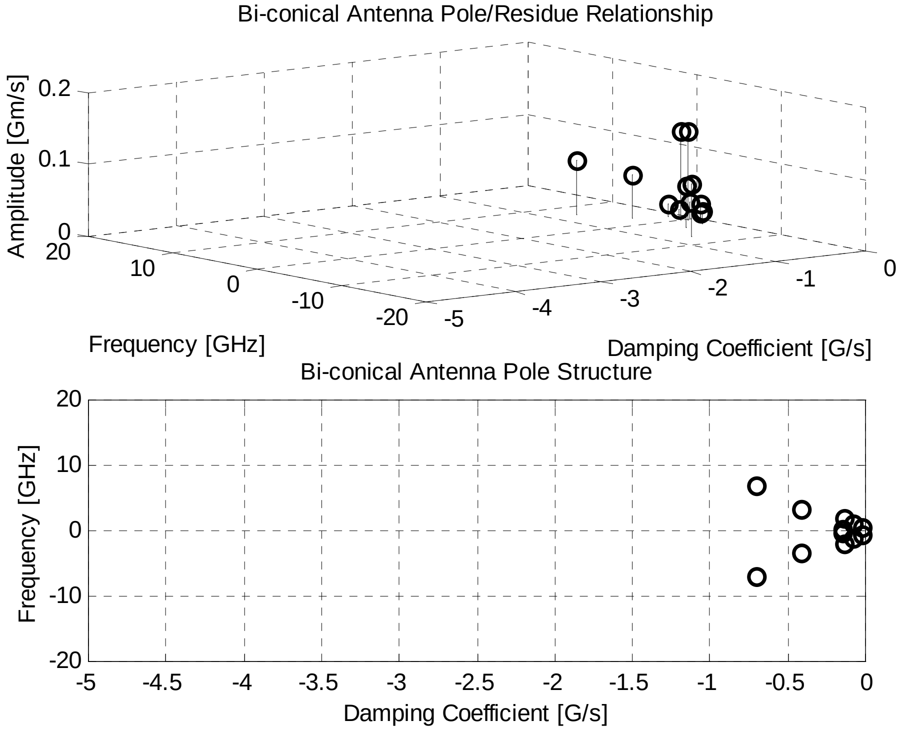
Bi-conical Antenna Pole/Residue Relationship

Bi-conical Antenna Pole Structure

Figure 5.29. Pole/Residue relationship and pole structure for a 12-pole model

The 52-pole model is investigated in order to achieve the most accurate representation. The 52-pole model describes minor local variations of the frequency domain spectrum as shown in Fig. 5.30. The phase variations are also described very accurately. One can notice that there is some variation past 14 GHz. The linear magnitude plot also shows the same trend as shown in Fig. 5.31. The time-domain realized effective length is completely described by the 52-pole model and is shown in Fig. 5.31. The pole/ residue relationship for different pole models shown in Fig. 5.32 indicates that most of the poles in 52-pole model have very low residue amplitude value.

The bi-conical antenna shows a similar pole/residue structure as in TEM horn antenna. The pole residue relationship for different pole models is shown in Fig. 5.33. The pole with a highest damping coefficient has resonant frequency of 7.1 GHz. The 7.1 GHz resonant pole (with slight shifts in frequency) appears in all pole/residue models with 12 and more parameters. The pole models investigated were: 20-, 30-, and 44-pole model.

Also, pole with resonant frequency of 0 Hz appears with high residue value. The 0 Hz pole basically provides an envelope in the time-domain and adjusts for the correct starting value while in the frequency domain models early frequencies up to the first resonant frequency of the antenna system.

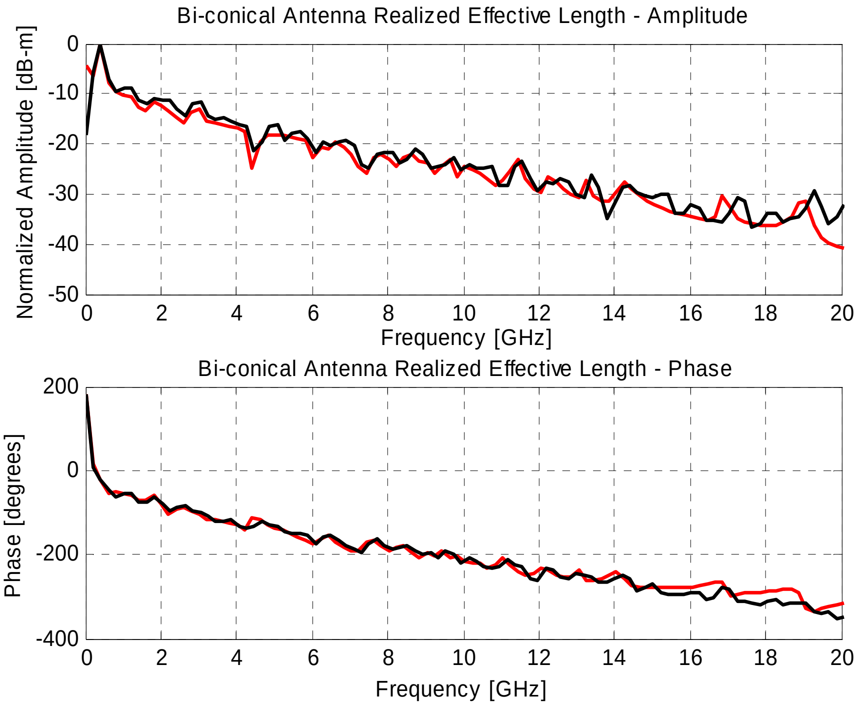

Figure 5.30. Comparison between 52-pole model approximation (red) and frequency-domain realized effective length (black)

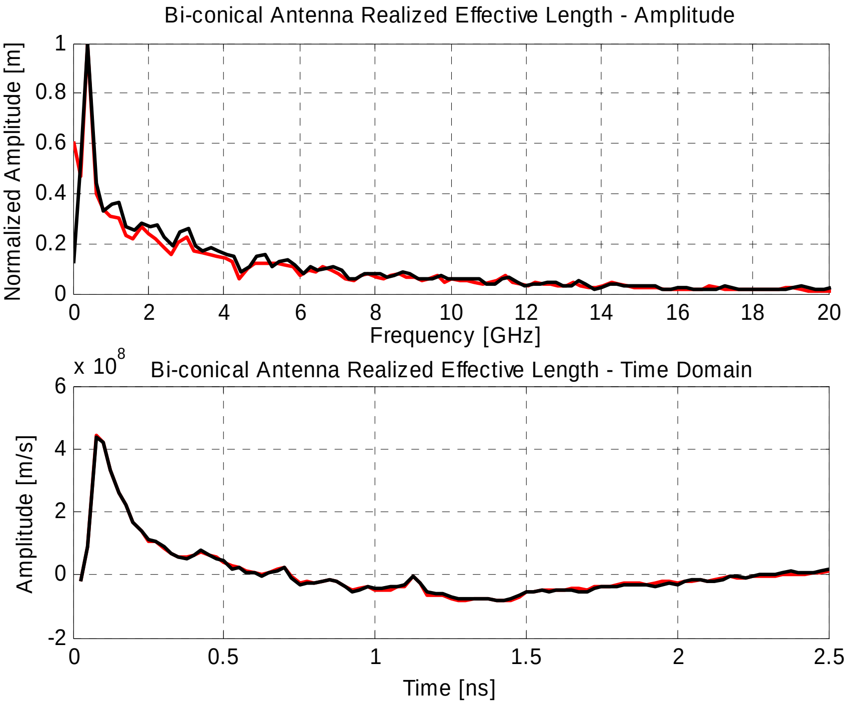

Figure 5.31. Frequency and time-domain realized effective length (black) vs. 52-pole model approximation (red)

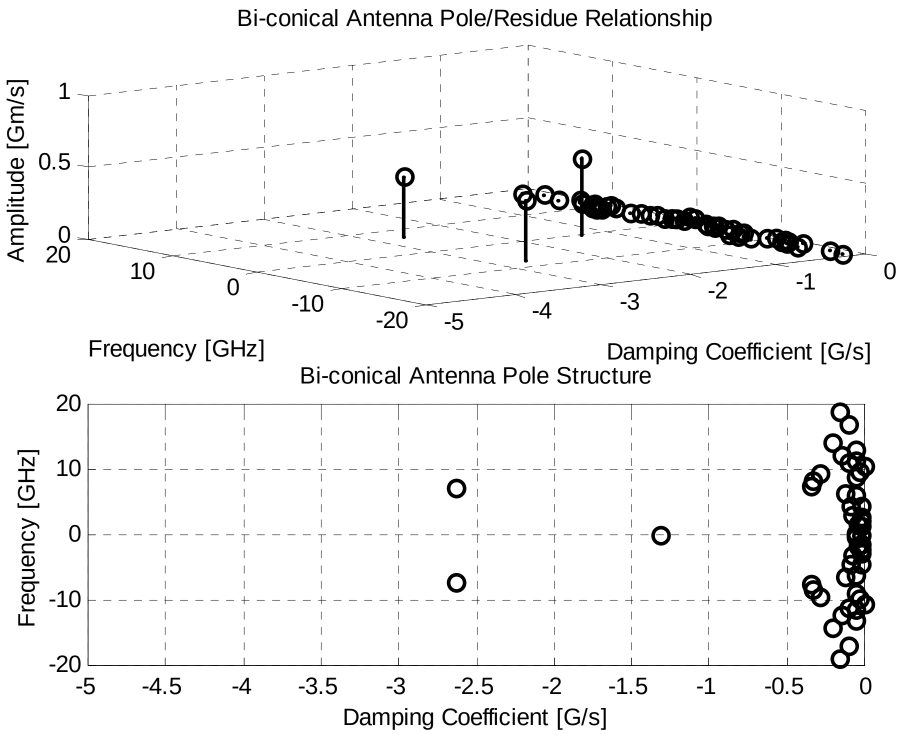

Figure 5.32. Pole/Residue relationship and pole structure for a 52-pole model

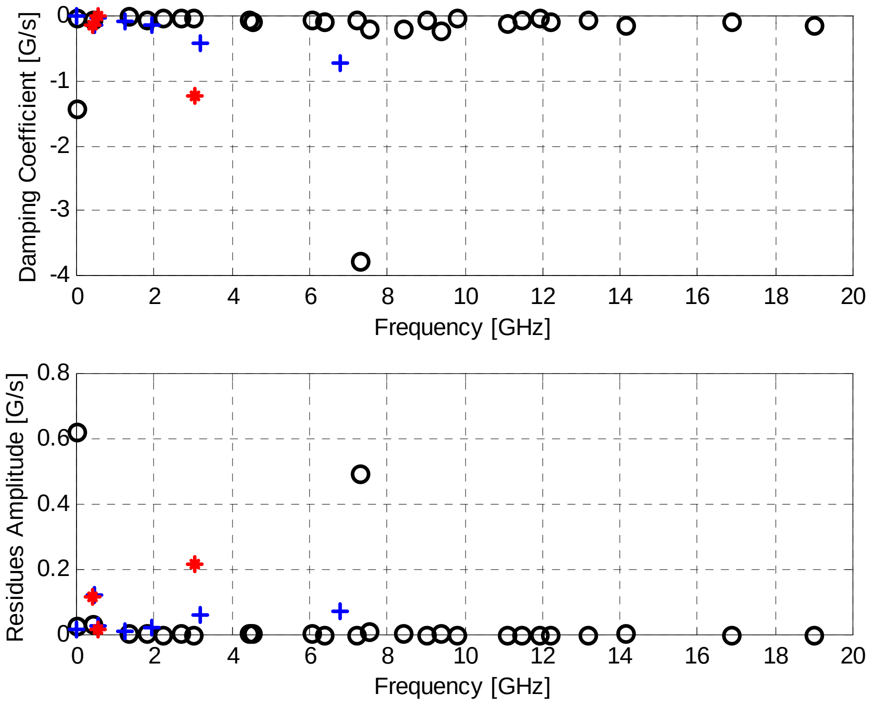

Figure 5.33. Pole/Residue comparison for different models: 6-pole model (*), 12-pole model (+), and 52-pole model (o)

Thus, it should be possible to remove residues with low amplitudes and obtain an accurate model. Some of the low residue poles might be modeling the noise and not representing the antenna structure. By removing low residue poles one can obtain an accurate 6-pole model of the bi-conical antenna. The criterion used was to eliminate all poles in a 52-model that are less than $0.02 \cdot 10^9$ in amplitude of the residue.

The new 6-pole model approximation of the frequency domain realized effective length is shown in Fig. 5.34. The new 6-pole model obtained by reducing the 52-pole model shows a much better approximation on a global level compared to 6-pole model shown in Fig. 5.24. The model overestimates the frequency-domain realized effective length by about 3.0 dB around 8.0 GHz. Also, very low frequencies, below the fundamental resonance, are not modeled very accurately. However, a new 6-pole model provides a significant improvement since it captures all the significant features of the bi-conical antenna. The phase is also approximated very accurately.

The time-domain response is shown in Fig. 5.35. The new 6-pole model approximation is in excellent agreement with the time-domain realized effective length. The model slightly overestimates the peak of the waveform.

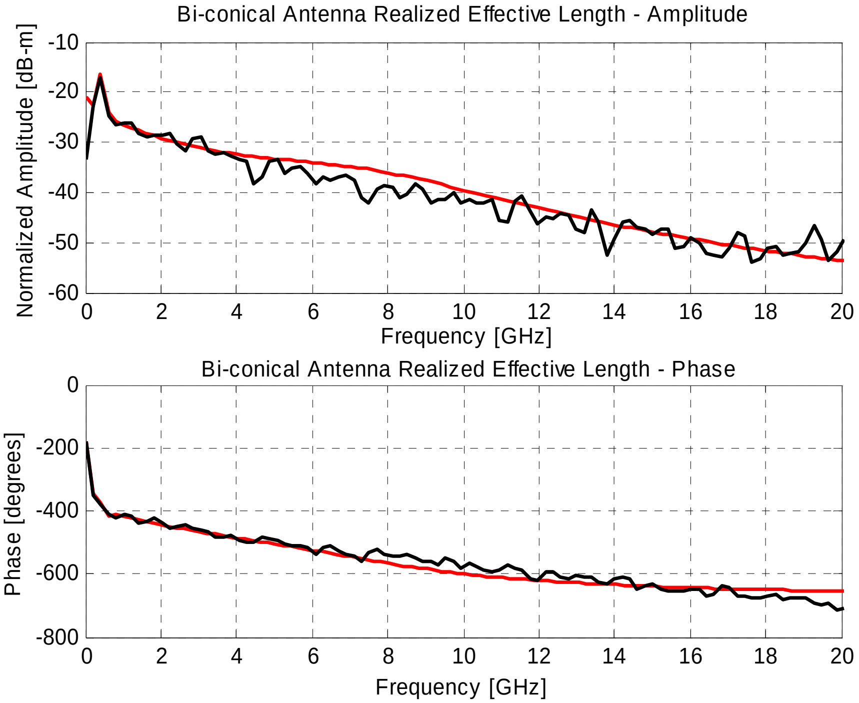

Figure 5.34. Comparison between new 6-pole model approximation (red) and frequency-domain realized effective length (black)

The pole/residue relationship is shown in Fig. 5.36. The composition of the new pole set is of the following frequencies: 0 Hz, 424 MHz, and 7.3 GHz. The pole with the highest residue value is located on the σ axis, corresponding to 0 Hz pole. The second pole with frequency of 0 Hz is located very close to jω axis. The second highest residue pole is 7.3 GHz with the highest damping coefficient value, representing a very broad peak centered at 7.3 GHz. The pole set at 424 MHz represents a fundamental resonance with a sharp peak.

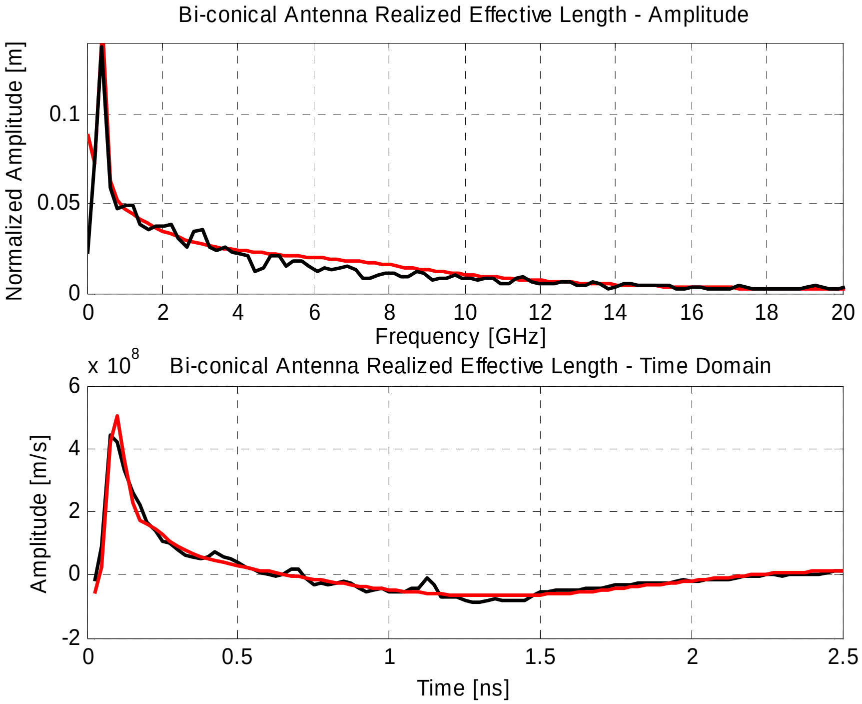

Figure 5.35. Frequency and time-domain realized effective length (black) vs. new 6-pole model approximation (red)

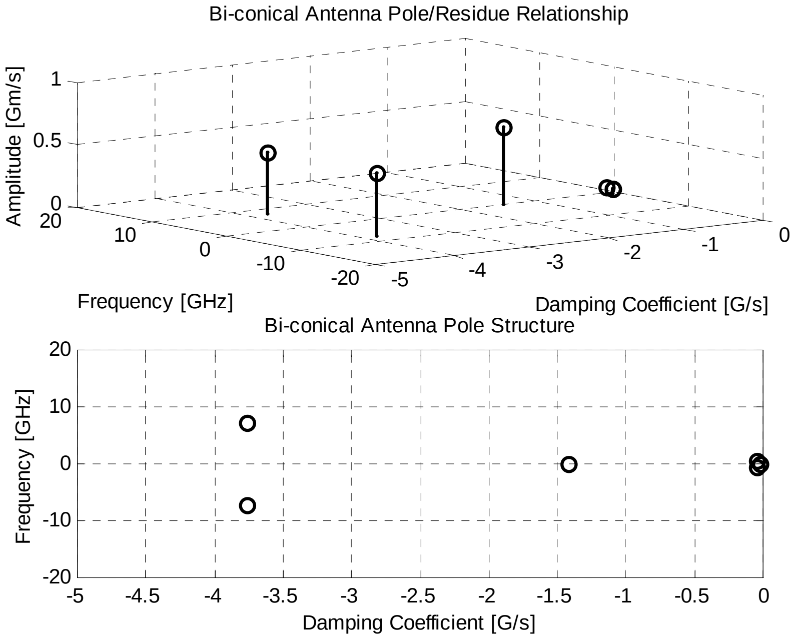

Figure 5.36 Pole/Residue relationship and pole structure for a new 6-pole model

It is demonstrated that the bi-conical antenna could be modeled with only six poles. The bi-conical antenna is modeled with a set of dc poles, a fundamental resonant frequency pole set with low damping coefficient, and a high damping coefficient pole representing a broad peak. The bi-conical antenna shows similar characteristics as the TEM Horn antenna.

In summary, the complex poles and residues for a 6-pole model for the boresight direction are:

$$s = 1\cdot 10^{9}\begin{bmatrix} -1.2453+3.0683i \\ -1.2453-3.0683i \\ -0.0562+0.3657i \\ -0.0562-0.3657i \\ -0.1286+0.0591i \\ -0.1286-0.0591i \end{bmatrix} \quad \vec{R}\left(0,\frac{\pi}{2}\right) = 1\cdot 10^{8}\begin{bmatrix} -1.0766-2.0250i \\ -1.0766+2.0250i \\ 0.3398+0.1422i \\ 0.3398-0.1422i \\ 0.6315+1.7585i \\ 0.6315-1.7585i \end{bmatrix}.$$

The complex poles and residues for a 12-pole model for the boresight direction are:

$$s = 1\cdot 10^{9}\begin{bmatrix} -0.7078-6.8117i \\ -0.7078+6.8117i \\ -0.4203-3.2095i \\ -0.4203+3.2095i \\ -0.1336-1.9570i \\ -0.1336+1.9570i \\ -0.0801-1.2387i \\ -0.0801+1.2387i \\ -0.0212-0.5434i \\ -0.0212+0.5434i \\ -0.1451-0.4151i \\ -0.1451+0.4151i \end{bmatrix} \quad \vec{R}\left(0,\frac{\pi}{2}\right) = 1\cdot 10^{8}\begin{bmatrix} -0.7512-0.0305i \\ -0.7512+0.0305i \\ -0.3202+0.5016i \\ -0.3202-0.5016i \\ 0.0530+0.1649i \\ 0.0530-0.1649i \\ 0.0449+0.1020i \\ 0.0449-0.1020i \\ -0.2057-0.0865i \\ -0.2057+0.0865i \\ 1.2379+0.0946i \\ 1.2379-0.0946i \end{bmatrix}.$$

The complex poles and residues for a new improved 6-pole model for the boresight direction are:

$$s = 1\cdot 10^{9}\begin{bmatrix} -3.7666-7.3121i \\ -3.7666+7.3121i \\ -0.0516-0.4238i \\ -0.0516+0.4238i \\ -1.4222+0.0000i \\ -0.0281-0.0000i \end{bmatrix} \quad \vec{R}\left(0,\frac{\pi}{2}\right) = 1\cdot 10^{8}\begin{bmatrix} -3.5703-3.4469i \\ -3.5703+3.4469i \\ 0.2995+0.1770i \\ 0.2995-0.1770i \\ 6.2128+0.0000i \\ -0.2753-0.0000i \end{bmatrix}.$$

5.6 1.0 GHz Resonant Monopole Minimal Model – Resonant Structure

The monopole antenna is an interesting structure since it provides distinct resonant frequencies and offers a good understanding of pole/residue modeling. The response of the single monopole was obtained using the TEM Horn antenna as a reference. The measurements were done using 122 by 122 cm (1 ft =12 in, 1 in = 2.54 cm) ground plane in order to eliminate a wide frequency balun and effects caused by an edge of the finite ground plane required for monopole type of structures. The distance between the reference planes of the monopole and the TEM Horn antenna was 1.3125 meters.

The s_{21} frequency response and equivalent time-domain response of the TEM horn and 1.0 GHz resonant monopole link is shown in Fig. 5.37. Compared to the TEM horn, the monopole exhibits many resonant frequencies. The response clearly shows odd resonant frequencies (e.g. 1,3,5, etc.). It is interesting to note that even resonant frequencies are present in the following fashion: 2, 6, 10, 14, 18 GHz. The even resonant frequencies at 4, 8, 12, and 16 GHz are not very significant.

The time-domain response reflects both the combined characteristics of the TEM Horn and the 1.0 GHz resonant monopole. The SNR ratio is greater than 20 dB up to 15.0 GHz. The duration of the time-domain response is in the interval 4.5 ns to 7.0 ns. The peak amplitude is $2.5\cdot 10^{8}$ Units/s.

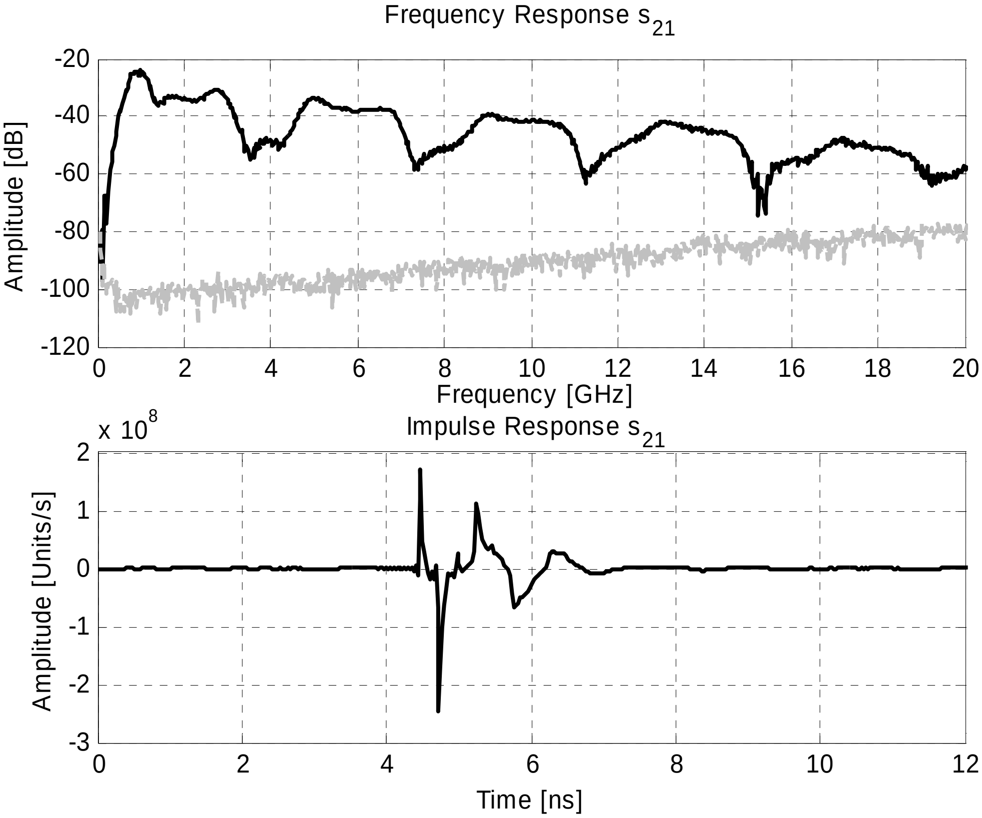

Figure 5.37. s_{21} frequency response (black) vs. noise (grey) and corresponding s_{21} impulse response for a monopole/TEM Horn antenna link

The monopole antenna exhibits many resonant frequencies as the amplitude response shows. Thus, a monopole requires a large number of poles indicating that resonant antenna systems require a larger number of poles compared to wide-band antenna systems. Using the MP method, 6-, 18-, and 39-pole models were investigated. The parameters used in the MP method are shown in Table 5.3.

Table 5.3. MP method parameters used in modeling 1.0 GHz resonant monopole

Model	**Time Window**[14] **[ns]**	**Singular Value Amplitude**
6	5.0 -> K=200	0.1
18	5.0 -> K=200	0.02
39	5.0 -> K=200	0.002

The singular value decomposition of the monopole realized effective length is shown in Fig. 5.38. The SVD shows only few values are dominant in the monopole response. The 10th singular value is almost 20 times smaller compared to the 1st singular value

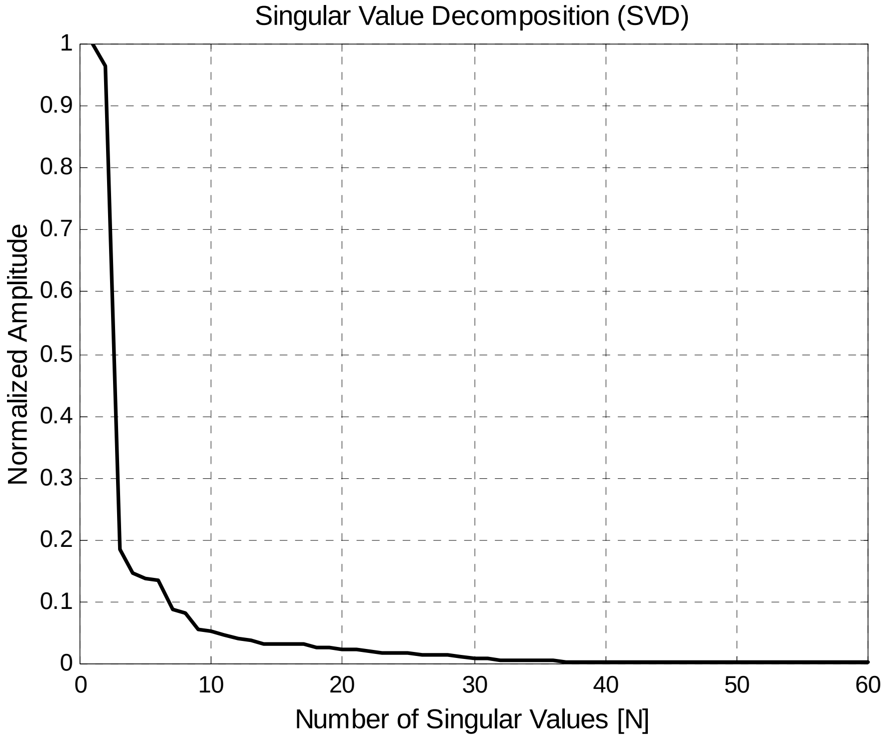

Figure 5.38. Singular value decomposition of a monopole antenna time-domain realized effective length

The 6-pole model frequency and time-domain responses are shown in Figs. 5.39 and 5.40, respectively.

---

[14] r= 1.3125 m distance between the antennas/100 MHz resolution in the frequency domain

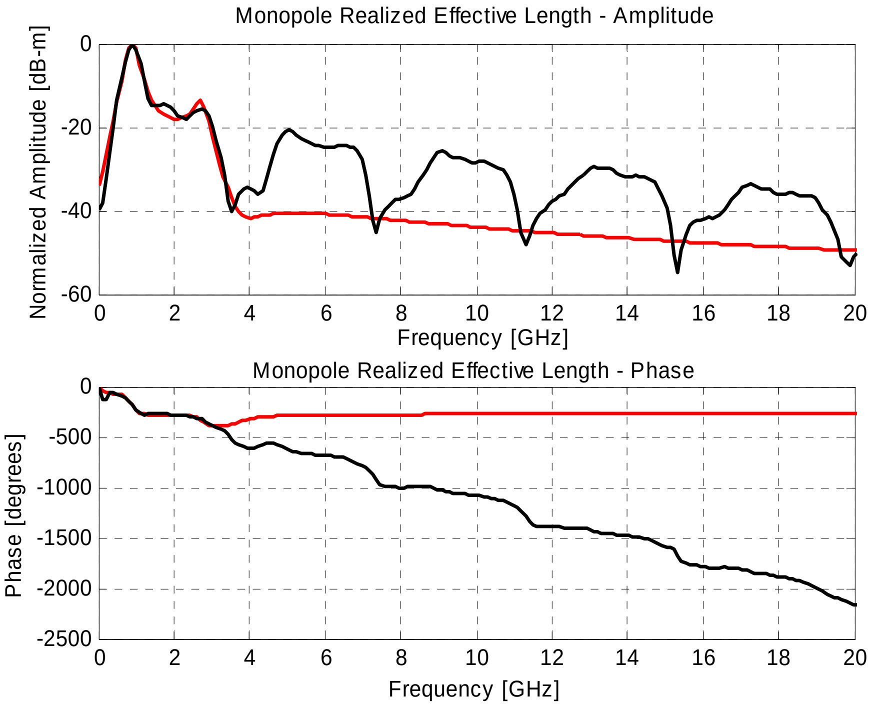

Figure 5.39. Comparison between 6-pole model approximation (red) and frequency-domain realized effective length (black)

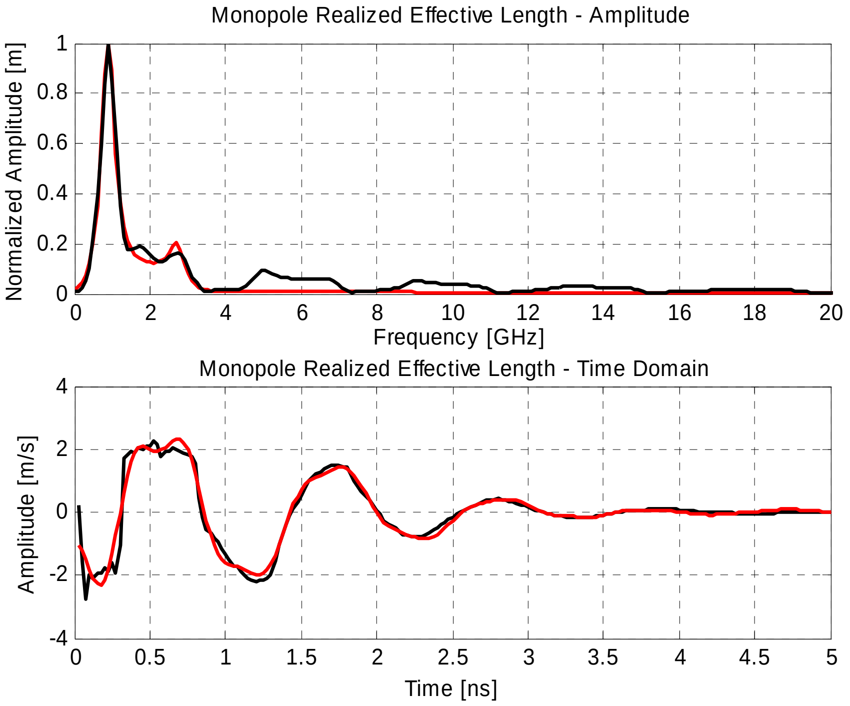

Figure 5.40. Frequency and time-domain realized effective length (black) vs. 6-pole model approximation (red)

The 6-pole model shows a good frequency-domain match both in amplitude and phase up to 4.0 GHz. The frequencies present in the 6-pole model are: 736 MHz, 970 MHz, and 2.75 GHz. It is striking to observe that a 6-pole model provides an accurate description of the time-domain realized effective length shown in Fig. 5.40. The only deviation the model exhibits is the minor details in the interval 0 to 0.75 ns. Thus, one can conclude that the time-domain response of the antenna is defined by low frequency contributions of the antenna, primarily the lowest resonant frequency.

The pole/residue relationship is shown in Fig. 5.41. As one would expect the poles are located close to the jω axes and are very low in residue amplitude compared to those of TEM Horn antenna. It is interesting to note that poles with distinct resonance frequency appear close to jω axis and poles have low residue amplitude.

The 18-pole model is investigated next. The 18-pole model provides a very good frequency domain match up to 8.0 GHz and a marginal match up to 14 GHz. The frequency domain amplitude and phase is shown in Fig. 5.42. The phase is linearly decreasing as the frequency increase. The 2000 degrees correspond to the time the pulse travels from the source to the tip of the monopole and back. In essence, this indicates that the monopole radiation is not caused only by the tip and source reflections but on contrary the monopole radiation occurs at each point on the antenna structure. The time-domain realized effective length is shown in Fig. 5.43. By adding additional 6 frequencies the antenna is completely described in the time-domain.

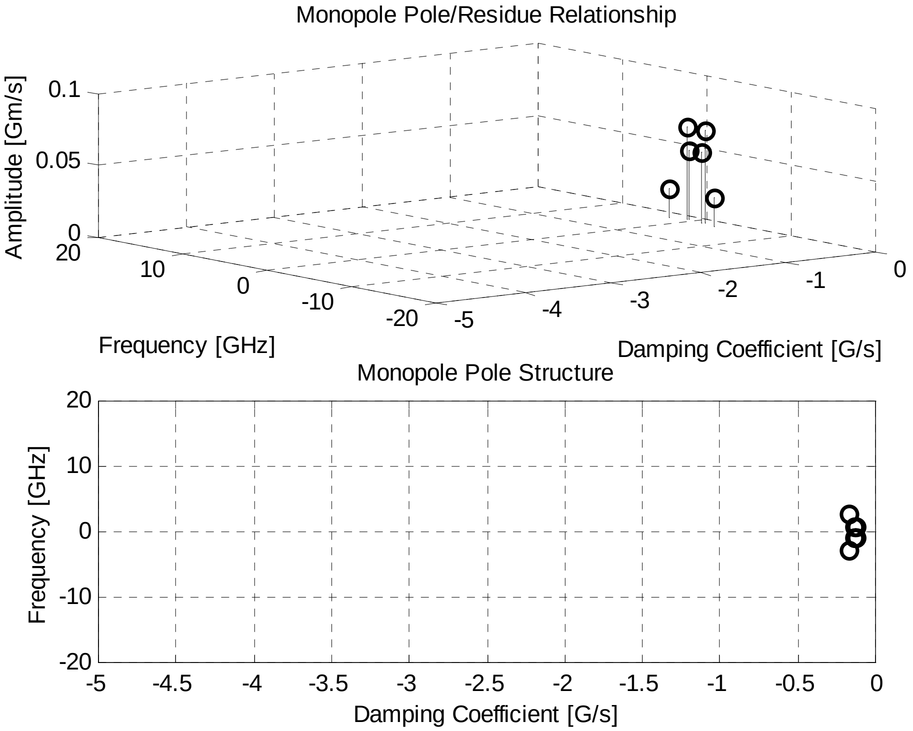

Figure 5.41. Pole/Residue relationship and pole structure for a 6-pole model

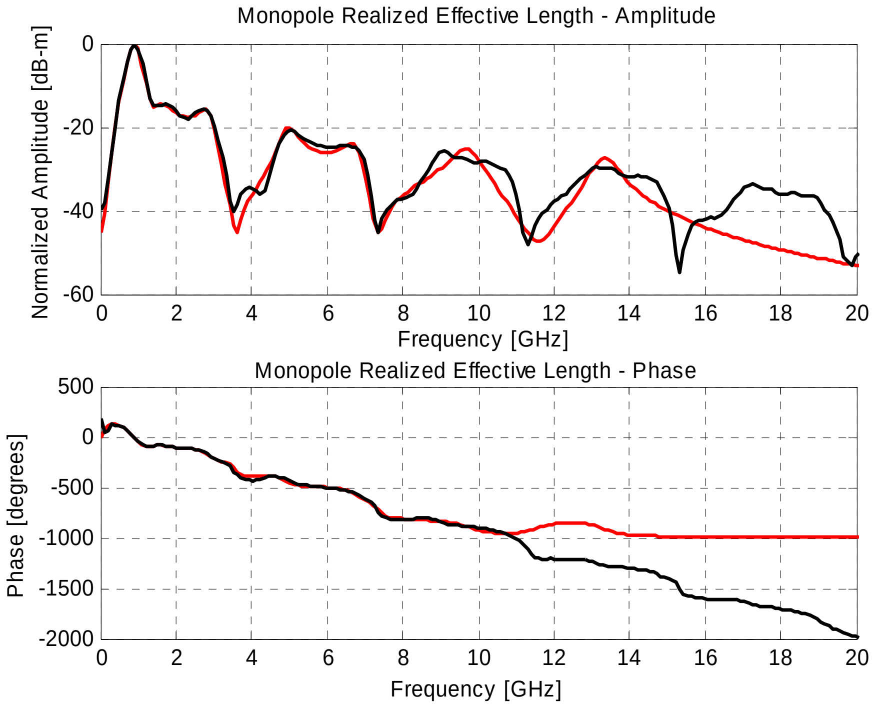

Figure 5.42. Comparison between 18-pole model approximation (red) and frequency-domain realized effective length (black)

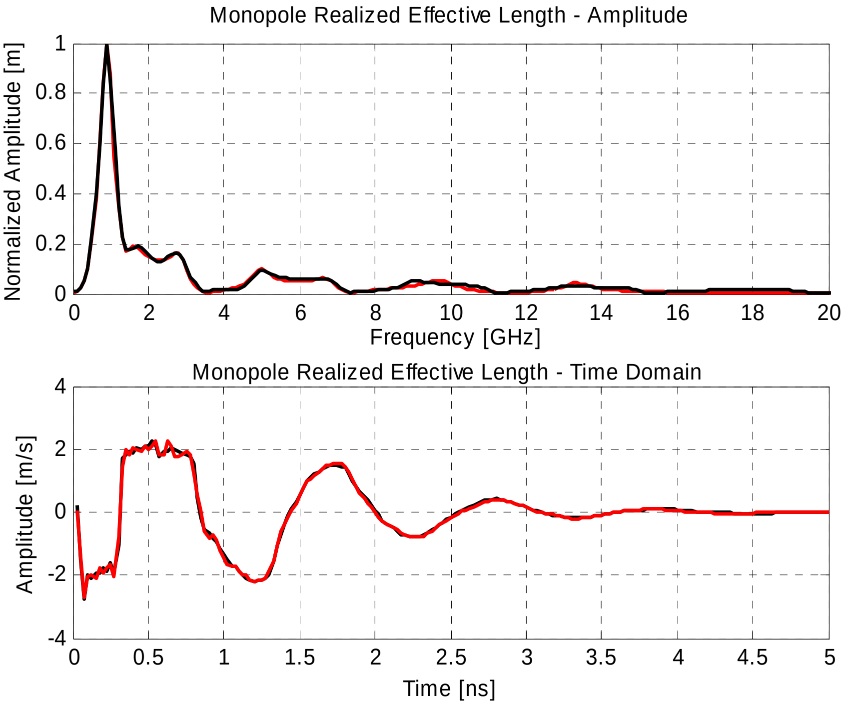

Figure 5.43. Frequency and time-domain realized effective length (black) vs. 18-pole model approximation (red)

The pole/residue relationship is shown in Fig. 5.44. The poles have damping coefficients that are smaller than –0.5 G/s and they are structured close to jω axis. By increasing the pole model, additional resonant frequencies appear: 5, 7, 9, and 13 GHz.

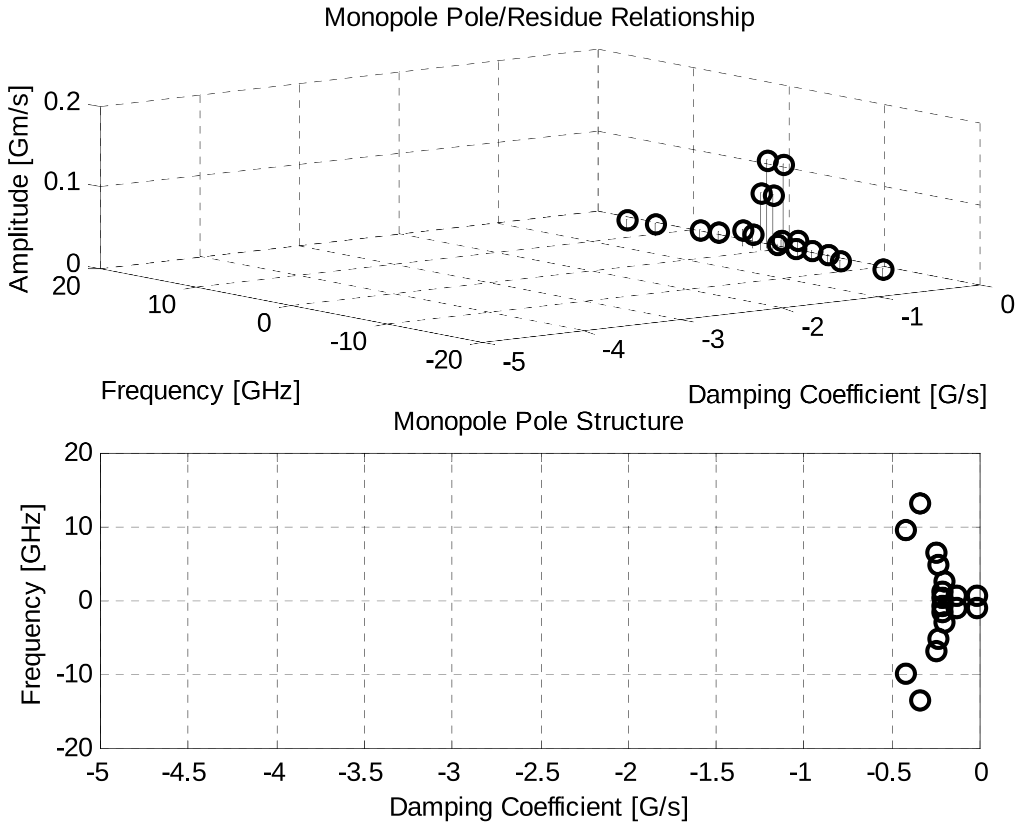

Figure 5.44. Pole/Residue relationship and pole structure for an 18-pole model

The 39-pole model investigated next shows a very accurate description of the 1.0 GHz resonant monopole antenna in both the time and frequency domain. The frequency domain response is shown in Fig. 5.45. Some variations are present in the frequency interval 15 to 17 GHz but overall match is very accurate. Also one can notice that the response is 30 dB down from the peak value at 10 GHz. The phase is also described very accurately with the model. The time representation is fully described and all the minor details are modeled to a high degree of the accuracy as shown in Fig. 5.46.

The pole/residue relationship of the 39-pole model is shown in Fig. 5.47. New poles are added at lower frequencies to model more accurately the response in between the resonant frequencies. The plot indicates that the poles with damping coefficients smaller than –0.5 G/s constitute the first layer that defines odd resonant frequencies and part of even frequencies (2, 6, 10, 14, 18 GHz) while the second layer, with damping coefficients greater than –0.5 G/s, captures the features of the frequencies in between.

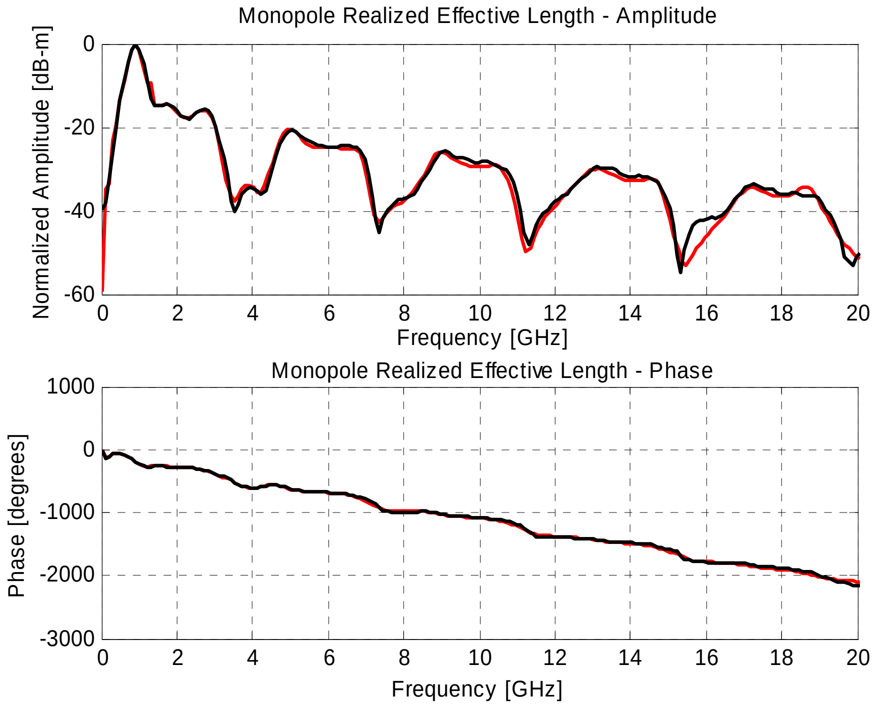

Figure 5.45. Comparison between 39-pole model approximation (red) and frequency-domain realized effective length (black)

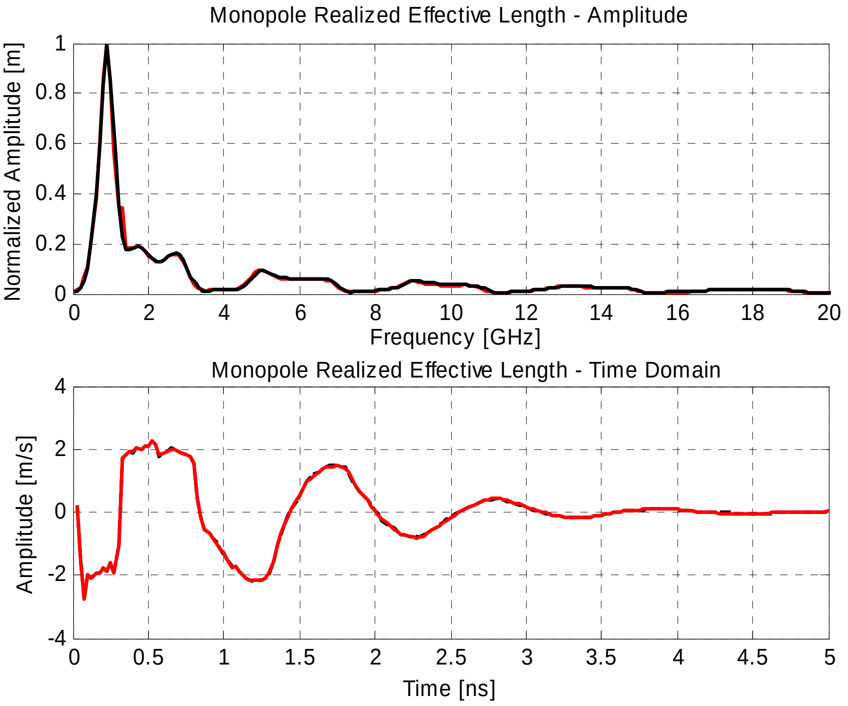

Figure 5.46. Frequency and time-domain realized effective length (black) vs. 39-pole model approximation (red)

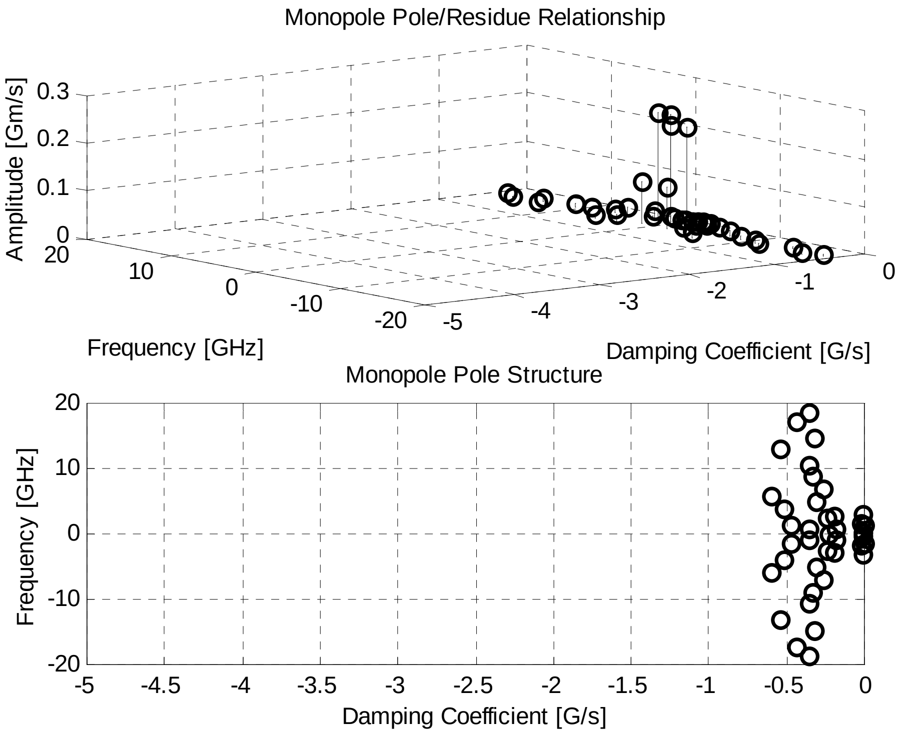

Figure 5.47. Pole/Residue relationship and pole structure for a 39-pole model

One can notice from the pole structure that major poles defining the monopole are 1.0, 3.0, and 7.0 GHz pole/residues. This is evident from a different pole model comparison shown in Fig. 5.48. Regardless of the model, the poles are distinguishable. This suggests that they uniquely define the response. After 10.0 GHz the waveform is 30 dB from the peak value. The time-domain is adequately approximated by 6 poles. However, for a good frequency-domain match up to 20 GHz a 39-pole model is required. The complex poles and residues for a 6-pole model at the boresight are

$$s = 1\cdot 10^9 \begin{bmatrix} -0.1750-2.7494i \\ -0.1750+2.7494i \\ -0.1230-0.9698i \\ -0.1230+0.9698i \\ -0.1339-0.7360i \\ -0.1339+0.7360i \end{bmatrix} \qquad \vec{R}\left(0,\frac{\pi}{2}\right) = 1\cdot 10^9 \begin{bmatrix} 0.4992-0.0172i \\ 0.4992+0.0172i \\ -0.9513-1.3026i \\ -0.9513+1.3026i \\ -0.0603-1.2236i \\ -0.0603+1.2236i \end{bmatrix}$$

The complex poles and residues for 18-pole model for boresight are

$$s = 1\cdot 10^{10}\begin{bmatrix} -0.0348-1.3318i \\ -0.0348+1.3318i \\ -0.0423-0.9737i \\ -0.0423+0.9737i \\ -0.0254-0.6763i \\ -0.0254+0.6763i \\ -0.0245-0.4938i \\ -0.0245+0.4938i \\ -0.0203-0.2867i \\ -0.0203+0.2867i \\ -0.0217-0.1494i \\ -0.0217+0.1494i \\ -0.0022-0.0971i \\ -0.0022+0.0971i \\ -0.0142-0.0942i \\ -0.0142+0.0942i \\ -0.0219-0.0664i \\ -0.0219+0.0664i \end{bmatrix} \quad \vec{R}\left(0,\frac{\pi}{2}\right) = 1\cdot 10^{9}\begin{bmatrix} 0.2328+0.0264i \\ 0.2328-0.0264i \\ 0.3575+0.0280i \\ 0.3575-0.0280i \\ 0.1377+0.2370i \\ 0.1377-0.2370i \\ -0.1350-0.2970i \\ -0.1350+0.2970i \\ 0.4572+0.2073i \\ 0.4572-0.2073i \\ -0.4178-0.0167i \\ -0.4178+0.0167i \\ 0.0110-0.0612i \\ 0.0110+0.0612i \\ -1.9932-1.8785i \\ -1.9932+1.8785i \\ 1.3881+1.1027i \\ 1.3881-1.1027i \end{bmatrix}$$

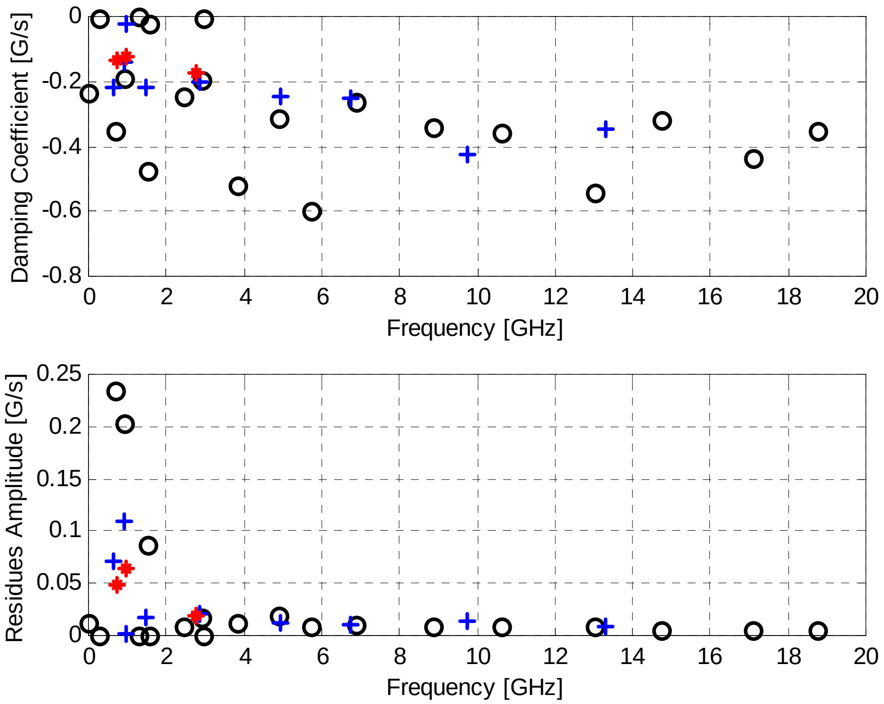

Figure 5.48. Pole/residue comparison for different models: 6-pole model (*), 18-pole model (+), and 39-pole model (o)

5.7 Cavity-Backed Archimedean Spiral Antenna– Circularly Polarized and Directional Antenna

A cavity-backed spiral antenna belongs to a class of frequency independent antennas. The properties of the spiral antenna have been discussed in detail in Chapter 3. A cavity–backed spiral was measured inside the anechoic chamber. The distance between the antenna reference planes was 1.7575 m.

The frequency domain and time-domain link response of 2 cavity-backed spiral antenna is shown in Fig. 5.49. The measured response is valid to 14 GHz since the data past 14 GHz is noise corrupted. The frequency amplitude response shows almost constant amplitude response. At the time of the measurements, a source problem existed that was explained in Chapter 3. The signal generator caused a noise level to go up as shown in Fig. 5.49. The time-domain response shows a chirp-type of response, which is characteristic for frequency independent antennas.

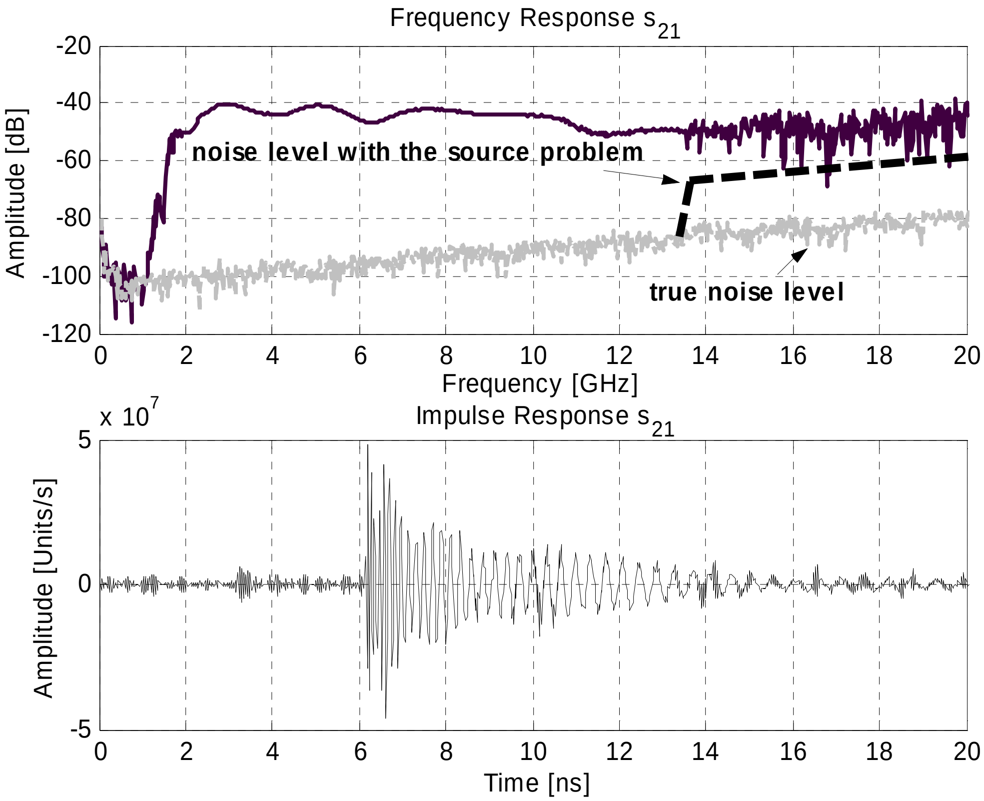

Figure 5.49. s_{21} frequency response (black) vs. noise (grey) and corresponding s_{21} impulse response for 2 cavity-backed spiral antenna link

It is interesting to notice that the SVD plot, shown in Fig. 5.50, shows a large number of poles that have singular values higher than 0.1. This indicates that the model must have around 40 poles to very accurately represent the spiral time-domain realized effective length.

The parameters used in pole/residue extraction using the MP method are shown in Table 5.4. The time-domain window used was 7.5 ns. The singular values used in the calculations had amplitude higher than 0.003. The residues with amplitudes higher than $0.007 \cdot 10^9$ where used in the 34-pole model, and the residues with the amplitudes higher than $0.016 \cdot 10^9$ where used in 28-pole model.

Table 5.4. MP method parameters used in the Archimedean spiral antenna modeling

Model	**Time Window**[15] **[ns]**	**Singular Value Amplitude**	**Residue Criteria**
34	7.5 -> K=300	0.003	$0.007 \cdot 10^9$
28	7.5 -> K=300	0.003	$0.016 \cdot 10^9$

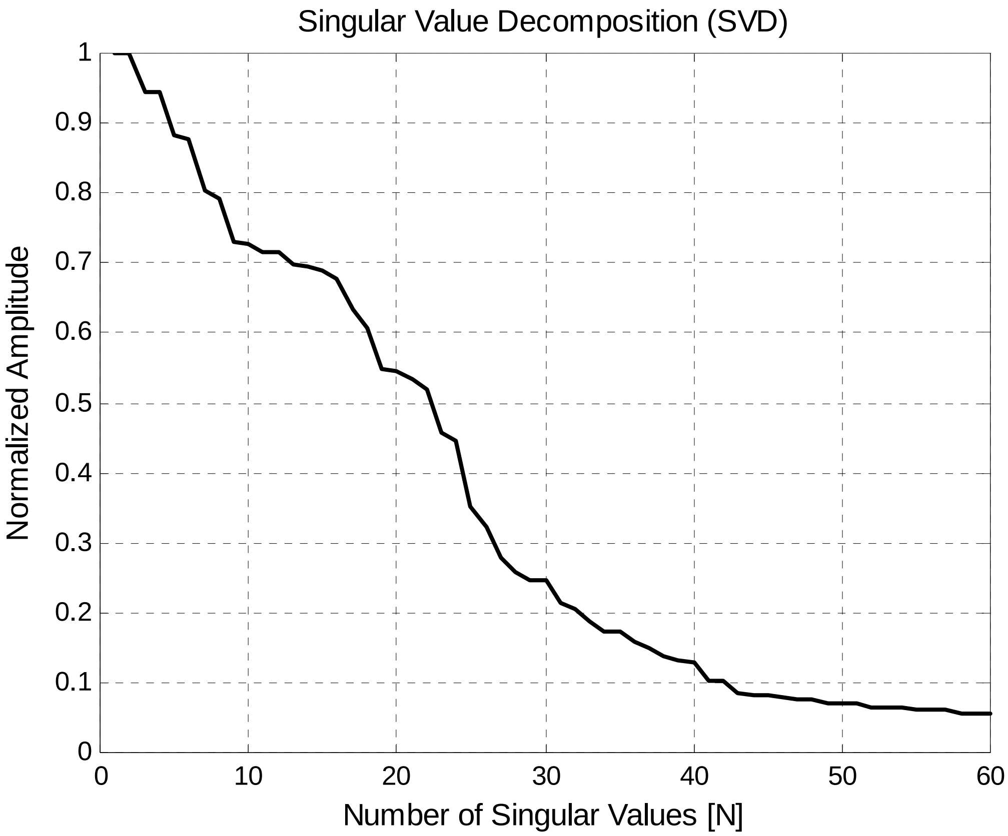

Figure 5.50. Singular value decomposition of cavity-backed spiral antenna time-domain realized effective length

The frequency domain response of the spiral antenna 34-pole model is shown in Fig. 5.51. The model shows a very good match for the whole frequency range, 0 to 20 GHz. There is some deviation from the model in the frequency range below 2.0 GHz, which is reflected also in the phase plot. However, as shown in Fig. 5.49 the data level is

---

[15] r= 1.7575 m distance between the reference planes/66.75 MHz resolution in the frequency domain

comparable to the noise level for frequencies below 2.0 GHz and above 14.0 GHz. The phase response shows a very nonlinear behavior.

The 28-pole model frequency response, shown in Fig. 5.54, shows a very good match up to 10.0 GHz and a marginal match up to 20 GHz. The phase response shows a good match up to 20 GHz.

The time-domain response shows excellent agreement between pole/residue model and measured realized effective length for both 34 and 28-pole model. The chirp duration is almost 10.0 ns. The time-domain response is shown in Figs. 5.52 and 5.55 for the 34-pole and 28-pole model, respectively. The pole structure for the 34-pole and 28-pole model is shown in Fig. 5.53 and Fig. 5.56, respectively.

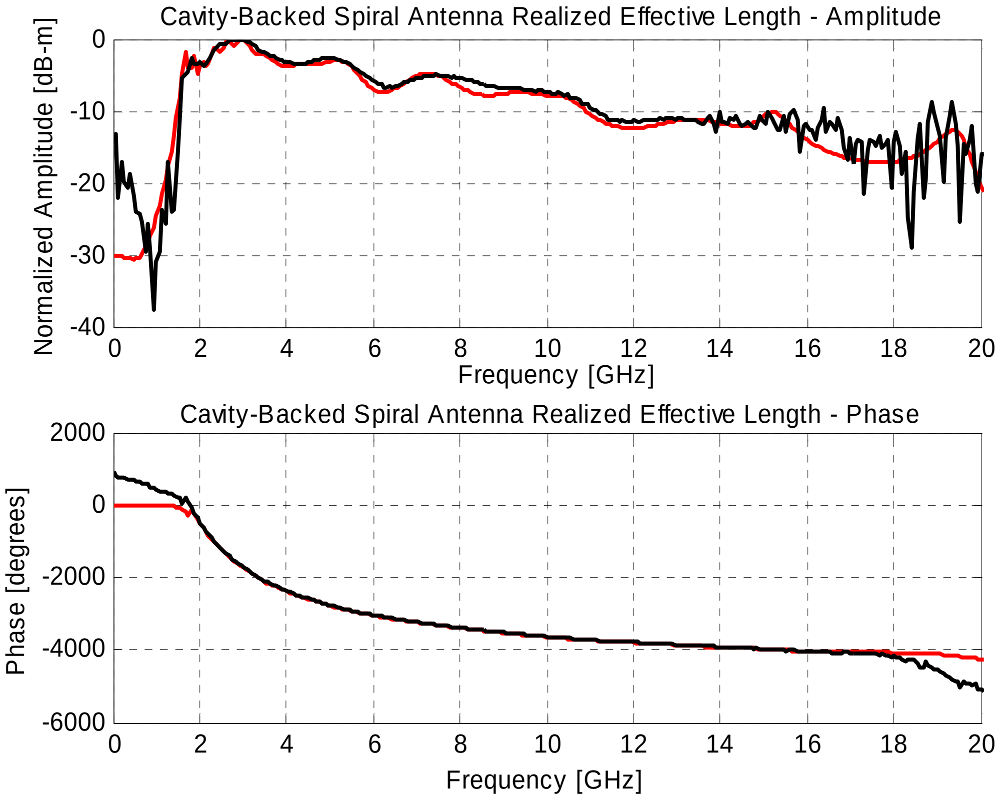

Figure 5.51. Comparison between 34-pole model approximation (red) and frequency-domain realized effective length (black)

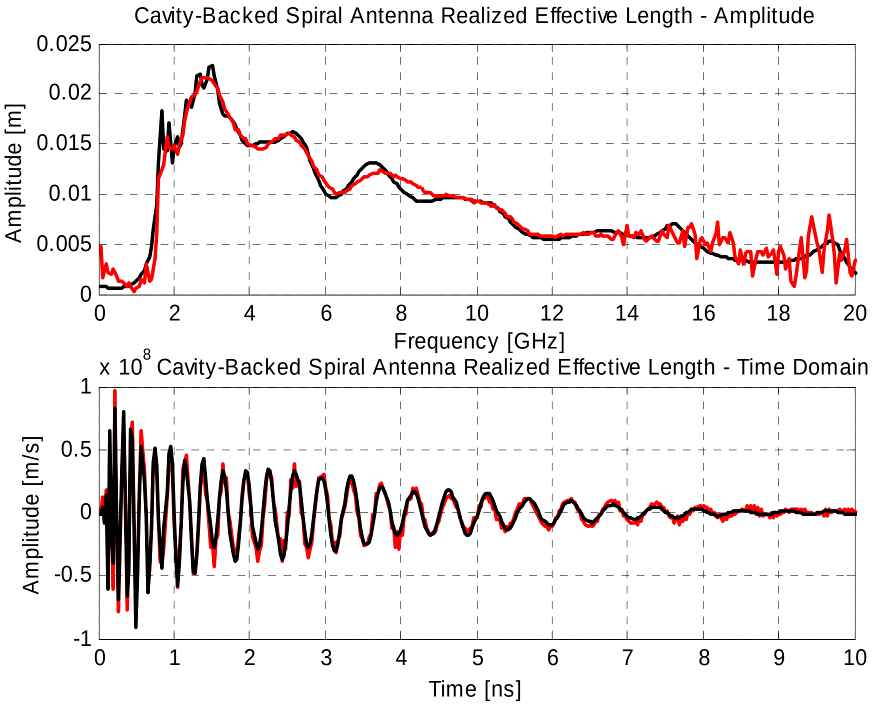

Figure 5.52. Frequency and time-domain realized effective length (black) vs. 34-pole model approximation (red)

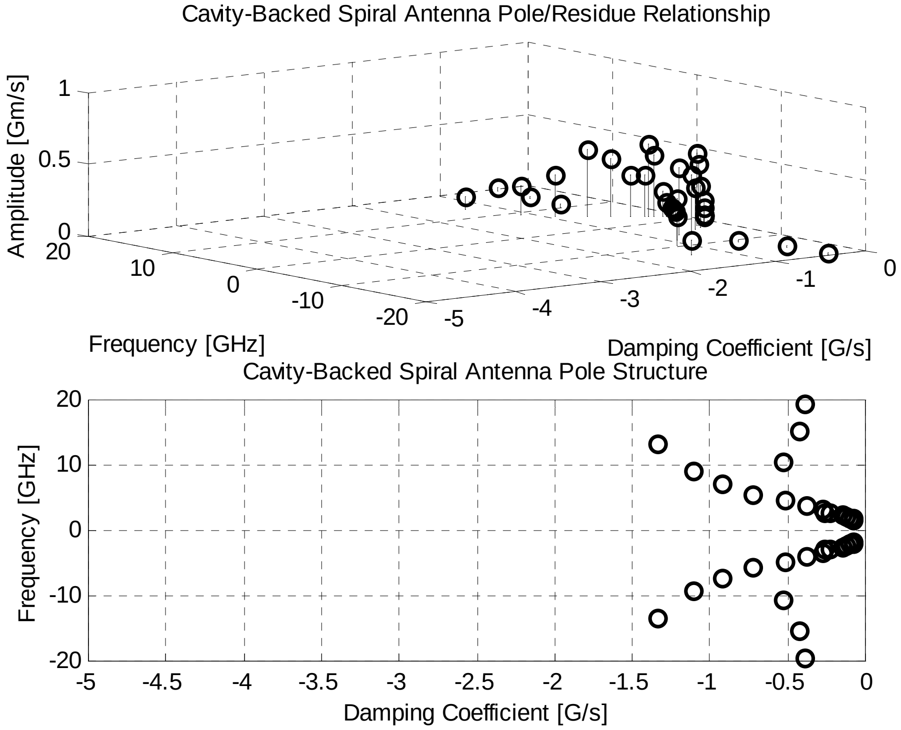

Figure 5.53. Pole/Residue relationship and pole structure for a 34-pole model

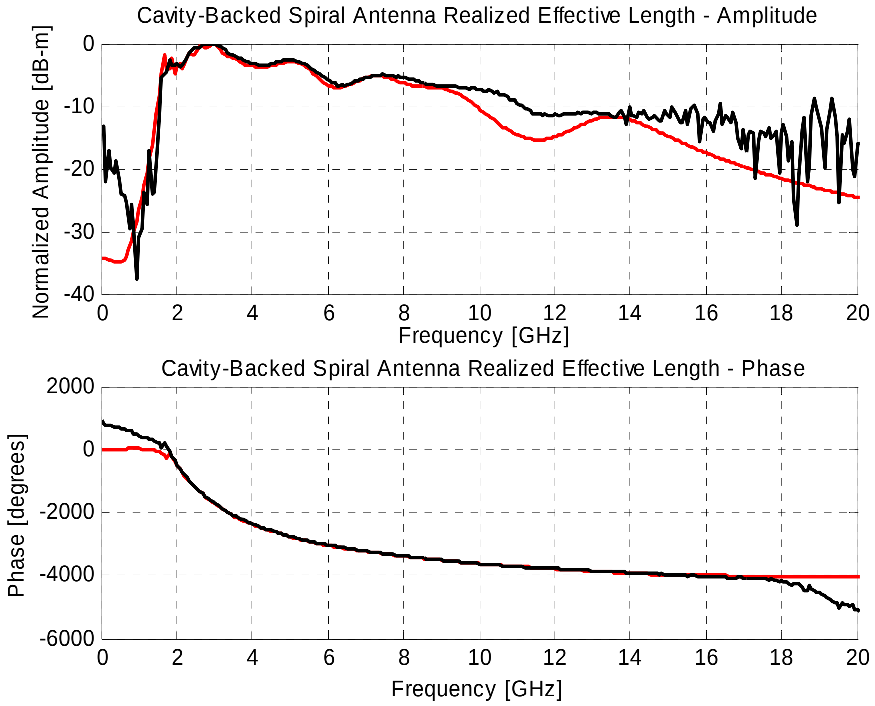

Figure 5.54. Comparison between new 28-pole model approximation (red) and frequency-domain realized effective length (black)

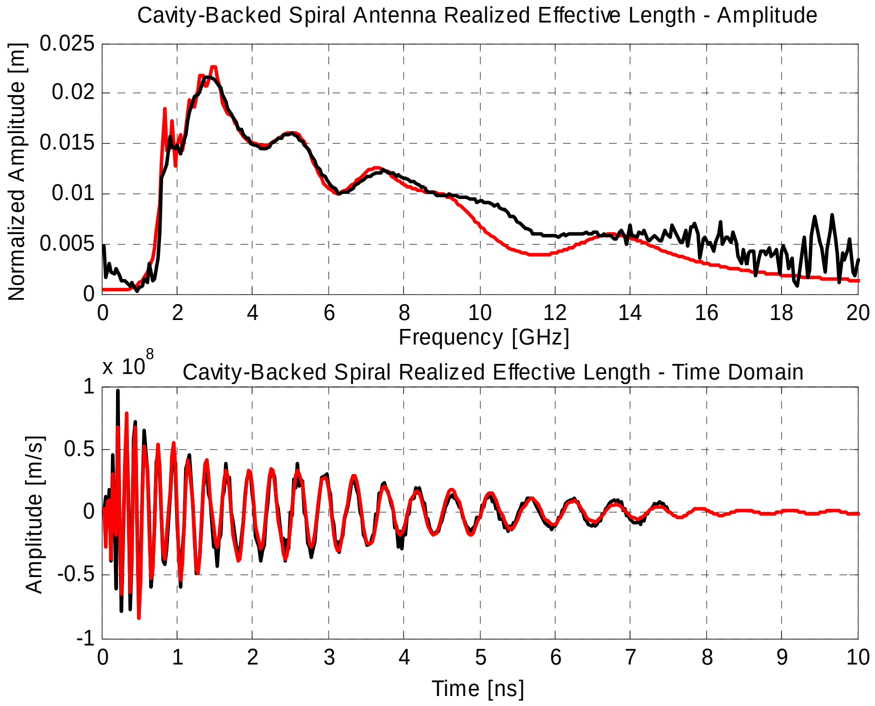

Figure 5.55. Frequency and time-domain realized effective length (black) vs. new 28-pole model approximation (red)

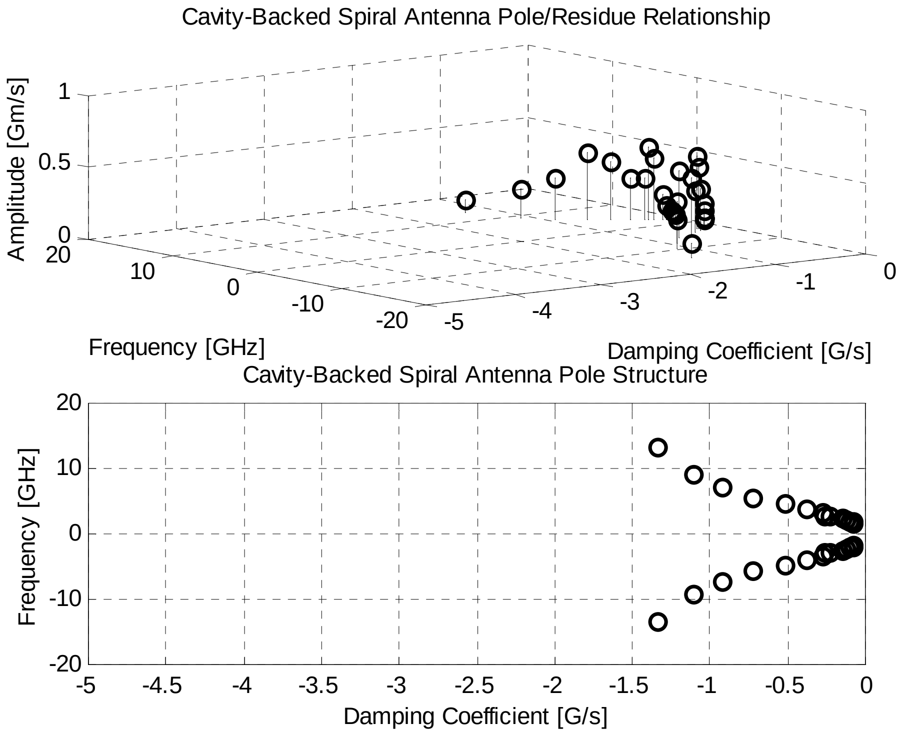

Figure 5.56. Pole/Residue relationship and pole structure for a new 28-pole model

The pole/residue model of a spiral antenna shows some interesting results. The poles are very closely spaced, but as the frequency increases, the poles move away from $j\omega$ axis. The corresponding residues are relatively strong compared to each other. This type of behavior indicates that the energy content of the Archimedean spiral is distributed among the frequencies, which is not the case with broadband or resonant antenna where the pulse shape and energy are dominated by low frequency poles.

5.8 Minimal Model Conclusions

Four antenna systems have been investigated in order to understand the trade-offs of the minimal pole/residue models. The antennas investigated fall in three categories: resonant, broadband, and frequency-independent antennas. There are distinct differences among the three classes of antennas in terms of modeling aspect.

The resonant structure is characterized by poles with low damping coefficients, which reflect in sharp peaks that are characteristic for the resonant structure. The resonant structure, monopole antenna, can be modeled with one dc pole and additional poles representing resonant frequencies close to the $j\omega$ axis. The second layer of poles models the effects in between resonant frequencies.

Poles with high damping coefficients, which reflect broad peaks, characterize the broadband structures. The wideband structures (e.g. TEM Horn and bi-conical antenna) can be modeled with a dc pole, a first resonant frequency pole, and additional high damping coefficient poles.

The minimal model analysis shows that the time-domain requires only a few poles to model the response for the TEM Horn, the 1.0 GHz resonant monopole, and the bi-conical antenna. However, the frequency domain requires a significant number of poles in order to accurately describe the response of a resonant structure; significantly fewer poles are needed for broadband structures. This suggests that most of the pulse energy is contained within the lowest resonant antenna frequencies in the time-domain responses. Higher order poles only model small variations of the time-domain realized effective length.

The frequency independent antenna, Archimedean spiral, can be modeled by a series of poles very closely spaced, a damped coefficient less than 1.5 G/s, with a behavior $\sigma(j\omega) \sim A\sqrt{\omega}$. These types of antennas require a large number of poles (34 poles or fewer) to model both time and frequency-domain realized effective length.

In conclusion, for time-domain base systems a few poles are often adequate to model the antenna response, except for the class of frequency independent antennas. Frequency-based resonant antennas require more poles. Broadband antennas require few poles in both the time and frequency domain. In Chapter 6, we will generate antenna patterns from pole/residue antenna model.

References

[5.1] R. Mittra, “Integral Equation Methods for Transient Scattering,” in *Transient Electromagnetic Fields*, pp. 73-128.

[5.2] M. L. Van Blaricum, R. Mittra, “A Technique for Extracting the Poles and Residues of a System Directly from Its Transient Response,” *IEEE Trans. Antennas Propagat.* , vol. 23, No. 6, pp. 777-781, Nov. 1975.

Chapter 6

Frequency Domain Pattern Synthesis from the Pole/Residue Antenna Models

The frequency-domain antenna pattern is obtained from the realized time-domain effective length pole/residue model. The Vivaldi antenna was used to prove this concept since the frequency-domain pattern data existed for a wide range of frequencies. The results show that once the residues and poles are known, the frequency-domain pattern can be obtained for any arbitrary frequency. To our knowledge, this concept is demonstrated for the first time. The work presented discusses trade offs concerning the size of the pole model and accuracy of the frequency domain patterns. The antenna pattern representations in both time and frequency domains are also discussed.

6.1 Pattern Synthesis from the Antenna Realized Time-Domain Effective Length Pole/Residue Model

By extracting the frequency-domain pattern from the antenna realized time-domain effective length pole/residue model one can obtain a simple representation that with few parameters describes the antenna radiation properties in both the time and frequency domain. The pole/residue modeling is based on measurements using the Vector Network Analyzer HP8510. The basic concept views the received waveform as [2.1]

$$\frac{v_r(j\omega)}{v_t(j\omega)} = \iint_{\Omega_t\,\Omega_r} \frac{j\omega\mu}{Z_0}\vec{h}_{Rr}(\theta_r,\phi_r,j\omega)\cdot\vec{C}(\theta_r,\phi_r,\theta_t,\phi_t,j\omega)\cdot\vec{h}_{Rt}(\theta_t,\phi_t,j\omega)\cdot\frac{e^{-j\beta r}}{4\pi r}\,d\Omega_r d\Omega_t\,, \tag{6.1}$$

where $d\Omega_t d\Omega_r$ represents the integration over receive and transmit solid angles with $\vec{C}$ representing the channel response. In Eq. (6.1), $\vec{h}_{Rr}$ and $\vec{h}_{Rt}$ represent the realized effective lengths of the receive and transmit antennas, respectively. The realized effective length includes the impedance mismatch not normally included in this term. The line-of-sight (LOS) link response in the time domain is given by [2.1]

$$v_r(t) = \frac{\mu}{Z_0}\frac{1}{4\pi r}\frac{\partial}{\partial t}\left[\vec{h}_{Rr}(\theta_r,\phi_r,t)\overset{\bullet}{\otimes}\vec{h}_{Rt}(\theta_t,\phi_t,t-r/c)\otimes v_t(t)\right] \tag{6.2}$$

where the notation $\overset{\bullet}{\otimes}$ indicates a dual dot product and time-convolution operation.

One has to note that by performing the s_{21} measurements, one measures the combined effects of the transmit/receive antennas and a channel as indicated in Eq. (6.1). The realized effective length of a single antenna may be obtained by using two identical antennas or a known reference antenna. Once the realized effective length of the single antenna is obtained, one can obtain a pole and residue approximation using the Matrix-Pencil method or an equivalent pole and residue extraction technique. The realized effective length can be described in terms of poles and residues in both time and frequency domains with the same set of parameters as outlined in Chapter 5. The representation of the realized effective length in terms of poles and residues is

$$\vec{h}_R(\theta,\phi,j\omega) = \sum_n^N \frac{\vec{R}_n(\theta,\phi)}{-s_n + j\omega} \tag{6.3}$$

$$\vec{h}_R(\theta,\phi,t) = \sum_n^N \vec{R}_n(\theta,\phi)e^{s_n t} \ . \tag{6.4}$$

Eq. (6.3) and (6.4) indicate that once the poles s_n and residues $\vec{R}_n(\theta,\phi)$ are determined it is easy to obtain the realized effective lengths in both time and frequency domain for an arbitrary direction. The factor N represents the total number of poles used. The poles come in complex conjugate pairs or negative real values in order to represent a real function. Thus, the actual number of frequencies present in the model is $N/2+k$[16]. Also, the poles are independent of the direction. Thus, the same set of poles is present in all of the directions.

If one observes the expression for the antenna radiated electric field in terms of the realized effective length

$$\vec{E}_{rad}(\theta,\phi,j\omega) = j\omega\mu\frac{e^{-j\beta r}}{4\pi r}I_t\vec{h}_R(\theta,\phi,j\omega)\,, \tag{6.5}$$

one can conclude that the antenna radiated electric field is proportional to the realized effective length and it is possible to extract the antenna frequency domain pattern for each frequency of interest. Once all the residues for the azimuth and elevation plane are obtained, one can reconstruct the frequency-domain patterns for an arbitrary frequency as follows:

$$\vec{h}(\theta,\phi,j\omega) = \sum_m \frac{\vec{R}_m(\theta,\phi)}{-s_m + j\omega}\,. \tag{6.6}$$

The pattern is the combination of all the residues and set of poles. The poles used in pattern calculations are the poles obtained from the boresight direction. Usually, one needs to associate the poles for different antenna directions in order to have a correct set

---

[16] k represents the number of poles in a model that are located on the σ axis. These poles model the antenna response below the fundamental frequency.

of poles to represent the antenna system. This association is required due to experimental error. As an alternative, the poles obtained from the boresight direction may be used for all directions, with care taken not to miss some poles that may not be represented adequately at the boresight. The poles obtained from the boresight measurement using the Vivaldi antenna provided a good set.

The time-domain antenna pattern can be obtained from the following expression:

$$\vec{h}_R(\theta,\phi,t)=\sum_n \vec{R}_n(\theta,\phi)e^{s_n t}\ . \tag{6.7}$$

This type of modeling is a very convenient way of describing the antenna system since only poles and residues are required to have a complete antenna characterization. Next, we will present a measurement setup and the procedure for obtaining the realized effective length of the antenna for different azimuth angles in order to extract the antenna frequency domain pattern. The measurement setup for measuring the antenna realized effective length and pattern directly in the frequency domain will also be discussed.

6.2 Antenna Pattern Measurements using a Vector Network Analyzer

The antenna pattern measurements are usually done using frequency-domain techniques by doing far-field and near-field measurements in the anechoic chamber or outdoor ranges. The frequency-domain measurements are performed mostly using a vector network analyzer. The time-domain measurements are preformed using a similar setup but measurements are performed using a pulse generator and a sampling oscilloscope [6.1].

The Vivaldi antennas were measured using two different setups. The Vivaldi antenna was used to prove this concept since the frequency-domain pattern data existed for a wide range of frequencies. Also, the Vivaldi antenna was used due to an integrated balun, which eliminated difficulties caused by using large ground planes in order to eliminate the balun structure.

The first type of measurement was performed using the vector network analyzer outside the anechoic chamber. The data was preconditioned by transforming it to the time-domain and windowing out the multi-path components in order to obtain a time-domain realized effective length of the antenna. Once the realized effective length was obtained for different antenna orientations, the frequency-domain patterns can be obtained using the Matrix-Pencil method (MP) and Eq. (6.4). The second set of measurements was performed using a near-field scanner (five foot model from Antcom®, Inc.). This setup measures the antenna pattern directly in the frequency domain.

The measurement setup used to measure two Vivaldi antennas outside the anechoic chamber is shown in Fig. 6.1. The distance between the reference planes of the measured Vivaldi antennas was 1.7925 meters. The antennas were measured in a laboratory room using a vector network analyzer. One antenna was stationary while the other antenna was rotated. The measurements were taken in the azimuth plane (Vivaldi antenna E-plane) at 5 degrees increments for all 360 degrees. For a complete characterization one needs to measure a complete sphere surrounding the antenna.

The measurement setup was elevated above the ground 74.3 cm. The measurement setup was elevated to avoid the reflections from the surrounding objects in the room (e.g. equipment rack, tables, computers). This particular arrangement provided significant multi-path from the ceiling reflection while all other reflections where significantly delayed in time. The reflections were delayed in time enough so they did not interfere with the main pulse radiated by antenna structure. Thus, one can apply a window in the time-domain in order to eliminate any multi-path components in the frequency-domain data set.

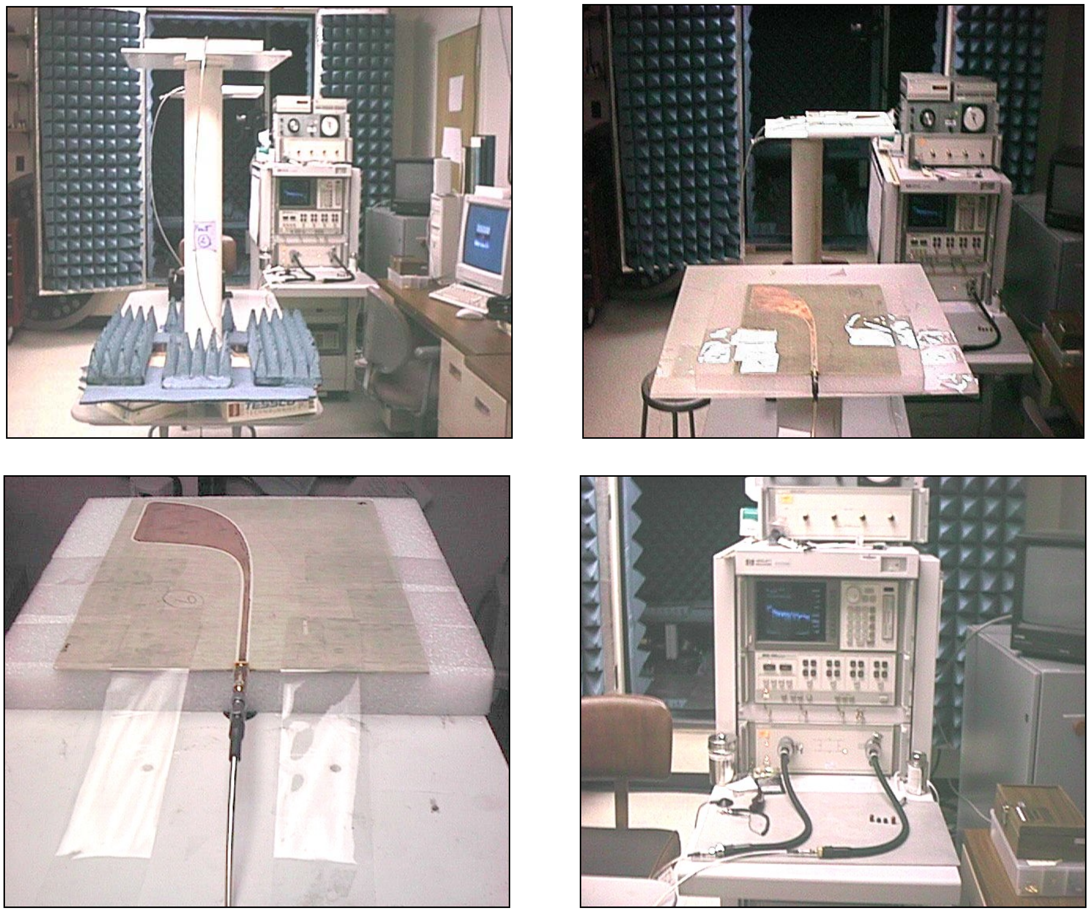

Figure 6.1. Measurement setup outside the anechoic chamber

The dimensions of the measurement setup are shown in Fig. 6.2. It was necessary to investigate major reflection points by calculating distances for the arrival times of line-of-sight components and all possible reflections. After examining the measurement setup it was concluded that the closest arrival time would have a reflection component from the ceiling. The height to the ceiling was about 92.4 cm. The reflected total path from the ceiling is about 2.56 m while the line of sight is 1.7985 m. If the distances are converted to time the line of sight component arrives after 5.9 ns while the multi-path component will arrive after 8.5 ns. Thus, the time difference is 2.6 ns. The time difference of 2.5 ns was used in choosing the time window for modeling purpose. The multi-path introduces asymmetries in antenna patterns and causes difficulties in modeling particular data using the Matrix-Pencil method.

It is also important that a multi-path component arrives after the main pulse (consisting of only antenna features) in order to have a correct characterization of the antenna structure. The monopole antenna would be an example where a diffraction of the leading edge (a reflection component) arrives at the same time the main pulse arrives. The back reflection, diffraction of a back edge, is visible since it is delayed in time (see Fig 3.9 in Chapter 3).

The multi-path component is not significant on the antenna boresight measurements. However, the multi-path becomes significant when an antenna is rotated since most of the radiation is directed towards the multi-path directions.

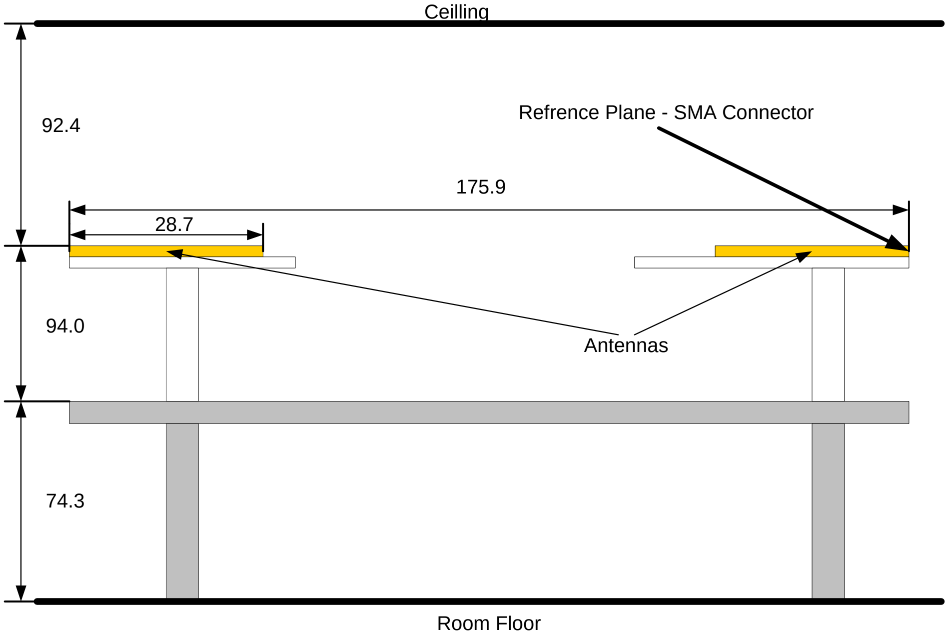

Figure 6.2. Measurement setup outside the anechoic chamber (all dimensions in cm)

The measurement setup shown in Figs. 6.1 and 6.2 was adjusted with the laser pointer. The laser pointer was used in order to set the calibration plane (SMA connector) as an antenna center of rotation/antenna phase center to the highest degree of accuracy possible.

Although some of the work has been done on analytically determining the antenna phase center usually the work is restricted to monopole antennas or aperture antennas [6.2,3]. The phase center in the frequency-domain measurements is not critical, as long the sphere surrounding the antenna is sampled fine enough, and it is determined by performing measurements, as is the case in the frequency-domain near-field measurements. Thus, an analytical approach to determine the phase center of the Vivaldi antenna was not attempted. The phase center of the antenna varies with frequency. In the case of the Vivaldi antenna the phase center for frequencies below 4.0 GHz is located closer to the antenna connector while for frequencies above 4.0 GHz the phase center is located at the aperture opening. Thus, by choosing the center of rotation at the antenna connector encompasses both low and high frequency patterns under the condition that the sphere surrounding the antenna is sampled finely enough. In fact, the starting point, distance *r* in Eq. (6.1), of the time-domain realized effective length indicates the location of the phase center. One can reconstruct the antenna frequency domain patterns above 4 GHz starting at the later times (e.g., 0.3 ns in Fig. 6.10). However, in order to reconstruct the patterns below 4 GHz one needs to start at 0 ns.

The realized effective length for an arbitrary azimuth angle was obtained by processing the measured frequency domain data as shown in Fig. 6.3. The measured data obtained by HP8510 was transformed in the time-domain and multi-path was windowed out by using a rectangular window; the time-domain data set was truncated before a multi-path component started to show. The window used was about 9.0 ns in duration. One has to note that by reducing the size of the data set in the time-domain the frequency resolution is reduced. However, the time-domain resolution always stays the same and it is defined by the highest measured frequency.

After the multi-path was eliminated the time-domain data was transformed back to the frequency-domain and divided by the realized effective length at the boresight in order to obtain the realized effective length at a particular angle. Once the frequency domain realized effective length was obtained, the inverse Fourier transform (IFFT) was performed to obtain the equivalent time-domain realized effective length. Using the poles obtained from the boresight direction, residues were calculated. This procedure was repeated for all 360 degrees in 5 degrees increments. Once all the residues were obtained the Vivaldi pattern was calculated using the Eq. (6.5).

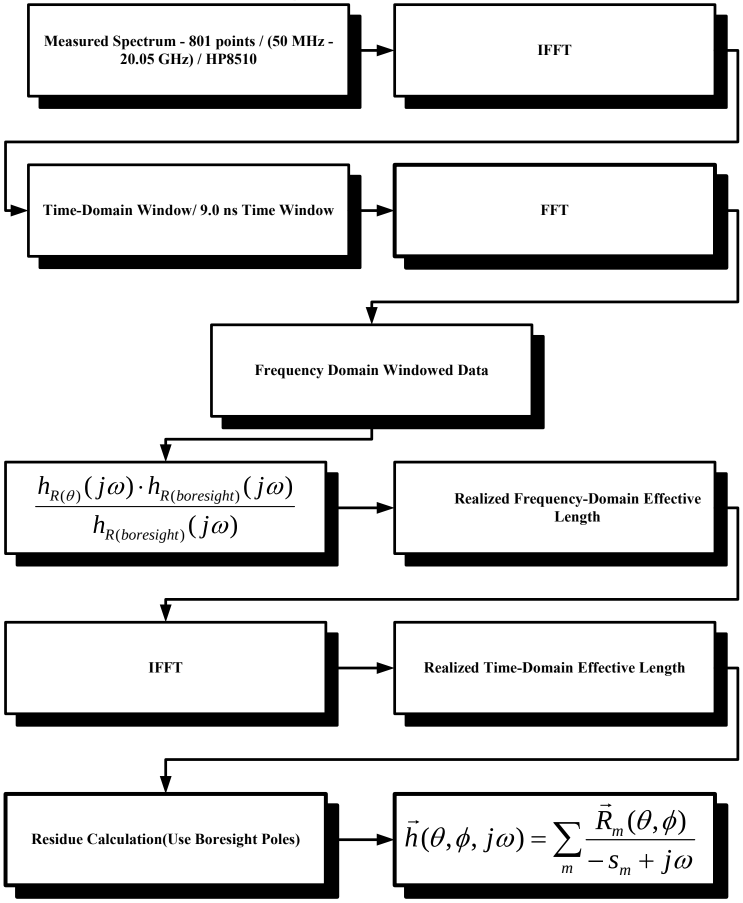

Figure 6.3. Data processing for pattern extraction from the time-domain realized effective length

Multiple IFFT/FFT transformations were required primarily to eliminate the multi-path. There is not a simple way to eliminate multi-path in the frequency domain. Thus, the inversion is required. In order to obtain a pole/residue model the MP requires a time-domain waveform. One solution to eliminate some of IFFT/FFT transforms would be to measure the waveform in the time-domain. Another solution is to process the data in the frequency domain (e.g. frequency domain Matrix- Pencil equivalent).

The Vivaldi antenna was measured inside the anechoic chamber using Antcom® near-field scanner. The measurement setup using the anechoic chamber is shown in Fig. 6.4. The AUT is placed on the positioner mast and rotated while the probe is stationary. Since the measurements are done at discrete frequencies different probes are used to cover particular frequency range. For the measurements in the range from 1.0–12.0 GHz five open waveguide probes were used. The software from Antcom collects the uncalibrated frequency-domain data at specified discrete frequencies from the HP8510. The data is collected at 5-degree increments in the azimuth plane (raw near-field data). The data is than displayed in the specified format. Antcom interpolates the points in between the measurements in order to generate data point for each degree in the azimuth plane (interpolated near-field data).

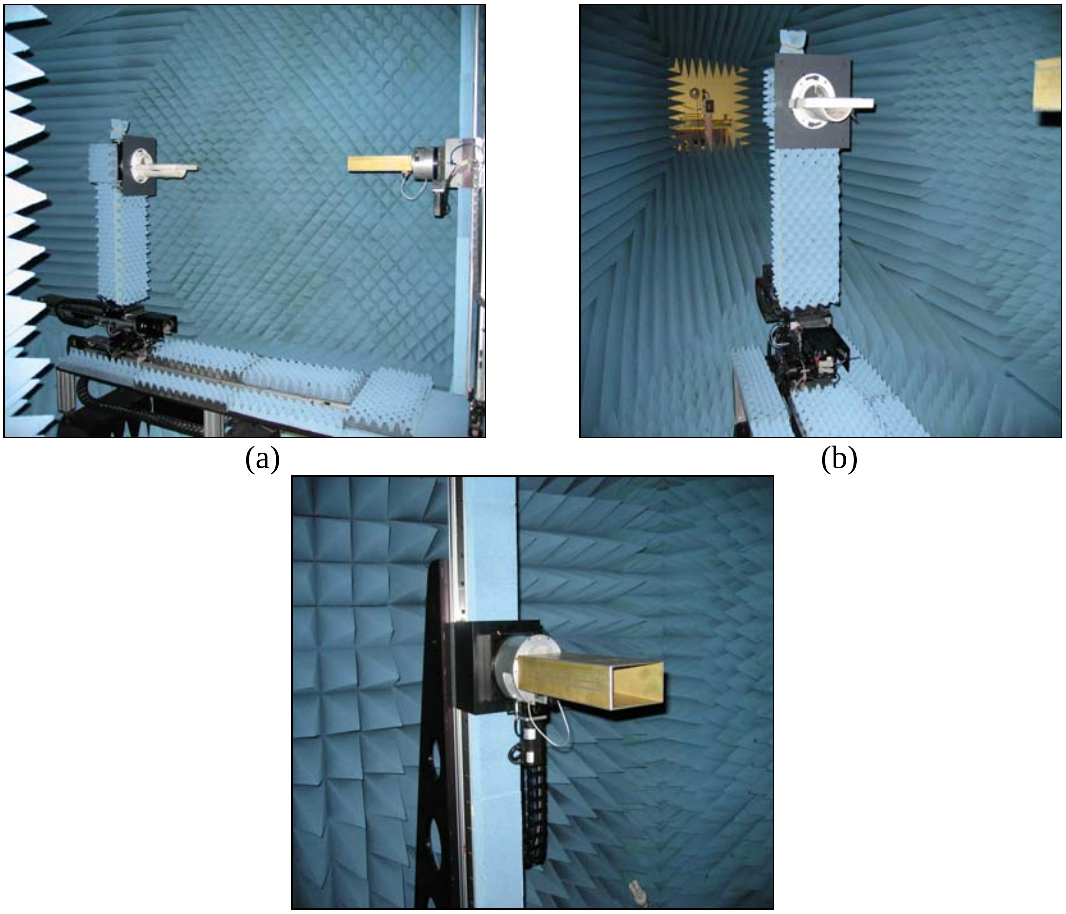
(a) (b)

(c)

Figure 6.4. Setup inside the anechoic chamber (a), antenna on the positioner mast (b), and the probe (c)

The near-field pattern measurements of the Vivaldi antenna shown in Fig. 6.5 show the variations among the raw near-field data, interpolated near-field data, and the simulated data using Fidelity [6.4]. The most notable differences in the pattern are at 1.0 GHz. The positioner mast, that antenna was placed on, certainly contributes to the differences in the back-lobe of the antenna pattern. Also some of the upper hemisphere differences could be contributed to the multi-path inside the chamber, since the absorbers inside the anechoic chamber have a limited performance at 1.0 GHz. For the antenna patterns from 2.1 GHz-12.0 GHz the variations are present at the backlobe due to a positioner mast. Also, variations are on the order of 1 to 3 dB, for angles 90 to 60 degrees, between simulated and measured near-field data.

In conclusion, one can notice the variations between raw/interpolated measured and simulated antenna patterns are around 1-3 dB in the upper hemisphere. In the lower hemisphere the measured results are different due to a positioner mast. However, the radiation pattern is around 12-20 dB (on average) down from the peak value. Thus, the lower hemisphere is not critical in antenna pattern evaluation. Next, two different time-domain antenna pattern representations will be presented.

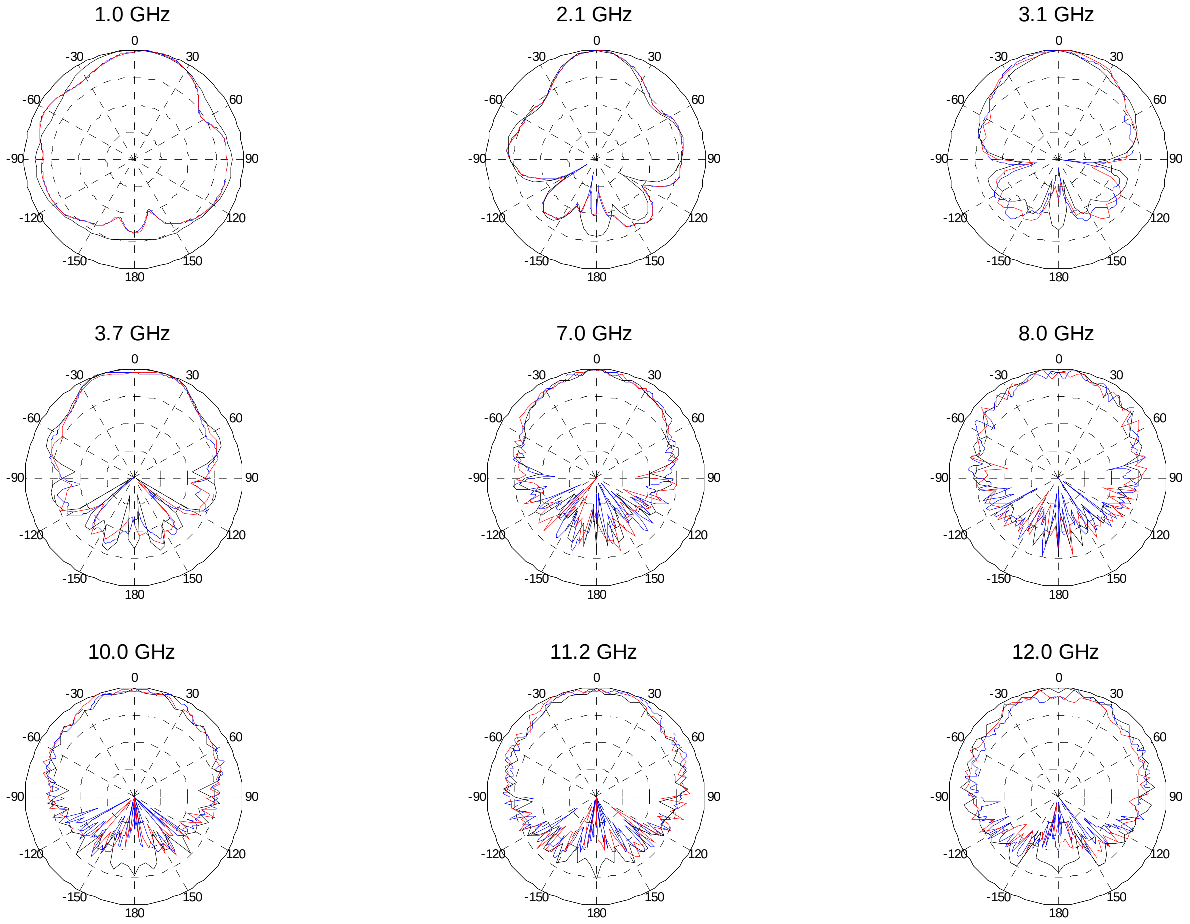

Figure 6.5. Comparison between raw near-field measurements (red), simulated using Fidelity (black), and near-field interpolated measurements (blue) – 10 dB/div.

6.3 Antenna Patterns -Time and Frequency Domain Representations

The antenna patterns could be described in both the time and frequency domain. The patterns in the frequency domain are usually shown as in Fig. 6.5. Each frequency is represented by unique pattern. The time-domain patterns can be displayed as peak time-domain realized effective length vs. angle as shown in Fig. 6.6. The antenna radiation characteristics in the time domain can be also represented as the realized time-domain effective length vs. angle. The latter representation is shown in Fig. 6.7.

The lower hemisphere, in Fig. 6.6, is not presented since the peak for the lower hemisphere is difficult to identify. One can notice from Fig. 6.7 that after 105 degrees the upper hemisphere peak is not distinguishable. Thus, it is not an accurate representation if one tries to represent the peak of the transient waveform. The correct representation would involve tracking the time where the boresight pulse occurs for all the antenna directions.

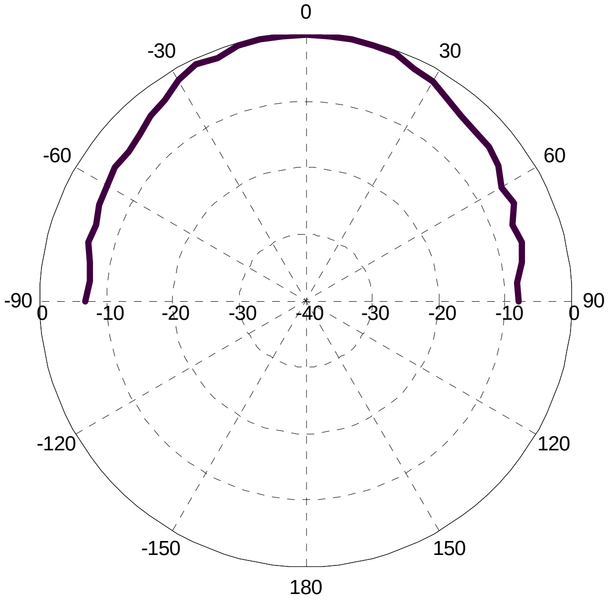

Figure 6.6. Vivaldi antenna measured peak realized effective length polar plot

The Vivaldi antenna peak transient plot shows the symmetry that is expected with this type of structure. The peak is located in the boresight direction. The antenna peak is decreased by 2.5 dB each 30 degrees reaching a value of –8 dB at the 90 degree angle.

The Vivaldi antenna transient pattern shown in Fig. 6.7 describes the antenna behavior in terms of the transient waveform for different azimuth angles. One can notice that the pulse is the strongest in the boresight direction. As the azimuth angle increases the pulse amplitude decreases. However, the general pulse shape is being preserved. One can notice that the early part of the waveform (duration of 0.3 ns), shown in Fig. 6.7, stays relatively constant throughout the transient pattern while the late part of the transient pattern changes in shape and amplitude.

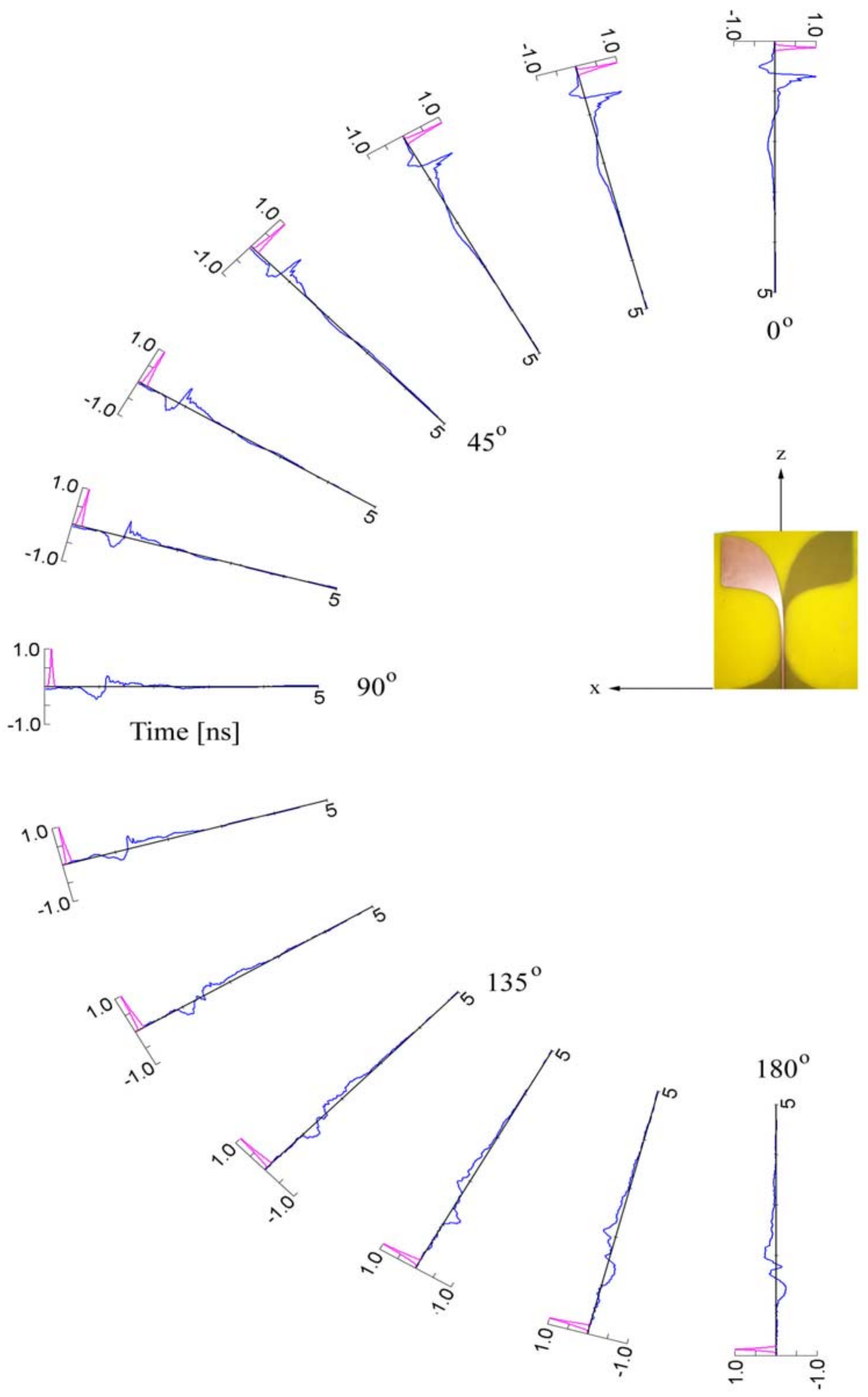

Figure 6.7. Vivaldi antenna transient pattern - measured realized time-domain effective length (blue) and incident pulse (magenta)

In order to have a complete antenna representation in both the time and frequency domains, different display formats need to be used. The antenna frequency domain pattern describes antenna radiation characteristics at the particular frequencies while the transient pattern shown in Fig 6.7 and peak transient pattern shown in Fig. 6.6 describes antenna radiation characteristics in the time domain.

Next, we will investigate the size of the pole/residue model in order to obtain frequency-domain antenna patterns. The patterns are obtained only for the E-plane in order to prove a concept. The pole models investigated are: 41-, 17-, and 4-pole model.

6.4 Pattern Synthesis using a Pole/Residue Model – 41 Pole/Residue Model

The Vivaldi antenna shows a “hybrid” type of operation compared to the monopole and TEM Horn antenna models. One can notice from Fig. 6.8 that the s_{21} response has approximately 20 features. These 20 features will result in the 40-pole/residue model. The SNR is better than 20 dB up to 18 GHz for the boresight direction.

The time-domain response shows a different response compared to that of the TEM Horn or the bi-conical antenna. The s_{21} time-domain response consists of a small initial peak followed by a larger amplitude peak and damped oscillations. The small amplitude oscillations beyond 9.0 ns are due to multi-path components.

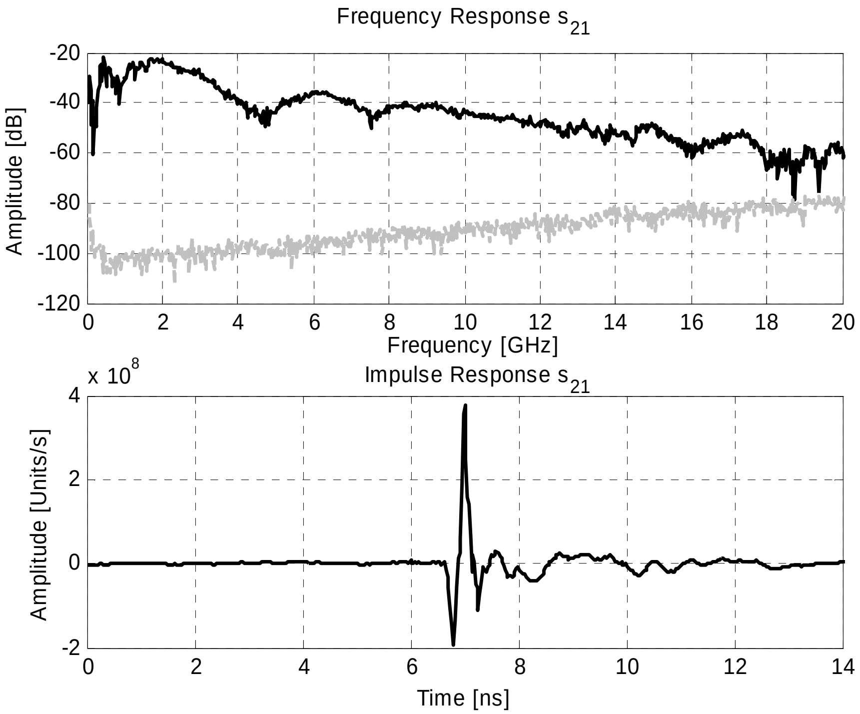

Figure 6.8. Measured s_{21} frequency response (black) vs. noise (grey) and corresponding s_{21} impulse response for a 2 Vivaldi antenna link

The singular value decomposition of the time-domain realized effective length is shown in Fig. 6.9. The 10th singular value is approximately 10 times smaller than the highest singular value. This indicates that the time-domain realized effective length can be represented by approximately 10 poles.

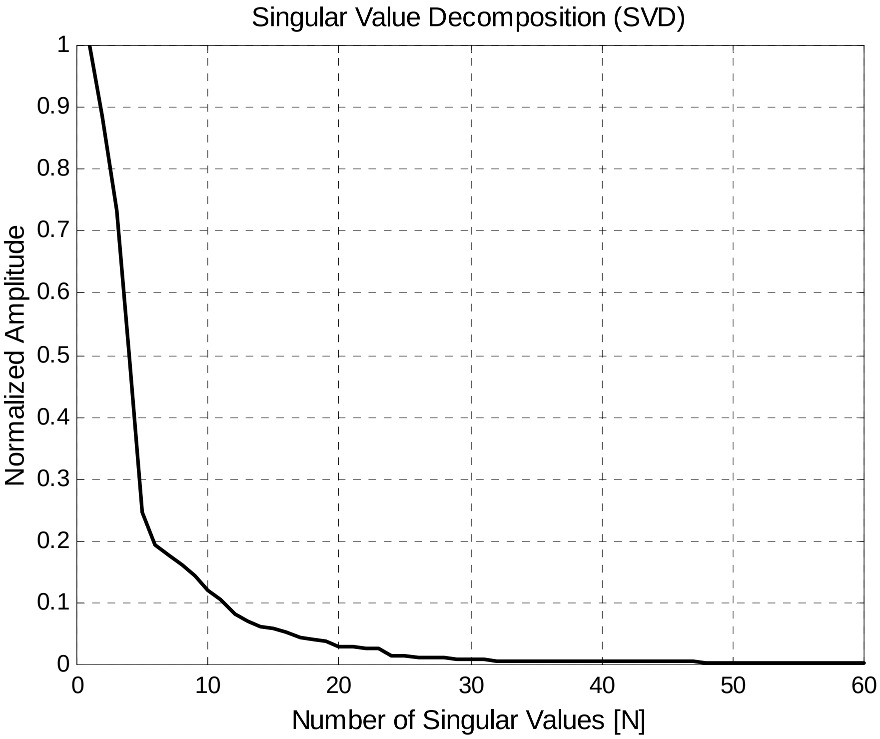

Figure 6.9. Singular value decomposition of a Vivaldi antenna time-domain realized effective length

The poles and residues were extracted using the Matrix-Pencil method (MP). The parameters used were: a time-domain window of 2.5 ns (*K*=100)[17], singular values greater than 0.002. The distance between the antennas used on the boresight was 1.8975 m.

The frequency-domain realized effective length is shown in Fig. 6.10. The 41-pole model shows a very good match up to 20.0 GHz. Few deviations are present between the model and the measured frequency-domain realized effective length. The frequency domain realized effective length is 20 dB down from the peak beyond 10.0 GHz. The phase is also represented very accurately up to 20.0 GHz in Fig. 6.10. The phase represents a distance, a time delay, which the pulse has to travel in order for radiation to occur.

The linear plot of the frequency domain and the time-domain realized effective length is shown in Fig. 6.11. The time-domain realized effective length is different from the one we are accustomed by TEM Horn and bi-conical antenna since it consists of the early part in the interval from 0 to 0.3 ns. The waveform past 0.3 ns is similar to the TEM

---

[17] 200.25 MHz resolution in the frequency domain

Horn and bi-conical structures. By including early time in duration of 0.3 ns, the pole model becomes more complicated. The late response (past 0.3 ns) can be modeled accurately up to 20.0 GHz with 17-pole model, which is not the case if early time is not included.

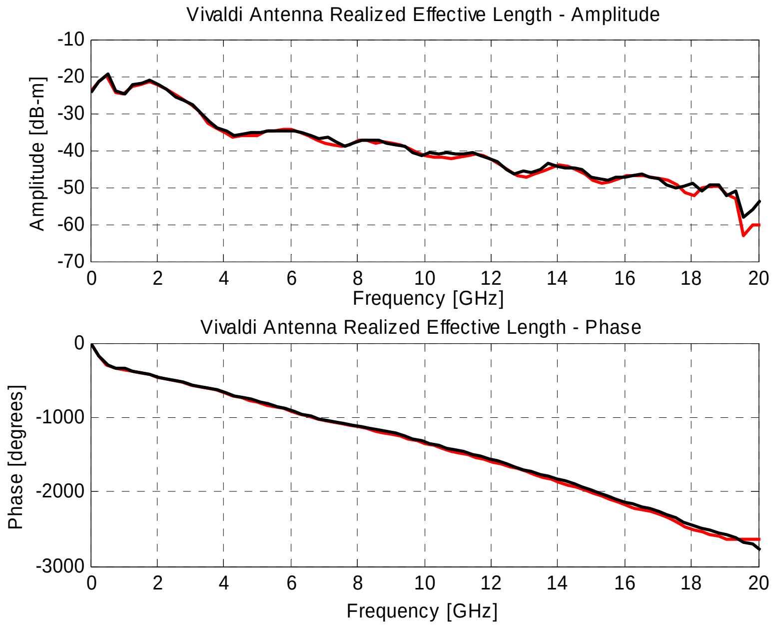

Figure 6.10. Comparison between 41-pole model approximation (red) and frequency-domain realized effective length (black)

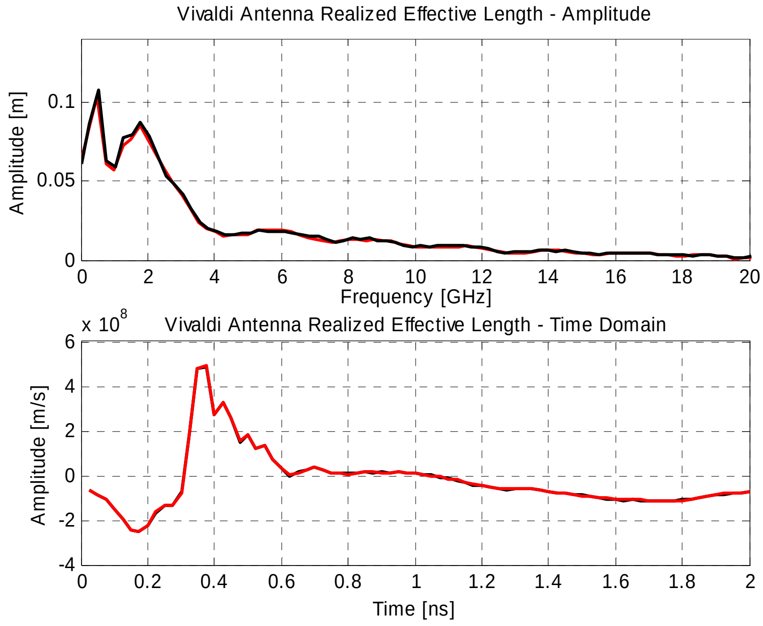

Figure 6.11. Frequency and time-domain realized effective length (black) vs. 41-pole model approximation (red)

However, if the early time, 0 to 0.3 ns, is not included one could not obtain the antenna patterns correctly since the early time has significant effects on the waveform in the frequency range of 1.0 to 4.0 GHz.

The pole/residue relationship is shown in Fig. 6.12. The first layer of poles (smaller than 0.2 G/s) is low in residues and damping coefficients while the second layer of poles (higher than 0.2 G/s) is higher in residue values and damping coefficients. This is different for the TEM Horn and bi-conical antenna where higher pole models have only a few poles with higher damping coefficients and residues.

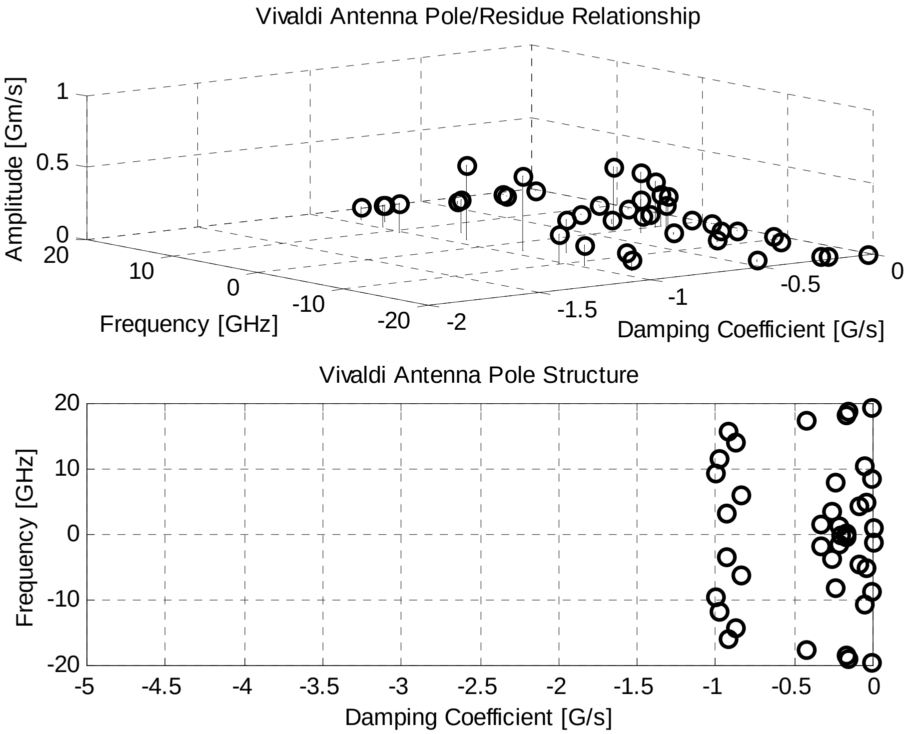

Figure 6.12. Pole/residue relationship and the pole structure for a 41-pole model

Next, we will discuss the pattern generation from pole and residue models. The same set of poles extracted from the boresight direction was used to calculate the residues for all the azimuth angles using Eq. (6.6). The patterns extracted from a 41-pole model are compared to interpolated near-field data (Fig. 6.13), raw near-field data (Fig. 6.14), and simulated data (Fig. 6.15).

The pattern variations for frequencies higher than 2.0 GHz, up to 45 degrees, show around 1 dB variation on average, both compared to simulated and near-field measurements. The pattern at 1.0 GHz is not in good agreement with the simulation or near-field measurements. The reasons for the deviation of the 1.0 GHz pattern are explained in the previous sections. The lower hemisphere shows variations which are due to the positioner mast when the measurements are performed inside the chamber. The raw near-field measurements show the same results. The simulations agree very well up to 60 degrees with the model. The lower hemisphere shows a deviation since the antenna was not simulated by considering the effects of the positioner and the anechoic chamber.

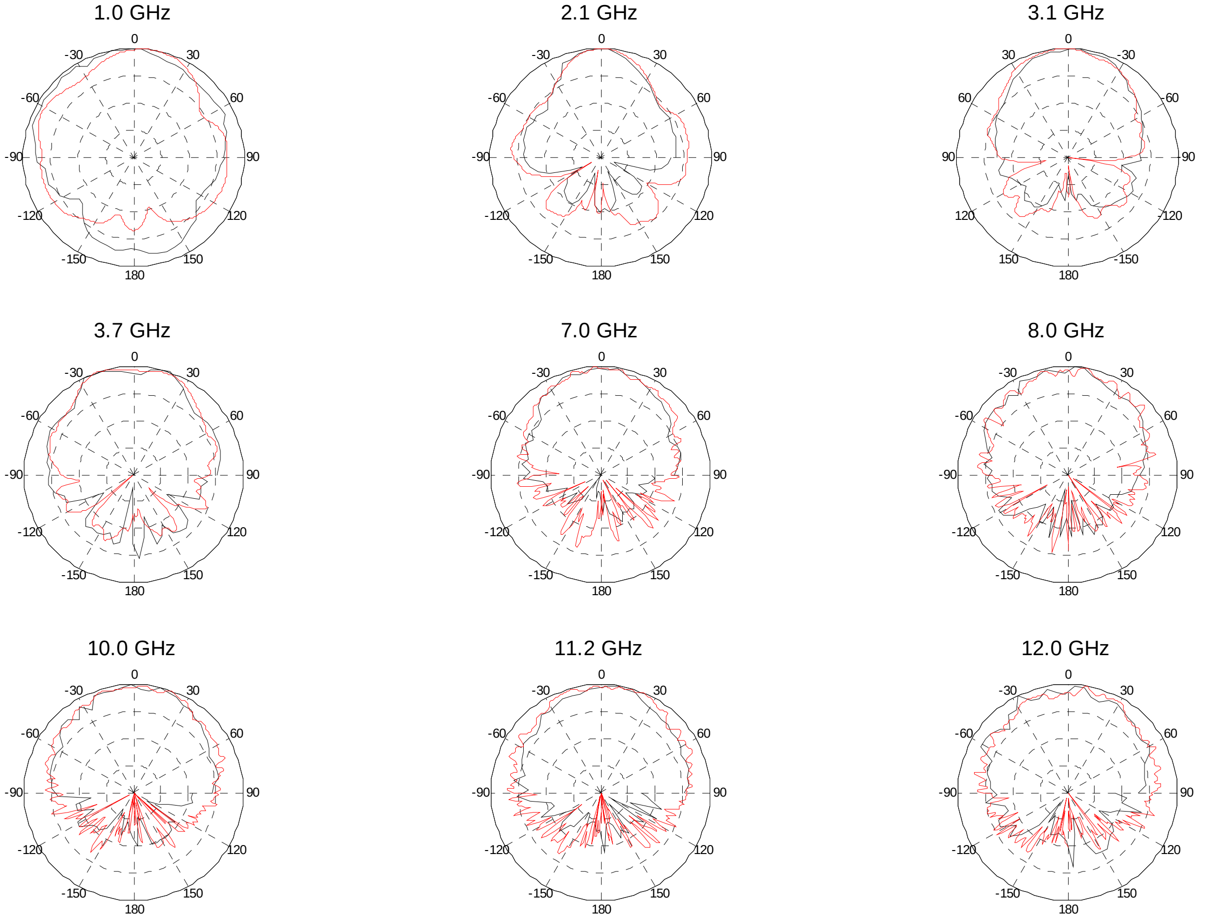
1.0 GHz

2.1 GHz

3.1 GHz

3.7 GHz

7.0 GHz

8.0 GHz

10.0 GHz

11.2 GHz

12.0 GHz

Figure 6.13. Patterns for the 41-pole model (black) compared to the interpolated near-field measurements (red) – 10 dB/div

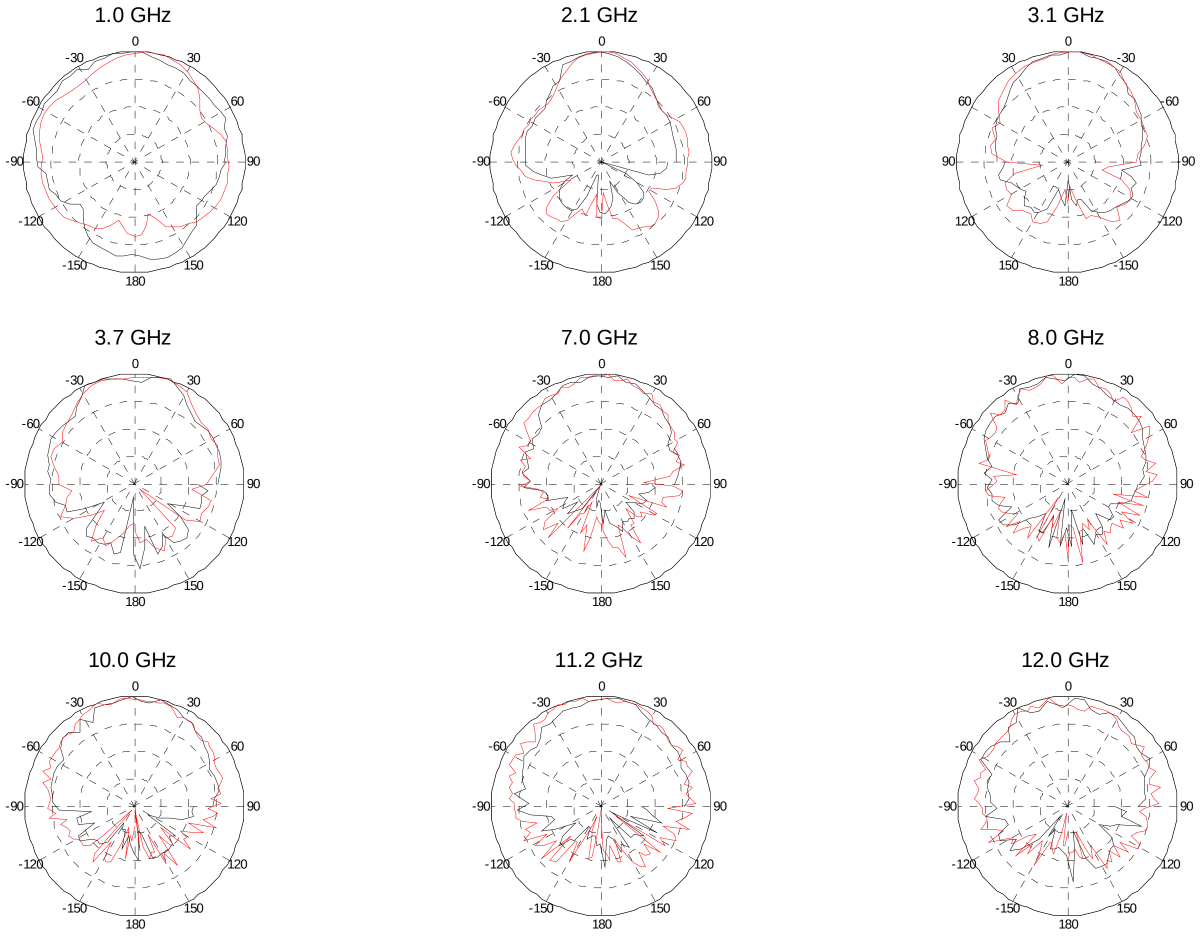

Figure 6.14. Frequency-domain patterns for the 41-pole model (black) compared to the raw near-field measurements (red) -10 dB/div

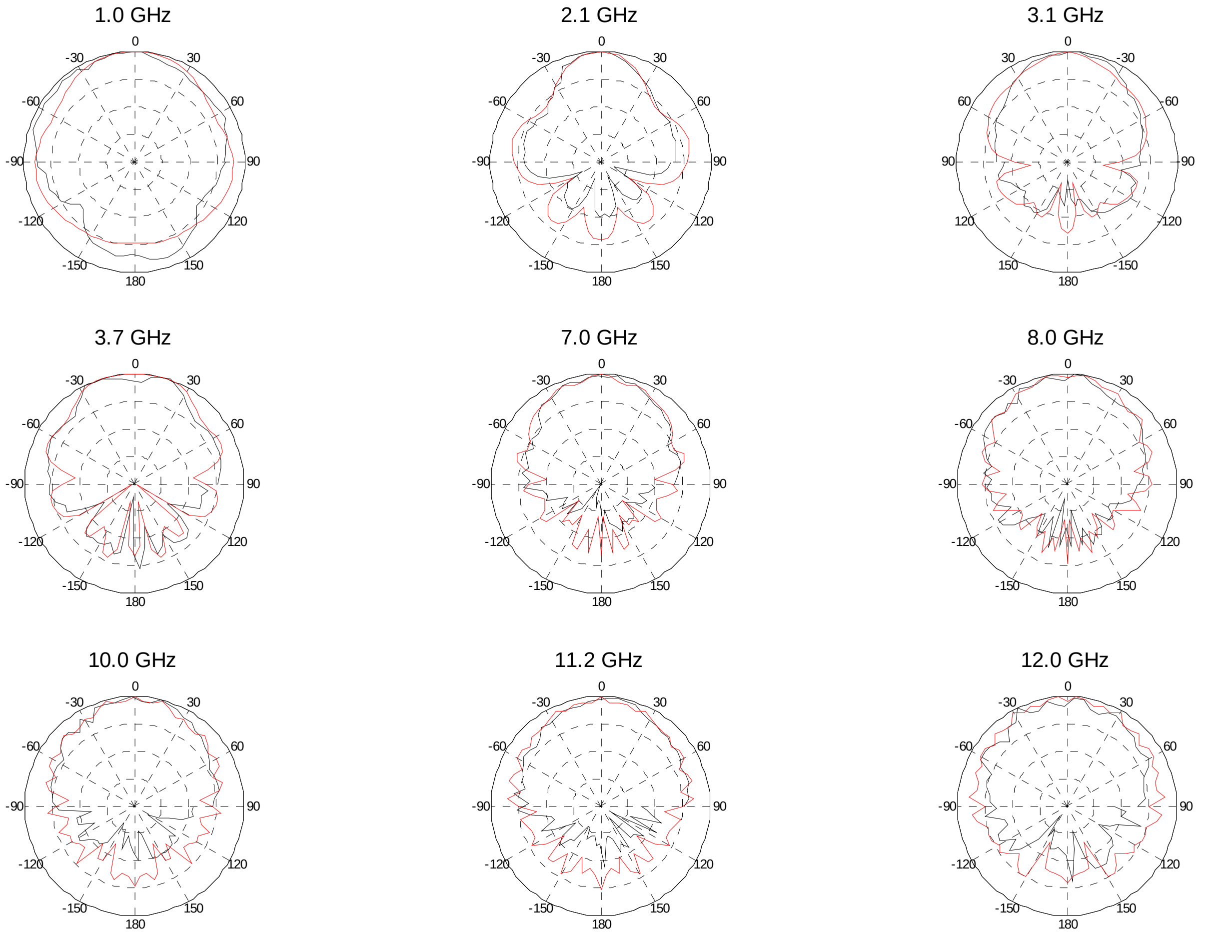

Figure 6.15. Patterns for the 41-pole model (black) compared to the simulated data using Fidelity [6.4] – 10 dB/div

6.5 Pattern Synthesis using a Pole/Residue Model – 17 Pole/Residue Model

The 17-pole model was obtained by restricting the measured data to the singular values that are 0.01 and higher compared to the peak singular value. The distance between antennas used in the boresight direction was 1.8975 m. The time-domain window used was 2.5 ns in duration.

The frequency-domain response is shown in Fig. 6.16. The boresight model shows a very good match up to 10.0 GHz and a marginal match up to 12.0 GHz. The phase also shows very good match up to 12.0 GHz.

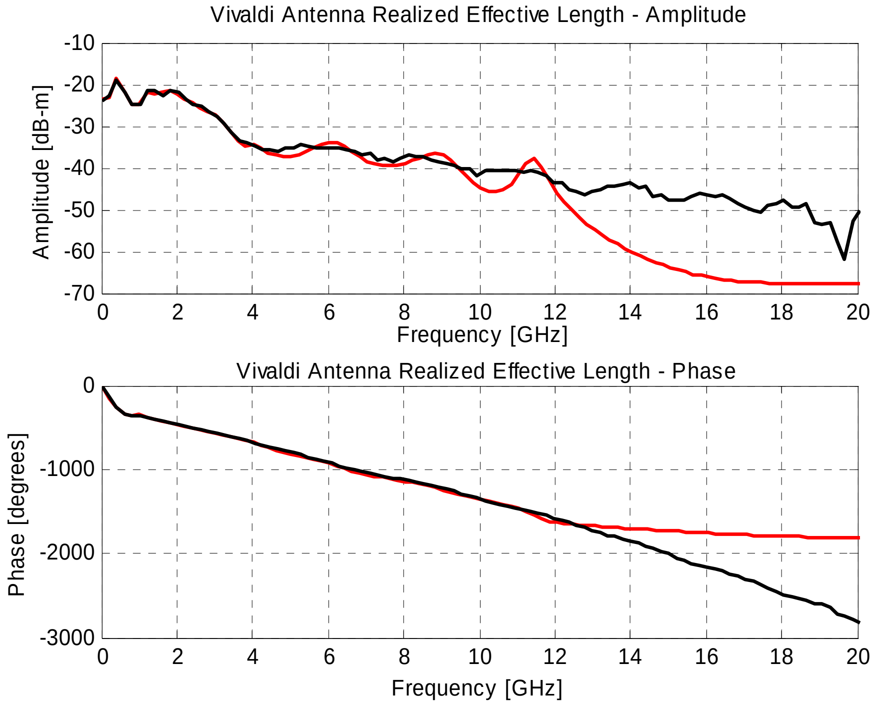

Figure 6.16. Comparison between 17-pole model approximation (red) and the frequency-domain realized effective length (black)

The time-domain waveform and 17-pole model approximation is shown in Fig. 6.17. The 17-pole model shows a very good agreement with the measured time-domain realized effective length. The pole/residue relationship plot shows that high frequency poles are not present as in the 41-pole model. The plot also shows that the second layer poles (damping coefficient higher than 0.5 G/s) are the dominant poles for the Vivaldi antenna. The low frequency pole (dc) and first resonant pole are dominant in terms of residue values.

The 17-pole model shows a good agreement to near-field patterns up to 70 degrees (1 dB of variation) in Figs. 6.19 and 6.20. The variations of 2-3 dB are present below 70 degrees. The simulations also show good agreement in the upper hemisphere (Fig. 6.21). The lower hemisphere is not represented very accurately due to the positioner mast.

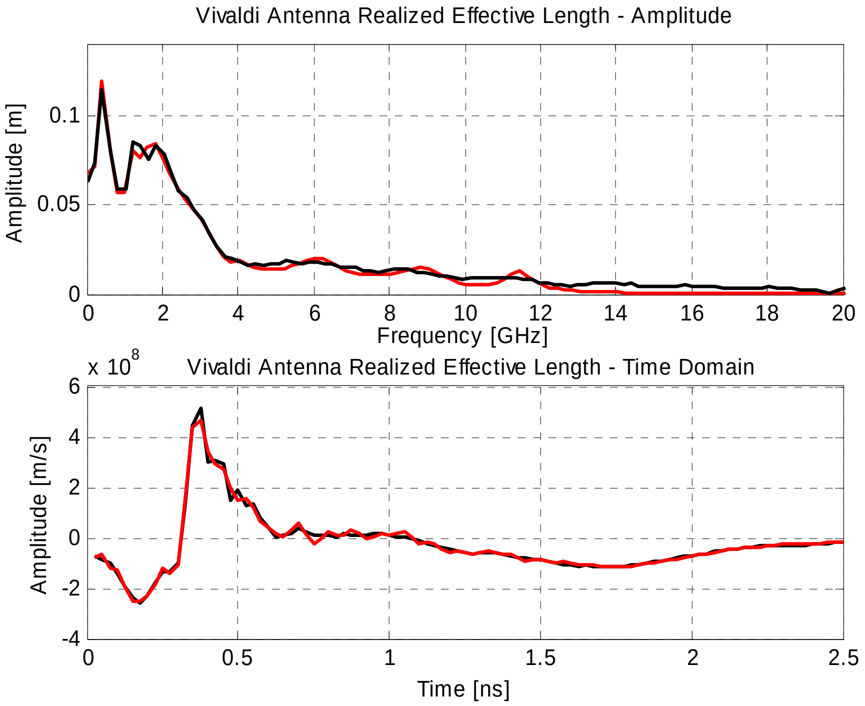

Figure 6.17. Frequency and time-domain realized effective length (black) vs. 17-pole model approximation (red)

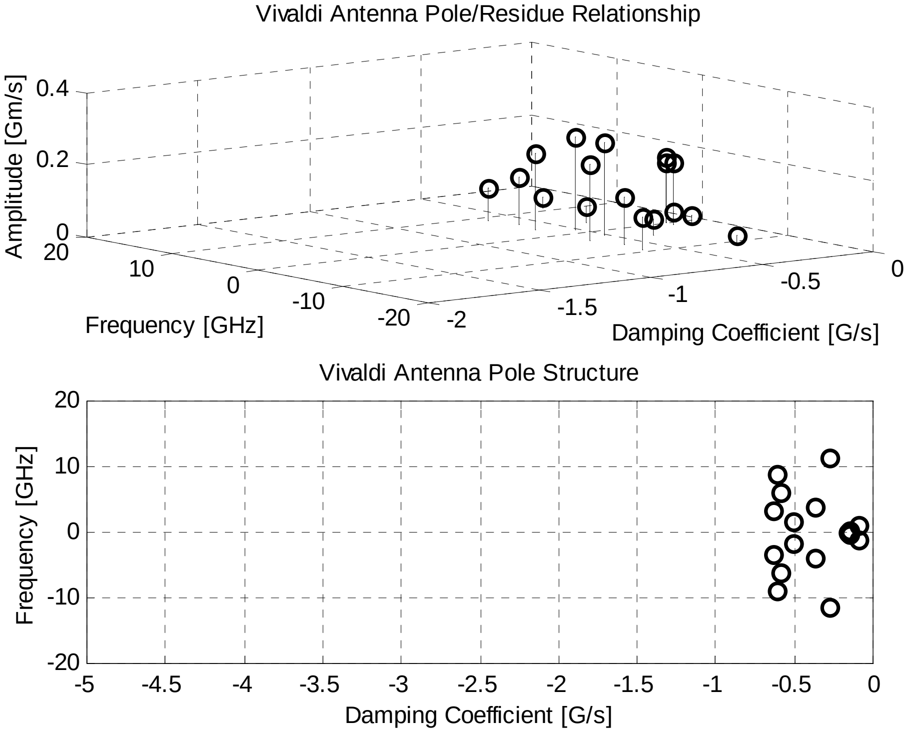

Figure 6.18. Pole/residue relationship and pole structure for a 17-pole model

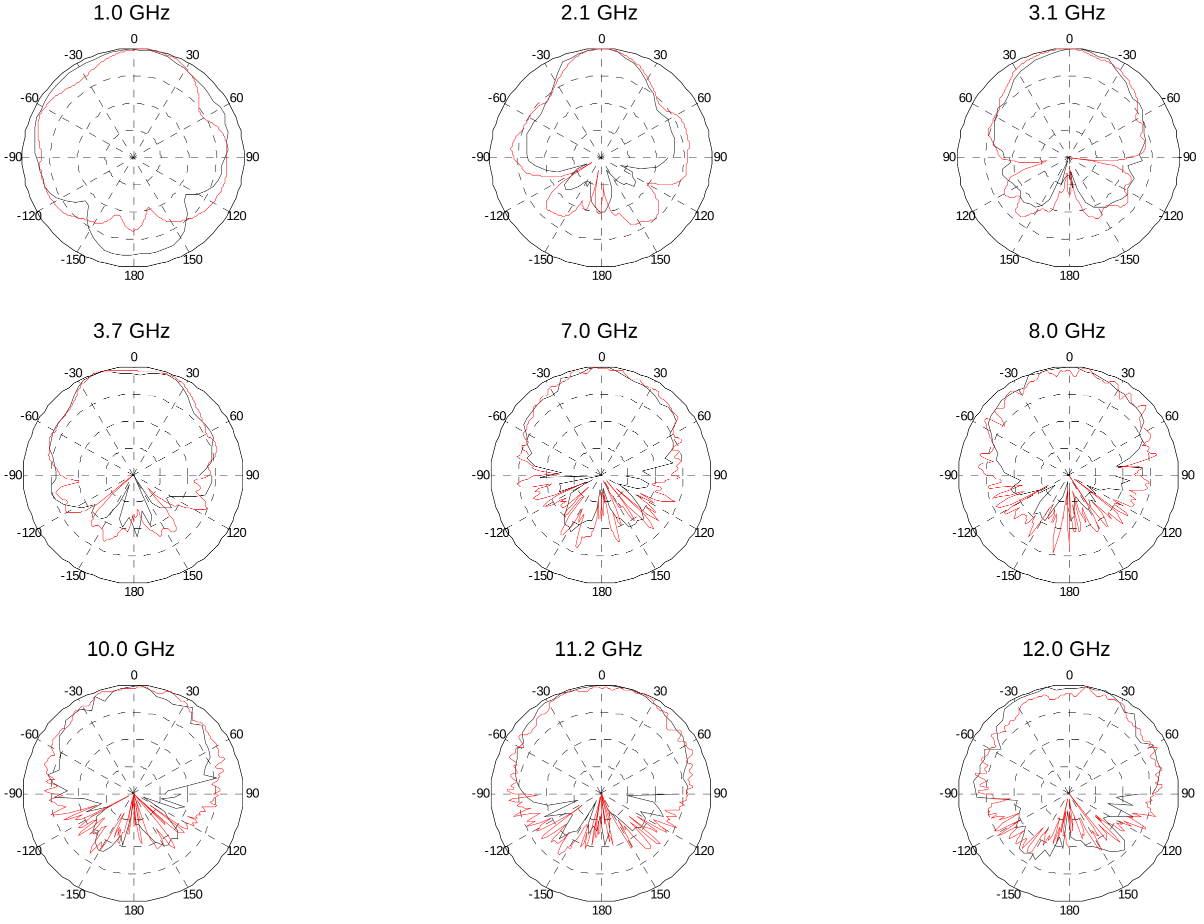

Figure 6.19. Patterns for the 17-pole model (black) compared to the processed near-field measurements (red) – 10 dB/div

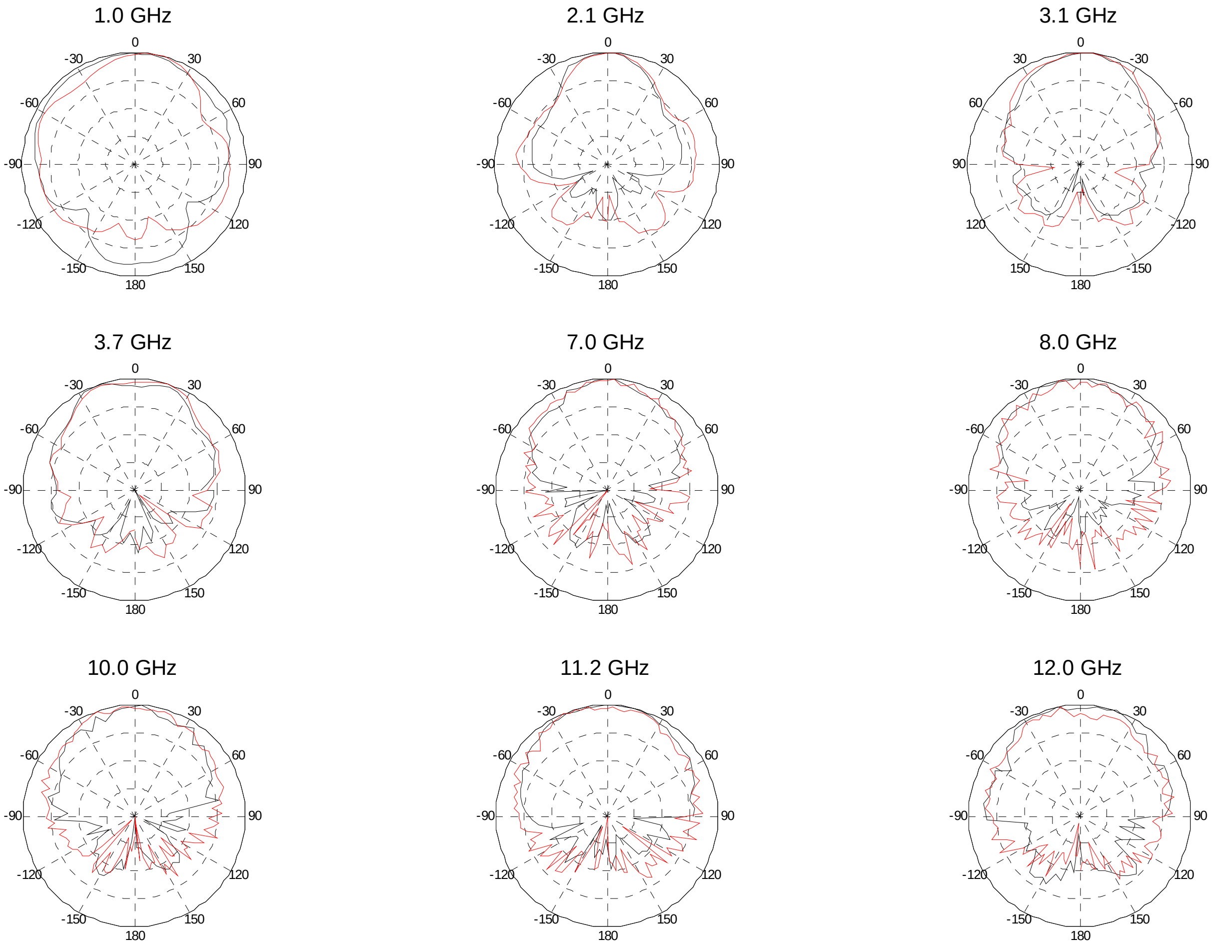

Figure 6.20. Patterns for the 17-pole model (black) compared to the raw near-field measurements (red) – 10 dB/div

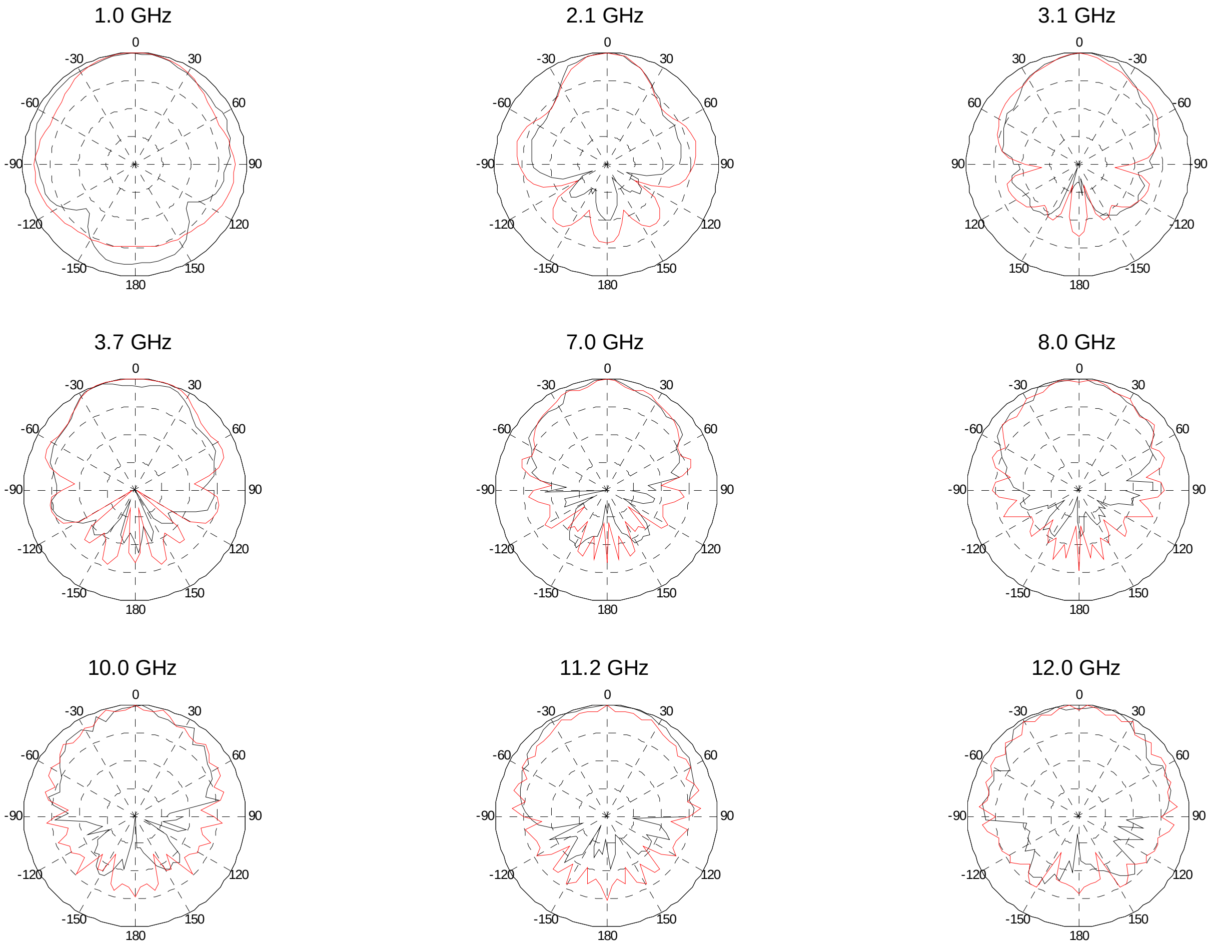

1.0 GHz

2.1 GHz

3.1 GHz

3.7 GHz

7.0 GHz

8.0 GHz

10.0 GHz

11.2 GHz

12.0 GHz

Figure 6.21. Frequency-domain patterns for the 41-pole model (black) compared to the simulated data using Fidelity [6.4] – 10 dB/div

6.6 Pattern Synthesis using a Pole/Residue Model – 4 Pole/Residue Model

The 4-pole model is obtained by restricting the data to the singular values that are larger than 0.08 compared to the peak value. The time-domain window used was 2.5 ns in duration. The distance between antennas was 1.8975 m.

The frequency-domain shows a reasonable match up to 3.0 GHz in Fig. 6.22. The lower frequencies up to fundamental resonant frequency are not represented correctly. The phase shows a good match up to 3.0 GHz.

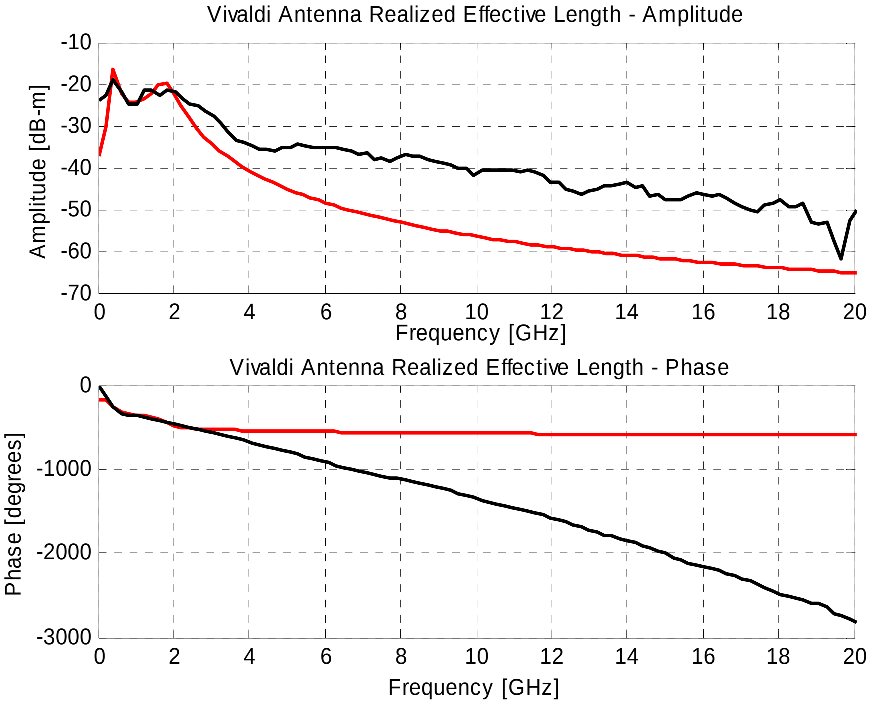

Figure 6.22. Comparison between 4-pole model approximation (red) and the frequency-domain realized effective length (black)

The time-domain match predicts the basic time-domain waveform oscillation but it is not very accurate in peak prediction, as shown in Fig. 6.23. The pole residue relationship shown in Fig. 6.24 shows four dominant poles at 400 MHz and 1.8 GHz. The 1.8 GHz pole set shows higher residue amplitude.

The patterns generated, using 4-pole model, are shown in Fig. 6.25. The patterns are compared to raw, interpolated, and simulated data. The 4-pole model data is shown for only the upper hemisphere. It is evident that a 4-pole model is not adequate to represent the antenna patterns. The 4-pole model shows marginal match at 3.0 GHz, which is expected since the model on the bore-sight approximates the realized effective length up to 3.0 GHz.

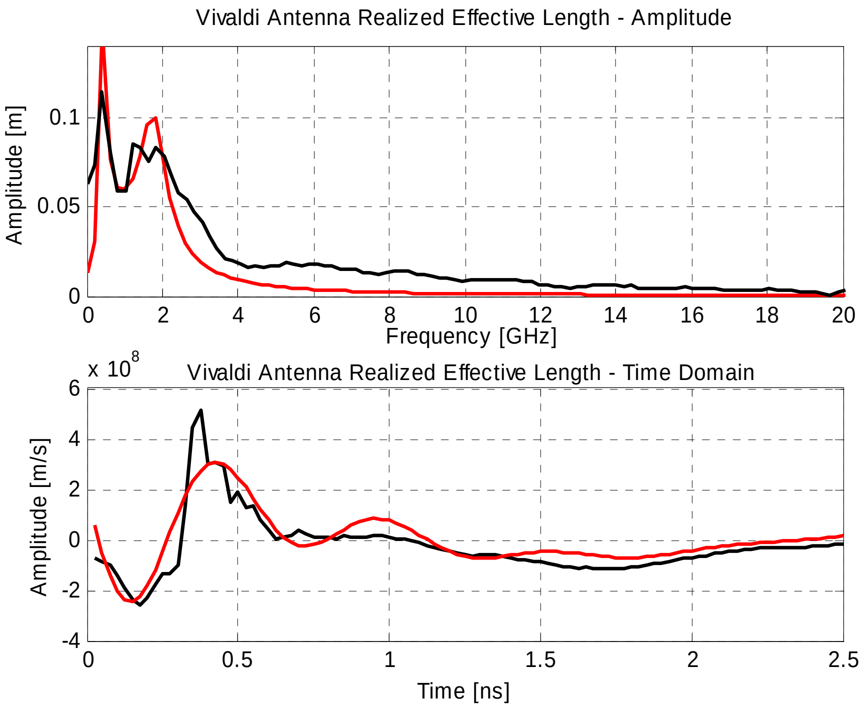

Figure 6.23. Frequency and time-domain realized effective length (black) vs. 4-pole model approximation (red)

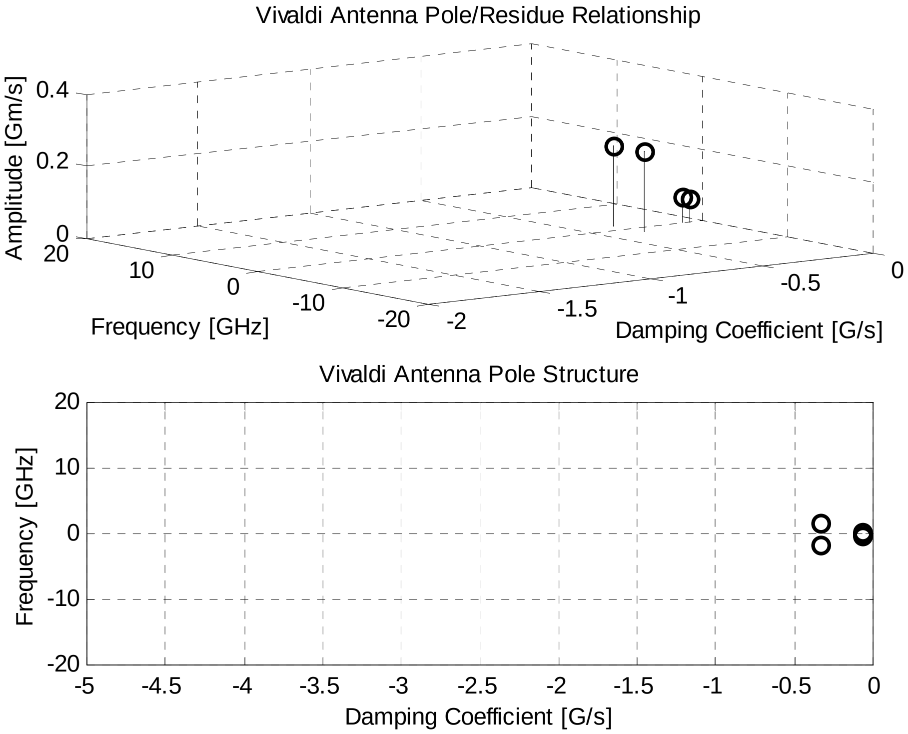

Figure 6.24. Pole/Residue relationship and pole structure for a 4-pole model

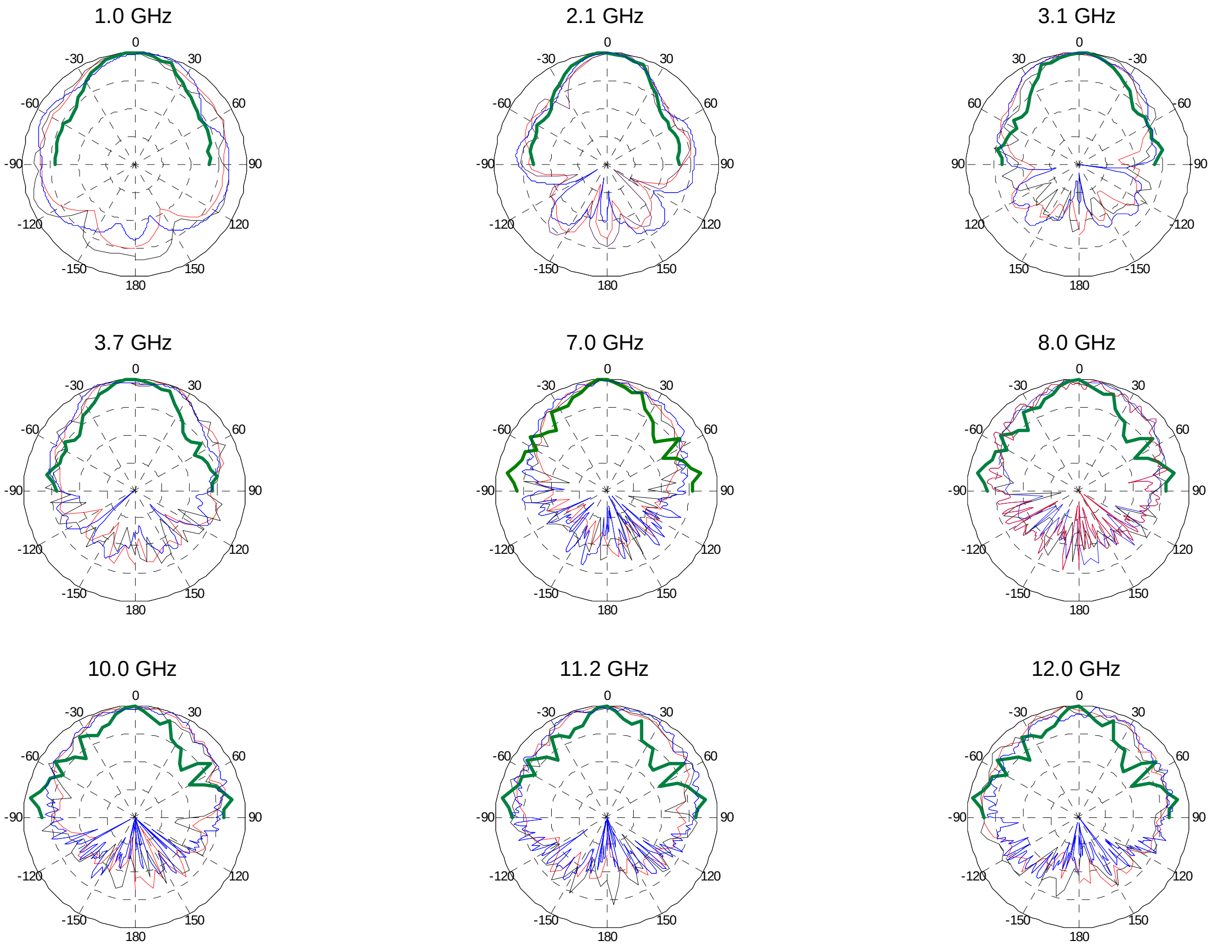

Figure 6.25. Patterns compared to the near-field measurements and simulations [6.4] for a 4-pole model – 10 dB/div

6.7 Comparison between Pole/Residue Models

The measured Vivaldi antenna, as mentioned previously, exhibits a “hybrid” operation compared to the TEM horn and monopole antennas. A broadband antenna (e.g. TEM Horn, bi-conical antenna) is characterized by a low frequency pole (usually real pole on the sigma axis), a fundamental resonance pole, and two additional poles with high residue and damping coefficient values (up to 20 GHz observation). However, the Vivaldi antenna (broadband antenna in nature) exhibits multiple high damping/residue poles.

The 4-pole model exhibits two dominant frequencies at 400 MHz and 1.8 GHz. The 400 MHz pole models the low frequency response (below the fundamental resonance), while the 1.8 GHz pole is a fundamental resonant pole. By increasing the pole model, the response is dominated by high damping coefficient poles that are lower in residue compared to fundamental pole but significantly higher compared to poles closer to jω axis. The high damping coefficient poles are: 3.2 GHz, 6.1 GHz, 8.9 GHz, and 11.8 GHz. These frequencies correspond to distinct features of the s_{21} response. The pole/residue relationships for different models are illustrated in Fig. 6.26.

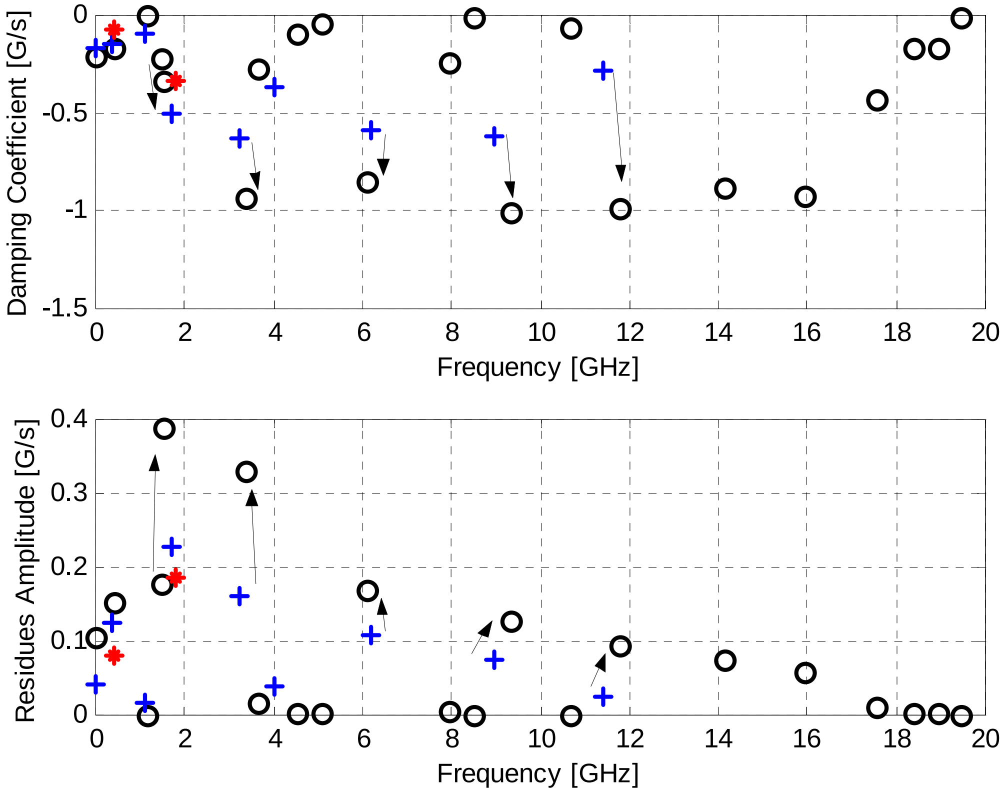

Figure 6.26. Pole/residue comparison for different models: 4-pole model (*), 17-pole model (+), and 41-pole model (o)

In Fig. 6.26 one can notice that there are some amplitude variations of residues among the models. The same effect is noticeable with the value of the damping coefficient. The reason for some of these variations is by increasing the pole set, new poles are created; a more accurate pole model is introduced, thus the total energy within a signal is redistributed to new poles. One has to note that the model cannot be arbitrarily increased since the method will start modeling noise.

As described in Chapter 5, the poles were eliminated based on two criteria: (a) singular value decomposition and (b) residue amplitude. The procedure is a very effective way of reducing the antenna model in order to obtain both a frequency and time-domain accurate antenna model. However, in the case of the Vivaldi antenna, Fig. 6.25 indicates a reduction in the 41-pole model based on residue amplitude criteria would result in the 17-pole model.

In summary, the complex poles for a 4-pole model, with the corresponding residue $\vec{R}(\theta,\phi)$ values in the boresight direction are given below:

$$s = 1\cdot 10^{9}\begin{bmatrix} -0.3330-1.7832i \\ -0.3330+1.7832i \\ -0.0716-0.3961i \\ -0.0716+0.3961i \end{bmatrix} \quad \vec{R}\left(0,\frac{\pi}{2}\right) = 1\cdot 10^{8}\begin{bmatrix} 0.0515+2.2497i \\ 0.0515-2.2497i \\ -0.3457-0.6121i \\ -0.3457+0.6121i \end{bmatrix}$$

The complex poles for 17-pole model with the corresponding residue $\vec{R}(\theta,\phi)$ values in the boresight direction are given as follows:

$$s = 1\cdot 10^{10}\begin{bmatrix} -0.0279+1.1420i \\ -0.0279-1.1420i \\ -0.0616+0.8970i \\ -0.0616-0.8970i \\ -0.0590+0.6171i \\ -0.0590-0.6171i \\ -0.0371+0.4004i \\ -0.0371-0.4004i \\ -0.0631+0.3225i \\ -0.0631-0.3225i \\ -0.0505+0.1727i \\ -0.0505-0.1727i \\ -0.0090+0.1090i \\ -0.0090-0.1090i \\ -0.0148+0.0390i \\ -0.0148-0.0390i \\ -0.0163+0.0000i \end{bmatrix} \quad \vec{R}\left(0,\frac{\pi}{2}\right) = 1\cdot 10^{8}\begin{bmatrix} -0.0616-0.2842i \\ -0.0616+0.2842i \\ -0.8563-0.1849i \\ -0.8563+0.1849i \\ -0.7928+1.0426i \\ -0.7928-1.0426i \\ 0.1167+0.4346i \\ 0.1167-0.4346i \\ 0.1896+2.1003i \\ 0.1896-2.1003i \\ 1.0936-2.3093i \\ 1.0936+2.3093i \\ 0.1568+0.1279i \\ 0.1568-0.1279i \\ -0.3729+1.6353i \\ -0.3729-1.6353i \\ 1.8455-0.0000i \end{bmatrix}$$

6.8 Conclusion

The concept of obtaining the frequency-domain patterns from a realized time-domain effective length is demonstrated using the Vivaldi antenna. Patterns in the upper hemisphere obtained from the time-domain realized effective length are in good agreement with the near-field measurements and simulations. The lower hemisphere shows deviations primarily due to the positioner mast needed for the frequency-domain pattern measurements. However, some errors can be attributed to IFFT/FFT transforms, the MP method, and some unresolved multi-path components.

The 41-pole model is adequate to describe an antenna pattern at any frequency in the range from 500 MHz - 20 GHz. The pattern variation for frequencies higher than 2.0 GHz up to 45 degrees is around 1 dB on average, both compared to simulation and near-field measurements. The model was not verified up to 20 GHz since the anechoic chamber is limited to around 12.0 GHz due to cable loss and limited dynamic range of the network vector analyzer.

The 17-pole model, reduced size model, is adequate to describe an antenna pattern at any frequency in the range from 500 MHz - 12 GHz. The 17-pole model shows good agreement to near-field patterns up to 70 degrees (1 dB of variation). Variations of 2-3 dB are present below 70 degrees. The simulations also show good agreement in the upper hemisphere.

The most notable differences in the pattern are at 1.0 GHz. The positioner mast the antenna is placed on, certainly contributes to the differences in the back-lobe of the antenna pattern. Also, some of the upper hemisphere differences result from the multipath inside the chamber since the absorber inside the anechoic chamber has a limited performance at 1.0 GHz. The difference in a lower hemisphere between the simulated patterns and patterns obtained using a pole/residue model could be attributed to noisy pole/residue values due to low signal to noise ratio.

One has to note that the 17-pole model is a set of 8+1 parameters. One parameter is a pole on the σ axis (models low frequency contributions) while the other poles are complex pairs. In order to have a real function, one needs complex conjugate pairs. Thus, in essence the17-pole model provides a set of 9 parameters (for each azimuth angle) that can describe the Vivaldi antenna frequency and time radiation characteristics at any frequency in the 500 MHz to 20 GHz range. Analogously, the 41-pole model provides a set of 20+1 parameters describing the radiation characteristics in the time and frequency domains for the Vivaldi antenna in the range of 500 MHz to 20.0 GHz. To our knowledge, this concept is demonstrated for the first time.

References

[6.1] J. D. Young, D. E. Svoboda, W. D. Burnside, ”A Comparison of Time- and Frequency-Domain Measurement Techniques in Antenna Theory,” *IEEE Trans. Antennas Propagat.*, communications, pp. 581-583, July 1973.

[6.2] J. M. Tranquilla and S. R. Best, ”Phase Center Variations for the Monopole Antenna,” *IEEE Trans. Antennas Propagat.* , vol. AP-34, No. 5, pp. 741-744, May 1986.

[6.3] D. Carter, ”Phase Centers of Microwave Antennas,” *IRE Trans. Antennas Propagat.* , pp. 597-600, October 1956.

[6.4] T. Yang, “Simulation of the Vivaldi Antenna,” *Internal Report – Virginia Tech Antenna Group*, April 6, 2004.

Chapter 7

Summary and Conclusions

A new methodology for characterizing antennas in both the time and frequency domain with one set of parameters has been presented in this work. Minimal modeling using the Matrix-Pencil method has been demonstrated. It has been shown that it is possible to obtain frequency-domain patterns from pole/residue models of the antenna realized effective length. Thus, a pole/residue model of the antenna realized effective length presents a complete antenna model in both the time and frequency domain. In essence, once the model is available one can obtain antenna pattern, directivity, and gain in the frequency domain, and at the same time one can obtain the radiated transient waveform for an arbitrary excitation waveform and an arbitrary antenna orientation.

7.1 Summary of the Results

The research has been preformed in multiple stages and each stage corresponds to one chapter of the thesis. First, basic elements of the methodology as development of effective length representation by W. A. Davis and SEM representation have been presented in Chapter 2. The properties of three classes of antennas in both the time and frequency domain were discussed in Chapter 3. That chapter laid the bases for all the measurements and led to a better understanding of antenna characteristics looking simultaneously at both of the domains. It greatly enhanced our understanding of the measured waveforms, which gave us a better understanding in how to accurately apply the spectral estimation techniques. In Chapter 4, spectral estimation techniques were improved and we came to a basic principle where one needs to understand the physical nature of the data before applying a spectral estimation method. Blindly applying spectral estimation methods always would lead to inaccurate results. In Chapter 5, pole/residue models were created for the antenna boresight direction using the Matrix-Pencil method. This gave a rise to a methodology for obtaining antenna frequency domain patterns from the pole/residue model described in Chapter 6. The following text gives a summary of all the results obtained through each individual chapter.

By using the antenna effective length one can model an antenna in both the time and frequency domain through the same set of parameters using the SEM representation. Since antennas are finite size objects, the SEM representation would only have singularities (poles/residues) on the left hand complex plane (passive systems).

Numerical methods for calculating the antenna effective length are very computationally intensive and antenna type selective. Thus, it becomes a question of convergence and accuracy of numerical results. Even though both numerical and measurement approaches provide some advantages and disadvantages, we took a measurement approach in obtaining the antenna effective length. To our knowledge, only a monopole was treated in such a measurement modeling approach. However, the results represent more a link response than a realized effective length of the monopole itself.

In Chapter 3, the processing in the time domain by HP8510 was investigated. It was found that the impulse response is obtained by using the chirp-z transform and a Kaiser-Bessel window with α=6 parameter. The step response is obtained by using effectively a low pass filter. A MATLAB® program was written that obtains the same results as HP8510 time-domain processing using FFT transforms.

All the antennas investigated exhibit a damped sinusoidal behavior due to the finite size of the antenna. A simple model is presented showing that in the time domain the fundamental resonant frequency has the most pronounced effect on the antenna pulse width and the basic pulse shape. This simple model approximates well the behavior of the class of traveling wave antennas: TEM Horn, Vivaldi antenna, bi-conical antenna, and ridged TEM Horn antenna.

The class of frequency-independent antennas exhibits a chirp type of response in the time domain. In the frequency domain, the response differs depending on the geometry of the frequency independent antenna, but is characterized by a nonlinear phase.

The class of resonant antennas suffers from very low efficiency. The pulse width is in duration of $5 \cdot 1/f_r$, where f_r is the fundamental resonance of the monopole antenna. The time-domain response is a damped sinusoid. The frequency response for a 5.0 GHz monopole link exhibits a $1/\omega^2$ behavior in the frequency domain due to a mismatch loss. The 1.0/1.1 GHz link shows distinct peaks in the frequency domain, which corresponds to resonant frequencies of the monopole antenna.

Due to a damped sinusoidal behavior of antennas it is possible to apply a damped sinusoidal model to approximate the measured results (e.g. Prony's method, Matrix-Pencil method).

It is shown in Chapter 4, through modest numerical results, that Prony's method works well if the Nyquist criterion is satisfied and the number of poles in the system is known. It is of the most importance to relate a physical interpretation of the waveform to Prony's method. Prony's method will always yield inaccurate results if used blindly. The new Prony's method formulations are introduced to handle double poles and variable sampling.

The presence of the double poles, when antennas in the link are identical, can be handled by using a new modified Prony's method that accommodates the extraction of double poles. In Chapter 5, we demonstrated a technique where a single antenna response is obtained and double poles are no longer present in the waveform.

Variable sampling, using a modified Prony's method formulation, gives better insights in the pole/residue extraction of the antenna systems and keeps the time-domain window of interest constant. By keeping the time-domain window of interest constant one can capture all the significant features of the particular response. The Matrix-Pencil method is a more elegant way of obtaining poles/residues of an antenna system and provides more accurate results.

The advantage of the frequency-domain spectral estimation methods is apparent if the measurements are performed in the frequency domain. Thus, one does not need to perform IFFT to obtain time-domain equivalent results and introduce more errors due to

Fourier transforms. However, the methods are not as convenient when comes to eliminating multi-path contributions and obtaining the minimal phase distance.

In Chapter 5 four antenna systems have been investigated in order to understand the trade-offs of the minimal pole/residue models. The antennas investigated fall in three categories: resonant, broadband, and frequency-independent antennas. There are distinct differences among the three classes of antennas in terms of modeling aspects.

The resonant structure is characterized by poles with low damping coefficients, which reflect in sharp peaks that are characteristic for the resonant structure. The resonant structure (monopole antenna) can be modeled with one dc pole and additional poles representing resonant frequencies close to the jω axis. The second layer poles model the effects between resonant frequencies.

Poles with high damping coefficients, which reflect broad peaks, characterize the broadband structures. The wideband structures (e.g. TEM Horn and bi-conical antenna) can be modeled with a dc pole, first resonant frequency pole, and additional high damping coefficient poles.

The minimal model analysis shows that the time-domain requires only a few poles to model the response of the TEM Horn, the 1.0 GHz resonant monopole, and the bi-conical antenna. However, the frequency domain requires a significant number of poles in order to accurately describe the response of a resonant structure; significantly fewer poles are needed for broadband structures. This suggests that most of the pulse energy is contained within the lowest resonant antenna frequencies in the time-domain responses. The higher order poles only model small variations of the time-domain realized effective length.

A frequency independent antenna (Archimedean spiral) can be modeled by a series of poles very closely spaced, damped coefficient less than 1.5 G/s, with a behavior $\sigma(j\omega) \sim A\sqrt{\omega}$. These types of antennas require a large number of poles (34 poles or fewer) to model both the time and frequency-domain realized effective length.

In conclusion, for time-domain base systems a few poles are often adequate to model the antenna response, except for the class of frequency independent antennas. For frequency-based systems, resonant antennas require more poles. Broadband antennas require few poles in both the time and frequency domain.

In Chapter 6, the concept of obtaining the frequency-domain patterns from the realized time-domain effective length is demonstrated using the Vivaldi antenna. Patterns in the upper hemisphere obtained from the time-domain realized effective length are in good agreement with near-field measurements and simulations. The lower hemisphere shows deviations primarily due to the positioner mast. However, some errors could be attributed to IFFT/FFT transforms, the MP method, and some unresolved multi-path components.

The 41-pole model could be adequate to describe the antenna pattern at any frequency in the range from 500 MHz - 20 GHz. The pattern variation for frequencies higher than 2.0 GHz up to 45 degrees is around 1 dB on average both compared to simulation and near-field measurements.

The 17-pole model is adequate to describe the antenna pattern at any frequency in the range from 500 MHz - 12 GHz. The 17-pole model shows good agreement to the near-field patterns up to 70 degrees (1 dB of variation). Variations of 2-3 dB are present below 70 degrees. The simulations also show good agreement in the upper hemisphere.

The most notable differences in the patterns are at 1.0 GHz. The positioner mast that antenna was placed on certainly contributed to the differences in the back-lobe of the antenna pattern. Also, some of the upper hemisphere differences could be contributed to the multi-path inside the chamber, since the absorbers inside the anechoic chamber have a limited performance at 1.0 GHz.

One has to note that a 17-pole model is a set of 8+1 parameters. One parameter is a pole on the σ axis (models low frequency contributions), while the other poles are complex. In order to have a real function, one needs a set of complex conjugate pairs. Thus, in essence a 17-pole model provides a set of 9 parameters (for each azimuth angle) that can describe the Vivaldi antenna frequency and time radiation characteristics at any frequency in 500 MHz to 12 GHz range. Analogously, the 41-pole model is a set of 20+1 parameters describing the radiation characteristics in the time and frequency domain of the Vivaldi antenna in the range of 500 MHz to 20.0 GHz.

The results presented led to some unique contributions. These contributions are outlined in the next section.

7.2 Contributions

The research presented led to one unique contribution:

- A new methodology for characterizing the antenna in both the time and frequency domain with one set of parameters

This contribution provides an antenna model that represents the following:

- A complete time and frequency domain characterization
- Minimal type of representation model (minimal data set to represent an antenna system)

Accurate minimal models in the antenna boresight direction are demonstrated for: TEM horn with only 8 parameters (16-pole model), monopole antenna model with 20+1 parameters (41-pole model), bi-conical antenna model with 3 parameters (6-pole model), and the Archimedean spiral antenna model with 17 parameters (34-pole model). The models presented model the antenna in the boresight direction in a frequency range from 500 MHz to 20.0 GHz. To our knowledge, this is the first time somebody demonstrated this type of modeling in terms of the antenna realized effective length. A significant development is also in demonstrating that it is possible to obtain the antenna frequency-domain patterns from pole/residue antenna models. This is demonstrated by using the Vivaldi antenna. To our knowledge, this is the first time someone demonstrated this concept. It was shown that a model of 8+1 parameters (17-pole model) could model any antenna frequency-domain pattern in the frequency range 500 MHz-12 GHz.

A modest contribution is achieved in obtaining poles and residues using Prony's method by using variable sampling. The variable sampling gives better insight into the pole/residue extraction of the antenna systems and keeps the time-domain window of interest constant. By keeping the time-domain window of interest constant one can capture all the significant features of the particular response without changing the spectral composition of the waveform of interest.

Other contributions that my work contributed to, but are original ideas of W. A. Davis, is the simple antenna model presented in Chapter 3, the explanation of the antenna differentiation aspect by band-limited nature of the antenna also in Chapter 3. This is also confirmed with a pole/residue models since it is shown that in the time-domain the lowest frequency pole/residue pairs determine the basic shape and duration of the time-domain antenna realized effective length.

7.3 Future Frontiers

The antenna modeling methodology could be applied to the design of communication systems and in ultra-wideband antenna measurements. This research also provides building blocks for designing efficient microwave X-wave generators or some other type of localized waves.

The models could be used in the design and simulation of communication systems. A communication engineer has at his disposal both time and frequency domain antenna “information”. If one were designing a multi-carrier system, a model would provide the antenna pattern, gain, and directivity. If one were designing an impulse modulation system, a model would provide a radiated transient waveform for any arbitrary excitation waveform and antenna orientation (pulse shape, amplitude, and duration).

On the other hand, there exists the possibility of making more efficient correlators since the model provides a set of basis functions defined by s-plane singularities. The s-plane singularities are the same regardless of the antenna orientation.

An antenna could be measured with this new modeling methodology. This would reduce the amount of time and data required to characterize an antenna system. One would first perform a measurement to determine the set of basis functions, s-plane singularities, usually at the antenna boresight. The s-plane singularities would be extracted using the Matrix-Pencil method. Then, one would perform measurements as a classical near field or far-field system at different points on a sphere surrounding the antenna. However, now one needs only to calculate residues, which is a straightforward task. The most optimal system would consist of a positioner system used in near-field system, a pulse generator as a transmitter, and a sampling scope as a receiver. This would reduce a measurement antenna time since instead of multiple single frequency measurements one would perform an impulse measurement that contains both time and frequency information.

The pole/residue models give a unique insight into antenna operation, thus they can be an aid in designing antennas. The mere fact that low frequency poles determine the basic shape of the radiated transient waveform sheds some light on how to design an antenna from a time-domain point of view.

Vita

Stanislav Licul was born in Pula, Republic of Croatia, on May 7, 1977. During the course of his studies, he worked at Motorola, Inc. and XM Satellite Radio, Inc. His duties included optimization of the paging/satellite receivers and design of antennas for satellite and mobile communications. His research encompasses modeling and design of ultra-wideband antennas and more efficient methods of measuring antennas in both the frequency and time domains. Stanislav Licul is a member of IEEE and Eta Kappa Nu. He was a scholarship member of the Virginia Tech Varsity Soccer Team and recipient of the Out of State Scholar Scholarship.